

ADVERTIMENT. L'accés als continguts d'aquesta tesi queda condicionat a l'acceptació de les condicions d'ús establertes per la següent llicència Creative Commons:  http://cat.creativecommons.org/?page_id=184

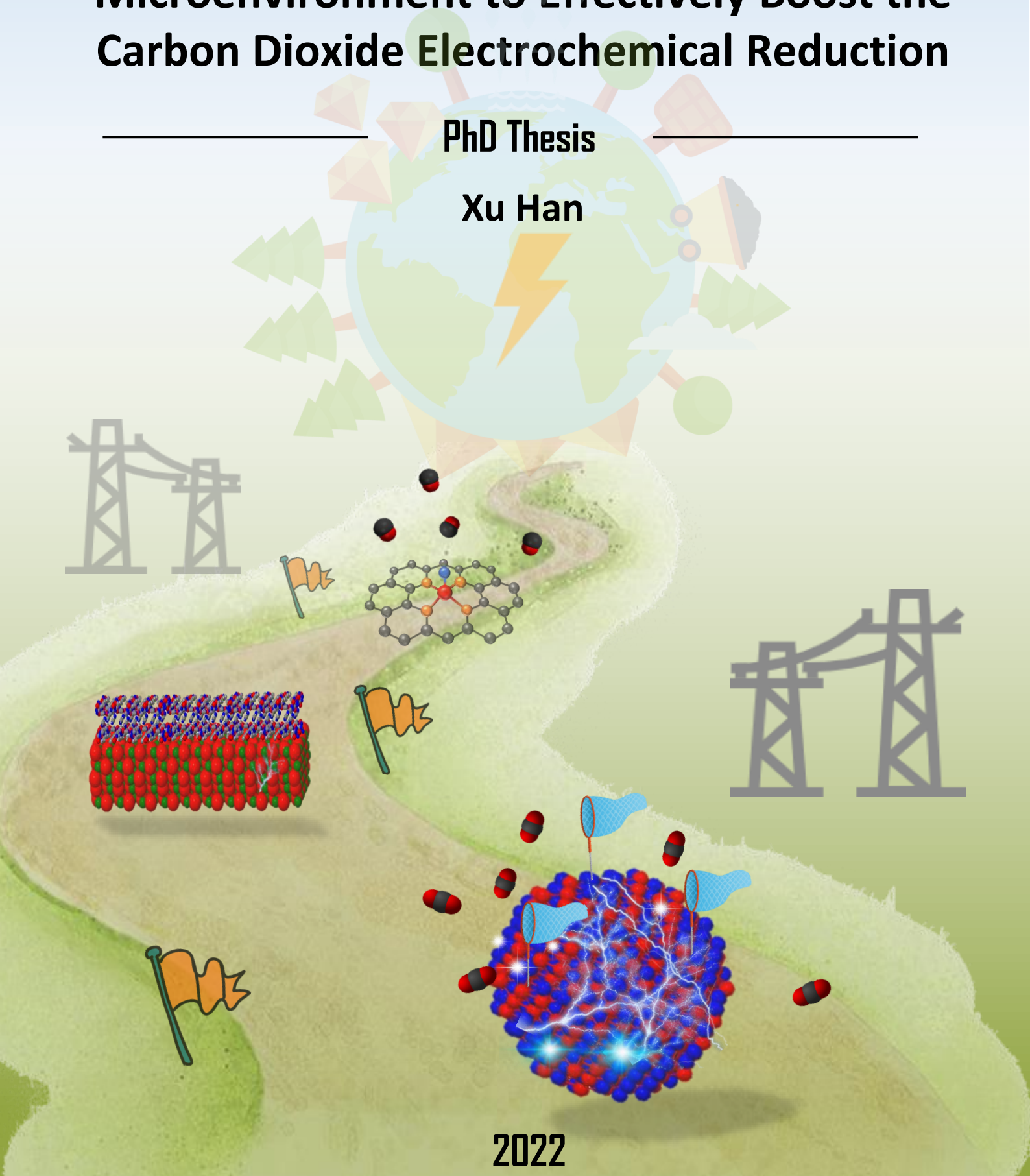
ADVERTENCIA. El acceso a los contenidos de esta tesis queda condicionado a la aceptación de las condiciones de uso establecidas por la siguiente licencia Creative Commons:  <http://es.creativecommons.org/blog/licencias/>

WARNING. The access to the contents of this doctoral thesis it is limited to the acceptance of the use conditions set by the following Creative Commons license:  <https://creativecommons.org/licenses/?lang=en>

Rational Design of the Catalysts Microenvironment to Effectively Boost the Carbon Dioxide Electrochemical Reduction

PhD Thesis

Xu Han



Doctorate Program in Materials Science

PhD Thesis

**Rational Design of the Catalysts
Microenvironment to Effectively Boost
the Carbon Dioxide Electrochemical
Reduction**

Xu Han

Director: Prof. Jordi Arbiol i Cobos

Institut Català de Nanociència i Nanotecnologia (ICN2), CSIC & BIST

Department of Chemistry, Faculty of Sciences

Universitat Autònoma de Barcelona (UAB)



Barcelona Institute of
Science and Technology



Jordi Arbiol i Cobos, ICREA Research Professor at Institut Català de Nanociència i Nanotecnologia (ICN2), CSIC & BIST

CERTIFY

that Mr. **Xu Han**, MSc in Physical Chemistry, carried out the work entitled “**Rational Design of the Catalysts Microenvironment to Effectively Boost the Carbon Dioxide Electrochemical Reduction**” under his direction and qualifies for the degree of Doctor in Materials Science.

And for that record, sign this certificate.

Prof. Jordi Arbiol i Cobos,

Xu Han

Bellaterra, May 2021

Table of Content

Acknowledgments	1
Abstract- English	3
Resum- Català	6
Resumen- Castellano	9
1. Introduction: Fundamental Concepts of CO₂ Electrochemical Reduction (eCO₂ RR)	12
1.1 Carbon neutrality	13
1.1.1 Background of carbon neutrality proposal	13
1.1.2 Connotation of carbon neutrality science	13
1.1.3 Challenges of achieving carbon neutrality	15
1.2 Electrochemical CO ₂ reduction	15
1.2.1 Fundamentals of electrochemical CO ₂ reduction	18
1.2.2 Mechanism of electrochemical CO ₂ reduction	22
1.3 Ex-situ and in-situ/operando characterization techniques to study the materials and reaction mechanism	25
1.3.1 In-situ and operando techniques	26
1.3.2 Infrared spectroscopy (IR)	26
1.3.3 Raman spectroscopy	28
1.3.4 X-Ray absorption spectroscopy (XAS)	29
1.3.4.1 Basic principle	29
1.3.4.2 Experiment setup	32
1.3.5 X-ray diffraction spectroscopy (XRD)	33
1.3.6 X-ray photoelectron spectroscopy (XPS)	34
1.3.7 Electron microscopy	34
1.3.7.1 Transmission Electron Microscopy (TEM)	34
1.3.7.2 Scanning Transmission Electron Microscopy (STEM)	35
1.3.7.3 High angle annular dark field (HAADF)	35
1.3.7.4 Annular bright field (ABF)	36
1.3.7.5 Integrated differential phase contrast (iDPC)	37
1.3.7.6 Energy-dispersive X-ray spectroscopy (EDS) and Electron energy loss spectroscopy (EELS)	37
1.4 System Design for CO ₂ electroreduction	39
1.4.1 Flow reactor	39
1.4.2 Liquid-phase electrolyzer	40
1.4.3 Gas-phase electrolyser	41
1.4.4 Ion-exchange membrane	41
1.4.5 Gas diffusion electrode (GDE)	42
1.4.6 Electrolyte engineering	43
1.4.6.1 Aqueous electrolytes	43
1.4.6.2 Organic electrolytes	44
1.4.6.3 Ionic liquids	44
1.4.6.4 Pressure	45
1.4.6.5 Temperature	45

1.5 Catalyst engineering.....	45
1.5.1 Metal-based catalysts.....	46
1.5.2 Carbon-based catalysts	46
1.5.2.1 Metal-nitrogen doped carbon catalyst	46
1.5.2.2 Metal-free carbon catalyst	47
1.5.3 Metal organic frameworks (MOFs).....	47
1.5.3.1 Pristine MOF.....	47
1.5.3.2 MOF derivatives	48
1.5.3.2.1 Carbon scaffolds	48
1.5.3.2.2 Metal oxides	49
1.5.3.2.3 Metal oxide-carbon composites	50
1.5.3.3 MOF composite	51
1.5.3.3.1 Metal-nanoparticles@MOFs	51
1.5.3.3.2 MOFs@functional materials	52
References.....	53
2. Methodology	61
2.1 Electrochemistry	62
2.1.1 Nernst equation	62
2.1.2 Scan rate.....	63
2.1.3 Electrochemical active surface area (ECSA)	63
2.1.4 Instantaneous Faraday efficiency	64
2.1.5 Average Faraday efficiency.....	65
2.2 Ink Preparation.....	66
References.....	67
3. Engineering the Interfacial Microenvironment of ZnO via Surface Hydroxylation to Realize the Global Optimization of Electrochemical CO₂ Reduction	68
3.1 Introduction	69
3.2 Experimental Section.....	71
3.2.1 Materials and Characterizations	71
3.2.2 Synthesis Methods	72
3.2.2.1 Preparation of ZIF-8	72
3.2.2.2 Preparation of Zn ₅ (OH) ₈ (NO ₃) ₂ (H ₂ O) ₂	72
3.2.2.3 Preparation of ZnO-OH.....	72
3.2.2.4 Preparation of D-ZnO	73
3.2.3 Preparation of Working Electrodes	73
3.2.4 Electrochemical Measurement	73
3.2.5 Calculation Method.....	73
3.2.6 DFT Calculations	73
3.3 Results and Discussion	75
3.3.1 DFT Presupposition	75
3.3.2 Sample Characterization	76
3.3.3 Electrochemical Performance	85
3.3.4 DFT Calculation	92
3.4 Summary	94

References.....	96
4. Surface functionalization of ZnO nanorods with a MOF shell for Boosting CO Production in Electrocatalytic CO₂ Reduction	100
4.1 Introduction	101
4.2 Experimental Section.....	103
4.2.1 Materials and Characterizations	104
4.2.2 Synthesis Methods	104
4.2.2.1 Preparation of ZIF-8.....	104
4.2.2.2 Preparation of ZnO Nanorods (ZnO NRs)	105
4.2.2.3 Preparation of ZnO NR@ZIF-8.....	105
4.2.3 Preparation of working electrodes.....	105
4.2.4 Electrochemical Measurement	106
4.2.5 Calculation Method.....	106
4.3 Results and Discussion	106
4.3.1 Sample Characterization	106
4.3.2 Electrochemical Performance	113
4.4 Summary	120
References.....	122
5. Site-Specific Axial Oxygen Coordinated FeN₄ Active Sites for Highly Selective Electroreduction of Carbon Dioxide.....	124
5.1 Introduction	125
5.2 Experimental Section.....	127
5.2.1 Materials and Characterizations	127
5.2.2 Synthesis Methods	128
5.2.2.1 Preparation of IRMOF-3	128
5.2.2.2 Preparation of ZIF-8	128
5.2.2.3 Preparation of Fe-IRMOF-3 and Fe-ZIF-8	127
5.2.2.4 Preparation of Disperse Fe-N-C (denoted as O-Fe-N-C and Fe-N-C)	129
5.2.2.5 Preparation of O-Fe-N-C-Acid.....	129
5.2.3 Preparation of working electrodes.....	129
5.2.4 Electrochemical Measurement	129
5.2.5 Calculation Method.....	129
5.2.6 XAFS Measurements	130
5.2.7 XAFS Analysis and Results	130
5.2.8 DFT Calculations.....	130
5.3 Results and Discussion	132
5.3.1 Sample Characterization	132
5.3.2 Electrochemical Performance	138
5.3.4 DFT Calculations.....	144
5.4 Summary	146
References.....	147
6. General Conclusions and Outlook.....	152
6.1 General Conclusions	153
6.2 Outlook	155

List of Publications.....	158
----------------------------------	------------

Acknowledgments

First and foremost, I would like to thank my supervisor Prof. Dr. Jordi Arbiol. He has given me the opportunity to be a member of the Advanced Electron Nanoscopy Group (GAe⁻N). His supervision, encouragement, and scientific attitudes encouraged me to move forward with my projects. Meanwhile, his unwavering support and belief in me have boosted my self-esteem as a researcher. Furthermore, I would also like to thank Prof. Dr. Daniel MasPOCH for his guidance and discussions. I really appreciate his encouragement and support when I was doing experiments at the Supermolecular Nanochemistry and Materials Group for more than one year. A similar debt of gratitude is owed to Dr. Inhar Imaz, from whom I have learned a great deal about MOFs preparation and applications. Meanwhile, I would like to express my thanks to Prof. Dr. Belen Ballesteros, Marcos Rosado, Francisco Belarre, Dr. Javier Saiz, Dr. Jessica Padilla Pantoja and Dr. Guillaume Sauthier who gave me their invaluable support on TEM maintenance, SEM operations and other characterization techniques.

Secondly, I would like to thank all members in GAe⁻N group (ICN2), Marc, Sara, Pengyi, Chiara, Zhifu, Ying, Shunrui, Ivan, Jérémy, Christian and Ting. During my PhD studies, they gave me a comfortable scientific environment and a pleasant memory during the past years. It has been an absolute pleasure to be a member of this group where professional as well as personal engagement is shown. More importantly, the kindnesses of the group members enabled me to quickly adapt to Catalan life, which will be a wonderful memory for me. Meanwhile, thanks to my friends at ICN2 and UAB: Junjie, Yunhui, Liming, Yang, Jieming, Qiuyue, Lei, Jiarui, Kai, Xudong, Jiahui, Nour and Guba *et al.* I also express my thanks to Dr. Weiqing Tang from East China University of Science and Technology (Shanghai, China) and Dr. Hong Liu from School of Physical Science and Technology ShanghaiTech University, who provided the DFT support to my work. In addition, thanks to all the technical staff and colleagues working at ICN2 and UAB for their technical support. I also would like to express my thanks to all the collaborators that provided me with TEM samples, Wei, Prof. Dr. Jan Fransær from

KU Leuven, Mengyao, Congcong, Ruifeng, Yong, Junshan, Yu, Xiang, Dawei, Prof. Dr. Andreu Cabot from IREC and Dr. Jian Li from EPFL, who gave me strong support on my TEM characterization works. Meanwhile, a similar debt of gratitude is owed to Dr. Marti Biset Peiro and Prof. Dr. Joan Ramon Morante Lleonart in IREC, who gave me a strong support to finish my research work.

Furthermore, I would like to thank Prof. Rafal E. Dunin-Borkowski and Prof. Dr. Knut Müller at Jülich (Germany) who gave me an opportunity to conduct the TEM research in their group for two months. Meanwhile, an equal amount of gratitude is extended to Prof. Kim Daasbjerg (Aarhus University, Denmark) for his hospitality and fruitful discussions during my three months research stay. Finally, I would like to acknowledge the scholarship I received from the German Academic Exchange Service (DAAD) and ICN2 Severo Ochoa Mobility Program for my stay in Germany.

In addition, I really appreciate China Scholarship Council (CSC), for the financial support, which made all the work possible.

Finally, thanks to my parents who gave me great support and understanding during my PhD period, and to my girlfriend Ting for her love, patience and understanding in the past years.

Thank you!

Xu Han

Barcelona, May 2022

Abstract - English

The excessive combustion of fossil fuels results in the emission of carbon dioxide (CO_2), which triggers increasing environmental problems, such as global warming, rising sea levels, extreme weather, and species extinction. Conversion of CO_2 into other value products plays a vital role to eliminate anthropogenic CO_2 in the atmosphere. Thereinto, electrochemical conversion of CO_2 powered by renewable energy to useful chemicals is considered as an elegant solution to achieve the carbon cycle.

However, due to the innerness of CO_2 molecules, products uncertainty and competitive hydrogen evolution reaction (HER), the main challenges in the field of CO_2 RR are the high overpotential requirement that represents the unfavourable thermodynamics and low Faradaic efficiency (FE) for the target products. To tame CO_2 more effectively, many excellent works have been reported on the mechanism of CO_2 RR. Focusing on the unfavourable factors appearing in the reaction mechanism, the optimization of existing catalysts or preparation of new catalysts could get more purposefully and advisably.

In this dissertation we only focused on CO_2 -to-CO conversion. Since CO is one of the most promising target products when it is evaluated between the marking prices and the cost of electricity. Besides, it is the simplest product only going through two electrons and two protons transform which is easier to explore and analyse optimized strategies. Theoretically, this conversion goes through the following steps. Firstly, inert gas CO_2 molecules should be adsorbed by chemically or physically at active states on the surface of catalysts. Next, through the proton-coupled electron transfer (PCET) process, the CO_2 transform into COOH^* intermediates. The state and property of this intermediate on the surface of the catalyst, such as stability, density and configuration will directly affect the generation of subsequent intermediates and products. When COOH^* intermediate goes through the next PCET process, the intermediate CO^* and water will generate. Unfortunately, the intermediate CO^* must have appropriate bond energy with the active site of the catalyst to get the final CO product. If this

energy is inappropriate, the catalyst will be poisoned and thus go to death, leading to a poor CO selectivity. We will optimize different key steps of CO₂-to-CO conversion by taking different strategies. The goal of the present dissertation is to improve certain steps on certain catalysts to realize improved activity and selectivity of the CO₂-to-CO conversion. The main idea is changing the local environment of active sites to make them more favourable for conversion. The whole work includes three parts, focusing on improving adsorption of CO₂, the transformation of CO₂ and desorption of CO₂ respectively to optimize activity and selectivity on catalysts.

In **Chapter 1**, we introduced the fundamental concepts of carbon neutrality and electrochemical CO₂ reduction which includes some important factors to evaluate this conversion. Meanwhile, a great deal of space is devoted to the introduction of characterization techniques. In addition to characterize catalysts themselves, in-situ/operando characterization techniques are also introduced to detect the reaction process and intermediates. These techniques provide more opportunities to reveal and explain the structure-property relationships during eCO₂ RR. For heterogeneous systems, systemic design for CO₂ electroreduction also could be optimized. Here, we summarized several systems and factors to improve the efficiency of CO₂ conversion.

In **Chapter 2**, we summarized the applied methodologies in this dissertation. This chapter includes details about electrochemical characterization techniques, such as cyclic voltammetry (CV), linear sweep voltammetry (LSV), electrochemical surface area (ECSA) and ink preparation. Specific synthesis procedures and experimental results for each studied material are presented in **Chapters 3-5**.

In **Chapter 3**, a ZnO-based catalyst functionalized with surficial -OH groups was prepared by a facile MOF-assisted strategy. The experiment and calculation results supported that delicate design of such interfacial microenvironment induced by CO₂-philic hydroxyl boosts the adsorption and activation of CO₂ during CO₂-to-CO conversion at the first step and more importantly this special structure could realize the global optimization of the whole conversion process.

In **Chapter 4**, a MOF layer directly grows on the surface of ZnO to construct the microenvironment which can promote the CO₂-to-CO conversion on the interface between ZnO and MOF. This porous layer with CO₂ affinity not only realizes high CO₂ concentration in the vicinity of active sites but also strengthens the local pH effect during the reaction process to suppress HER. In addition, the interfacial microenvironment could enhance whole material stability under CO₂ RR conditions.

In **Chapter 5**, an atomically dispersed FeN₄ catalyst functionalized with an axial bonded O-containing coordination has been constructed via utilizing an oxygen and nitrogen-rich MOFs (IRMOF-3) as the precursor. The obtained FeN₄-O active site exhibits an enhanced FE_{CO}, which is higher than that of the reported unmodified FeN₄ sites and even higher than many other state-of-the-art SACs catalysts. Transmission electron microscopy (TEM) and X-ray absorption spectroscopy (XAS) were used to characterize the local environment of active sites. Both experimental and theoretical results further proved that such rationally engineering the coordination environment of FeN₄ to change the electronic structure via hydroxide subgroups can effectively boost the CO₂ RR activity through reducing the binding energies of CO desorption and disfavoring HER.

Finally, **Chapter 6** summarizes the general conclusions of this dissertation, along with a brief outlook. Several targets we proposed need to be realized in the future to achieve carbon neutrality.

Resum - Català

La combustió excessiva de combustibles fòssils provoca l'emissió de diòxid de carboni (CO_2), que desencadena problemes ambientals creixents, com l'escalfament global, l'augment del nivell del mar, el clima extrem i l'extinció d'espècies. La conversió de CO_2 en altres productes de valor té un paper vital per eliminar el CO_2 antropogènic de l'atmosfera. En aquest sentit, la conversió electroquímica del CO_2 alimentat amb energies renovables en productes químics útils es considera una solució elegant per aconseguir el cicle del carboni.

No obstant això, a causa de la interioritat de les molècules de CO_2 , la incertesa del producte i la reacció competitiva d'evolució d'hidrogen (HER), els principals reptes en el camp del CO_2 RR són l'elevat requisit de sobrepotencial que representa la termodinàmica desfavorable i la baixa eficiència Faradaica (FE). Per controlar el CO_2 de manera més eficaç, s'han informat molts treballs sobre el mecanisme del CO_2 RR. Centrant-nos en els factors desfavorables que apareixen en el mecanisme de reacció, l'optimització dels catalitzadors existents o la preparació de nous catalitzadors podria ser la proposta més aconsellable.

En aquesta tesi només ens centrem en la conversió de CO_2 a CO. El CO és un dels productes objectiu més prometedors quan s'avalua entre els preus de mercat i el cost de l'electricitat. A més, és el producte més senzill que només passa per una transformació de dos electrons i dos protons, que és més fàcil d'explorar i analitzar estratègies optimitzades. Teòricament, aquesta conversió passa pels passos següents: En primer lloc, les molècules de CO_2 de gas inert s'han d'adsorbir en estats actius a la superfície dels catalitzadors. A continuació, mitjançant el procés de transferència d'electrons acoblats a protons (PCET), el CO_2 es transforma en intermedis COOH^* . L'estat i la propietat d'aquest intermedi a la superfície del catalitzador, com ara l'estabilitat, la densitat i la configuració, afectaran directament la generació de productes intermedis i finals. Quan el COOH^* intermedi passa pel següent procés PCET, es genera el CO^* intermedi i aigua. Malauradament, el CO^* intermedi ha de tenir una

energia d'enllaç adequada amb el lloc actiu del catalitzador per obtenir el producte final de CO. Si aquesta energia és inadequada, el catalitzador estarà mort o la selectivitat del CO es veurà molt afectada. Optimitzarem el catalitzador d'òxid metàl·lic anterior o sintetitzarem un nou catalitzador per ajustar diferents passos clau de la conversió de CO₂ a CO mitjançant diferents estratègies. L'objectiu de la tesi és millorar determinats passos per a determinats catalitzadors per aconseguir una millora de la productivitat i la selectivitat de la conversió de CO₂ a CO. La idea principal és canviar l'entorn local del lloc actiu que sigui més favorable per a la conversió. Tot el treball inclou tres parts, centrades en l'adsorció de CO₂, la transformació de CO₂ i la desorció de CO₂ respectivament per optimitzar els catalitzadors.

Al capítol 1 hem introduït els conceptes fonamentals de neutralitat de carboni i reducció electroquímica de CO₂ que inclou els fonaments de la RR de CO₂ electroquímica, i alguns factors importants per avaluar aquesta conversió. A la introducció hem detallat les tècniques de caracterització utilitzades. A més de caracteritzar els mateixos catalitzadors, també es poden utilitzar tècniques de caracterització in-situ/operando per detectar el procés de reacció i els intermedis. Aquestes tècniques ofereixen més oportunitats per revelar i explicar les relacions estructura-propietat. Per als catalitzadors heterogenis, el disseny del sistema per a l'electroreducció de CO₂ també podria millorar encara més l'eficiència de la conversió de CO₂.

Al capítol 2 hem resumit les metodologies aplicades en aquesta tesi. Aquest capítol inclou detalls sobre les tècniques de caracterització electroquímica, com ara la voltametria cíclica (CV), la voltametria d'escombrat lineal (LSV), la superfície electroquímica (ECSA) i la preparació de la tinta. Els procediments de síntesi específics i els resultats experimentals per a cada material estudiat es presenten als capítols 3-5. Al capítol 3, es va preparar un catalitzador basat en ZnO funcionalitzat amb grups -OH superficials mitjançant una estratègia fàcil assistida per MOFs. Els resultats experimentals i els càlculs teòrics donen suport a que aquest microentorn interfacial induït per l'hidroxil CO₂-fílic augmenta l'adsorció i l'activació del CO₂ durant la

conversió de CO_2 a CO en el primer pas i, el que és més important, aquesta estructura especial podria realitzar l'optimització global de tot el procés de conversió.

Al capítol 4, la capa MOF creix directament a la superfície de ZnO per construir el microentorn que pot promoure la conversió de CO_2 a CO a la interfície entre el ZnO i el MOF. Aquesta capa porosa amb afinitat al CO_2 no només aconsegueix una alta concentració de CO_2 a les proximitats dels llocs actius, sinó que també reforça l'efecte del pH local durant el procés de reacció per suprimir la HER. A més, el microentorn interfacial podria millorar l'estabilitat del material en condicions de CO_2 RR.

Al capítol 5, s'ha construït un catalitzador de FeN_4 dispersat atòmicament funcionalitzat amb una coordinació que conté O enllaçat axialment mitjançant l'ús d'un MOF ric en oxigen i nitrogen (IRMOF-3) com a precursor. El lloc actiu $\text{FeN}_4\text{-O}$ obtingut presenta una FE_{CO} millorada, que és superior a la dels centres actius de FeN_4 no modificats reportats i fins i tot superior a molts altres catalitzadors SAC d'última generació. La microscòpia electrònica de transmissió (TEM) i l'espectroscòpia d'absorció de raigs X (XAS) es van utilitzar per caracteritzar l'entorn local dels centres actius. Tant els resultats experimentals com els teòrics van demostrar, a més, que l'enginyeria racional de l'entorn de coordinació de FeN_4 mitjançant subgrups d'hidròxid pot augmentar eficaçment l'activitat de CO_2 RR mitjançant la reducció de les energies d'unió de la desorció de CO i desafavorir la HER.

Finalment, el capítol 6 resumeix les conclusions generals d'aquesta tesi, juntament amb una breu visió de futur. En definitiva, 'els diversos objectius que hem proposat sahurien de complir en el futur per poder aconseguir la neutralitat del cicle del carboni.

Resumen – Castellano

La combustión excesiva de combustibles fósiles da como resultado la emisión de dióxido de carbono (CO_2), lo que desencadena crecientes problemas ambientales, como el calentamiento global, el aumento del nivel del mar, el clima extremo y la extinción de especies. La conversión de CO_2 en otros productos de valor juega un papel vital para eliminar el CO_2 antropogénico en la atmósfera. En este sentido, la conversión electroquímica de CO_2 alimentado por energía renovable en productos químicos útiles se considera una solución elegante para lograr el ciclo del carbono.

Sin embargo, debido a la interioridad de las moléculas de CO_2 , la incertidumbre de los productos y la reacción competitiva de evolución de hidrógeno (HER), los principales desafíos en el campo de CO_2 RR son el alto requisito de sobrepotencial que representa la termodinámica desfavorable y la baja eficiencia Faradaica (FE) para el producto final que tenemos como objetivo s. Para controlar el CO_2 de manera más efectiva, se han reportado muchos trabajos sobre el mecanismo de CO_2 RR. Centrándonos en los factores desfavorables que aparecen en el mecanismo de reacción, la optimización de los catalizadores existentes o la preparación de nuevos catalizadores podría ser más útil y conveniente.

En esta disertación sólo nos enfocamos en la conversión de CO_2 a CO. El CO es uno de los productos objetivo más prometedores cuando se evalúa entre los precios de mercado y el costo de la electricidad. Además, es el producto más simple que sólo pasa por la transformación de dos electrones y dos protones, lo que es más fácil de explorar y analizar estrategias optimizadas. Teóricamente, esta conversión pasa por los siguientes pasos. En primer lugar, las moléculas de gas inerte CO_2 deben adsorberse en estado activo en la superficie de los catalizadores. A continuación, a través del proceso de transferencia de electrones acoplados a protones (PCET), el CO_2 se transforma en COOH^* intermedios. El estado y la propiedad de este producto intermedio en la superficie del catalizador, como la estabilidad, la densidad y la configuración, afectarán directamente a la generación del producto intermedio y posterior. Cuando el intermedio COOH^* pasa por el siguiente proceso PCET, se

generará el CO^* intermedio y el agua. Desafortunadamente, el CO^* intermedio debe tener una energía de enlace adecuada con el sitio activo del catalizador para obtener el producto final de CO . Si esta energía es inapropiada, el catalizador podría deteriorarse o la selectividad del CO se vería muy afectada. En este trabajo, hemos optimizado el catalizador de óxido de metal o hemos sintetizado un nuevo catalizador para ajustar diferentes pasos clave de la conversión de CO_2 a CO mediante la adopción de diferentes estrategias. El objetivo de la disertación es mejorar ciertos pasos para que ciertos catalizadores logren mejorar la productividad y la selectividad de la conversión de CO_2 a CO . La idea principal es que cambie el entorno local del centro activo que sea más favorable para la conversión. El trabajo completo incluye tres partes, que se centran en la adsorción de CO_2 , la transformación de CO_2 y la desorción de CO_2 , respectivamente, para optimizar los catalizadores.

En el Capítulo 1 introducimos los conceptos fundamentales de la neutralidad de carbono y la reducción electroquímica de CO_2 , que incluye los fundamentos de la RR electroquímica de CO_2 y algunos factores importantes para evaluar esta conversión. Mientras tanto, se dedica la introducción para detallar las técnicas de caracterización. Además de caracterizar los propios catalizadores, las técnicas de caracterización in-situ/operando también se pueden utilizar para detectar el proceso de reacción y los productos intermedios. Estas técnicas brindan más oportunidades para revelar y explicar las relaciones estructura-propiedad. Para catalizadores heterogéneos, el diseño del sistema para la electrorreducción de CO_2 también podría mejorar aún más la eficiencia de la conversión de CO_2 . En la última parte, resumimos algunos materiales generales utilizados en CO_2 RR.

En el Capítulo 2, resumimos las metodologías aplicadas en esta tesis. Este capítulo incluye detalles sobre las técnicas de caracterización electroquímica, como la voltamperometría cíclica (CV), la voltamperometría de barrido lineal (LSV), el área superficial electroquímica (ECSA) y la preparación de la tinta. Los procedimientos de síntesis específicos y los resultados experimentales para cada material estudiado se presentan en los Capítulos 3-5.

En el Capítulo 3, se preparó un catalizador basado en ZnO funcionalizado con grupos -OH superficiales mediante una estrategia sencilla asistida por MOFs. Los resultados experimentales y los cálculos teóricos respaldan que este microambiente interfacial inducido por el hidroxilo CO₂-fílico aumentan la adsorción y activación de CO₂ durante la conversión de CO₂ a CO en el primer paso y, lo que es más importante, esta estructura especial podría realizar la optimización global de todo el proceso de conversión.

En el Capítulo 4, la capa de MOF crece directamente sobre la superficie de ZnO para construir el microambiente que puede promover la conversión de CO₂ a CO en la interfaz entre ZnO y MOF. Esta capa porosa con afinidad por el CO₂ no solo genera una alta concentración de CO₂ en la vecindad de los centros activos, sino que también fortalece el efecto del pH local durante el proceso de reacción para suprimir la HER. Además, el microambiente interfacial podría mejorar la estabilidad de todo el material en condiciones de CO₂ RR.

En el Capítulo 5, se ha construido un catalizador basado en FeN₄ disperso atómicamente funcionalizado con una coordinación que contiene O enlazada axialmente mediante la utilización de MOFs ricos en oxígeno y nitrógeno (IRMOF-3) como precursor. El sitio activo FeN₄-O obtenido exhibe un FE_{CO} mejorado, que es más alto que el de los sitios FeN₄ no modificados reportados e incluso más alto que muchos otros catalizadores SAC de última generación. La microscopía electrónica de transmisión (TEM) y la espectroscopia de absorción de rayos X (XAS) se utilizaron para caracterizar el entorno local de los sitios activos. Tanto los resultados experimentales como los teóricos demostraron además que la ingeniería racional del entorno de coordinación de FeN₄ a través de subgrupos de hidróxido puede impulsar de manera efectiva la actividad de la CO₂ RR al reducir las energías de unión de la desorción de CO y desfavorecer la HER.

Finalmente, el Capítulo 6 resume las conclusiones generales de esta tesis, junto con una breve perspectiva. Varios objetivos de los que hemos propuesto deberían cumplirse en el futuro para lograr la neutralidad del ciclo del carbono.

Chapter 1

Introduction: Fundamental Concepts of CO₂ Electrochemical Reduction

1.1 Carbon neutrality

1.1.1 Background of carbon neutrality proposal

CO₂ has been proved as a key mechanism for global warming, via global temperature stack and transient modelling, during the last deglaciation.^{1,2} This covariation of CO₂ concentration and temperature will affect the environment of all living things on this planet such as rising sea levels, extreme weather, and species extinction. To address the global climate change, realize the progress of civilization and economy, and the sustainable development of ecosystem on the earth, the 21st United Nations Climate Change (UNFCCC) Conference adopted the Paris Climate Agreement in December 2015, proposing the goal of achieving “net zero emissions” of CO₂, or carbon neutrality which gives a reasonable chance of limiting warming to 1.5 °C around 2050 (**Figure 1.1**).³

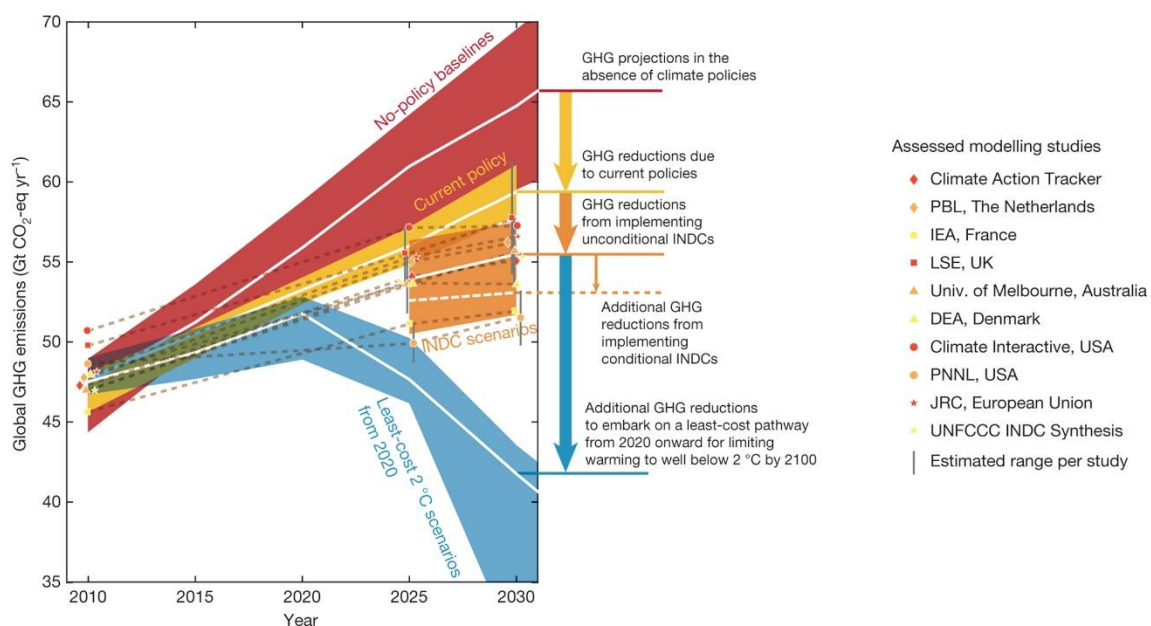


Figure 1.1 Global greenhouse gas (GHG) emissions as implied by Intended Nationally Determined Contributions (INDCs) compared to no-policy baseline, current-policy and 2 °C scenarios.

1.1.2 Connotation of carbon neutrality science

For carbon neutrality, in a broad sense, there is a dynamic balance between carbon-emitting systems and carbon sink systems in our whole planet. In a narrow sense and theoretical connotation, carbon neutrality science refers to a discipline that studies how to minimize the footprint of human activities on the natural environment for the

purpose of striking a dynamic balance between carbon emissions caused by human activities and the carbon cycle system on the earth through the ordered replacement of fossil energy sources with carbon-free new energy sources relying on economic and industrial policies and energy technologies. It is a cross-discipline between energy science and social science. So far, there are several technological methodologies to realize this grand goal such as carbon emission reduction technologies, zero-carbon emissions technologies, negative carbon emissions technologies and carbon economy technologies. In other words, the core of carbon neutrality is to reduce and even eliminate CO₂ emissions.⁴

Considering the duality of CO₂, it can be converted into organic matter in the ecosystem or produce greenhouse effect. The CO₂ could be divided into “grey carbon” and “black carbon”. Compare with black one, grey one could be used or sequestered by humans through artificial green conversion by CO₂ to production of chemical products. This method can reduce the concentration of CO₂ at the atmosphere. The core methodology to realize the goal of carbon neutrality is CO₂ capture, utilization, and storage (CCUS) or CO₂ capture and storage (CCS), as shown in **Figure 1.2**. The main objective of this field is to promote a technological revolution, which will be able to decrease the proportion of “black carbon” and even make it disappear in the future.⁴

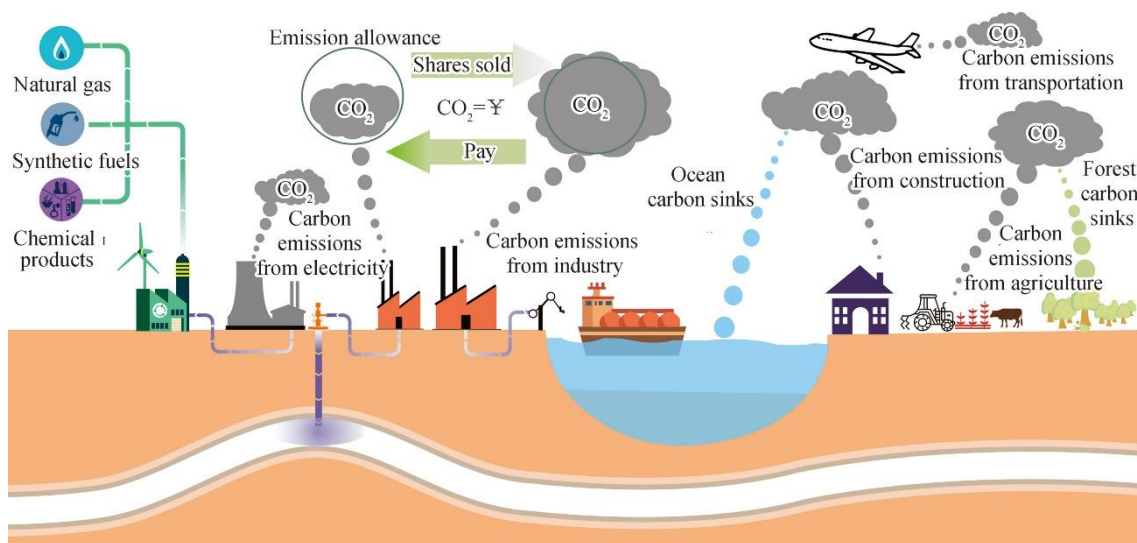


Figure 1.2 Composition of carbon industry system with CCUS/CCS.

1.1.3 Challenges of achieving carbon neutrality

Firstly, fossil energy will still dominate the global energy consumption structure for a long time. As shown in **Figure 1.3**⁵, the petroleum and other liquid fuels will occupy the main demand in the next few decades. When we look at this trend in a longer term, the renewables use grows to nearly the same level by 2050. New energy sources take up and completely replace fossil fuels is challenging following such a trend. Secondly, the utilization of new energy resources, which are intermittent and variable in spatial distribution such as solar energy and wind energy are also limited on the large-scale development of new energy. Therefore, CO₂ recycling enables the storage of renewable electricity from intermittent sources in a dense and versatile form, provides a renewable carbon feedstock to chemical industries, and adds value to CO₂ captured at industrial point sources or directly from the air.

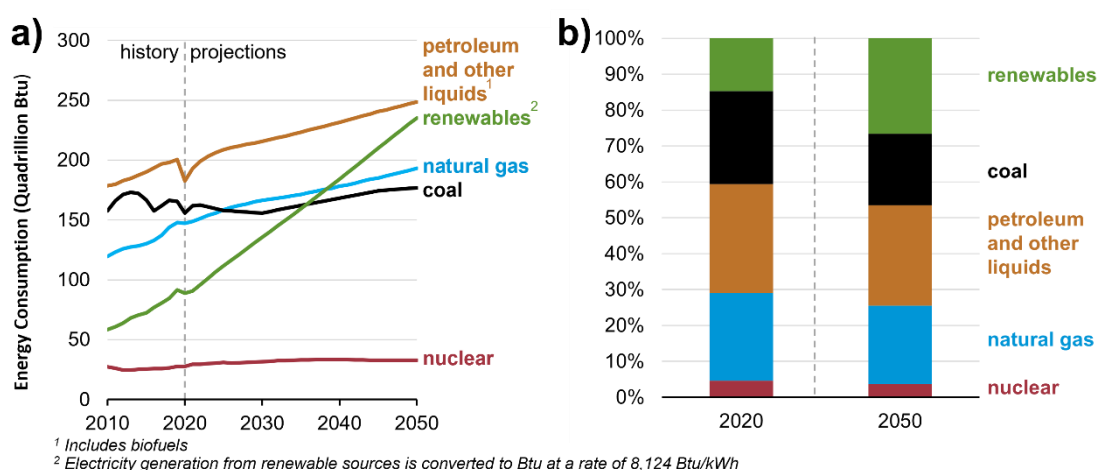


Figure 1.3 Current and Projected Energy Consumption and Share by Energy Source (From EIA International Energy Outlook 2020).

- (a) Global energy consumption by energy source.
- (b) Share of energy consumption by source.

1.2 Electrochemical CO₂ reduction

The electrochemical CO₂ reaction reduction (eCO₂RR) enables the storage of the intermittent renewable electricity with CO₂ molecules into higher-value chemical products from raw chemicals to transportation fuels in a dense and versatile form to meet different requirements (**Table 1.1**).⁶ Theoretically, by transferring multiple

protons and electrons, various kinds of gas and liquid products could be obtained by eCO₂RR, as listed in **Table 1.2**. C₁ products such as carbon dioxide (CO), formic acid (HCOOH), methanol (CH₃OH), methane (CH₄), C₂ products such as ethylene (C₂H₄), acetic acid (CH₃COOH) and ethanol (CH₃CH₂OH), and C₃ products such as propanol (C₃H₇OH). Usually, the higher-carbon hydrocarbon products mean a higher energy density and market price (**Table 1.2**).^{7,8} However, these higher energy density products require more protons and electrons with longer coupling steps in the eCO₂RR.⁹

Table 1.1 Products of electrochemical CO₂ reduction and redox potential at pH=7

Half-reactions	Electrode Potentials (vs. RHE) at pH=7
$\text{CO}_2(\text{g}) + \text{e}^- \rightarrow \text{CO}_2^{\cdot -}$	-1.48
$\text{CO}_2(\text{g}) + 2\text{e}^- + 2\text{H}^+ \rightarrow \text{HCOOH} (\text{l})$	-0.250
$\text{CO}_2(\text{g}) + 2\text{e}^- + 2\text{H}^+ \rightarrow \text{CO}(\text{g}) + \text{H}_2\text{O}(\text{l})$	-0.106
$\text{CO}_2(\text{g}) + 2\text{e}^- + 4\text{H}^+ \rightarrow \text{HCHO}(\text{l}) + \text{H}_2\text{O}(\text{l})$	-0.070
$\text{CO}_2(\text{g}) + 4\text{e}^- + 4\text{H}^+ \rightarrow \text{C}(\text{s}) + 2\text{H}_2\text{O}(\text{l})$	0.21
$\text{CO}_2(\text{g}) + 6\text{e}^- + 6\text{H}^+ \rightarrow \text{CH}_3\text{OH}(\text{l}) + \text{H}_2\text{O}(\text{l})$	0.016
$\text{CO}_2(\text{g}) + 8\text{e}^- + 8\text{H}^+ \rightarrow \text{CH}_4(\text{g}) + 2\text{H}_2\text{O}(\text{l})$	0.169
$2\text{CO}_2(\text{g}) + 8\text{e}^- + 8\text{H}^+ \rightarrow \text{CH}_3\text{COOH}(\text{l}) + 2\text{H}_2\text{O}(\text{l})$	0.11
$2\text{CO}_2(\text{g}) + 10\text{e}^- + 10\text{H}^+ \rightarrow \text{CH}_3\text{CHO}(\text{l}) + 3\text{H}_2\text{O}(\text{l})$	0.06
$2\text{CO}_2(\text{g}) + 12\text{e}^- + 12\text{H}^+ \rightarrow \text{C}_2\text{H}_4(\text{g}) + 4\text{H}_2\text{O}(\text{l})$	0.064
$2\text{CO}_2(\text{g}) + 12\text{e}^- + 12\text{H}^+ \rightarrow \text{CH}_3\text{CH}_2\text{OH} (\text{l}) + 3\text{H}_2\text{O}(\text{l})$	0.084
$2\text{H}^+ + 2\text{e}^- \rightarrow \text{H}_2$	0

In order to achieve the economic feasibility of the eCO₂RR process, several indicators have been presented as performance guidelines related to the current density, Faradaic efficiency (FE) conversion for different target products, and catalyst durability.⁶ To estimate the economic feasibility, the stepwise and direct reduction of

different products needs to be considered rationally (**Table 1.3**).^{9,10} For example, target eCO₂RR products such as CO and HCOOH only need two electrons and two or three steps from CO₂ in which low overpotentials are needed and high Faradaic efficiencies could be obtained. In contrast, for higher energy density products, more electrons and complicated steps lead to lower single-phase Faradaic efficiency. Thus, CO and HCOOH are the most promising target products when considering the market prices of eCO₂RR products and the cost of electricity.¹¹ In terms of the separation cost, the acquisition and purification of gas product CO is undoubtedly a cheaper and more convenient choice from the liquid electrolyte. Besides, CO as a component of syngas (H₂ and CO as main components for chemical synthesis) could be processed downstream by Fischer-Tropsch chemistry to synthesize a series of organic chemical products.¹² In addition, the minimum cost for CO₂ reduction to CO is \$0.13/kg, and the cost for CO₂ reduction to C₂H₄ is \$0.78/kg. However, when the CO product is used for C₂H₄ formation, the cost will be reduced by 40%, which means that a stepwise tandem process CO₂ → CO → C₂H₄ would be more economical than the one step process CO₂ → C₂H₄.¹³ Therefore, the electrocatalytic conversion of CO₂ to CO is an economically and technologically approach to realize the industrial eCO₂RR (**Table 1.3**).¹⁴ Besides, for CO and HCOOH, due to their relatively simple reaction process, it is reasonable to think that investigation of reaction mechanisms by using advanced characterization technologies could provide new insights, critical evaluations, and guidance to this field with regard to research directions and best practises.^{15–17}

Table 1.2 Energy density of liquid fuel

products	molecular formula	energy density (MJ L ⁻¹)
formic acid	HCOOH	7.4
methanol	CH ₃ OH	15.9
ethanol	C ₂ H ₅ OH	21.9
ethylene glycol	(CH ₂ OH) ₂	20.7
1-propanol	n-C ₃ H ₇ OH	24.7
glycerol	C ₃ H ₈ O ₃	22.4
1-butanol	n-C ₄ H ₉ OH	26.9
1-pentanol	n-C ₅ H ₁₁ OH	28.5
2-methylfuran	C ₅ H ₆ O	27.6

Table 1.3 Industrial use and indicative market prices of main reported products

products	Industrial Use	market prices (\$/kg)
HCOOH	organic synthesis; preservative and antibacterial agent	0.74
CO	methanol production; Fischer–Tropsch synthesis	0.60
CH ₃ OH	formaldehyde and acetic acid production; gasoline additive	0.58
CH ₄	fuel; reforming to syn gas	0.18
C ₂ H ₄	raw materials for polyethylene, ethylene oxide, and ethylbenzene synthesis	1.3
C ₂ H ₆	ethylene formation; refrigeration systems	4.0
C ₂ H ₅ OH	fuel; solvent; antiseptics; formation of ethyl ethers and esters	1.0
CH ₃ COOH	synthesis of vinyl acetate and ethyl acetate; food processing	2.9
CH ₃ CHO	organic synthesis	4.5

1.2.1 Fundamentals of electrochemical CO₂ reduction

The performance of electrocatalysis can be quantitatively measured for several important metrics, such as the onset potential, overpotential (η), current density (j), Tafel slope, Faradaic efficiency (FE), energy efficiency (EE), turnover number (TON), and turnover frequency (TOF).

- 1) Onset potential is the lowest potential applied for the formation of certain products from CO₂ reduction, which is one of the common indexes for CO₂ reduction activity evaluation. The following recorded low overpotentials are inherently the most susceptible to sensitivity issues during product analysis, due to challenges in product measurements at low current densities.
- 2) Overpotential (η), featuring the cell's voltage efficiency, is the difference between the actual applied potential and theoretical thermodynamic potential required to drive the electrocatalysis reaction (onset potential). The catalysts with excellent CO₂ reduction performance usually show a low overpotential for generating certain products. The overpotential of a certain product is calculated as

$$\eta = E - E_{eq} \quad (1.1)$$

where E is the actual electrode potential, and E_{eq} is the standard potential for the formation of certain products. η is negative for CO₂RR and a higher overpotential corresponds to a lower (or more negative) electrode potential.

- 3) Current density (j), featuring the rate constant of the overall electrochemical reaction, is the total current per unit area of the cathode calculated for CO₂ reduction, which is important for electrocatalytic reaction estimation. Because it governs the size of the electrolyser for a given production rate. The current density is calculated as

$$j = \frac{I}{A} \quad (1.2)$$

where I is the current applied, and A is the geometric surface area of the working electrode.

- 4) Tafel slope, gaining mechanistic insights, can be used to describe the reaction kinetics and is related to the overpotential and logarithm of the current density of certain products.¹⁸ Moreover, the analysis of Tafel slope provides a method to understand the reaction mechanism because this analysis can be employed to identify the rate-limiting step of the reaction. Generally, single-electron transfer from CO₂ to form CO₂^{•-} (ET) and chemical proton transfer (PT) from the electrolyte are the rate-limiting steps for CO₂ conversion with a Tafel slope of approximately 118 and 59 mVdec⁻¹, respectively in **Table 1.4**.¹⁹

Most notably, Tafel analysis is only appropriate within a specific overpotential range. For an electrochemical reaction of the form given in eq 1.3, the full Butler–Volmer equation (eq 1.4) can be simplified to the Tafel equation (eq 1.5) only if the overpotential is sufficiently high so that the rate of the reverse reaction is negligible comparing to that of the forward reaction, that is, $\exp\left(\frac{\eta\beta F}{RT}\right) \ll \exp\left(\frac{\eta(\beta-1)F}{RT}\right)$.



$$j = nFk^0 \left[a_R \exp\left(\frac{\eta\beta F}{RT}\right) - a_O \exp\left(\frac{\eta(\beta-1)F}{RT}\right) \right] \quad (1.4)$$

$$j = -nFk^0 \left[a_O \exp\left(\frac{\eta(\beta-1)F}{RT}\right) \right] \quad (1.5)$$

Table 1.4 Proposed rate expressions and corresponding Tafel slopes.

	step	rate expression ^{a,b}	type ^c	Tafel slope	[H ⁺] order ^d
A.1	$\text{CO}_2 + e^- + * \leftrightarrow (\text{CO}_2^-)_{\text{ad}}$	$j_{\text{CO}} = Fk_{\text{aCO}_2}^0 \theta_{\text{a}} \exp\left(\frac{E(\beta-1)F}{RT}\right)$	ET	118	0
A.2	$(\text{CO}_2^-)_{\text{ads}} + \text{H}_2\text{O} \leftrightarrow \text{COOH}_{\text{ad}} + \text{OH}^-$	$j_{\text{CO}} = Fk^0 K_{\text{A.1}} a_{\text{CO}_2} \exp\left(-\frac{EF}{RT}\right)$	PT	59	0
A.3	$\text{COOH}_{\text{ads}} + \text{H}_2\text{O} + e^- \leftrightarrow \text{CO}_{\text{ad}} + \text{OH}^-$	$j_{\text{CO}} = Fk^0 \frac{K_{\text{A.1}} K_{\text{A.2}} a_{\text{CO}_2} a_{\text{H}^+}}{K_{\text{W}}} \exp\left(\frac{EF}{RT}(\beta-2)\right)$	PCET	39	1
A.4	$\text{CO}_{\text{ad}} \leftrightarrow \text{CO} + *$	$j_{\text{CO}} = Fk^0 \frac{K_{\text{A.1}} K_{\text{A.2}} K_{\text{A.3}} a_{\text{CO}_2} a_{\text{H}^+}^2}{K_{\text{W}}^2} \exp\left(-\frac{2EF}{RT}\right)$	D	30	2
B.1	$\text{CO}_2 + \text{H}_2\text{O} + e^- + * \leftrightarrow \text{COOH}_{\text{ad}} + \text{OH}^-$	$j_{\text{CO}} = Fk_{\text{aCO}_2}^0 \theta_{\text{a}} \exp\left(\frac{E(\beta-1)F}{RT}\right)$	PCET	118	0
B.2	$\text{COOH}_{\text{ad}} + \text{H}_2\text{O} \leftrightarrow \text{COOH}_{\text{ad}} \cdots \text{H}^+ + \text{OH}^-$	$j_{\text{CO}} = Fk^0 \frac{K_{\text{B.1}} a_{\text{CO}_2} a_{\text{H}^+}}{K_{\text{W}}} \exp\left(-\frac{EF}{RT}\right)$	PT	59	1
B.3	$\text{COOH}_{\text{ad}} \cdots \text{H}^+ + e^- \leftrightarrow \text{CO}_{\text{ad}} + \text{H}_2\text{O}$	$j_{\text{CO}} = Fk^0 \frac{K_{\text{B.1}} K_{\text{B.2}} a_{\text{CO}_2} a_{\text{H}^+}^2}{K_{\text{W}}} \exp\left(\frac{EF}{RT}(\beta-2)\right)$	ET	39	2
B.4	$\text{CO}_{\text{ad}} \leftrightarrow \text{CO} + *$	$j_{\text{CO}} = Fk^0 \frac{K_{\text{B.1}} K_{\text{B.2}} K_{\text{B.3}} a_{\text{CO}_2} a_{\text{H}^+}^2}{K_{\text{W}}^2} \exp\left(-\frac{2EF}{RT}\right)$	D	30	2
C.1	$\text{CO}_2 + \text{H}_2\text{O} + e^- + * \leftrightarrow \text{COOH}_{\text{ad}} + \text{OH}^-$	$j_{\text{CO}} = Fk_{\text{aCO}_2}^0 \theta_{\text{a}} \exp\left(\frac{E(\beta-1)F}{RT}\right)$	PCET	118	0
C.2	$\text{COOH}_{\text{ad}} + \text{H}_2\text{O} + e^- \leftrightarrow \text{CO}_{\text{ad}} + \text{H}_2\text{O} + \text{OH}^-$	$j_{\text{CO}} = Fk^0 \frac{K_{\text{C.1}} a_{\text{CO}_2} a_{\text{H}^+}}{K_{\text{W}}} \exp\left(\frac{EF}{RT}(\beta-2)\right)$	PCET	39	1
C.3	$\text{CO}_{\text{ad}} \leftrightarrow \text{CO} + *$	$j_{\text{CO}} = Fk^0 \frac{K_{\text{C.1}} K_{\text{C.2}} a_{\text{CO}_2} a_{\text{H}^+}^2}{K_{\text{W}}^2} \exp\left(-\frac{2EF}{RT}\right)$	D	30	2

^aReduction currents are negative based on the convention in eq1.1; for clarity, negative signs have been removed for current density in **Table 1.4**. ^bAssuming water, rather than bicarbonate or hydronium ions, as the proton donor. ^cAssuming a β value of 0.5. ^dET: electron transfer, PT: proton transfer, PCET: proton-coupled electron transfer, D: desorption.

The overpotential must be kept sufficiently low so that the reaction rate is kinetically controlled in determining Tafel slopes. Otherwise, the observed Tafel

slope will be convoluted by mass transport limitations. It means that Tafel slopes measured at low current densities and electrode potentials (overpotentials) without significant electrolyte/electrode interactions are more reliable. At high potentials, reaction rates are governed by the mass transfer of CO₂ or protons to the electrode surface.²⁰ Therefore, it is critical to ensure that the Tafel slopes are measured only under conditions controlled by electrokinetics.

- 5) Faradaic efficiency (*FE*), featuring the process selectivity, is the proportion of the electrons consumed to produce certain products and total electrons consumed during the CO₂ reaction. In fact, the *FE* towards certain products improves sometimes because the competing product may just be suppressed *e.g.*, hydrogen evolution reaction (HER). It is used to reflect the catalyst selectivity toward CO₂ electrocatalytic conversion. The *FE* of a certain product is calculated as follows:

$$FE_{product} = \frac{\alpha n F}{Q} \quad (1.6)$$

where α is the number of the electrons transferred for producing the certain product, n is the mole number of the certain product produced, F is the Faraday constant of 96485,3 C mol⁻¹, and Q is the total charge supplied.

- 6) The energetic efficiency (*EE*) is a parameter that reflects the utilization of overall energy toward the desired product. *EE* can be calculated by the equation below:

$$\varepsilon_{energetic} = \frac{E_{eq}}{E_{eq} + \eta} \times \varepsilon_{Faradaic} \quad (1.7)$$

Where E_{eq} and η are the equilibrium potential and overpotential, respectively.

- 7) Turnover number (TON), featuring the catalytic stability and turnover frequency (TOF), featuring the catalytic efficiency, are the parameters that are used to describe the catalytic activity. TON is the yield of certain products obtained using a unit catalyst, and TOF is the yield of certain products acquired using a unit catalyst in a unit time.

1.2.2 Mechanism of electrochemical CO₂ reduction

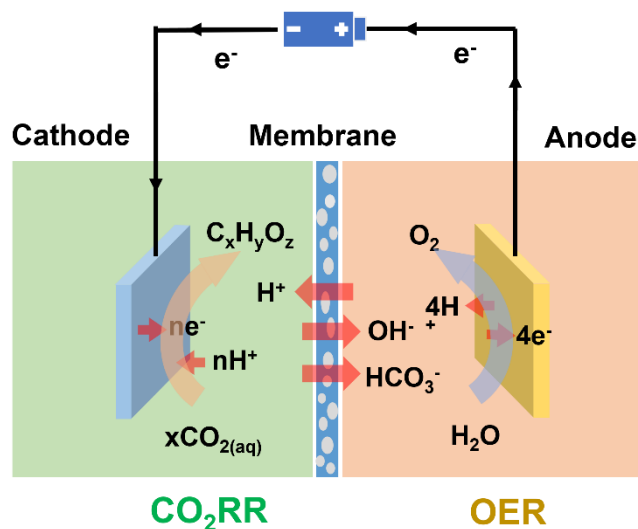
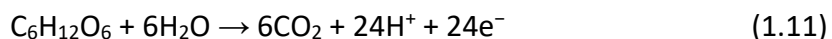
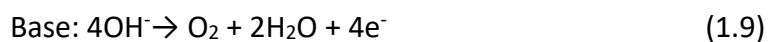
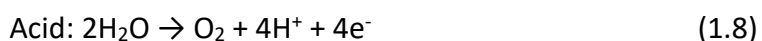


Figure 1.4 A schematic of the H-type reaction cell for the electrochemical reduction of CO₂. The cell system is composed of a cathode, membrane, anode, and electrolyte.

CO₂ reduction electrolyzers consist of an anode, a cathode, and an electrolyte, as shown in **Figure 1.4**. At the anode, the oxygen evolution reaction (OER) is performed. Normally, the water oxidation as a counter half-reaction for eCO₂RR completes the electrochemical circuit (eq 1.8 and 1.9). To improve the economic value or lower the oxidizing potentials than those needed for OER, other oxidation reactions could also be conducted, such as chloride oxidation (eq 1.10) or wastewater (glucose) oxidation (eq 1.11).



At the cathode, gaseous CO₂ is continuously supplied to the catholyte to form saturated CO₂ in the aqueous electrolyte by the chemical equilibrium between the gas and liquid phases. Then, the dissolved CO₂ in the bulk electrolyte could be transported to the cathode surface by convection and diffusion where it is captured and adsorbed

by catalyst and undergoes proton couple and electron transfer to get final carbon products. The CO_2 dissolved in the electrolyte contains bicarbonate (HCO_3^-) and carbonate (CO_3^{2-}) anions produced by the following equilibriums:



According to the acid-dissociation constants and the rate coefficients for these reactions the conversion of CO_2 to HCO_3^- is a relatively slow reaction, while the conversion of HCO_3^- into CO_3^{2-} rapidly equilibrates, as shown in **Table 1.5**.²¹ The speciation of an aqueous solution in equilibrium with CO_2 depends on the bulk pH, as shown in **Figure 1.5**. As the bulk pH of the solution increases, it becomes increasingly saline since a greater fraction of the dissolved carbon is present as HCO_3^- and CO_3^{2-} anions. Due to the “salting-out” effect, the solubility of CO_2 decreases with increasing the solution salinity.²¹ With the precipitation of alkali carbonates, the bulk CO_2 concentration decreases precipitously above $\text{pH}=10.6$. However, because the conversion of CO_2 into HCO_3^- is low, the CO_2 can exist in relatively alkaline conditions momentarily.²² Between the catholyte and anolyte is a membrane to aid the mobility of ions and inhibit the crossover of gaseous products.

Table 1.5 acid-dissociation and kinetic rate constants for the formation of bicarbonate and carbonate anions.

Reaction	pKa	$K \text{ (s}^{-1}\text{)}$
$\text{CO}_2 + \text{H}_2\text{O} \rightarrow \text{HCO}_3^- + \text{H}^+$	6.37	0.0371
$\text{HCO}_3^- \rightarrow \text{CO}_3^{2-} + \text{H}^+$	10.25	59.44

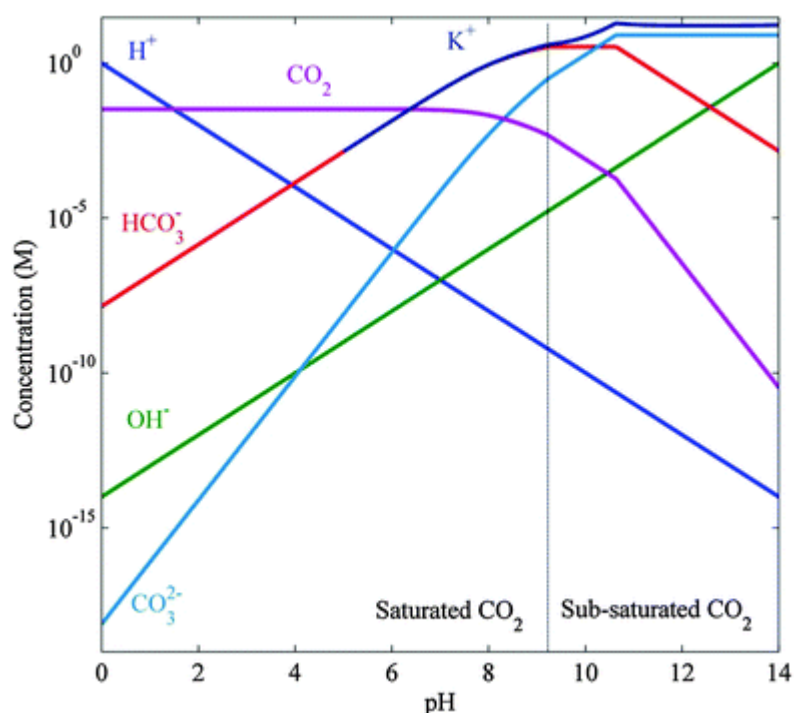


Figure 1.5 Concentration of carbon dioxide, hydrogen, hydroxyl, bicarbonate, carbonate, and potassium ions as a function of bulk pH of the potassium bicarbonate/carbonate electrolyte at 25 °C and a total pressure of 1 atm.

For CO and HCOOH products, the activation of stable CO_2 experience various reaction pathways with forming the different intermediates proposed based on experimental observation and theoretical calculations.^{23,24} For CO production, $^*\text{COOH}$ and $^*\text{CO}$ are the key intermediates during $\text{CO}_2 \rightarrow \text{CO}$.²⁵ At low $^*\text{COOH}$ adsorption energies, the activation of CO_2 through the C atom is the rate-determining step (RDS), whereas at high $^*\text{COOH}$ adsorption energies, the desorption of CO is the RDS. The key intermediates binding to the electrocatalyst surface through the C atom will scale with the $^*\text{COOH}$ adsorption energy. In other words, since both $^*\text{COOH}$ and $^*\text{CO}$ bind to the electrode surface through the C atom, increasing the stability of $^*\text{COOH}$ also increases the stability of $^*\text{CO}$. As a results of this linear scaling relationship, binding $^*\text{COOH}$ more strongly on the surface of catalysts will show lower CO evolution activity which illustrates that the desorption of $^*\text{CO}$ is the RDS. Therefore, the linear scaling relation between the adsorption energies of $^*\text{COOH}$ and $^*\text{CO}$ needs to be broken to improve the electrocatalysts activity for CO evolution.

For HCOOH production, the $\ast\text{OCHO}$ and $\ast\text{HCOOH}$ are the key intermediates during $\text{CO}_2 \rightarrow \text{HCOOH}$.^{26–28} At low $\ast\text{OCHO}$ adsorption energies, the activation of CO_2 through the O atoms is the RDS, whereas at high $\ast\text{OCHO}$ adsorption energies the desorption of HCOO^- is the RDS. Although the eCO_2RR for both CO and HCOOH needs two electron and two proton (Figure 1.6), the carbon- and oxo-philicity of electrocatalysts determine the orientation in which CO_2 interacts with the catalyst surface, which in turn determines the initial reaction pathways and final products.

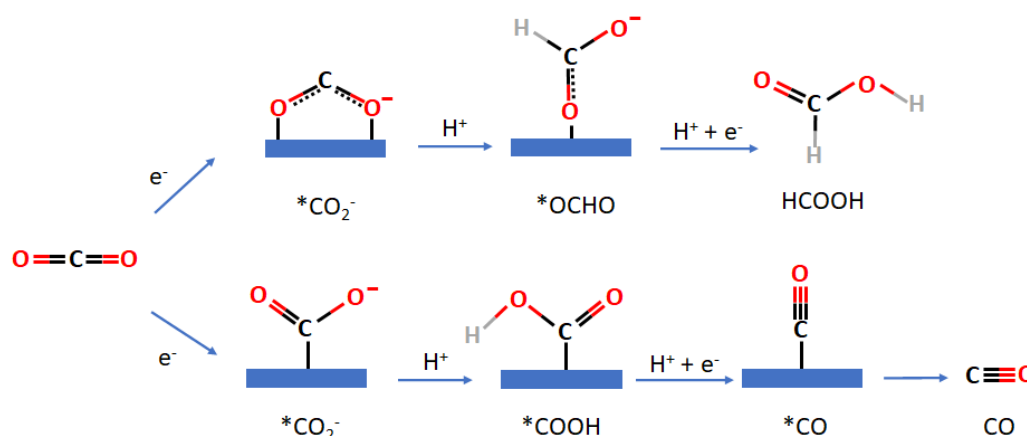


Figure 1.6 Possible pathways and intermediates for HCOOH and CO during electrochemical CO_2 reduction.

1.3 Ex-situ and *in-situ*/operando characterization techniques to study the materials and reaction mechanism

In order to offer reliable evidence for the theoretical and experimental studies to screen new catalysts and catalytic systems, identification of eCO_2RR under real operating conditions plays a significant role.^{29,30} There are several key factors that influence the performance of the eCO_2RR : the composition and structure of the electrocatalyst surface; the triple interfaces of the solid, liquid and gas; and the nature of the components of the liquid electrolyte.¹³ Most *in-situ* and operando studies use infrared (IR) spectroscopy or Raman spectroscopy to identify the state or structures of the chemical species in solution and on the electrode surface, UV-Vis spectroscopy to learn about the electronic structures of molecular complexes,³¹ X-ray absorption spectroscopy to understand the local geometric environment and the electronic state of molecular complexes or the electrode itself, scanning electrochemical microscopy

(SECCM) can track the surface, crystal facet and grain boundary information in real-time and the X-ray photo-electron spectroscopy (XPS) technique can be performed to detect the chemical shift from local environment, valence states and coordination species of the elements. Besides, transmission electron microscopy (TEM) and related spectroscopies, able to visualize atomic-scale structures and chemical environments, are powerful tools for the advanced characterization of catalytic materials, including in-situ experimental conditions.

1.3.1 In-situ and operando techniques

In-situ describes the collection of spectra from the catalyst under environmental conditions similar to those occurring during the eCO₂RR, or under conditions relevant to the catalytic operation. It means that the condition is not the genuine condition and sometimes we have to make a compromise to meet the requirement of the selected equipment.

Operando combines the *in-situ* characterization of a working catalyst during genuine reaction conditions with simultaneous measurement of the catalytic activity and selectivity. The condition is genuine, and the equipment makes a compromise to meet the requirements for the catalytic conditions.^{32–34}

1.3.2 Infrared spectroscopy (IR)

Infrared spectroscopy has become an indispensable tool in electrochemistry, particularly in electrocatalysis, since it allows in-situ, non-destructive and label-free analysis of species at the electrode-electrolyte interface. During the reaction process, the CO₂ molecule, intermediate species, and possible reduction products could be detected by IR spectroscopy via unique vibrational modes in molecules called fingerprint spectra.³⁵ Besides, the information regarding the geometry and orientation of molecules adsorbed on catalytic surfaces could be obtained via monitoring the functional groups, molecular symmetry, as well as intramolecular and intermolecular interaction with IR.^{36,37} IR can be used for different systems such as heterogeneous systems (with bulk metallic electrodes)³⁸ and homogeneous systems (with molecular

catalysts)³⁹. In-situ IR could monitor the interaction between molecules in a solution and a catalyst surface.

There are several measurement configurations which are widely used for the study of electrochemical reactions such as transmission, external reflection, and internal reflection. However, most of the studies of CO₂RR involve the use of a liquid electrolyte. This poses a significant challenge for IR spectroscopic experiments, due to the strong IR absorption by the electrolyte such as aqueous solution, protic, or aprotic solution. To solve it, D₂O could be used instead of H₂O as the electrolyte/solvent. Another one is the internal reflection (called attenuated total reflection, ATR) configuration which maximizes the signal from the samples and minimizes that of the solution (**Figure 1.7**). Modern Fourier transform infrared (FTIR) spectrometers allow fast acquisition of spectra, making it possible to study CO₂RR *in-situ* in real time.⁴⁰ The surface enhanced infrared absorption spectroscopy (SEIRAS) represents a variation of conventional infrared spectroscopy and exploits the signal enhancement exerted by the plasmon resonance of nanostructured metal thin films.

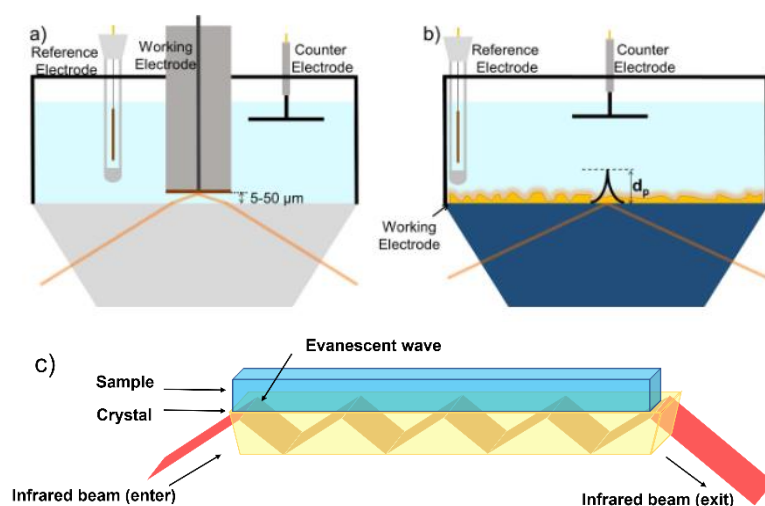


Figure 1.7 The two measurement configurations of infrared experiments at the electrode-electrolyte interface: a) external reflection and b) internal reflection. c) Light undergoes multiple internal reflections in the crystal of high refractive index, shown in yellow. The sample is in contact with the crystal.

In the external reflection configuration, commonly known as infrared reflection absorption spectroscopy (IRAS), the IR beam is directed to the electrode surface under an angle of 60-70° and then reflected towards the detector (**Figure 1.7a**). The IR beam strikes through the electrode surface from the outside of the electrochemical cell, through a window made of IR transparent material and exits the electrochemical cell through another window on its way to the detector. The IR beam light was absorbed by the electrolyte layer which decrease the signal intensity. To mitigate this problem, the working electrode is placed at a short distance from the IR transparent window.

The internal reflection configuration makes that the IR beam does not travel through the electrolyte to reach the electrode surface (**Figure 1.7b**). Instead, an ATR crystal, made by ZnSe, Ge, Si, or diamond, is used as a propagation medium for the IR radiation. The ATR crystal has a high refractive index and the IR beam is directed through the crystal in such a fashion that it undergoes a total internal reflection (**Figure 1.7c**). Above the surface of the crystal, an electric field arises, called the evanescent wave. When the sample contact with the surface of the crystal, the evanescent wave can penetrate a few hundreds of nanometres to a few micrometres inside the sample. The molecules or species at this distance could interact with the evanescent wave, which is attenuated when the absorption takes place. When the IR beam reaches the detector, the spectrum is recorded.

ATR-SEIRAS has the properties of ATR coupled to those of SEIRAS. The main advantages of ATR-SEIRAS over IRAS are (i) the increased sensitivity to adsorbed species, (ii) the significantly lower interference from the bulk of the electrolyte and (iii) the significantly decreased IR drop and transport limitations. ATR-SEIRAS has been widely used in in-situ or operando conditions.

1.3.3 Raman spectroscopy

IR is a kind of absorption spectroscopy, but the Raman spectroscopy is a scattering spectroscopy. Compared to IR spectroscopy, Raman spectroscopy does not suffer from the strong absorption by aqueous electrolytes.⁴¹ Besides, like the SEIRAS effect for IR spectroscopy, the surface enhancement Raman scattering (SERS) effect could alleviate

the drawback of low signal intensities. Because of its high sensitivity for the detection of the reaction species present in low concentrations close to the electrode surface, it could lead to a better understanding of the mechanisms governing CO₂RR with various metals.^{42,43}

The experiment setup for Raman spectroscopy involves the use of a monochromatic radiation source (a laser) to excite the substrate, a filter which blocks the elastically scattered light and let only the inelastically scattered light pass through an edge filter, a notch filter or a laser-line filter and finally a detector (**Figure 1.8**). For laser, visible light lasers such as the HeNe 633 nm and the Ar⁺ 514 nm could be competent to achieve the surface-enhanced Raman spectroscopy.

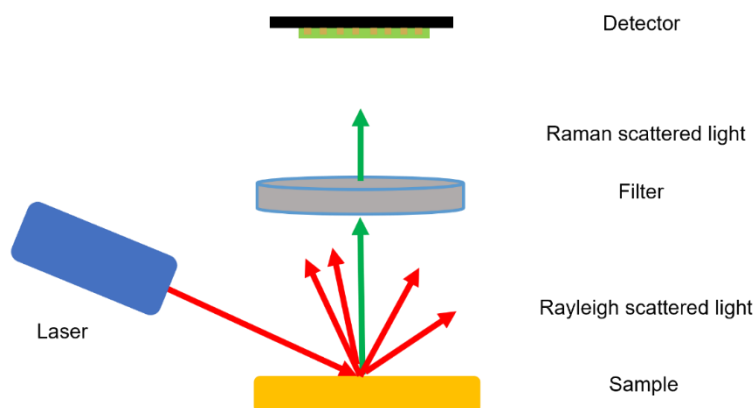


Figure 1.8 Schematic representation of a Raman scattering experiment.

1.3.4 X-Ray absorption spectroscopy (XAS)

1.3.4.1 Basic principle

X-ray is a powerful tool to obtain oxidation states, electronic structures, and local bonding environments of different materials including bulk, nanoscale, or even single atoms, crystalline and amorphous materials, as well as homogeneous and heterogeneous materials.⁴⁴ Besides, by using in-situ characterization, it could provide information under reaction conditions which gives a new insight into the reaction mechanism.

It uses the X-ray as light to pass through the sample, and the transmitted X-ray can be collected afterwards. According to Beer-Lambert law, the attenuation of transmitted X-ray intensity could be used to speculate on the fine structure of the material by the obtained coefficient. In other words, a typical X-ray absorption is a plot of the absorption coefficient vs. the energy of X-ray photons.

$$I_t = I_0 e^{-\mu(E)t} \quad (1.14)$$

I_0 is the incident X-ray intensity, I_t is the transmitted X-ray intensity, t is the sample thickness, and $\mu(E)$ is the absorption coefficient that is a smooth function of the photon energy varying approximately as $\mu(E) \sim dZ^4/mE^3$. d notes the target density while Z and m are the atomic number and mass. $\mu(E)$ decreases with the increase of the photon energy. When the photon energy equals the binding energy of a core electron, a new absorption channel is available in which the photon is annihilated by creating a photoelectron and a core-hole. This leads to a sharp increase in the absorption coefficient, as shown in **Figure 1.9**.

When the incident X-ray energy is lower than the binding energy of the electron, the electrons could not be excited to jump into the lowest unoccupied state or the vacuum. The lack of X-ray and electron interaction leads to a flat region (**Figure 1.9a**). Pre-edge features are treated as a sign of broken inversion symmetry. Small energy shifts of the absorption edge itself can be caused by the charge transfer between the absorber and the neighbouring atoms. More pronounced shifts can result from changes in the first nearest neighbour bond lengths.

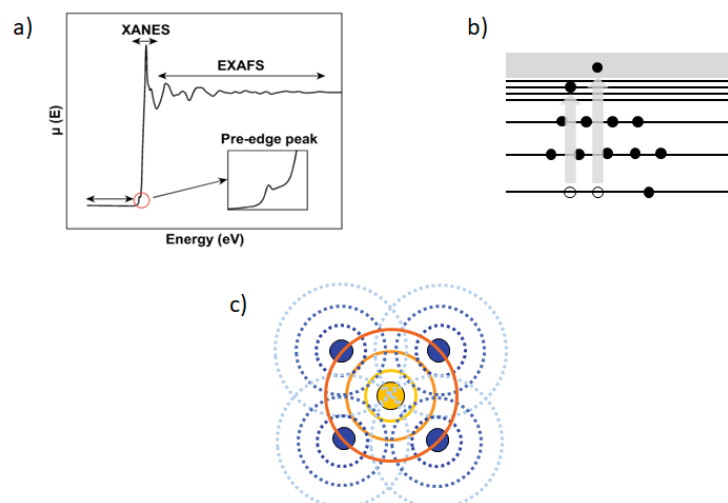


Figure 1.9 a) Schematic of XAS including the pre-edge, XANES, and EXAFS regions. b) Schematic of the X-ray absorption process and electron excited process, the black circles correspond to electrons. c) Schematic showing the absorbing atom (yellow) and its first nearest neighbours (blue). An interference pattern is created by the outgoing (solid orange lines) and reflected (dashed blue line) photoelectron waves.

When a photon with X-ray energies can be absorbed, a photoelectron will be excited to unoccupied bound states of the absorbing atom. The energy difference between the core level and the unoccupied states presents a strong increase of the absorption coefficient at particular X-ray energies. The region in the spectrum of absorption coefficient vs. photo energy is close to the absorption edge named the X-ray absorption near edge structure (XANES) or the near edge X-ray absorption fine structure (NEXAFS) (**Figure 1.9a**). It exhibits the characteristic features for different oxidation states of the absorbing atom and is sensitive to the chemical bonding.^{45,46} Meanwhile, the strong multiple scattering effects from three-dimensional geometry of the crystal structure influence the XANES features. For higher X-ray energies, the photoelectron is promoted to a free or continuum state. The region in the spectrum is called extended X-ray absorption fine structure (EXAFS). The wave propagates outwards and is scattered at neighbouring atoms. The geometry of the absorber environment and the photoelectron wavelength could be affected by the outgoing and scattered waves interference. The photoelectron wavelength is inversely proportional to the photoelectron momentum and therefore to the changes with the photon energy. Therefore, EXAFS is independent of the chemical bonding and depends

on the atomic arrangement around the absorber. It contains information about the coordination number, interatomic distance, and structural and thermal disorder around particular atomic species.³⁸

1.3.4.2 Experiment setup

X-rays with high photon energies (above 5-10 keV) are called hard X-rays, while those with lower energy are called soft X-rays. Since the wavelengths of hard X-rays are similar to the size of atoms, they are also useful for determining crystal structures by X-ray crystallography. This technique can also be used for in-situ measurements.⁴⁹ By contrast, soft X-rays could probe the lower energy 2p electron excitations to the 3d shell.^{48,50} Such transitions are more sensitive to electronic structure changes and the acquired spectra can offer more information than high-energy transitions. In this way, the formation and reduction of oxides can be monitored *in-situ*.⁵¹ However, soft X-ray radiation is easily absorbed in air. The attenuation length of 600 eV X-rays in water is less than 1 micrometre. For the hard X-rays (energy > 5keV), the higher momentum photons are unaffected by air and thus enable *in-situ* measurements. According to the characteristic features of the target catalyst, we could select an appropriate *in-situ* technique.

In addition to different X-rays light source, the signal collection methods also have different features. There are three basic modes for XAS signal collections **Figure 1.10**.⁵² In general, the absorption coefficient is detected either by directly measuring the intensities of incoming (I_0) and transmitted beam (I_t) (transmission mode) or indirectly by measuring the intensity of the incoming beam (I_0) and of the decay products such as fluorescent X-ray (I_f) or Auger electrons (I_{ey}) (fluorescence or electron yield mode).

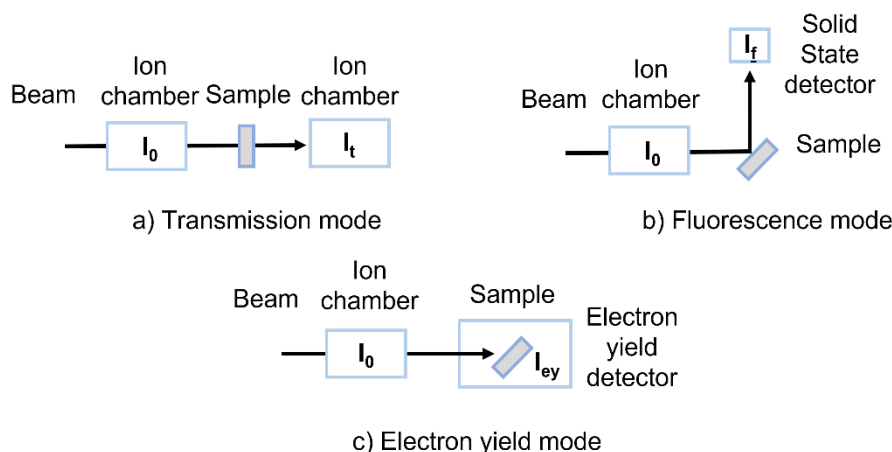


Figure 1.10 Schematic of the experiment setup for the different XAS detection modes.

Table 1.6 Comparison of different XAS detection modes.

Different XAS detection modes	Features	Limits
Transmission Mode	Having a common energy dependence	samples must be highly homogeneous, of constant thickness and free of pinholes.
Fluorescence Mode	Highly dilute and non-homogeneous samples no “self-absorption” effect,	“Self-absorption” effects
Electron Yield Mode	measuring samples in the soft X-ray regime, surface sensitive	Not bulk sensitivity

1.3.5 X-ray diffraction spectroscopy (XRD)

Unlike XAS, the XRD is a form of elastic scattering.⁵³ The crystalline structure leads to constructive interference of the incident beam followed by diffraction into specific directions and every crystalline structure has a unique diffraction pattern. Unlike TEM, XRD provides average information such as average grain size, crystallinity, strain and crystal defects. In addition to qualitative analysis, it could provide quantitative analysis. In comparison to TEM and XPS, which require high vacuum environments for in-situ characterization, it is relatively easy to operate experiments with XRD under *in-situ* conditions.⁵⁴

Table 1.7 Comparison between XRD and XAS

	X-ray diffraction spectroscopy	X-ray absorption spectroscopy
Feature	Crystallinity, lattice parameter	Valence state, bond length, coordination number, degree of disordering
Limitation	Unable to obtain information on amorphous materials	Unable to study low atomic number elements

1.3.6 X-ray photoelectron spectroscopy (XPS)

The X-ray photoelectron spectroscopy (XPS) technique could be used to detect the chemical shift of certain elements on the materials surface, through which the change of the local chemical environment, valence states and coordination species of the element can be precisely identified.⁵⁵ Near ambient pressure X-ray photoelectron spectroscopy (AP-XPS) could probe the catalyst under different experimental conditions.⁵⁶ However, suffering from the limited detection depth, it is hard to uncover the inner structural changes of the catalysts.

1.3.7 Electron microscopy

1.3.7.1 Transmission Electron Microscopy (TEM)

TEM is a kind of instrument that make use of the properties of electrons, both as particles and as waves.^{57,58} It could generate a tremendous range of signals including images, diffraction patterns, and different kinds of spectra (**Figure 1.11**). Benefiting from the implementation of the aberration correctors⁵⁹, TEM realized the observation of atomic structure which could not be achieved by other methods of characterization.^{60,61} High-resolution (HR) TEM uses broad and parallel beam to collect coherent signals.⁶² The results show a strong thickness- and defocus-dependent nature even reversing the contrast in some situations. Without simulations, it is difficult to interpret the images.⁶³ For energy conversion process, *in-situ* TEM is an irreplaceable and powerful tool for directly visualizing these complex processes at the atomic scale in real time and operando conditions.^{64–70}

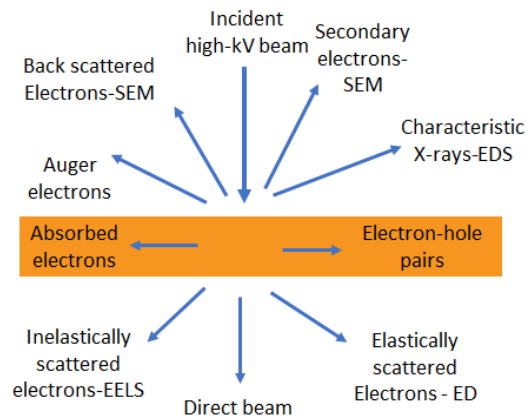


Figure 1.11 The main signals that are produced when high-energy electrons hit a specimen.

1.3.7.2 Scanning Transmission Electron Microscopy (STEM)

STEM employs a convergent incident beam that scans the sample point by point and collects the scattered electrons. Because scattered electrons with different information could reach different positions, detectors with different geometries could collect different information. For example, high angle annular dark field (HAADF-STEM), bright-field (BF-STEM) and annular bright-field (ABF-STEM)⁷¹ images have been widely used for materials characterization.⁷²

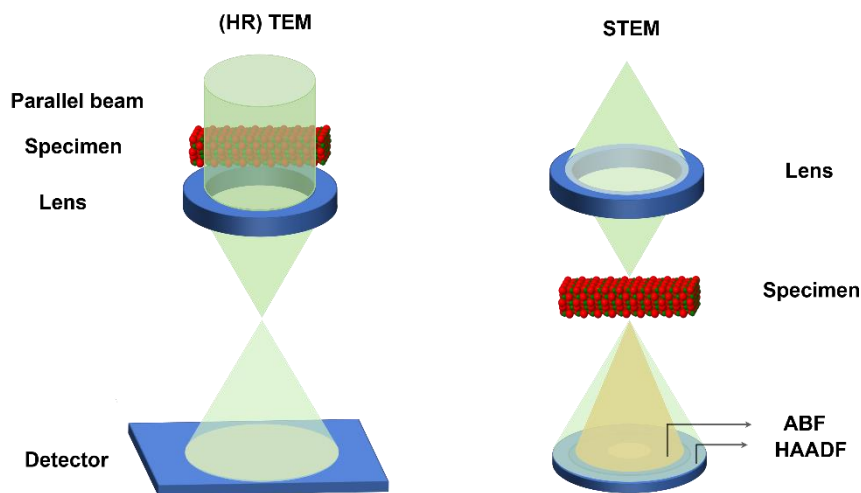


Figure 1.12 Typical image modes of (HR)TEM (left) and STEM (right).

1.3.7.3 High angle annular dark field (HAADF)

HAADF has become the most widely used image method of STEM. Due to no diffraction contrast, the intensity of it is approximately proportional to the square of

the atomic number Z ($I_{\text{HAADF}} \sim Z^2$).⁷³ In other words, the brightness (intensity) of the spots in the image reflects the atomic number which makes the image of the heavy atoms more obvious.^{74,75} Besides, without the phase contrast, thickness or defocus of specimen could not change the whole image contrast.⁷⁶ However, there are several disadvantages for HAADF-STEM images. Compared to heavy elements, the light ones show weaker contrast, especially when the gap of Z is super large. Lower utilization of electrons through the specimen leads to longer time for image acquisition and images distortion or destruction. All these limitations make it unsuitable for fast *in-situ* experiments.

1.3.7.4 Annular bright field (ABF)

Owing to smaller collected angles, information of coherent electron beams could be present in ABF-STEM images via phase contrast. The intensity of contrast is proportional to the $Z^{1/3}$.⁷⁷ Although the contrast between heavy elements and light elements is not as obvious as the ones in HAADF, ABF could easily show light and heavy elements which could provide more details about the specimen in certain cases (**Figure 1.12**).^{78,79} Due to the poor signal-to-noise ratio and reversable contrast with defocus, the process of acquiring good images gets complicated and time-consuming.

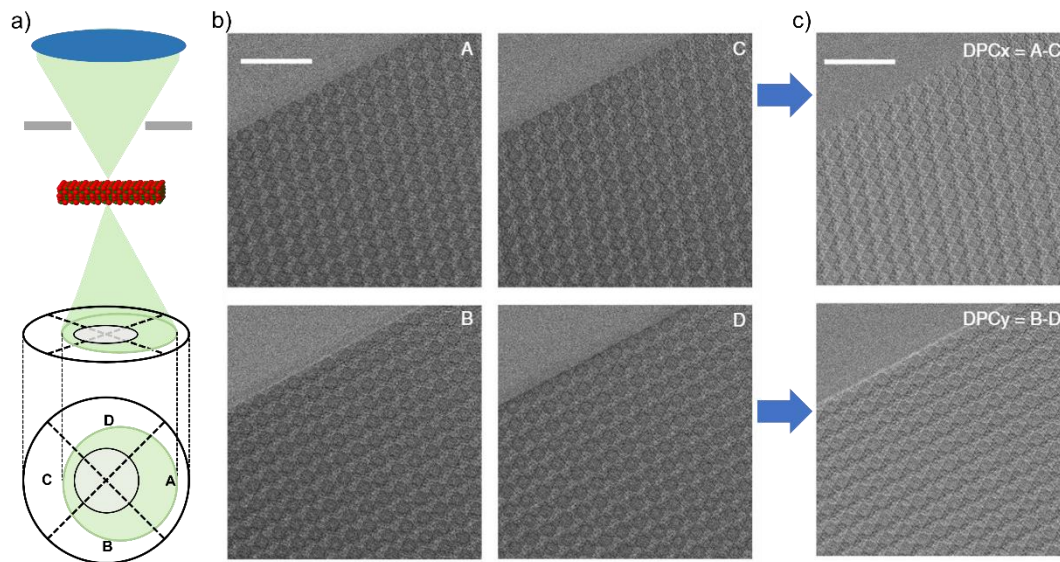


Figure 1.13 a) The schematic set-up of iDPC-STEM. The electron beam was deflected by the potential field in specimens and detected by the four segments of DPC detector. b) Four images detected by the four segments (A-D) of DPC detector, respectively. Scale bar, 20 nm. c) The DPC image obtained from the four images in b. Scale bar, 20 nm.

1.3.7.5 Integrated differential phase contrast (iDPC)

Recently, a new approach based on the two-dimensional (2D) integration of differential phase contrast (iDPC) images has been developed.^{80,81} The iDPC approach enabled the linear imaging of the projected electrostatic potential in lattice, which made the resulting contrast proportional to the atomic number and enhanced the contrasts of light elements comparable with the metal atoms (**Figure 1.13**).^{82–85} Unlike HAADF and ABF, the iDPC utilizes almost every electron interacting with the specimen to image. Besides, compared to HRTEM, lower electron dose is sufficient to get high signal-to-noise-ratio atomic resolution.⁸⁶ Therefore, this strategy is especially suitable for electron beam sensitive materials.

1.3.7.6 Energy-dispersive X-ray spectroscopy (EDS) and Electron energy loss spectroscopy (EELS)

Spectroscopic techniques could be used for the elemental analysis of our materials by employing detectors integrated within electron microscopes.^{87–89} When incident electron beam goes through the specimen, the X-rays generated during this interaction can be collected by the EDS detectors at certain stereo radians.

When the incident electrons are inelastically scattered, the energy loss of these electrons can also be recorded by EELS spectrometers. In addition to the elemental or compositional distribution like EDS, EELS can provide information about the electronic structure on the local atoms.⁹⁰ There are several differences needed to be considered when choosing between these two approaches (**Table 1.8**).

Table 1.8 Comparison between EDS and EELS.

Item	EDS	EELS
Signal-to-background ratio	high	medium or low
Thickness requirements	both thin and thick	thin
Detection efficiency	low	high
Element range	better for heavy elements ($Z > 30$)	better for light elements ($Z < 30$)
Specimen at high temperature	dose not work	works
Energy resolution	low	high
Signal interference from TEM column and grid	yes	no
Information provided	only chemical	chemical and electronic
Ease of use	simple	complex
Ease of interpretation	simple	complex
Carbon contamination sensitive	no	yes

The EELS includes three main regions: zero loss, low energy loss, and high energy loss regions. For zero-loss peak from the elastic scattering electrons and transmitted ones, these electrons could be used for instrument calibration to adjust the energy loss zero to agree with the maximum of the zero-loss peak. Besides, zero-loss peak should be as narrow as possible and not a broad peak. The reasons of broadening are the energy differences or dispersion of the electrons emitted from the gun and on the other hand, the limited energy resolution of the spectrometer.⁹¹ The low energy loss peak ($\Delta E < 50$ eV) following zero-loss peak is created by the inelastic scattering from outer-shell electrons. During this process, valence electrons experience a collective plasma resonance. The plasma excitation spectrum can image localized optical excitations to reveal the dielectric constant and charge density distribution of the interest part of materials.^{92,93} When the valence electrons transit from the valence to the conduction band, the energy loss of incident electrons is equal to the band gap width.

Then, the electron intensity decreases rapidly, making it convenient to use a logarithmic scale for the record intensity. Superimposed on this smoothly decreasing intensity are features that represent inner-shell excitations; they take the form of edges ($\Delta E > 50$ eV) rather than peaks, the inner-shell intensity rising rapidly and then falling more slowly with increasing energy loss. The sharp rise occurs at the ionization threshold, whose energy-loss coordinate is approximately the binding energy of the corresponding atomic shell. These ionization edges in the energy-loss spectrum

present the corresponding elements in the specimen because the energy of ionization threshold depends on the atomic number of the scattering atom. For those atomic numbers lower than 13, the K-absorption edge is used and for heavier elements, L- or M-edges can be used instead. In addition, the valence electron (low loss) peaks and the ionization edges have fine structures reflecting the crystallographic or electronic structures of the specimen.⁹⁴

The electronic structures of specimen could be acquired from the energy range of about 30 eV above the absorption edge energy in the EELS core-loss spectrum.^{95,96} When an electron transits from a core orbital to unoccupied states, information of atomic environment, such as bonding conditions, valence states, and orbital information, could be acquired. Compared with XANES (we mentioned above), ELNES combined with STEM provides local electronic structure with atomic spatial resolution.

1.4 System Design for CO₂ electroreduction

According to technoeconomic analysis (TEA), target performance metrics of current density ($> 300 \text{ mA cm}^{-2}$), FE (80-90%), cell voltage ($< 1.8 \text{ V}$), and stability ($> 80\,000 \text{ h}$) need to be achieved to make products economically viable.^{12,17,97,98} In addition to the catalyst itself, electrolyzer architectures and electrolytes could affect the catalytic behaviours, which accelerate the technology toward its envisioned application of neutralizing CO₂ emissions on a global scale.⁹⁹

1.4.1 Flow reactor

Most electrochemical CO₂ reduction studies have been conducted in H-cell architecture in CO₂ saturated electrolytes at ambient pressure (**Figure 1.4**).^{100,101} It is a useful platform to study reaction kinetics, reveal active sites and evaluate intrinsic activity by using well-defined surfaces, shape, controlled nanoparticles, and homogeneous mass transport. However, the current density is limited ($< 100 \text{ mA cm}^{-2}$) and the solubility of CO₂ in water is only $34 \times 10^{-3} \text{ M}$ which are not higher enough to meet industrial applications and commercial demands. There is a roughly 3 orders of magnitude difference in the CO₂ diffusion boundary layer thickness ($50 \text{ }\mu\text{m}$ in an H-cell

and 50 nm in a gas-diffusion layer).¹⁰² This difference allows for higher maximum current densities in a flow reactor but the concentration of CO₂ in aqueous solution remains fundamentally restricted under ambient conditions. Besides, pressurized electrolytes could supply enough CO₂ to the catalyst layer to sustain higher current densities. Alternatively, the delivery of humidified gaseous CO₂ to the cathode could further overcome the mass transport limitations by increasing the concentration of available reactant molecules (**Figure 1.14**).¹⁰³ Besides, this vapour-fed systems have been highlighted as a promising approach to integrate catalyst development with reactor design under practical operational conditions.¹⁰¹

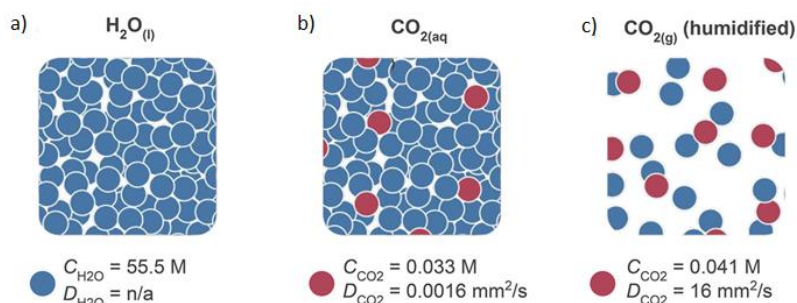


Figure 1.14 Cartoon illustrating the relative saturated concentrations and diffusion coefficients (C and D , respectively) for (a) water, (b) CO₂ in aqueous solution, and (c) humidified gaseous CO₂. Values at room temperature and pressure are indicated.

1.4.2 Liquid-phase electrolyzer

Several main architectures have been designed for CO₂ electrolyzers based on water electrolyzers (**Figure 1.15a**). A general flow cell architecture is the liquid-phase electrolyzer.¹⁰⁴ It consists of three flow channels, one for each of the CO₂ gas, catholyte and anolyte. The gas diffusion electrode separates the catholyte and gas channel. The ion-exchange membrane could prevent eCO₂RR products from crossing over to the anode where they can be oxidized back into CO₂. In the meantime, it could restrict evolved O₂ at the anode to the cathode. However liquid electrolyte also brings instability in the system due to impurity deposition on the catalyst and the potential penetration of liquid electrolyte into the gas diffusion electrode or flooding.

1.4.3 Gas-phase electrolyser

The gas-phase electrolyser contains a PEM in direct contact with both the anode and cathode to form a membrane electrode assembly (**Figure 1.15b**).¹⁰³ This zero-gap membrane could minimize ohmic losses by largely eliminating the ionic transport through the liquid electrolyte layer. For gas-phase reactor, the humidity is mandatory through a liquid electrolyte on the anode side and/or through humidification of the gas inlet stream, to keep the membrane hydrated during operation. Without catholyte, the electrolyte instability, such as electrolyte impurity deposition onto the catalysts and generation of bicarbonate/carbonate salts, can be removed.

1.4.4 Ion-exchange membrane

We can choose different types of ion-exchange membranes, depending on the products of interest. The basic principle is that for ionic CO₂RR products, using the wrong type of ion-exchange membrane can prevent product crossover and loss. Cation (or proton)-exchange membranes (CEMs) such as Nafion facilitate the flow of positive ions from the anode to the cathode. Anion-exchange membranes (AEMs) facilitates anion (*e.g.*, OH⁻, HCO₃⁻, CO₃²⁻) transport from the cathode to the anode during CO₂ reduction. AEM enable CO₂ reduction to occur in a basic environment by transporting OH⁻ produced from the CO₂RR to facilitate the flow of ionic current. AEMs show the best performance in many CO₂ flow cell configurations. The basic catalyst interface could suppress the HER by reducing the local H⁺ production and therefore, increase the selectivity. In CO₂ reactors under basic conditions, OH⁻ ions rapidly react in the presence of CO₂ to form HCO₃⁻ and CO₃²⁻. AEMs facilitate the transport of all these ions from the cathode to the anode, but bicarbonate and carbonate anions have considerably lower ion mobilities than OH⁻ and the build-up of these larger ions can inhibit membrane ion transport and reduce CO₂ reduction efficiency. Bipolar membranes (BPMs) facilitate the dissociation of water into their ionic counterparts under reverse bias, driving OH⁻ to the anode and H⁺ to the cathode.¹⁰⁵ This mechanism offers a distinct advantage which maintains a constant pH on both sides of the cell during the reaction process, thereby enabling the use of inexpensive anode (nickel

foam) and cathode catalyst materials. However, it always requires higher voltage to drive electrolysis, which reduces the overall energy efficiency.¹⁰⁶

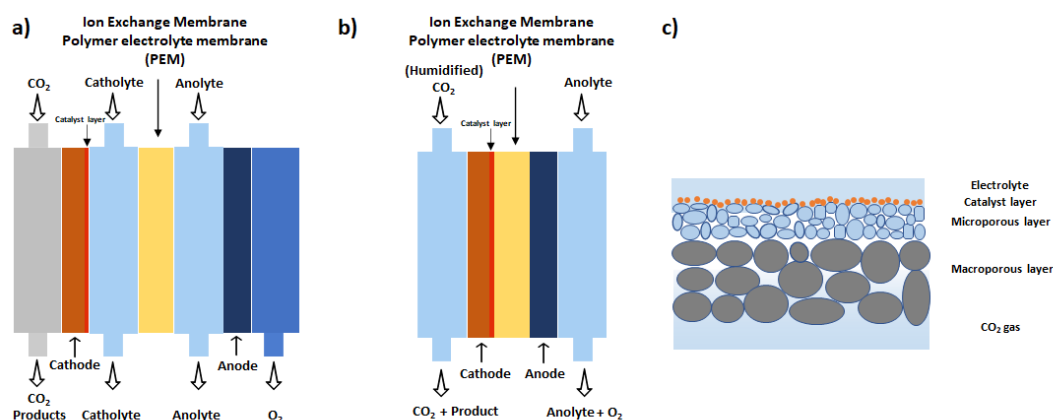


Figure 1.15 Schematic representation of a) liquid-phase and b) gas-phase electrolyzers. c) schematic representation of a gas diffusion electrode.

1.4.5 Gas diffusion electrode (GDE)

Gas diffusion electrode serving as the heart of most water electrolyzers is integral to both gas- and liquid-phase CO₂ electrolyser (**Figure 1.15c**).^{107,108} CO₂ enables to be quickly transferred to the catalyst surface, thereby resulting in a higher current density by bypassing the slow uptake of CO₂ by the electrolyte and minimizing the mass-transfer limitations. The GDE includes catalyst layer and a hydrophobic porous conductive structure that is composed of a microporous layer and a macroporous substrate. The microporous layer enhances interfacial electrical connection and prevents flooding. The microporous layer is commonly composed of a mixture of carbon black nanoparticles and a hydrophobic polymer, usually polytetrafluoroethylene (PTFE), and forms a layer with pores on the order of 200 nm. The macroporous substrate serves the function of providing mechanical stability and electrical contact, as well as distributing gas through its macroscale pores. The carbon cloth or nonwoven carbon materials with a pore size in the range of 1-100 μm are typical macroporous substrates.¹⁰⁹

1.4.6 Electrolyte engineering

The electrolyte serves as a medium to transfer protons and/or intermediate species and concentration, buffering capacity, pH value, conductivity, as well as cation and anion types, and has a great influence on the catalyst activity and selectivity.¹⁰⁸ Although organic electrolytes and ionic liquids have been used¹¹⁰, the majority of eCO₂RR studies have been performed in aqueous electrolytes.^{111,112}

The pH of the electrolyte is central to reaction selectivity and overpotential. HER easily takes place in neutral and alkaline aqueous electrolytes by cathodic polarization, usually competing with CO₂ reduction. HER is prevalent particularly in acidic solution, whereas CO₂ molecules do not exist in a basic solution. Thus, most of CO₂ reduction studies were performed in neutral electrolyte solutions. OH⁻ is generated at the electrode when the H₂O molecule is involved with a cathodic reduction. Because the rate of neutralization between OH⁻ and CO₂ is slow in aqueous solutions at ambient temperature, the pH adjacent to the electrode becomes higher than that of the bulk solution. CO₂ molecules are present in nonequilibrium high pH regions at the electrode/electrolyte interface. The local pH effects might not change in the intrinsic kinetics of the desired reaction CO₂RR but just suppress the competing unwanted reaction HER to improve selectivity.^{113,114} The enhancement of pH is more significant in solutions, such as K₂SO₄, KCl and NaClO₄, which do not release protons.

1.4.6.1 Aqueous electrolytes

Cation effects have received great attention in the field of the eCO₂RR, especially the effects of alkali metals. The large cations more likely absorb on the cathode and result in a less negative outer Helmholtz plane potential, thus altering the hydrogen coverage on the electrode surface and repelling H⁺ ions from the electrode. On the contrary, small cations are hydrated strongly, which prevent adsorption of the cation on the electrode surface furtherly.^{115,116} Alternatively, larger cations provide stronger buffering abilities, maintain a lower pH, and keep the local dissolved CO₂ concentration higher. In addition, larger cation can reduce charge transfer resistances by helping to

stabilize the $\text{CO}_2^{\bullet-}$ on the electrode surface and improve the current density at the same applied potentials.¹¹⁷

Anions include non-buffering anions and buffering anions. Non-buffering anions show halide effects which depend on the size and concentration of halide. The weakly solvated anions, interact directly with the electrode surface and can destabilize the $\text{CO}_2^{\bullet-}$ intermediate, unlike smaller, more hydrated, anions that are located further away. In addition to the reaction kinetics, the cost and conductivity of the electrolyte solution are also considered.¹¹⁸

1.4.6.2 Organic electrolytes

Compared to water, the organic electrolytes have higher CO_2 solubility. In terms of the molecular catalysts, they are prone to hydrolysis or cannot be solved in aqueous electrolytes. The organic electrolytes can be further categorized into protic and aprotic solvents. The reaction pathway might be different in different solvents. For example, in aprotic solvents, the competitive HER could be avoided and a large overpotential is needed to form $\text{CO}_2^{\bullet-}$ radical anion. In addition, the concentration of water as a reagent can be accurately regulated and the reaction mechanism may be easily studied. Aprotic solvents commonly used are propylene carbonate (PC), acetonitrile (AN), DMF, THF (tetrahydrofuran) and dimethyl sulfoxide (DMSO). In protic solvents, protons could be transferred from the solvent to the intermediate or to promote the formation of CO. Protic solvents commonly used are methanol, ethanol, and formic acid.

1.4.6.3 Ionic liquids

Compared with isotropic aqueous solutions, ionic liquids are anisotropic fluids and exhibit the properties of an extended cooperative network of supramolecular-like species. These unique properties could lead to a different reaction mechanism and activities.^{15,119}

The main roles of ionic liquids are absorbing CO_2 and stabilizing $\text{CO}_2^{\bullet-}$. The adsorption capacity of ionic liquids comes from physical adsorption and chemical adsorption.¹²⁰ During the formation of $\text{CO}_2^{\bullet-}$ process, ionic liquids could decrease the thermodynamic

barrier which is the rate-determining step in ionic liquids. In addition, the anions and cations in current density and viscosity play a significant role. However, despite the advantages presented by the ionic liquids for the CO₂RR, there are some drawbacks that need to be considered carefully, such as their high cost and their environmental toxicity.

1.4.6.4 Pressure

The enhanced CO₂ solubility in aqueous electrolytes of H cell reactor allows for higher CO₂RR current densities. This benefit could also be improved in the flow cells. The influence of pressure is manifold. It could improve the selectivity of CO₂RR^{121,122} and modulate the selectivity between eCO₂RR products and overpotentials¹²³. In addition, the bubble size in the liquid electrolyte when operating at high current densities could be reduced to minimize the bubble-induced blockages of the electrode active area and the ohmic losses.

1.4.6.5 Temperature

At lower temperature, the increased CO₂ solubility improves the selectivity for CO₂RR as compared to HER. While the dominant products of CO₂RR do not change significantly with temperature on most catalysts.^{124,125}

1.5 Catalyst engineering

The key parameters for a catalyst to become interesting for commercial CO₂RR applications are the high activity, high selectivity, long-term durability, and the capacity towards valuable products.¹²⁶ Here, we summarize several strategies published to achieve high selectivity via rational design of different catalysts. In this thesis, we just focus on the heterogeneous catalysts. The main strategies followed to tune the properties of catalysts are: 1) tailor the electronic structure of the active sites, by changing the coordination state, constructing spatial confinement, or introducing doping or 2) tailor the apparent physical structures, by changing the morphologies and dimensions, to increase the utilization of active sites.³⁰

1.5.1 Metal-based catalysts

Metal and metal-based electrodes are the most common and popular electrocatalysts for eCO₂RR.¹²⁷ Various metal-based electrocatalysts with different anionic compositions (metals, alloys, oxides, sulphides, selenides, and others) have been developed. Many researches have focused on this kind of catalysts including the reaction mechanism, interface, surface, defect, phase, and morphology control. Based on various reaction routes, intermediates (*COOH, *OCOH, *CO, etc.) and main products, electrocatalysts can be generally categorized into three different groups: 1) Zn,^{45,128} Ag^{129,130} Au¹³¹ and Pd¹³² thermodynamically favour the adsorption of *COOH over *OCOH, and thus CO is their main product (**Figure 1.6 bottom**); 2) Ga, In, Sn^{52,133,134} and Bi thermodynamically favour *OCOH adsorption over *COOH thus yielding formate (**Figure 1.6 top**)^{9,135} 3) The last group, including Cu as its best choice,²⁰ could stabilize both *COOH and *CO and offer the possibility for C₂₊ product formation.

Other metals like Pt and Ni have lower hydrogen evolution reaction (HER) overpotentials and strong binding capabilities with *CO intermediates. Therefore, HER will be the predominant process in the presence of water. Single-atom catalysts (SACs) for the same metal, however, could show high CO selectivity by tailoring intrinsic electronic structures.¹³⁶

1.5.2 Carbon-based catalysts

1.5.2.1 Metal-nitrogen doped carbon catalysts

To improve the number of active sites which could promote the eCO₂RR activity and selectivity of catalysis and avoid generating undesirable active sites, single-atom catalysts with individual metal atoms dispersed on solid substrates which serve as the bridge between homogeneous and heterogeneous catalysts could address these issues.^{137–139} Compared to the bulk metal catalyst, there are several advantages for single-atom catalysts (SACs).¹⁴⁰ Firstly, their maximized atom-utilization efficiency reduces the high synthesis cost caused by the large excess of metal. Besides, the charge density and electronic structure of the metal atoms could be manipulated by

incorporating metal atoms in different coordination environment.¹⁴¹ The use of SACs helps to overcome the high activation barriers and the sluggish eCO₂RR kinetics because the valence electrons in the d-state are close to the Fermi level, provide fast electron transfer and promote the adsorption of CO₂ or intermediates.¹⁴² Ni-based SACs are a good example. As we mentioned, metallic Ni tends to serve as catalyst for HER under eCO₂RR, but the Ni atomic sites could reduce CO₂ to CO with high selectivity. Many works exploited the coordination environment of this active site to furtherly improve the performance of CO₂RR. Li and co-workers synthesized Ni-based SACs with three N atom coordination showing a unique electronic structure of Ni^{δ+} (0 < δ < 2). Other SACs could also be prepared with a different nitrogen coordination number.¹⁴³ Subsequently, Wang and co-workers reported a Ni site coordinated with four N atoms and one axial O. This axial traction strategy could optimize the electronic structure of the typical Ni-N₄ moiety and decrease the free energy barrier of CO₂* to COOH* intermediate, thus boosting the reaction kinetic of the eCO₂RR. Similar strategies could be used to improve Fe-based SACs.¹⁴¹

1.5.2.2 Metal-free carbon catalyst

Compared to the research on metal-based catalysts, investigations of carbon-based catalysts for CO₂ reduction are relatively rare. The heteroatom incorporation and functional group modification are used to enhance the electrochemical activity of pristine carbon.^{144,145} Besides, the nanostructure such as carbon nanotubes, carbon fibre or porous carbon, could influence the catalytic performance.^{146–148}

1.5.3 Metal organic frameworks (MOFs)

1.5.3.1 Pristine MOF

Metal organic frameworks consist on inorganic building blocks and multidentate organic ligands.¹⁴⁹ They exhibit unprecedented functionalities and properties deriving from the structural distinctiveness and diversities of their inorganic part and organic ligands.^{150,151} In addition to directly using MOFs, they could also be used as supporting substrates to load other active materials in different ways or as sacrificial materials to

derive various nanostructures by using different treatment methods.^{152,153} Generally, MOFs can be used as precursors of other electrocatalysts, as electrocatalysts and as supports.¹⁵⁴ Because they combine inorganic metallic species with organic moieties, decomposition of MOFs at higher temperatures under different conditions could be used to prepare a variety of products from porous carbon to metal oxides, metal sulphides, metal carbides, metals and metal oxide decorated carbon composites with the unique advantages of controlled porosity and higher active surface.

1.5.3.2 MOF derivatives

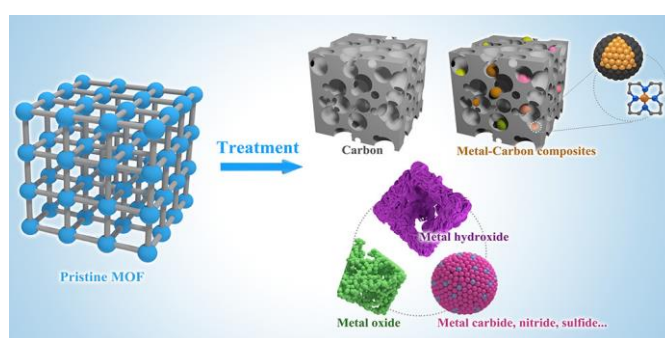


Figure 1.16 MOF-derived materials.¹⁵⁵

1.5.3.2.1 Carbon scaffolds

For the carbonaceous materials with the desired inherent properties, MOFs consisted on an inorganic part and an organic part. In order to get final carbon-based materials, we should remove the metallic species first.^{152,156–158} Meaning that the carbonization process should include two processes, the decomposition of MOFs and the removal of the metallic species. The produced gas from ligands or metal nodes could promote to form hierarchically porous structures.¹⁵⁹ One of the most common approaches is using Zn-based MOFs to derive carbon materials. The boiling point of zinc is 908 °C lower than most metals. It is easier to remove zinc during thermal treatment. However, even in an inert atmosphere, Zn could be converted into zinc oxide (ZnO) which has higher boiling point. In addition, the carbon formatted from the decomposition of the MOF could reduce ZnO into Zn leaving behind highly porous carbon.^{158,160} When other metals with higher boiling points such as iron (Fe), cobalt (Co), or copper (Cu), serve as inorganic parts, carbonized samples could retain the metallic species. Acid wash

treatment is a way to remove them totally. In addition, selected organic ligands and encapsulated additives or under specific atmosphere such as NH_3 , H_2S and PH_3 gases could dope various atoms in the porous carbon skeletons.¹⁶¹

1.5.3.2.2 Metal oxides

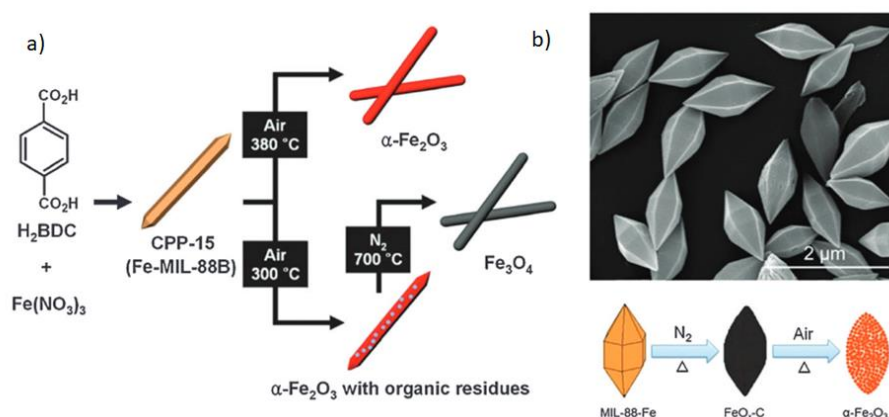


Figure 1.17 (a) Selective preparation of hematite ($\alpha\text{-Fe}_2\text{O}_3$) and magnetite (Fe_3O_4) nanorods from coordination polymer particle nanorods. (b) SEM image of as-prepared MIL-88-Fe and illustration of the fabrication of spindle-like porous $\alpha\text{-Fe}_2\text{O}_3$.

Synthesis of nanostructured metal oxides for electrochemical applications has been the subject of intense investigation with particular interest in controlling the shape, size, and composition of the resulting metal oxides. MOFs pyrolysis strategy has emerged to be a promising candidate providing the opportunity to tailor metal oxide structures in several ways. The inherent properties of MOFs could be inherited into metal oxides. The different calcination conditions could get different metal oxides with different properties. For example, MIL-88B could be used to synthesize hematite ($\alpha\text{-Fe}_2\text{O}_3$) via direct thermal conversion but MIL-88B (Fe) could transfer into magnetite (Fe_3O_4) via a two-step method (calcination followed by heating in inert atmosphere) (**Figure 1.17a**).¹⁶² Using MIL-88B (Fe) as a sacrificial template via a two-step thermolysis method including carbonization in an N_2 environment and oxidation in air, spindle like mesoporous structures of Fe_2O_3 with a surface area of $75 \text{ m}^2\text{g}^{-1}$ were obtained (**Figure 1.17b**).¹⁶³ However, one-step oxidation of MIL-88B only gets a lower surface area product. David and co-workers reported that Fe_2O_3 microboxes with hierarchically structure shells have been synthesized simply by annealing Prussian blue (PB) microcubes. Iron oxide shells with anisotropic properties could be synthesized

during oxidative decomposition of PB microbes (**Figure 1.18**). The thermolytic temperature plays a critical role in defining the shape of the final product. At 350 °C, the PB could decompose into Fe₂O₃ microboxes. When the temperature increased to 550 °C, porous Fe₂O₃ microboxes were obtained. However, hierarchical microboxes containing Fe₂O₃ nanoplatelets were prepared at 650 °C. MOFs could serve as the substrate to prepare multiple metallic MOF-derived materials which could be fabricated with mixed metal oxides with unique features such as improved electrical, chemical, and magnetic properties. The “escape-by-crafty-scheme” strategy was reported to prepare spinel metal-oxide nanoparticles, such as CoMn₂O₄, ZnMn₂O₄ and NiMn₂O₄.^{164,165}

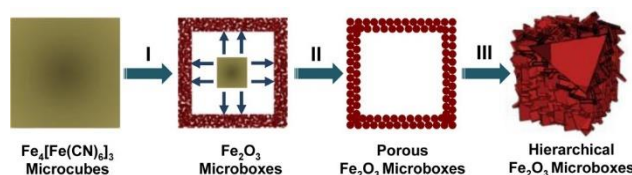


Figure 1.18 Formation of hollow Fe₂O₃ microboxes and evolution of the shell structure with the increasing calcination temperature.

1.5.3.2.3 Metal oxide-carbon composites

Because MOFs are composed of inorganic building blocks and organic ligands, part of the carbon from organic ligands could be reserved under certain annealing conditions to get special metal oxide-C composites.¹⁶⁶ The carbon layer could avoid the appearance of agglomeration during annealing process and control particles sizes precisely. Park and co-workers reported that the metal-organic framework IRMOF-1 could produce hierarchically porous carbon-coated ZnO quantum dots via a one-step-controlled pyrolysis. The carbon covered on the ZnO could decrease the agglomeration which improve the electrochemical performance.¹⁶⁷ Gascon and co-workers reported that highly dispersed iron carbides embedded in a matrix of porous carbon were produced when a metal organic framework was used as catalyst precursor.

1.5.3.3 MOF composite

In many cases, pristine MOFs could not show desirable performance to meet the requirement of different energy and catalysis applications due to their poor conductivity and limited functionality.¹⁶⁸ The combination of MOFs with functional materials is an easier way to overcome the deficiencies of the separate parts and even obtain a final composite that can outperform the properties of each single component.^{169,170} Various functional materials, including metal or metal oxide nanoparticles, carbon nanotubes, quantum dots and other conductive substrates, have been used to synthesize MOF composites. There are two general ways to combine functional materials into MOFs. One is by encapsulating the functional materials inside MOFs; the other is using the functional materials as substrates to support MOFs.

1.5.3.3.1 Metal-nanoparticles@MOFs

The encapsulated materials such as metal or metal oxide nanoparticles,^{171,172} polyoxometalates,^{173,174} and quantum dots can serve as the active sites or performance-enhancing auxiliaries while the MOF crystal may serve as support to stabilize and confine these materials. The strong interactions and synergistic effects between them contribute greatly to the relevant applications.^{168,175} For example, adsorption of CO₂ on the surface of a catalyst is a prerequisite in order to get a high CO₂ conversion. However, the non-polar CO₂ always weakly interacts with catalysts. More important, CO₂ conversion processes are always carried out in aqueous solution, which has poor solubility of CO₂ and low CO₂ concentration. MOFs with high surface areas and CO₂ affinities could serve as CO₂ sorbent materials to aid in enhanced adsorption of CO₂, which indirectly benefit the catalytic activity.

There are two main methods to synthesize this kind of composite. One method is the so-called “bottle-around-ship” strategy. It means that MOFs “shell” grow on the surface of the synthesized “core” based on inorganic nanoparticles. According to different applications and properties of the inorganic and the organic parts, several typical methods are summarized in **Table 1.9**.¹⁶⁹ The other strategy is named “ship-in-bottle”, where the incipient wetness impregnation has been one of most common methods.

Table 1.9 Comparison of the different synthetic methods.

	CAAS (Capping agent-assisted synthesis)	ITAS (Inorganic template-assisted synthesis)	One-pot	EGS (Epitaxial growth synthesis)
Advantages	Most versatile method	“Clean” surface of NPs	Direct	“Clean” surface of NPs (sandwich composites)
	Tunable synthetic parameters		Potentially scalable	Tunable shell thickness
	Allow large lattice mismatches			
Disadvantages	Remaining bridging agent that may block the active sites	Limited core and shell candidates (shape, morphology, size)	Remaining capping agent	Similar structure needed for core and shell
	Multiple-steps synthesis	Relative low chemical stability of the shell MOF	Challenging synthesis	More complex synthesis (sandwich composites)
		Multiple-steps synthesis	Lack of properties control	

1.5.3.3.2 MOFs@functional materials

MOFs serving as the main active species can be supported by functional substrates which could avoid MOFs from aggregation and deactivation. Besides, special substrates like carbon nanotubes or reduced graphene oxide could also enhance the mechanical stability and conductivity of the final catalyst system.^{176,177} Besides, the MOFs or covalent organic frameworks (COF) themselves serving as a kind of functional materials could be used as active shells.¹⁷⁸ Through hierarchical molecular assembly of metal building units and organic linkers, different functional moieties could be concentrated in a single crystalline material. Compared to simple mixing MOFs with functional materials, this kind of composite has high designability. This integrated methodology is defined as “heterogeneity with order”, which is a very foreword sub-discipline in the field of MOF synthesis.^{179–182}

Considering the instability of MOFs especially in aqueous acidic and basic solutions, not to mention certain harsh application conditions of electrocatalytic reactions, higher requirements are placed on the stability of MOFs.¹⁸³

References

1. Shakun, J. D. *et al.* Global warming preceded by increasing carbon dioxide concentrations during the last deglaciation. *Nature* **484**, 49–54 (2012).
2. Anderson, K. & Peters, G. The trouble with negative emissions. *Science* **354**, 182–183 (2016).
3. Rogelj, J. *et al.* Paris Agreement climate proposals need a boost to keep warming well below 2 °C. *Nature* **534**, 631–639 (2016).
4. Zou, C. *et al.* Connotation, innovation and vision of “carbon neutrality.” *Nat Gas Industry B* **8**, 523–537 (2021).
5. Ding, S., Hülsey, M. J., Pérez-Ramírez, J. & Yan, N. Transforming Energy with Single-Atom Catalysts. *Joule* **3**, 2897–2929 (2019).
6. Zhao, K. & Quan, X. Carbon-Based Materials for Electrochemical Reduction of CO₂ to C₂+ Oxygenates: Recent Progress and Remaining Challenges. *ACS Catal.* **11**, 2076–2097 (2021).
7. Yang, K. D., Lee, C. W., Jin, K., Im, S. W. & Nam, K. T. Current Status and Bioinspired Perspective of Electrochemical Conversion of CO₂ to a Long-Chain Hydrocarbon. *J Phys. Chem. Lett.* **8**, 538–545 (2017).
8. Grubel, K., Chouyyok, W., Heldebrant, D. J., Linehan, J. C. & Bays, J. T. Octane-On-Demand: Onboard Separation of Oxygenates from Gasoline. *Energy Fuels* **33**, 1869–1881 (2019).
9. Han, N., Ding, P., He, L., Li, Y. & Li, Y. Promises of Main Group Metal-Based Nanostructured Materials for Electrochemical CO₂ Reduction to Formate. *Adv. Energy Mater.* **10**, 1902338 (2020).
10. Tu, W., Zhou, Y. & Zou, Z. Photocatalytic Conversion of CO₂ into Renewable Hydrocarbon Fuels: State-of-the-Art Accomplishment, Challenges, and Prospects. *Adv. Mater.* **26**, 4607–4626 (2014).
11. Newman, J., Hoertz, P. G., Bonino, C. A. & Trainham, J. A. Review: An Economic Perspective on Liquid Solar Fuels. *J. Electrochem. Soc.* **159**, A1722–A1729 (2012).
12. Jin, S., Hao, Z., Zhang, K., Yan, Z. & Chen, J. Advances and Challenges for the Electrochemical Reduction of CO₂ to CO: From Fundamentals to Industrialization. *Angew. Chem. Int. Ed.* **60**, 20627–20648 (2021).
13. Li, L., Li, X., Sun, Y. & Xie, Y. Rational design of electrocatalytic carbon dioxide reduction for a zero-carbon network. *Chem. Soc. Rev.* (2022) doi:10.1039/d1cs00893e.
14. Alberio, J., Peng, Y. & García, H. Photocatalytic CO₂ Reduction to C₂+ Products. *ACS Catal.* **10**, 5734–5749 (2020).
15. Rosen, B. A. *et al.* Ionic Liquid-Mediated Selective Conversion of CO₂ to CO at Low Overpotentials. *Science* **334**, 643–644 (2011).
16. Zhu, D. D., Liu, J. L. & Qiao, S. Z. Recent Advances in Inorganic Heterogeneous Electrocatalysts for Reduction of Carbon Dioxide. *Adv. Mater.* **28**, 3423–3452 (2016).
17. Zhang, W. *et al.* Progress and Perspective of Electrocatalytic CO₂ Reduction for Renewable Carbonaceous Fuels and Chemicals. *Adv. Sci.* **5**, 1700275 (2017).
18. Lee, C. W. *et al.* New challenges of electrokinetic studies in investigating the reaction mechanism of electrochemical CO₂ reduction. *J. Mater. Chem. A* **6**, 14043–14057 (2018).
19. Dunwell, M., Luc, W., Yan, Y., Jiao, F. & Xu, B. Understanding Surface-Mediated Electrochemical Reactions: CO₂ Reduction and Beyond. *ACS Catal.* **8**, 8121–8129 (2018).
20. Nitopi, S. *et al.* Progress and Perspectives of Electrochemical CO₂ Reduction on Copper in Aqueous Electrolyte. *Chem. Rev.* **119**, 7610–7672 (2019).
21. Singh, M. R., Clark, E. L. & Bell, A. T. Effects of electrolyte, catalyst, and membrane composition and operating conditions on the performance of solar-driven electrochemical reduction of carbon dioxide. *Phys. Chem. Chem. Phys.* **17**, 18924–18936 (2015).
22. Clark, E. L. & Bell, A. T. Direct Observation of the Local Reaction Environment during the Electrochemical Reduction of CO₂. *J. Am. Chem. Soc.* **140**, 7012–7020 (2018).
23. Feaster, J. T. *et al.* Understanding Selectivity for the Electrochemical Reduction of Carbon Dioxide to Formic Acid and Carbon Monoxide on Metal Electrodes. *ACS Catal.* **7**, 4822–4827 (2017).

24. Kortlever, R., Shen, J., Schouten, K. J. P., Calle-Vallejo, F. & Koper, M. T. M. Catalysts and Reaction Pathways for the Electrochemical Reduction of Carbon Dioxide. *J. Phys. Chem. Lett.* **6**, 4073–4082 (2015).
25. Hansen, H. A., Varley, J. B., Peterson, A. A. & Nørskov, J. K. Understanding Trends in the Electrocatalytic Activity of Metals and Enzymes for CO₂ Reduction to CO. *J. Phys. Chem. Lett.* **4**, 388–392 (2013).
26. Yoo, J. S., Christensen, R., Vegge, T., Nørskov, J. K. & Studt, F. Theoretical Insight into the Trends that Guide the Electrochemical Reduction of Carbon Dioxide to Formic Acid. *ChemSuschem* **9**, 358–363 (2016).
27. Bi, Q.-Y. *et al.* Efficient Subnanometric Gold-Catalyzed Hydrogen Generation via Formic Acid Decomposition under Ambient Conditions. *J. Am. Chem. Soc.* **134**, 8926–8933 (2012).
28. Yoo, J. S., Abild-Pedersen, F., Nørskov, J. K. & Studt, F. Theoretical Analysis of Transition-Metal Catalysts for Formic Acid Decomposition. *ACS Catal.* **4**, 1226–1233 (2014).
29. Handoko, A. D., Wei, F., Jenndy, Yeo, B. S. & Seh, Z. W. Understanding heterogeneous electrocatalytic carbon dioxide reduction through operando techniques. *Nat. Catal.* **1**, 922–934 (2018).
30. Seh, Z. W. *et al.* Combining theory and experiment in electrocatalysis: Insights into materials design. *Science* **355**, (2017).
31. Zheng, W., Liu, M. & Lee, L. Y. S. Electrochemical Instability of Metal–Organic Frameworks: In Situ Spectroelectrochemical Investigation of the Real Active Sites. *ACS Catal.* **10**, 81–92 (2020).
32. Bañares, M. A. Operando Spectroscopy: the Knowledge Bridge to Assessing Structure–Performance Relationships in Catalyst Nanoparticles. *Adv. Mater.* **23**, 5293–5301 (2011).
33. Bañares, M. A. Operando methodology: combination of in situ spectroscopy and simultaneous activity measurements under catalytic reaction conditions. *Catal. Today* **100**, 71–77 (2005).
34. Li, X., Yang, X., Zhang, J., Huang, Y. & Liu, B. In Situ/Operando Techniques for Characterization of Single-Atom Catalysts. *ACS Catal.* **9**, 2521–2531 (2019).
35. Kas, R. *et al.* In-Situ Infrared Spectroscopy Applied to the Study of the Electrocatalytic Reduction of CO₂: Theory, Practice and Challenges. *Chemphyschem* **20**, 2904–2925 (2019).
36. Yang, K., Kas, R. & Smith, W. A. In Situ Infrared Spectroscopy Reveals Persistent Alkalinity near Electrode Surfaces during CO₂ Electroreduction. *J. Am. Chem. Soc.* **141**, 15891–15900 (2019).
37. Baruch, M. F., Pander, J. E., White, J. L. & Bocarsly, A. B. Mechanistic Insights into the Reduction of CO₂ on Tin Electrodes using in Situ ATR-IR Spectroscopy. *ACS Catal.* **5**, 3148–3156 (2015).
38. Zu, X. *et al.* Efficient and Robust Carbon Dioxide Electroreduction Enabled by Atomically Dispersed Sn^{δ+} Sites. *Adv. Mater.* **31**, 1808135 (2019).
39. Tory, J., Setterfield-Price, B., Dryfe, R. A. W. & Hartl, F. [M(CO)₄(2,2'-bipyridine)] (M=Cr, Mo, W) Complexes as Efficient Catalysts for Electrochemical Reduction of CO₂ at a Gold Electrode. *Chemelectrochem* **2**, 213–217 (2015).
40. Zakaria, S. N. A. *et al.* Insight into the Nature of Iron Sulfide Surfaces During the Electrochemical Hydrogen Evolution and CO₂ Reduction Reactions. *ACS Appl. Mater. Inter.* **10**, 32078–32085 (2018).
41. Deng, Y. & Yeo, B. S. Characterization of Electrocatalytic Water Splitting and CO₂ Reduction Reactions Using In Situ/Operando Raman Spectroscopy. *ACS Catal.* **7**, 7873–7889 (2017).
42. Figueiredo, M. C., Ledezma-Yanez, I. & Koper, M. T. M. In Situ Spectroscopic Study of CO₂ Electroreduction at Copper Electrodes in Acetonitrile. *ACS Catal.* **6**, 2382–2392 (2016).
43. Oberst, J. L., Jhong, H.-R. “Molly,” Kenis, P. J. A. & Gewirth, A. A. Insight into the electrochemical reduction of CO₂ on gold via surface-enhanced Raman spectroscopy and N-containing additives. *J. Solid State Electr.* **20**, 1149–1154 (2016).
44. Wang, M., Árnadóttir, L., Xu, Z. J. & Feng, Z. In Situ X-ray Absorption Spectroscopy Studies of Nanoscale Electrocatalysts. *Nano-micro. Lett.* **11**, 47 (2019).

45. Rosen, J. *et al.* Electrodeposited Zn Dendrites with Enhanced CO Selectivity for Electrocatalytic CO₂ Reduction. *ACS Catal.* **5**, 4586–4591 (2015).
46. Mistry, H. *et al.* Highly selective plasma-activated copper catalysts for carbon dioxide reduction to ethylene. *Nat. Commun.* **7**, 12123 (2016).
47. Eilert, A., Roberts, F. S., Friebe, D. & Nilsson, A. Formation of Copper Catalysts for CO₂ Reduction with High Ethylene/Methane Product Ratio Investigated with In Situ X-ray Absorption Spectroscopy. *J. Phys. Chem. Lett.* **7**, 1466–1470 (2016).
48. Genovese, C. *et al.* Operando spectroscopy study of the carbon dioxide electro-reduction by iron species on nitrogen-doped carbon. *Nat. Commun.* **9**, 935 (2018).
49. Binninger, T. *et al.* Electrochemical Flow-Cell Setup for In Situ X-ray Investigations: I. Cell for SAXS and XAS at Synchrotron Facilities. *J. Electrochem. Soc.* **163**, H906–H912 (2016).
50. Luna, P. D. *et al.* Catalyst electro-redeposition controls morphology and oxidation state for selective carbon dioxide reduction. *Nat. Catal.* **1**, 103–110 (2018).
51. Weng, Z. *et al.* Active sites of copper-complex catalytic materials for electrochemical carbon dioxide reduction. *Nat. Commun.* **9**, 415 (2018).
52. Dutta, A. *et al.* Probing the chemical state of tin oxide NP catalysts during CO₂ electroreduction: A complementary operando approach. *Nano. Energy* **53**, 828–840 (2018).
53. Chang, C.-J. *et al.* In situ X-ray diffraction and X-ray absorption spectroscopy of electrocatalysts for energy conversion reactions. *J. Mater. Chem. A* **8**, 19079–19112 (2020).
54. Chang, C.-J. *et al.* Dynamic Reoxidation/Reduction-Driven Atomic Interdiffusion for Highly Selective CO₂ Reduction toward Methane. *J. Am. Chem. Soc.* **142**, 12119–12132 (2020).
55. Eilert, A. *et al.* Subsurface Oxygen in Oxide-Derived Copper Electrocatalysts for Carbon Dioxide Reduction. *J. Phys. Chem. Lett.* **8**, 285–290 (2017).
56. Nguyen, L., Tao, F. F., Tang, Y., Dou, J. & Bao, X.-J. Understanding Catalyst Surfaces during Catalysis through Near Ambient Pressure X-ray Photoelectron Spectroscopy. *Chem. Rev.* **119**, 6822–6905 (2019).
57. Zhu, Y. *et al.* Unravelling surface and interfacial structures of a metal–organic framework by transmission electron microscopy. *Nat Mater* **16**, 532–536 (2017).
58. Wiktor, C., Meledina, M., Turner, S., Lebedev, O. I. & Fischer, R. A. Transmission electron microscopy on metal–organic frameworks – a review. *J. Mater. Chem. A* **5**, 14969–14989 (2017).
59. Urban, K. W. Is science prepared for atomic-resolution electron microscopy? *Nat. Mater.* **8**, 260–262 (2009).
60. Chen, Q. *et al.* Imaging Beam-Sensitive Materials by Electron Microscopy. *Adv. Mater.* **32**, 1907619 (2020).
61. Song, K. *et al.* Atomic-Resolution Imaging of Halide Perovskites Using Electron Microscopy. *Adv. Energy Mater.* **10**, 1904006 (2020).
62. Su, D. Advanced electron microscopy characterization of nanomaterials for catalysis. *Green Energy Environment* **2**, 70–83 (2017).
63. Zhang, D. *et al.* Atomic-resolution transmission electron microscopy of electron beam-sensitive crystalline materials. *Science* **359**, 675–679 (2018).
64. Fan, Z. *et al.* In Situ Transmission Electron Microscopy for Energy Materials and Devices. *Adv. Mater.* **31**, 1900608 (2019).
65. Li, Y. *et al.* Cryo-EM Structures of Atomic Surfaces and Host-Guest Chemistry in Metal-Organic Frameworks. *Matter* **1**, 428–438 (2019).
66. Wiktor, C., Turner, S., Zacher, D., Fischer, R. A. & Tendeloo, G. V. Imaging of intact MOF-5 nanocrystals by advanced TEM at liquid nitrogen temperature. *Micropor Mesopor Mat.* **162**, 131–135 (2012).
67. Li, Y. *et al.* Unravelling Degradation Mechanisms and Atomic Structure of Organic-Inorganic Halide Perovskites by Cryo-EM. *Joule* **3**, 2854–2866 (2019).
68. Huang, W. *et al.* Dynamic Structure and Chemistry of the Silicon Solid-Electrolyte Interphase Visualized by Cryogenic Electron Microscopy. *Matter* **1**, 1232–1245 (2019).

69. Zhang, C. *et al.* Recent Progress of In Situ Transmission Electron Microscopy for Energy Materials. *Adv. Mater.* **32**, 1904094 (2020).
70. Wei, S. *et al.* Direct observation of noble metal nanoparticles transforming to thermally stable single atoms. *Nat. Nanotechnol.* **13**, 856–861 (2018).
71. Mata, M. de la *et al.* Polarity Assignment in ZnTe, GaAs, ZnO, and GaN-AlN Nanowires from Direct Dumbbell Analysis. *Nano. Lett.* **12**, 2579–2586 (2012).
72. Vorobyeva, E. *et al.* Atom-by-Atom Resolution of Structure–Function Relations over Low-Nuclearity Metal Catalysts. *Angew. Chem. Int. Ed.* **131**, 8816–8821 (2019).
73. Krivanek, O. L. *et al.* Atom-by-atom structural and chemical analysis by annular dark-field electron microscopy. *Nature* **464**, 571–574 (2010).
74. Zhang, L. *et al.* Graphene Defects Trap Atomic Ni Species for Hydrogen and Oxygen Evolution Reactions. *Chem* **4**, 285–297 (2018).
75. Liu, G. *et al.* MoS₂ monolayer catalyst doped with isolated Co atoms for the hydrodeoxygenation reaction. *Nat. Chem.* **9**, 810–816 (2017).
76. Feng, S. *et al.* In situ formation of mononuclear complexes by reaction-induced atomic dispersion of supported noble metal nanoparticles. *Nat. Commun.* **10**, 5281 (2019).
77. Wen, Y., Shang, T. & Gu, L. Analytical ABF-STEM imaging of Li ions in rechargeable batteries. *Microscopy* **66**, 25–238(2017).
78. Findlay, S. D. *et al.* Robust atomic resolution imaging of light elements using scanning transmission electron microscopy. *Appl. Phys. Lett.* **95**, 191913 (2009).
79. Okunishi, E., Sawada, H. & Kondo, Y. Experimental study of annular bright field (ABF) imaging using aberration-corrected scanning transmission electron microscopy (STEM). *Micron* **43**, 538–544 (2012).
80. Carlsson, A., Alexandrou, I., Yücelen, E., Bosch, E. G. T. & Lazić, I. Low Dose Imaging Using Simultaneous iDPC- and ADF-STEM for Beam Sensitive Crystalline Structures. *Microsc. Microanal.* **24**, 122–123 (2018).
81. Lazić, I., Bosch, E. G. T. & Lazar, S. Phase contrast STEM for thin samples: Integrated differential phase contrast. *Ultramicroscopy* **160**, 265–280 (2016).
82. Jiang, Z. *et al.* Filling metal–organic framework mesopores with TiO₂ for CO₂ photoreduction. *Nature* **586**, 549–554 (2020).
83. Zhou, Y. *et al.* Local structure evolvement in MOF single crystals unveiled by scanning transmission electron microscopy. *Chem. Mater.* **32**, 4966–4972 (2020).
84. Liu, L. *et al.* Direct Imaging of Atomically Dispersed Molybdenum that Enables Location of Aluminum in the Framework of Zeolite ZSM-5. *Angew. Chem. Int. Ed.* **59**, 819–825 (2020).
85. Shen, B. *et al.* Atomic Spatial and Temporal Imaging of Local Structures and Light Elements inside Zeolite Frameworks. *Adv. Mater.* **32**, 1906103 (2019).
86. Shen, B., Chen, X., Shen, K., Xiong, H. & Wei, F. Imaging the node-linker coordination in the bulk and local structures of metal-organic frameworks. *Nat. Commun.* **11**, 2692 (2020).
87. Zhao, C. *et al.* Ionic Exchange of Metal–Organic Frameworks to Access Single Nickel Sites for Efficient Electroreduction of CO₂. *J. Am. Chem. Soc.* **139**, 8078–8081 (2017).
88. Wang, G. *et al.* Photoinduction of Cu Single Atoms Decorated on UiO-66-NH₂ for Enhanced Photocatalytic Reduction of CO₂ to Liquid Fuels. *J. Am. Chem. Soc.* **142**, 19339–19345 (2020).
89. Chen, Z. *et al.* Stabilization of Single Metal Atoms on Graphitic Carbon Nitride. *Adv. Funct. Mater.* **27**, 1605785 (2017).
90. Krivanek, O. L. *et al.* Progress in ultrahigh energy resolution EELS. *Ultramicroscopy* **203**, 60–67 (2019).
91. Idrobo, J. C. & Zhou, W. A short story of imaging and spectroscopy of two-dimensional materials by scanning transmission electron microscopy. *Ultramicroscopy* **180**, 156–162 (2017).
92. Nelayah, J. *et al.* Mapping surface plasmons on a single metallic nanoparticle. *Nat. Phys.* **3**, 348–353 (2007).

93. Zhan, W., Venkatachalapathy, V., Aarholt, T., Kuznetsov, A. Yu. & Prytz, Ø. Band gap maps beyond the delocalization limit: correlation between optical band gaps and plasmon energies at the nanoscale. *Sci. Rep.* **8**, 848 (2018).
94. Chung, H. T. *et al.* Direct atomic-level insight into the active sites of a high-performance PGM-free ORR catalyst. *Science* **357**, 479–484 (2017).
95. Zhou, S. *et al.* Engineering electrocatalytic activity in nanosized perovskite cobaltite through surface spin-state transition. *Nat. Commun.* **7**, 11510 (2016).
96. Haruta, M., Kurata, H., Komatsu, H., Shimakawa, Y. & Isoda, S. Site-resolved oxygen K-edge ELNES of the layered double perovskite $\text{La}_2\text{CuSnO}_6$. *Phys. Rev. B* **80**, 165123 (2009).
97. Kibria, M. G. *et al.* Electrochemical CO_2 Reduction into Chemical Feedstocks: From Mechanistic Electrocatalysis Models to System Design. *Adv. Mater.* **31**, 1807166 (2019).
98. Burdyny, T. & Smith, W. A. CO_2 reduction on gas-diffusion electrodes and why catalytic performance must be assessed at commercially-relevant conditions. *Energy Environ. Sci.* **12**, 1442–1453 (2019).
99. Kas, R. *et al.* Electrochemical CO_2 reduction on nanostructured metal electrodes: fact or defect? *Chem. Sci.* **11**, 1738–1749 (2020).
100. Li, T., Cao, Y., He, J. & Berlinguette, C. P. Electrolytic CO_2 Reduction in Tandem with Oxidative Organic Chemistry. *ACS Central Sci.* **3**, 778–783 (2017).
101. Weekes, D. M., Salvatore, D. A., Reyes, A., Huang, A. & Berlinguette, C. P. Electrolytic CO_2 Reduction in a Flow Cell. *Acc. Chem. Res.* **51**, 910–918 (2018).
102. Endrődi, B. *et al.* Continuous-flow electroreduction of carbon dioxide. *Prog. Energy. Combust. Sci.* **62**, 133–154 (2017).
103. Reyes, A. *et al.* Managing Hydration at the Cathode Enables Efficient CO_2 Electrolysis at Commercially Relevant Current Densities. *ACS Energy Lett.* **5**, 1612–1618 (2020).
104. Higgins, D., Hahn, C., Xiang, C., Jaramillo, T. F. & Weber, A. Z. Gas-Diffusion Electrodes for Carbon Dioxide Reduction: A New Paradigm. *ACS Energy Lett.* **4**, 317–324 (2019).
105. Li, Y. C. *et al.* Electrolysis of CO_2 to Syngas in Bipolar Membrane-Based Electrochemical Cells. *ACS Energy Lett.* **1**, 1149–1153 (2016).
106. Vargas-Barbosa, N. M., Geise, G. M., Hickner, M. A. & Mallouk, T. E. Assessing the Utility of Bipolar Membranes for use in Photoelectrochemical Water-Splitting Cells. *ChemSusChem* **7**, 3017–3020 (2014).
107. Yang, K., Kas, R., Smith, W. A. & Burdyny, T. Role of the Carbon-Based Gas Diffusion Layer on Flooding in a Gas Diffusion Electrode Cell for Electrochemical CO_2 Reduction. *ACS Energy Lett.* **6**, 33–40 (2021).
108. Malkhandi, S. & Yeo, B. S. Electrochemical conversion of carbon dioxide to high value chemicals using gas-diffusion electrodes. *Curr. Opin. Chem. Eng.* **26**, 112–121 (2019).
109. Cindrella, L. *et al.* Gas diffusion layer for proton exchange membrane fuel cells—A review. *J. Power Sources* **194**, 146–160 (2009).
110. Vasilyev, D. V. & Dyson, P. J. The Role of Organic Promoters in the Electroreduction of Carbon Dioxide. *ACS Catal.* **11**, 1392–1405 (2021).
111. Sharma, P. P. & Zhou, X. Electrocatalytic conversion of carbon dioxide to fuels: a review on the interaction between CO_2 and the liquid electrolyte. *WIREs Energy Environ* **6**, (2017).
112. Jones, J., Prakash, G. K. S. & Olah, G. A. Electrochemical CO_2 Reduction: Recent Advances and Current Trends. *Isr. J. Chem.* **54**, 1451–1466 (2014).
113. Hall, A. S., Yoon, Y., Wuttig, A. & Surendranath, Y. Mesostructure-Induced Selectivity in CO_2 Reduction Catalysis. *J. Am. Chem. Soc.* **137**, 14834–14837 (2015).
114. Yoon, Y., Hall, A. S. & Surendranath, Y. Tuning of Silver Catalyst Mesostructure Promotes Selective Carbon Dioxide Conversion into Fuels. *Angew. Chem. Int. Ed.* **55**, 15282–15286 (2016).
115. Ayemoba, O. & Cuesta, A. Spectroscopic Evidence of Size-Dependent Buffering of Interfacial pH by Cation Hydrolysis during CO_2 Electroreduction. *ACS Appl. Mater. Interfaces* **9**, 27377–27382 (2017).

116. Singh, M. R., Kwon, Y., Lum, Y., Ager, J. W. & Bell, A. T. Hydrolysis of Electrolyte Cations Enhances the Electrochemical Reduction of CO₂ over Ag and Cu. *J. Am. Chem. Soc.* **138**, 13006–13012 (2016).
117. Thorson, M. R., Siil, K. I. & Kenis, P. J. A. Effect of Cations on the Electrochemical Conversion of CO₂ to CO. *J. Electrochem. Soc.* **160**, F69–F74 (2012).
118. Varela, A. S., Ju, W., Reier, T. & Strasser, P. Tuning the Catalytic Activity and Selectivity of Cu for CO₂ Electroreduction in the Presence of Halides. *ACS Catal.* **6**, 2136–2144 (2016).
119. Corvo, M. C. *et al.* Solvation of Carbon Dioxide in [C₄mim][BF₄] and [C₄mim][PF₆] Ionic Liquids Revealed by High-Pressure NMR Spectroscopy. *Angew. Chem. Int. Ed.* **125**, 13262–13265 (2013).
120. Simon, N. M. *et al.* Carbon Dioxide Capture by Aqueous Ionic Liquid Solutions. *Chemsuschem* **10**, 4927–4933 (2017).
121. Hara, K., Kudo, A. & Sakata, T. Electrochemical reduction of carbon dioxide under high pressure on various electrodes in an aqueous electrolyte. *J. Electroanal. Chem.* **391**, 141–147 (1995).
122. Hara, K., Tsuneto, A., Kudo, A. & Sakata, T. Electrochemical Reduction of CO₂ on a Cu Electrode under High Pressure: Factors that Determine the Product Selectivity. *J. Electrochem. Soc.* **141**, 2097–2103–2097–2103 (1994).
123. Dufek, E. J., Lister, T. E. & Stone, S. G. Sampling dynamics for pressurized electrochemical cells. *J. Appl. Electrochem.* **44**, 849–855 (2014).
124. Kaneco, S. *et al.* Electrochemical conversion of carbon dioxide to methane in aqueous NaHCO₃ solution at less than 273 K. *Electrochim. Acta.* **48**, 51–55 (2002).
125. Dufek, E. J., Lister, T. E. & McIlwain, M. E. Bench-scale electrochemical system for generation of CO and syn-gas. *J. Appl. Electrochem.* **41**, 623–631 (2011).
126. Qiao, J., Liu, Y., Hong, F. & Zhang, J. A review of catalysts for the electroreduction of carbon dioxide to produce low-carbon fuels. *Chem. Soc. Rev.* **43**, 631–675 (2013).
127. Kuhl, K. P. *et al.* Electrocatalytic Conversion of Carbon Dioxide to Methane and Methanol on Transition Metal Surfaces. *J. Am. Chem. Soc.* **136**, 14107–14113 (2014).
128. Luo, W., Zhang, J., Li, M. & Züttel, A. Boosting CO Production in Electrocatalytic CO₂ Reduction on Highly Porous Zn Catalysts. *ACS Catal.* **9**, 3783–3791 (2019).
129. Bohra, D. *et al.* Lateral Adsorbate Interactions Inhibit HCOO[–] while Promoting CO Selectivity for CO₂ Electrocatalysis on Silver. *Angew. Chem. Int. Ed.* **131**, 1359–1363 (2019).
130. Ma, M., Trześniewski, B. J., Xie, J. & Smith, W. A. Selective and Efficient Reduction of Carbon Dioxide to Carbon Monoxide on Oxide-Derived Nanostructured Silver Electrocatalysts. *Angew. Chem. Int. Ed.* **55**, 9748–9752 (2016).
131. Chen, Y., Li, C. W. & Kanan, M. W. Aqueous CO₂ Reduction at Very Low Overpotential on Oxide-Derived Au Nanoparticles. *J. Am. Chem. Soc.* **134**, 19969–19972 (2012).
132. Nguyen, L. *et al.* Reduction of Nitric Oxide with Hydrogen on Catalysts of Singly Dispersed Bimetallic Sites Pt₁Co_m and Pd₁Co_n. *ACS Catal.* **6**, 840–850 (2016).
133. Zheng, X. *et al.* Sulfur-Modulated Tin Sites Enable Highly Selective Electrochemical Reduction of CO₂ to Formate. *Joule* **1**, 794–805 (2017).
134. Li, F., Chen, L., Knowles, G. P., MacFarlane, D. R. & Zhang, J. Hierarchical Mesoporous SnO₂ Nanosheets on Carbon Cloth: A Robust and Flexible Electrocatalyst for CO₂ Reduction with High Efficiency and Selectivity. *Angew. Chem. Int. Ed.* **129**, 520–524 (2017).
135. Zhao, S. *et al.* Advances in Sn-Based Catalysts for Electrochemical CO₂ Reduction. *Nanomicro Lett.* **11**, 62 (2019).
136. Jiang, K. *et al.* Transition-Metal Single Atoms in a Graphene Shell as Active Centers for Highly Efficient Artificial Photosynthesis. *Chem* **3**, 950–960 (2017).
137. Yang, X.-F. *et al.* Single-Atom Catalysts: A New Frontier in Heterogeneous Catalysis. *Acc. Chem. Res.* **46**, 1740–1748 (2013).
138. Zhang, X. *et al.* Boosting Electrocatalytic Activity of Single Atom Catalysts Supported on Nitrogen-Doped Carbon through N Coordination Environment Engineering. *Small* 2105329 (2022) doi:10.1002/smll.202105329.

139. Jin, H. *et al.* Unprecedentedly high activity and selectivity for hydrogenation of nitroarenes with single atomic Co₁-N₃P₁ sites. *Nat. Commun.* **13**, 723 (2022).
140. Qu, Q., Ji, S., Chen, Y., Wang, D. & Li, Y. The atomic-level regulation of single-atom site catalysts for the electrochemical CO₂ reduction reaction. *Chem. Sci.* **12**, 4201–4215 (2021).
141. Zhang, T. *et al.* Site-Specific Axial Oxygen Coordinated FeN₄ Active Sites for Highly Selective Electroreduction of Carbon Dioxide. *Adv. Funct. Mater.* 2111446 (2022) doi:10.1002/adfm.202111446.
142. Zhang, T. *et al.* Quasi-double-star nickel and iron active sites for high-efficiency carbon dioxide electroreduction. *Energy Environ. Sci.* **14**, 4847–4857 (2021).
143. Wang, X. *et al.* Regulation of Coordination Number over Single Co Sites: Triggering the Efficient Electroreduction of CO₂. *Angew. Chem. Int. Ed.* **130**, 1962–1966 (2018).
144. Duan, X. *et al.* Metal-Free Carbon Materials for CO₂ Electrochemical Reduction. *Adv. Mater.* **29**, 1701784 (2017).
145. Liu, S. *et al.* Identifying Active Sites of Nitrogen-Doped Carbon Materials for the CO₂ Reduction Reaction. *Adv. Funct. Mater.* **28**, 1800499 (2018).
146. Kumar, B. *et al.* Renewable and metal-free carbon nanofibre catalysts for carbon dioxide reduction. *Nat. Commun.* **4**, 2819 (2013).
147. Wu, J. *et al.* Achieving Highly Efficient, Selective, and Stable CO₂ Reduction on Nitrogen-Doped Carbon Nanotubes. *ACS Nano* **9**, 5364–5371 (2015).
148. Wu, J. *et al.* Incorporation of Nitrogen Defects for Efficient Reduction of CO₂ via Two-Electron Pathway on Three-Dimensional Graphene Foam. *Nano Lett.* **16**, 466–470 (2016).
149. Furukawa, H., Cordova, K. E., O’Keeffe, M. & Yaghi, O. M. The Chemistry and Applications of Metal-Organic Frameworks. *Science* **341**, 1230444 (2013).
150. Wang, Y., Hou, P., Wang, Z. & Kang, P. Zinc Imidazolate Metal–Organic Frameworks (ZIF-8) for Electrochemical Reduction of CO₂ to CO. *Chemphyschem* **18**, 3142–3147 (2017).
151. Liang, Z., Qu, C., Guo, W., Zou, R. & Xu, Q. Pristine Metal–Organic Frameworks and their Composites for Energy Storage and Conversion. *Adv. Mater.* **30**, 1702891 (2018).
152. Sun, J.-K. & Xu, Q. Functional materials derived from open framework templates/precursors: synthesis and applications. *Energy Environ. Sci.* **7**, 2071–2100 (2014).
153. Wang, H., Zhu, Q.-L., Zou, R. & Xu, Q. Metal-Organic Frameworks for Energy Applications. *Chem* **2**, 52–80 (2017).
154. Liang, Z., Zhao, R., Qiu, T., Zou, R. & Xu, Q. Metal-organic framework-derived materials for electrochemical energy applications. *Energychem* **1**, 100001 (2019).
155. Qiu, T. *et al.* Metal–Organic Framework-Based Materials for Energy Conversion and Storage. *ACS Energy Lett.* **5**, 520–532 (2020).
156. Yang, S. J. *et al.* MOF-Derived Hierarchically Porous Carbon with Exceptional Porosity and Hydrogen Storage Capacity. *Chem. Mater.* **24**, 464–470 (2012).
157. Zhong, H. *et al.* ZIF-8 Derived Graphene-Based Nitrogen-Doped Porous Carbon Sheets as Highly Efficient and Durable Oxygen Reduction Electrocatalysts. *Angew. Chem. Int. Ed.* **53**, 14235–14239 (2014).
158. Liu, B., Shioyama, H., Jiang, H., Zhang, X. & Xu, Q. Metal–organic framework (MOF) as a template for syntheses of nanoporous carbons as electrode materials for supercapacitor. *Carbon* **48**, 456–463 (2010).
159. Zhao, R. *et al.* A pore-expansion strategy to synthesize hierarchically porous carbon derived from metal-organic framework for enhanced oxygen reduction. *Carbon* **114**, 284–290 (2017).
160. Liu, B., Shioyama, H., Akita, T. & Xu, Q. Metal-Organic Framework as a Template for Porous Carbon Synthesis. *J. Am. Chem. Soc.* **130**, 5390–5391 (2008).
161. Zhang, P. *et al.* ZIF-derived in situ nitrogen-doped porous carbons as efficient metal-free electrocatalysts for oxygen reduction reaction. *Energy Environ Sci* **7**, 442–450 (2013).
162. Zhang, L., Wu, H. B., Madhavi, S., Hng, H. H. & Lou, X. W. (David). Formation of Fe₂O₃ Microboxes with Hierarchical Shell Structures from Metal–Organic Frameworks and Their Lithium Storage Properties. *J. Am. Chem. Soc.* **134**, 17388–17391 (2012).

163. Xu, X., Cao, R., Jeong, S. & Cho, J. Spindle-like Mesoporous α -Fe₂O₃ Anode Material Prepared from MOF Template for High-Rate Lithium Batteries. *Nano. Lett.* **12**, 4988–4991 (2012).
164. Mahata, P., Sarma, D., Madhu, C., Sundaresen, A. & Natarajan, S. CoMn₂O₄ spinel from a MOF: synthesis, structure and magnetic studies. *Dalton Trans.* **40**, 1952–1960 (2011).
165. Zhao, J. *et al.* Spinel ZnMn₂O₄ nanoplate assemblies fabricated via “escape-by-crafty-scheme” strategy. *J. Mater. Chem.* **22**, 13328–13333 (2012).
166. Santos, V. P. *et al.* Metal organic framework-mediated synthesis of highly active and stable Fischer-Tropsch catalysts. *Nat. Commun.* **6**, 6451 (2015).
167. Yang, S. J. *et al.* Preparation and Exceptional Lithium Anodic Performance of Porous Carbon-Coated ZnO Quantum Dots Derived from a Metal–Organic Framework. *J. Am. Chem. Soc.* **135**, 7394–7397 (2013).
168. Chen, L. & Xu, Q. Metal–Organic Framework Composites for Catalysis. *Matter* **1**, 57–89 (2019).
169. Dai, S., Tissot, A. & Serre, C. Recent Progresses in Metal–Organic Frameworks Based Core–shell Composites. *Adv. Energy Mater.* **12**, 2100061 (2022).
170. Liu, Y. & Tang, Z. Multifunctional Nanoparticle@MOF Core–Shell Nanostructures. *Adv. Mater.* **25**, 5819–5825 (2013).
171. Wang, S. *et al.* Boosting Electrocatalytic Hydrogen Evolution over Metal–Organic Frameworks by Plasmon-Induced Hot-Electron Injection. *Angew. Chem. Int. Ed.* **58**, 10713–10717 (2019).
172. Pipelzadeh, E., Rudolph, V., Hanson, G., Noble, C. & Wang, L. Photoreduction of CO₂ on ZIF-8/TiO₂ nanocomposites in a gaseous photoreactor under pressure swing. *Appl. Catal. B* **218**, 672–678 (2017).
173. Kong, X., Lin, Z., Zhang, Z., Zhang, T. & Lin, W. Hierarchical Integration of Photosensitizing Metal–Organic Frameworks and Nickel-Containing Polyoxometalates for Efficient Visible-Light-Driven Hydrogen Evolution. *Angew. Chem. Int. Ed.* **128**, 6521–6526 (2016).
174. Wei, T. *et al.* POM-based metal-organic framework/reduced graphene oxide nanocomposites with hybrid behavior of battery-supercapacitor for superior lithium storage. *Nano. Energy* **34**, 205–214 (2017).
175. Das, S. *et al.* Core–shell structured catalysts for thermocatalytic, photocatalytic, and electrocatalytic conversion of CO₂. *Chem. Soc. Rev.* **49**, 2937–3004 (2020).
176. Mao, Y. *et al.* Foldable interpenetrated metal-organic frameworks/carbon nanotubes thin film for lithium–sulfur batteries. *Nat. Commun.* **8**, 14628 (2017).
177. Jahan, M., Bao, Q. & Loh, K. P. Electrocatalytically Active Graphene–Porphyrin MOF Composite for Oxygen Reduction Reaction. *J. Am. Chem. Soc.* **134**, 6707–6713 (2012).
178. Wang, F. *et al.* Uncovering two kinetic factors in the controlled growth of topologically distinct core–shell metal–organic frameworks. *Chem. Sci.* **10**, 7755–7761 (2019).
179. Deng, H. *et al.* Multiple Functional Groups of Varying Ratios in Metal–Organic Frameworks. *Science* **327**, 846–850 (2010).
180. Luo, T.-Y. *et al.* Multivariate Stratified Metal–Organic Frameworks: Diversification Using Domain Building Blocks. *J. Am. Chem. Soc.* **141**, 2161–2168 (2019).
181. Choi, K. M., Jeon, H. J., Kang, J. K. & Yaghi, O. M. Heterogeneity within Order in Crystals of a Porous Metal–Organic Framework. *J. Am. Chem. Soc.* **133**, 11920–11923 (2011).
182. Feng, L. *et al.* Uncovering Two Principles of Multivariate Hierarchical Metal–Organic Framework Synthesis via Retrosynthetic Design. *ACS Cent. Sci.* **4**, 1719–1726 (2018).
183. Howarth, A. J. *et al.* Chemical, thermal and mechanical stabilities of metal–organic frameworks. *Nat. Rev. Mater.* **1**, 15018 (2016).

Chapter 2

Methodology

2.1 Electrochemistry

Electrochemistry is the study of the chemical processes that cause electrons to move. Electrochemistry is used to evaluate the eCO₂RR processes involving electron and proton transfers. Cyclic voltammetry (CV) serves as a powerful and popular electrochemical technique, and is employed to investigate the reduction and oxidation processes taking place in molecular species. CV is also a key technique to study the electron transfer-initiated catalytic reactions. **Figure 2.1a** shows the relationship between time and applied potential. The working electrode potential is ramped linearly from E_1 to a switching potential E_2 and then back to E_1 with a different scan rate. The resulting cyclic voltammogram depicts the current that flows as a function of the applied potential **Figure 2.1b**.¹

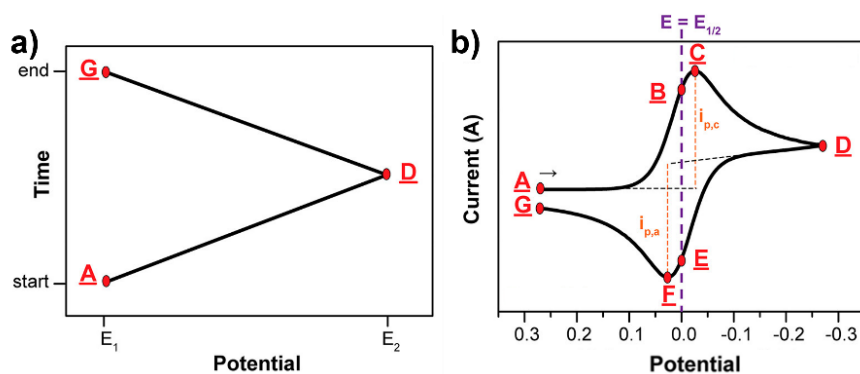


Figure 2.1 (a) Representation of the cyclic voltammetry potential ramping and (b) the resulting current as a function of the applied potential with annotation of initial (A), switching (D), and end potentials (G). $i_{p,c}$, $i_{p,a}$, and $E_{1/2}$ define the cathodic and anodic peak currents and the half-wave potential, respectively. The reduction is shown in the right direction here.

2.1.1 Nernst equation

The peaks appearing in a cyclic voltammogram could be explained via Nernst equation (2.1). E is the potential of the electrochemical cell or applied potential. E^0 is the standard potential for redox couple. F is Faraday's constant, R is the universal gas constant, n is the number of electrons, and T is the temperature. As the potential is scanned negatively from point A to point D, when the applied potential is more positive than E^0 , only a flat line named the capacitive current response is observed. At point C, where the cathodic current ($i_{p,c}$) peak is observed, the current is dictated by the delivery of additional oxidized analyte via diffusion from the bulk solution. When scanning to more negative potentials, the rate of diffusion of

species with oxidate state becomes slower and current decreases as the scan continues. At points B and E, the concentration of oxidized and reduced analyte at the electrode surface are equal.

$$E = E^0 + \frac{RT}{nF} \ln \frac{(\text{Ox})}{(\text{Red})} = E^0 + 2.3026 \frac{RT}{nF} \log_{10} \frac{(\text{Ox})}{(\text{Red})} \quad (2.1)$$

2.1.2 Scan rate

The scan rate is the potential change over time. Faster scan rates lead to higher currents because of the decrease in the size of the diffusion layer. The Randles-Sevcik equation (2.2) is used to describe the relation between the peak current $i_p(\text{A})$ and the scan rate. $A (\text{cm}^2)$ is the geometric surface area, n is the number of electrons transferred in the redox event, $D_o (\text{cm}^2 \text{ s}^{-1})$ is the diffusion coefficient of the oxidized analyte, and $C^0 (\text{mol cm}^{-3})$ is the bulk concentration of the analyte.

$$i_p = 0.446nFAC^0 \left(\frac{nFvD_o}{RT} \right)^{1/2} \quad (2.2)$$

2.1.3 Electrochemical active surface area (ECSA)

As the activity improvement of catalysts may originate from the intrinsic activity and/or the increased number of active sites, to deconvolute these two factors we should compare the intrinsic activity of the catalysts by normalizing the j to the electrochemical surface area.

The electrochemical surface area (ECSA) is estimated from the capacitance measurements by measuring the double-layer capacitance (C_{dl}) in the H-cell.² Cyclic voltammetry was performed at different scan rates in a non-Faradaic region, where only double-layer charging, and discharging is relevant. The absolute electrochemical double-layer capacitive current density is performed by averaging the cathodic and anodic current density at the middle potential for each scan rate. These capacitive currents were plotted against the scan rate and the slope of this plot was divided by 2 to obtain the value of C_{dl} .

$$j_c = vC_{dl} \quad (2.3)$$

2.1.4 Instantaneous Faraday efficiency^{3,4}

The electrocatalytic performance of different catalysts was measured at room temperature by using a H-cell with two-compartments separated by a cation exchange membrane (Nafion N-117 membrane) with a continuously Ar or CO₂ gas injection. Each compartment contained 70 ml electrolyte (0.5 M NaHCO₃ made from de-ionized water). In a typical experiment, a standard three electrode setup in 0.5 M NaHCO₃ solution was assembled: an Ag/AgCl electrode as reference electrode, a Pt plate as auxiliary electrode and a carbon paper coated with the different samples as working electrode (surface area = 1 cm²). The potentials were measured versus Ag/AgCl and converted to the reversible hydrogen electrode (RHE) according to the following equation: $E_{RHE} = E^0_{Ag/AgCl} + E_{Ag/AgCl} + 0.059 \times \text{pH}$, pH=7. All electrochemical results were showed without iR-compensation by using a computer-controlled BioLogic VMP3 electrochemical workstation. Meanwhile, the *I*-*t* was performed to reach a stable state at -0.70 V vs. RHE in Ar-saturated 0.5 M NaHCO₃ (pH=8.5). In addition, the linear sweep voltammetry (LSV) curves were performed in Ar-saturated and CO₂-saturated 0.5 M NaHCO₃.

Before the electrochemical CO₂ reduction experiments, an average rate of 20 ml min⁻¹ Ar was injected into cathodic electrolyte in order to form an Ar-saturated solution. During electrochemical CO₂ reduction experiments, the CO₂ gas was delivered at an average rate of 20 ml min⁻¹ at room temperature and ambient pressure, measured downstream by a volumetric digital flowmeter. The gas phase composition was analyzed by gas chromatography (GC) during potentiostatic measurements every 20 min.

During electrolysis, CO₂ gas (Airgas, 99.995 %) was delivered into the cathodic compartment containing CO₂-saturated electrolyte at a rate of 20.0 standard cubic centimeters per minute (sccm, monitored by Alicat Scientific mass flow controller) and vented into a gas chromatograph. The gas products were sampled after a continuous electrolysis of 15 min under each potential and liquid products are analyzed using ¹H nuclear magnetic resonance

(¹H NMR) spectroscopy. The partial current density for a given gas product was calculated as below:

$$j_i = x_i \times v \times \frac{n_i F P_0}{RT} \times (\text{electrode area})^{-1} \quad (2.4)$$

Where x_i is the volume fraction of certain product determined by online GC referenced to calibration curves from three standard gas samples, v is the flow rate, n_i is the number of electrons involved, $P_0 = 101.3$ kPa, F is the Faraday constant, and R is the gas constant. The corresponding FE at each potential is calculated by

$$FE = \frac{j_i}{j} \times 100\% \quad (2.5)$$

2.1.5 Average Faraday efficiency⁵

The electrocatalytic performance of different catalysts was measured at room temperature by using a H-cell with two-compartments separated by a cation exchange membrane (Nafion N-117 membrane). The electrolyte was saturated with CO₂ by purging with the gas for 15 min prior to electrolysis. The cell was sealed during electrolysis. To increase the mass transport of the reagents during electrolysis, vigorous stirring is required. After each electrolysis, 250 μL gas from the headspace was taken and injected into the Agilent Technologies 7890B gas chromatography (GC) system to identify and quantify products. The corresponding FE at each potential is calculated by

$$FE = \frac{n_x n_{cat} F}{Q} 100\% \quad (2.6)$$

Where n_x is the molar amount of certain product, n_{cat} is the number of electrons needed to form one product molecule, and Q is the charge passed during the electrolysis.

Even at the same potential, the FE could not keep the same value all the time. Especially, for the catalyst instability, catalysts degrade within hours. A few advantages of the CO₂ gas flow cell method for GC measurements are: 1) the gas product concentration can be tuned by changing the CO₂ gas flow rate and therefore the FE measurements can be accurate even for small currents; 2) the gas sample injection by auto GC valve switching can be highly

dependable with small error ranges; 3) by programming the GC auto valve switching every certain amount of time, the electrolysis can be continuously operated and analyzed for unattended long-term stability tests.

2.2 Ink Preparation³

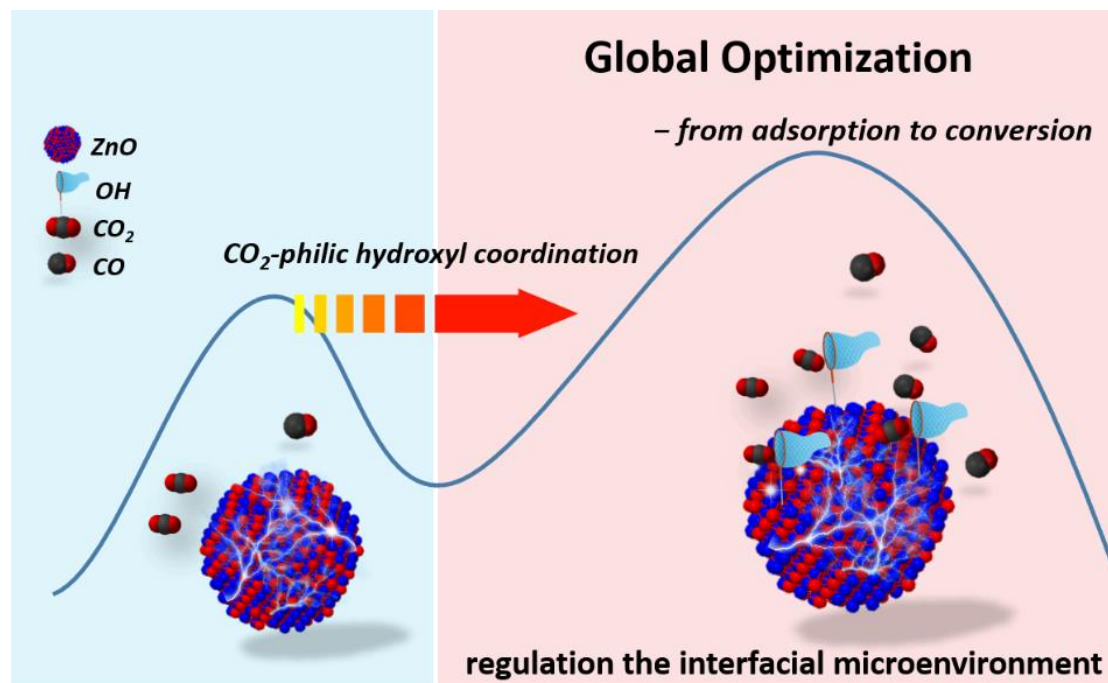
5 mg of the different synthesized samples and 100 μL 5 wt% Nafion solutions were dissolved in ethanol (1 mL) and ultrasonicated for 30 min to form an evenly suspension for the further electrochemical experiments. To prepare the working electrode, 500 μL of the above as-prepared inks were dropped onto the two sides of the carbon paper electrode with $1\times 1\text{ cm}^2$ and then dried at room temperature for a few minutes, giving a catalyst loading mass of $\sim 3\text{ mg/cm}^2$.

References

1. Elgrishi, N. *et al.* A Practical Beginner's Guide to Cyclic Voltammetry. *J. Chem. Educ.* **95**, 197–206 (2018).
2. Luo, W., Zhang, J., Li, M. & Züttel, A. Boosting CO Production in Electrocatalytic CO₂ Reduction on Highly Porous Zn Catalysts. *ACS Catal.* **9**, 3783–3791 (2019).
3. Zhang, T. *et al.* Quasi-double-star nickel and iron active sites for high-efficiency carbon dioxide electroreduction. *Energy Environ. Sci.* **14**, 4847–4857 (2021).
4. Jiang, K. *et al.* Metal ion cycling of Cu foil for selective C–C coupling in electrochemical CO₂ reduction. *Nat. Catal.* **1**, 111–119 (2018).
5. Li, S. *et al.* Low-Valence Zn^{δ+} (0<δ<2) Single-Atom Material as Highly Efficient Electrocatalyst for CO₂ Reduction. *Angew. Chem. Int. Ed.* **60**, 22826–22832 (2021).

Chapter 3

Engineering the Interfacial Microenvironment of ZnO via Surface Hydroxylation to Realize the Global Optimization of Electrochemical CO₂ Reduction



A ZnO-based catalyst functionalized with surficial –OH groups was prepared by a facile MOF-assisted strategy. The experiment and calculation results support that this interfacial microenvironment induced by CO₂-philic hydroxyl boosts the adsorption and activation of CO₂ during CO₂-to-CO conversion to realize the global optimization of the reaction.

3.1 Introduction

Anthropogenic CO₂ emission arising from transportation and social development is causing harmful environmental effects and global warming. The electrochemical CO₂ reduction reaction (eCO₂ RR) into various fuels and value-added chemicals is a promising method to eliminate excessive greenhouse gas and realize energy reuse towards carbon recycling.¹⁻⁶ Carbon monoxide (CO) is one of the most promising target products when it is evaluated between the market prices and the cost of electricity, especially the electricity that is generated sustainably (i.e. from photovoltaics, hydro or wind turbines, geothermal power stations, etc.). In addition, it is an important raw material for top-level organic chemical products.⁷⁻¹⁰ Theoretically, CO₂-to-CO conversion goes through the following steps: 1) adsorption of CO₂ and activation through a proton-coupled electron transfer process to generate COOH* intermediates; 2) the adsorbed COOH* intermediate is further reduced to form CO* and water, and 3) CO* is desorbed from the surface of the catalyst to form the CO product.¹¹⁻¹⁴ Due to the poor solubility of CO₂ in the aqueous electrolyte, the transformation of CO₂ from the gas feed to the surface of active sites is a minimum prerequisite for the follow-up steps of eCO₂ RR, thus limiting the overall conversion efficiency.^{15,16} Over the past decade, substantial efforts have been made to enhance mass transport of CO₂ and trapped CO₂ molecules at the surface of catalysts via different strategies (i.e. tailoring morphology, size and surface modification).

Zinc oxide (ZnO), characterized by its huge reserves and for being cost- and environmentally friendly, has been widely investigated for generating CO with moderate selectivity.¹⁷⁻²³ The oxidation state of Zn in ZnO as a clear active site provides infinite possibilities to enhance the eCO₂ RR efficiency.²⁰⁻²³ For example, an increased number of active sites could be induced by modulating the ZnO morphology to expose abundant edge facets;¹⁹ the ratio of H₂/CO obtained on ZnO electrocatalysts could be tuned through controlling the defects and facets.²¹ However, almost no attention has been paid to the interfacial microenvironment between ZnO and CO₂, a key factor to

affect its adsorption and activation. Generally, the adsorption and activation of non-polar CO₂ occurs only at the interface of the solid electrocatalyst with the liquid electrolyte and CO₂ molecules by weak interaction.^{14,24-26}

Introducing carbon dioxide-philic functional groups on the catalyst surface, which force the interaction with CO₂ molecules, is an appealing route to manipulate the interface to enhance CO₂ affinities.^{14,27-31} It is also anticipated that the CO₂-philic functional groups on the surface could modulate the electronic structure of the catalyst to further manipulate the formation of the sequent intermediates in the CO₂-to-CO conversion.^{14,30} With this in mind, -OH groups, a kind of CO₂-philic functional groups have been, for the first time, introduced on the surface of ZnO catalysts (ZnO-OH) via a simple ZIF-8-assisted (ZIF stands to Zeolitic Imidazolate Frameworks) method. Compared to the commercial ZnO, the ZnO-OH exhibited a much higher selectivity towards CO at a relatively lower applied potential and reached a FE_{CO} maximum of 85 % at -0.95 V vs. RHE, which is the best value among the state-of-art ZnO-based catalysts reported to date. DFT calculations indicated the existence of strong attraction between the ZnO-OH and the CO₂ molecule, which is beneficial to the adsorption of CO₂. Furthermore, the hydroxyl groups play an important role in facilitating the formation of the follow-up intermediates (COOH* and CO*), simultaneously limiting the undesired hydrogen evolution reaction (HER). All the results reveal the crucial role of CO₂-philic -OH groups in promoting the interfacial adsorption and activation of CO₂ to realize the global optimization of CO₂ electroreduction, which benefits the understanding of the relevant mechanism and rational design of future high-active electrocatalysts.

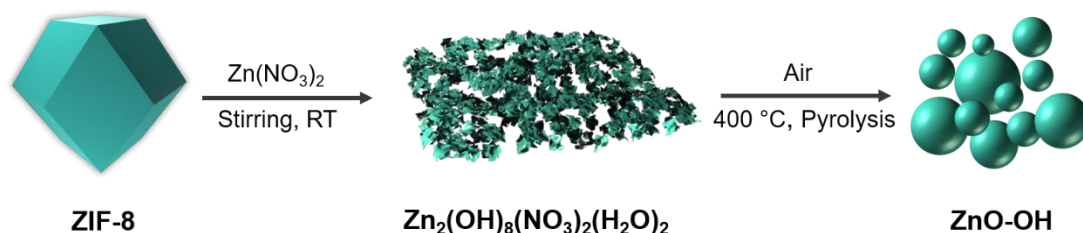


Figure 3.1 Schematic illustration for the formation process of the ZnO-OH.

As shown in **Figure 3.1**, ZnO with rich surficial –OH is synthesized via a novel MOF-assisted procedure. ZIF-8 was initially synthesized based on previous literature.³² Then, ZIF-8 as a precursor was transformed into a hydroxide intermediate by virtue of adding a given amount of $\text{Zn}(\text{NO}_3)_2$ solution at room temperature. Afterwards, the ZnO with rich surficial –OH (ZnO-OH) was obtained through pyrolysis of the above hydroxide intermediate under air. The detailed synthesis information is shown in **Section 3.2**. Meanwhile, in order to clarify the uniqueness of the ZnO-OH obtained by our method, a reference as-prepared ZIF-8 sample without $\text{Zn}(\text{NO}_3)_2$ treatment (D-ZnO sample) was synthesized through a direct pyrolysis under air. In addition, commercial ZnO was also used as a reference sample and was labelled as C-ZnO. We will introduce all samples below.

3.2 Experimental Section

3.2.1 Materials and Methods

Materials: If not specified, all chemical reagents were purchased from Sigma-Aldrich. Zinc nitrate hexahydrate ($\text{Zn}(\text{NO}_3)_2 \cdot 6\text{H}_2\text{O}$), 2-methylimidazole (2-mim), commercial zinc oxide (ZnO), ethanol and sodium bicarbonate (NaHCO_3) were all of analytical grade and used as received without further purification. Meanwhile, all solutions were prepared with Milli-Q water ($\text{DI-H}_2\text{O}$, Ricca Chemical, ASTM Type I). The Nafion (N-117 membrane, 0.18 mm thick) was purchased from Alfa Aesar and kept in 0.5 M NaOH solution. The carbon paper was also purchased from Alfa Aesar.

Characterization: The X-ray diffraction patterns (XRD) were obtained through a Bruker D4 X-ray powder diffractometer using $\text{Cu K}\alpha$ radiation (1.54184 \AA). Field emission scanning electron microscopy (FESEM) images were collected on a FEI Magellan 400 L scanning electron microscope. The transmission electron microscopy (TEM) and high angle annular dark field scanning TEM (HAADF-STEM) images were obtained in a Tecnai F20 field emission gun microscope with a 0.19 nm point-to-point resolution at 200 kV equipped with an embedded Quantum Gatan Image Filter for EELS analyses.

Images have been analyzed by means of Gatan Digital Micrograph software. X-ray photoelectron spectroscopy (XPS) was performed on a Phoibos 150 analyser (SPECS GmbH, Berlin, Germany) in ultra-high vacuum conditions (base pressure 4×10^{-10} mbar) with a monochromatic aluminum K α X-ray source (1486.74 eV). Binding energies (BE) were determined using the C 1s peak at 284.5 eV as a charge reference. Brunauer-Emmett-Teller (BET) surface areas were measured using nitrogen adsorption at 473 K.

3.2.2 Synthesis Methods

3.2.2.1 Preparation of ZIF-8

The fabrication process of ZIF-8 is similar to the reported in literature.³³ A methanol aqueous solution containing 2-methylimidazole ($C_4H_6N_2$, 50 mL, 1.230 g) was added into the methanol aqueous solution of $Zn(NO_3)_2 \cdot 6H_2O$ (50 mL, 1.115 g) under magnetic stirring at room temperature to form a homogeneous solution. After reaction for 24 h without stirring, the sample was then taken out, washed with methanol several times, and vacuum dried overnight.

3.2.2.2 Preparation of $Zn_5(OH)_8(NO_3)_2(H_2O)_2$

100 mg ZIF-8 was etched by immersing into an ethanol solution (100 mL) containing 0.5 g of $Zn(NO_3)_2 \cdot 6H_2O$ with stirring for 30 min. The obtained $Zn_5(OH)_8(NO_3)_2(H_2O)_2$ sample was then taken out, washed with ethanol, and dried in vacuum oven overnight. Similarly, a series of $Zn_5(OH)_8(NO_3)_2(H_2O)_2$ powders were prepared by changing the amount of $Zn(NO_3)_2 \cdot 6H_2O$ addition (denoted as ZIF-8-x, x represents the amount of $Zn(NO_3)_2 \cdot 6H_2O$ addition).

3.2.2.3 Preparation of ZnO-OH

As-prepared $Zn_5(OH)_8(NO_3)_2(H_2O)_2$ powders were put at the porcelain boat. Subsequently, the samples were placed in a tube furnace and heated at 400 °C for 90 min with heating rate of 10 °C/min at air to yield ZnO-OH. We also prepared the ZnO-OH-x (x represents the amount of $Zn(NO_3)_2 \cdot 6H_2O$ addition).

We denoted the ZnO-OH-0.4 and ZnO-OH-0.6 as L-ZnO-OH and H-ZnO-OH, which were prepared by pyrolysis of $\text{Zn}_5(\text{OH})_8(\text{NO}_3)_2(\text{H}_2\text{O})_2$ that were treated by 0.4 or 0.6 g $\text{Zn}(\text{NO}_3)_2 \cdot 6\text{H}_2\text{O}$, respectively.

3.2.2.4 Preparation of D-ZnO

As-prepared ZIF-8 powders were put at the porcelain boat. Subsequently, the samples were placed in a tube furnace and heated at 400 °C for 90 min with heating rate of 10 °C/min in air to yield D-ZnO.

3.2.3 Preparation of working electrodes

The detailed information has been shown in **Chapter 2**.

3.2.4 Electrochemical Measurement

The detailed information has been shown in **Chapter 2**.

3.2.5 Calculation Method

The detailed information has been shown in **Chapter 2**.

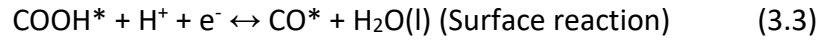
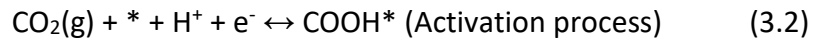
3.2.6 DFT Calculations

The spin-polarized DFT calculations with projector augmented wave (PAW) method were performed using the Vienna Ab initio Simulation Package (VASP) code. The generalized gradient approximation of Perdew-Burke-Ernzerhof (PBE) with van der Waals correlation was employed to optimize the geometric structures. The convergence criteria were 0.05 eV/Å in force and 1×10^{-5} eV in energy and the plane wave cutoff was 550 eV. The Monkhorst–Pack mesh k -point grids was $3 \times 3 \times 1$ for all models. All the vacuum thicknesses were higher than 15 Å. The binding energy (E_b) of CO_2 with ZnO or ZnOH slab was defined as:

$$E_b = E_{\text{total}} - E_{\text{slab}} - E_{\text{CO}_2} \quad (3.1)$$

where E_{CO_2} , E_{slab} , E_{total} are the energies of the CO_2 molecule in gas phase, the corresponding clean slab system (clean ZnO and ZnOH slab), and the total energies of the adsorbed system, respectively.

The whole process of CO_2 electrochemical reduction to CO mainly includes the following three steps:



Where the $*$, COOH^* and CO^* represent free site, adsorption state of COOH and CO, respectively. The (g) represent the gas phase. The reaction free energies of each steps were calculated by following formula:

$$G = E_{\text{DFT}} + E_{\text{ZPE}} - TS + E_{\text{sol}} \quad (3.5)$$

Where E_{DFT} is the DFT calculated energy, E_{ZPE} is the zero-point energy, T (=298.15 K) is temperature, S is the entropy, and E_{sol} is solvation correction and for CO^* was stabilized by 0.1 eV and COOH^* by 0.25 eV.

3.3 Results and Discussion

3.3.1 DFT Presupposition

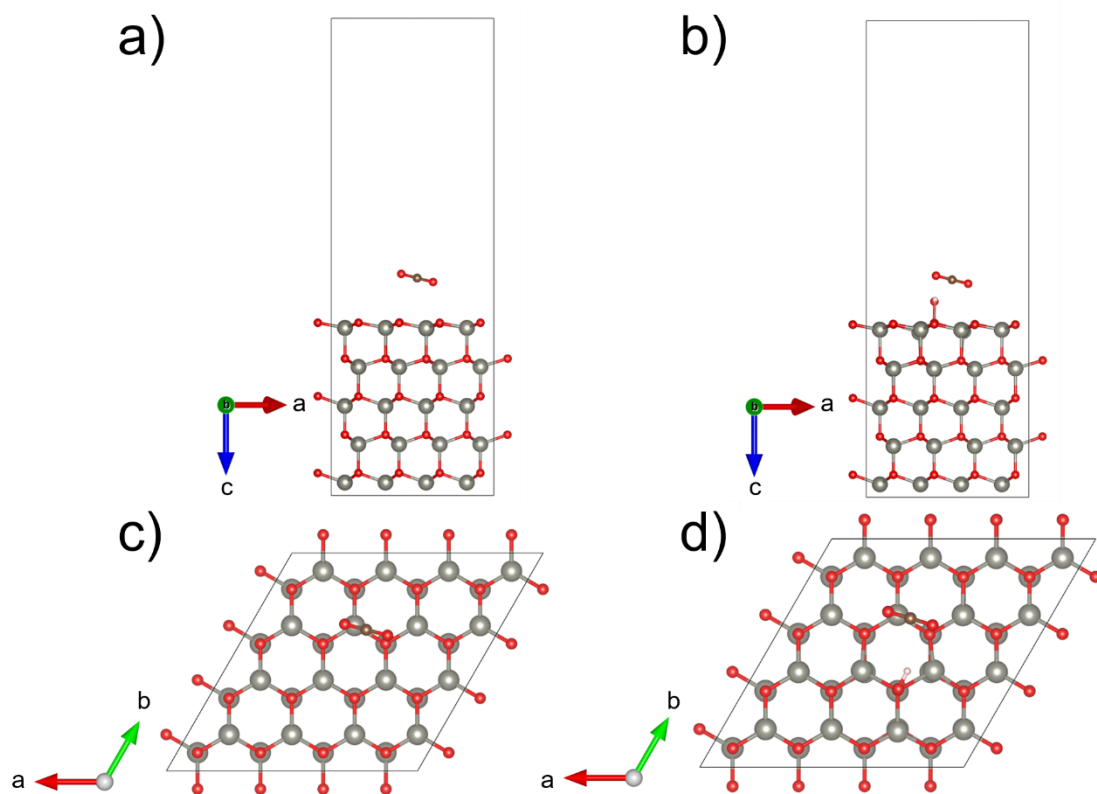


Figure 3.2 Top and side view models for the (a and c) ZnO slab and (b and d) ZnO-OH slab.

In order to understand the influence of the -OH group on the CO_2 adsorption, density functional theory (DFT) was firstly used to calculate the free energy of CO_2 adsorption on two representative models for ZnO and ZnO-OH (**Figure 3.2**). Compared to the negligible adsorption Gibbs free energy of CO_2 molecule on the pristine ZnO (-0.0028 eV), a much larger adsorption energy of -0.1466 eV was observed on ZnO-OH, revealing that the CO_2 adsorption on the ZnO-OH is more feasible. The increase in the CO_2 adsorption affinity is beneficial for the following eCO_2 RR and in parallel, inhibits the reduction of protons (hydrogen evolution) in the electrolyte.^{27,30}

3.3.2 Sample Characterization

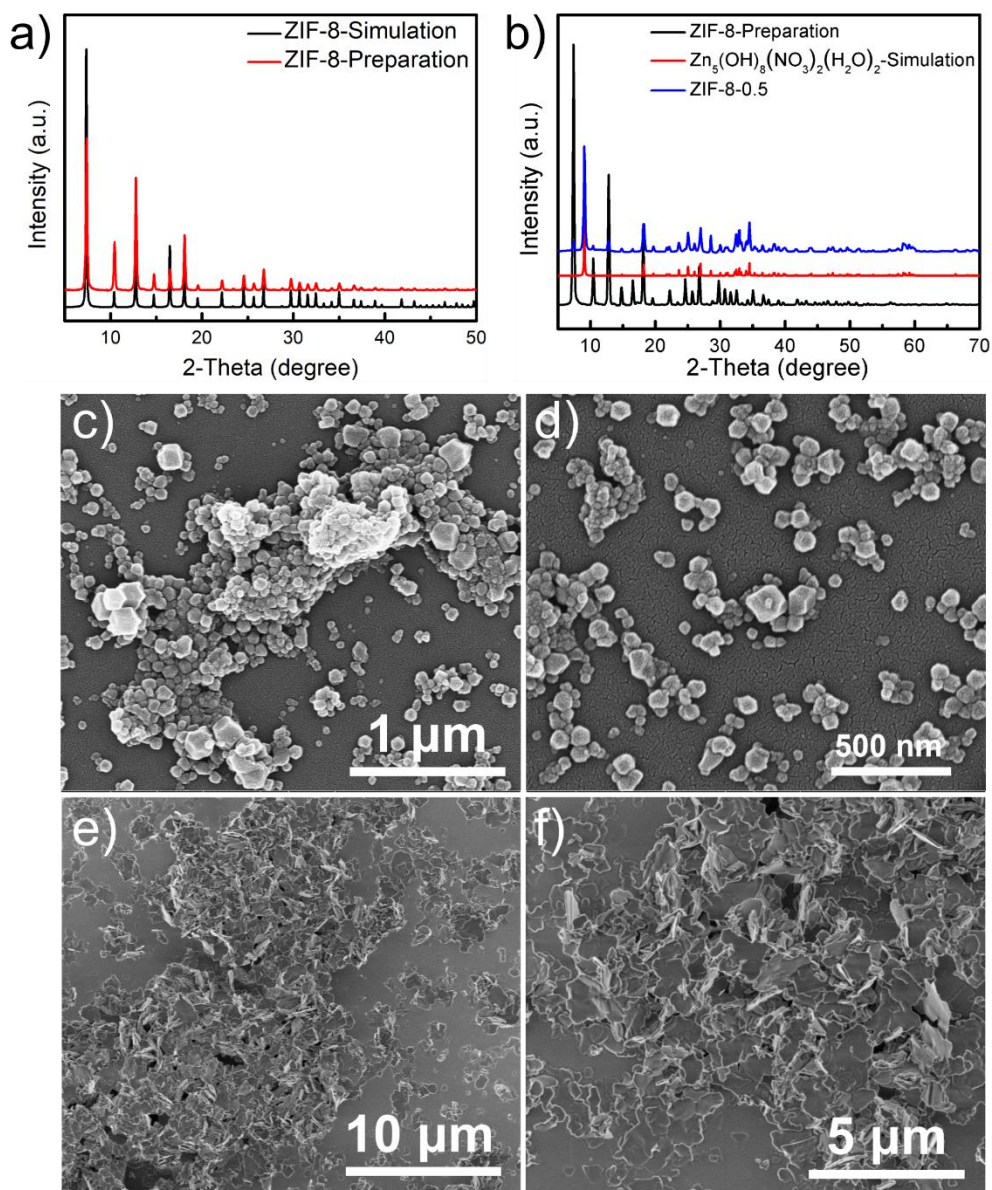


Figure 3.3 XRD patterns of (a) ZIF-8 and (b) corresponding hydroxide intermediate. SEM images of (c, d) ZIF-8 and (e, f) $\text{Zn}_5(\text{OH})_8(\text{NO}_3)_2(\text{H}_2\text{O})_2$.

The high crystallinity of the as-prepared ZIF-8 and the corresponding hydroxide intermediate were firstly confirmed by powder X-ray diffraction (XRD) measurements. The ZIF-8 samples exhibited similar crystal patterns as expected for the standard ZIF-8 structure (**Figure 3.3a**).^{33,36} In the case of the hydroxide intermediate sample, new diffraction peaks belonging to the $\text{Zn}_5(\text{OH})_8(\text{NO}_3)_2(\text{H}_2\text{O})_2$ phase appeared, indicating that the treatment changed the crystal structure of the pristine ZIF-8 (**Figure 3.3b**).^{37,38}

Field emission scanning electron microscopy (FE-SEM) revealed that the characteristic rhombic dodecahedral morphology of the ZIF-8 sample (**Figures 3.3c-d**), which is different from the sheet-shaped nanostructures of $\text{Zn}_5(\text{OH})_8(\text{NO}_3)_2(\text{H}_2\text{O})_2$ sample (**Figures 3.3e-f**).

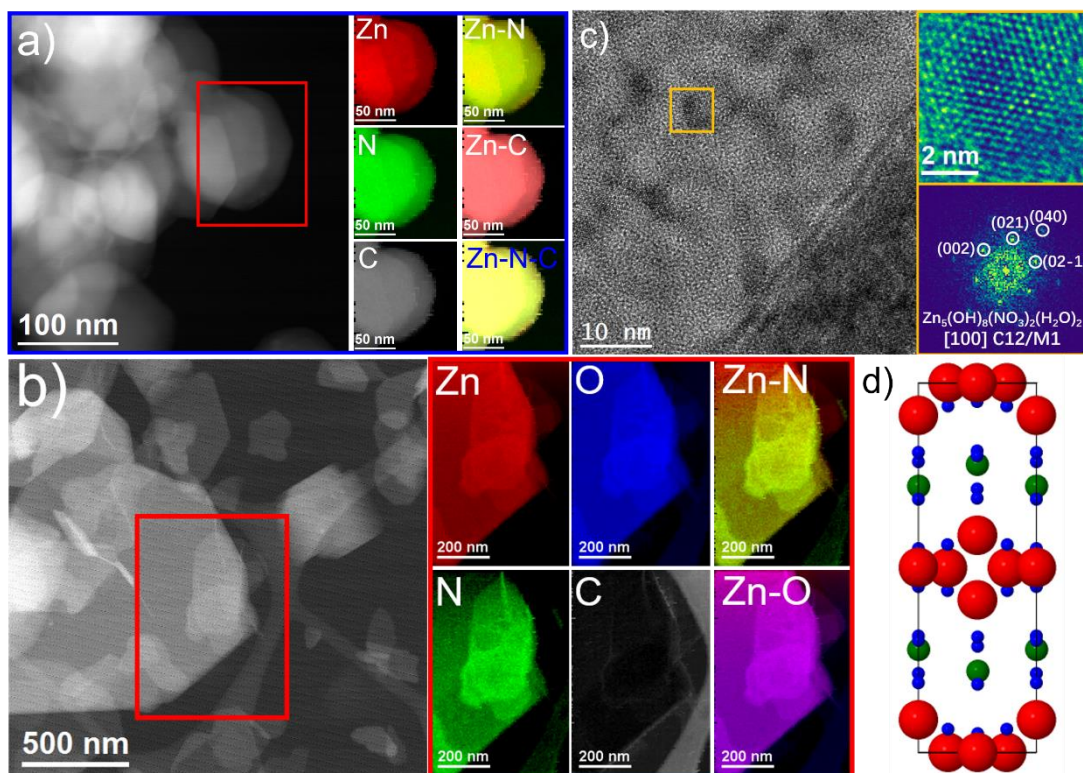


Figure 3.4. (a) HAADF-STEM image of ZIF-8 and representative EELS chemical composition maps obtained from the red squared area of the STEM micrograph. (b) HAADF-STEM image of $\text{Zn}_5(\text{OH})_8(\text{NO}_3)_2(\text{H}_2\text{O})_2$ and representative EELS chemical composition maps obtained from the red squared area of the STEM micrograph (c) HRTEM micrograph of $\text{Zn}_5(\text{OH})_8(\text{NO}_3)_2(\text{H}_2\text{O})_2$ sample and detail of the orange squared region and its corresponding power spectrum as well as (d) unit cell illustration of the $\text{Zn}_5(\text{OH})_8(\text{NO}_3)_2(\text{H}_2\text{O})_2$ (Zn, N and O atoms are represented in red, green and blue, respectively).

TEM analyses show that the ZIF-8 crystals have a homogeneous morphology. Elemental composition maps indicated the homogeneous distribution of Zn, N and C in ZIF-8 (**Figure 3.4a**). In **Figure 3.4b** we show the elemental composition maps of another area of the $\text{Zn}_5(\text{OH})_8(\text{NO}_3)_2(\text{H}_2\text{O})_2$ sample, adding also the O distribution. In addition, high resolution TEM (HRTEM) analyses further proved that ZIF-8 successfully transformed into $\text{Zn}_5(\text{OH})_8(\text{NO}_3)_2(\text{H}_2\text{O})_2$ structure. **Figure 3.4c** shows a HRTEM

micrograph of the $\text{Zn}_5(\text{OH})_8(\text{NO}_3)_2(\text{H}_2\text{O})_2$ sample, together with a magnified detail of the orange squared region and its corresponding power spectrum, which reveals that this sample has a crystal phase that is in agreement with the $\text{Zn}_5(\text{OH})_8(\text{NO}_3)_2(\text{H}_2\text{O})_2$ monoclinic phase (space group =I A3-) with $a=19.4800 \text{ \AA}$, $b=6.2380 \text{ \AA}$, and $c=5.5170 \text{ \AA}$. From the crystalline domain in **Figure 3.4c**, the $\text{Zn}_5(\text{OH})_8(\text{NO}_3)_2(\text{H}_2\text{O})_2$ lattice fringe distances were measured to be 0.282 nm, 0.276 nm, 0.162 nm and 0.276 nm, at 60.33° , 92.41° and 120.44° which could be interpreted as the monoclinic $\text{Zn}_5(\text{OH})_8(\text{NO}_3)_2(\text{H}_2\text{O})_2$ phase, visualized along its [100] zone axis.

Table 3.1. Comparison between the experimental and the theoretical bulk plane spacing distances and angles between planes.

Spot	Experimental (nm)	$\text{Zn}_5(\text{OH})_8(\text{NO}_3)_2(\text{H}_2\text{O})_2$ (C12/M1) [100]
1	0.282	0.275 (002)
2	0.276 (60.33° vs Spot 1)	0.271 (60.48°) (021)
3	0.162 (92.41° vs Spot 1)	0.156 (90.00°) (040)
4	0.276 (120.44° vs Spot 1)	0.271 (119.52°) (02-1)

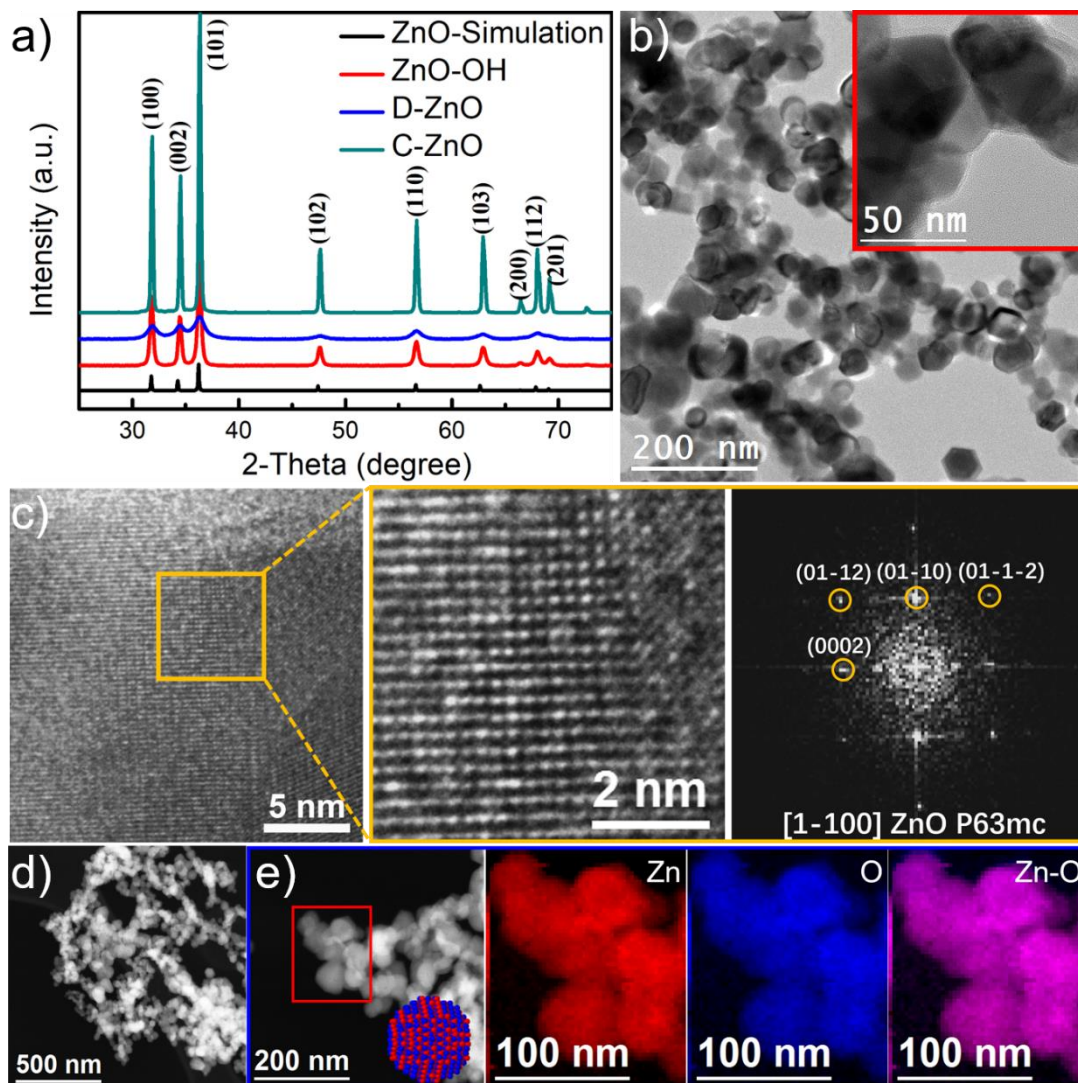


Figure 3.5. (a) XRD patterns. (b) BF TEM images showing the morphology of the ZnO-OH sample. The inset corresponds to a magnified detail of the studied area; (c) HRTEM image (left) and corresponding magnified detail (middle) with the corresponding indexed FFT spectrum (right); (d) HAADF STEM image; (e) HAADF STEM image and representative EELS chemical composition maps obtained from the red squared area in the STEM micrograph. Individual maps obtained from the Zn $L_{2,3}$ -edges at 1020 eV (red), O K-edges at 532 eV (blue) and Zn-O composite map. Inset in (e) shows a 3D atomic supercell model of a ZnO nanoparticle (Zn and O atoms are represented in red and blue, respectively).

As shown in **Figure 3.5a**, all samples clearly showed a similar diffraction pattern to that of simulated ZnO, indicating the successful synthesis of the ZnO skeleton.^{20,21} To investigate the morphology and phase evolution processes, TEM images of the three ZnO-OH samples were obtained (**Figure 3.5b**). The as-prepared ZnO-OH and the corresponding ZnO-based samples exhibited similar quasi-spherical shapes with

irregular sizes. Electron energy loss spectroscopy (EELS) demonstrated the uniform distribution of Zn and O throughout this sample. In addition, TEM was used to reveal the morphologies and compositional distributions of D-ZnO and C-ZnO samples. As shown in **Figure 3.6**, Similar spherical nanoparticles with irregular sizes can be found in both samples, meanwhile, a homogenous distribution of Zn and O presented in both samples. HRTEM (**Figure 3.5c** and **Figure 3.7**) analyses showed that all the ZnO-based sample displayed the typical hexagonal wurtzite ZnO phase (space group=P63/mmc) with $a=b=3.2900 \text{ \AA}$, $c=5.3000 \text{ \AA}$.³⁹⁻⁴² Electron energy loss spectroscopy (EELS) demonstrated the uniform dispersion of Zn and O throughout all the samples (**Figure 3.5e**).

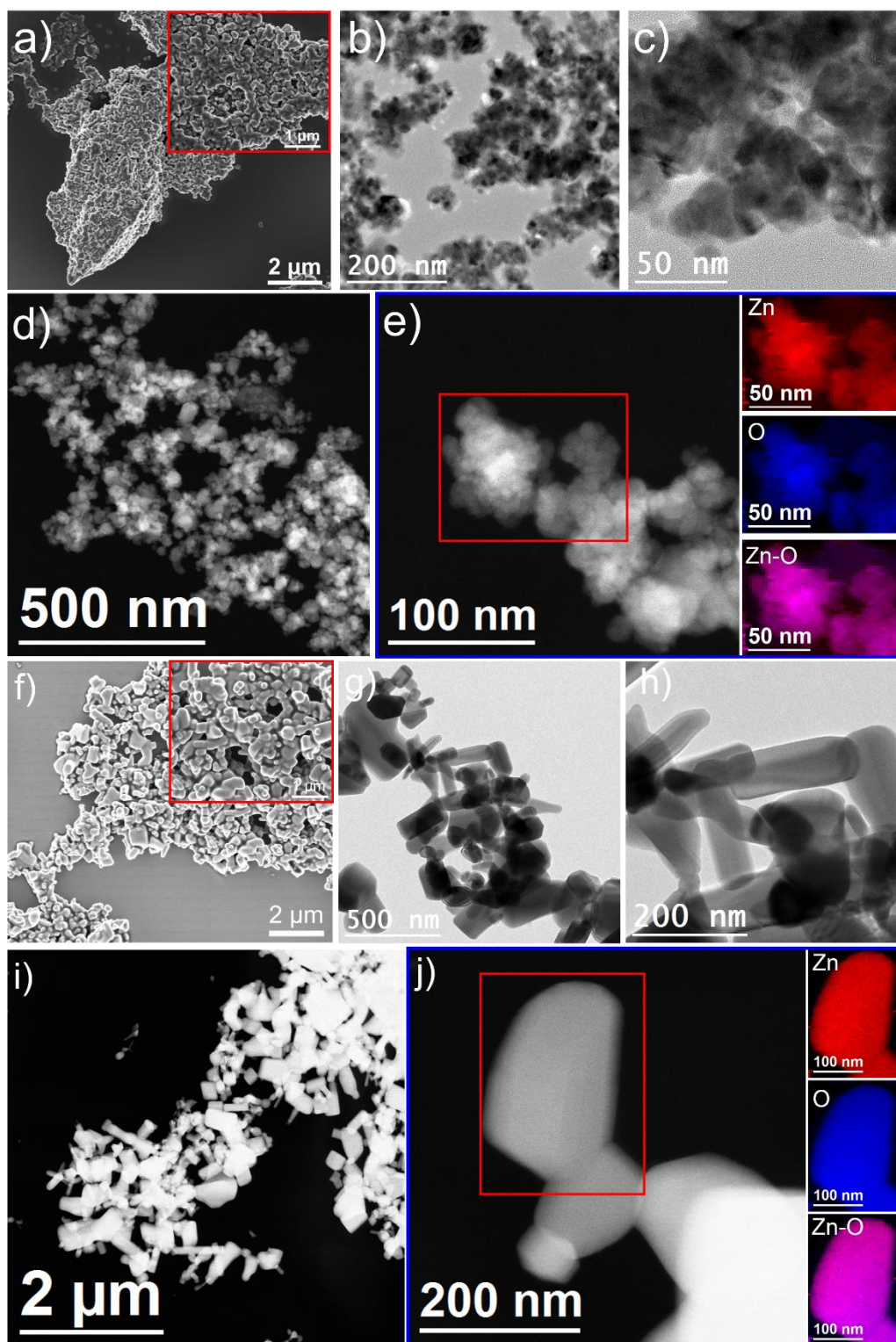


Figure 3.6. (a-d) SEM, BF TEM and HAADF-STEM images of D-ZnO and (e) representative EELS chemical composition maps obtained from the red squared area of the STEM micrograph. Individual Zn $L_{2,3}$ -edges at 1020 eV (red) and O K-edges at 532 eV (blue) as well as composites of Zn-O. (f-i) SEM, BF TEM and HAADF STEM image of C-ZnO and (j) representative EELS chemical composition maps obtained from the red squared area of the STEM micrograph. Individual Zn $L_{2,3}$ -edges at 1020 eV and O K-edges at 532 eV (blue) as well as composites of Zn-O.

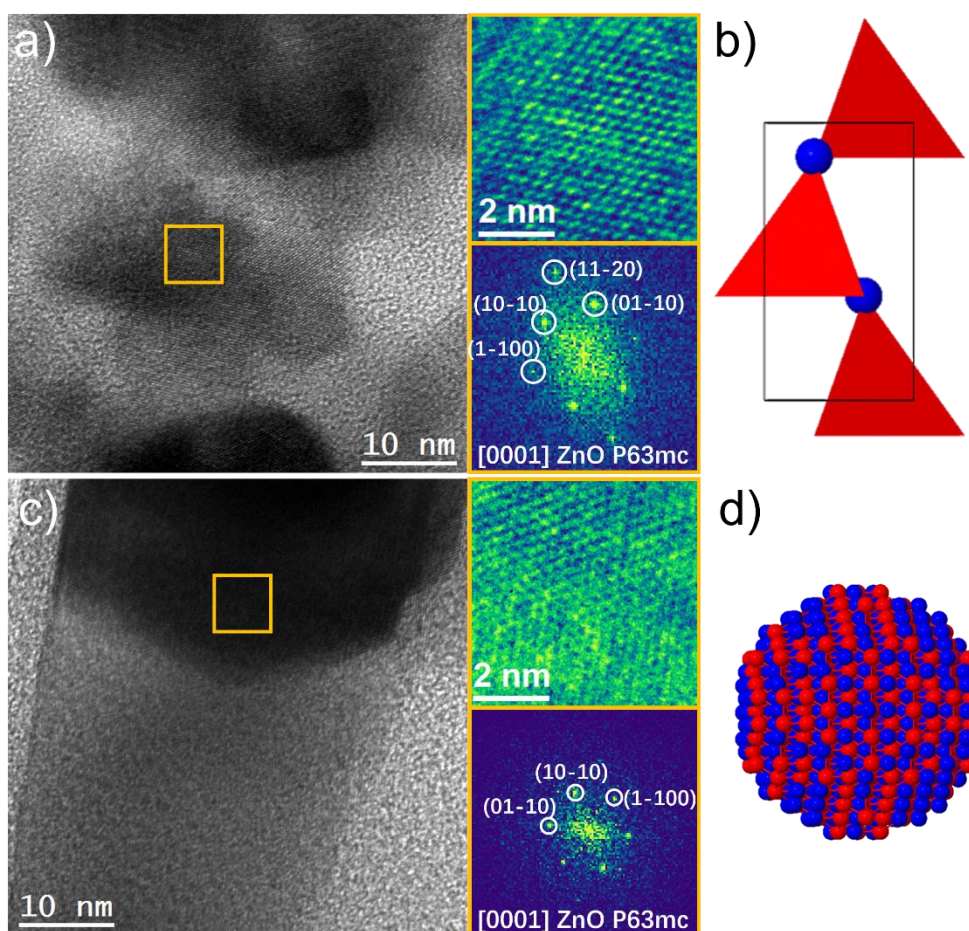


Figure 3.7. (a-b) HRTEM micrograph of D-ZnO sample and detail of the orange squared region and its corresponding power spectrum as well as 1*1*1 unit cell crystal model of ZnO. (Zn and O atoms are represented in red and blue, respectively). (c-d) HRTEM micrograph of C-ZnO sample and detail of the orange squared region and its corresponding power spectrum as well as a simulation of a ZnO nanoparticle. (Zn and O atoms are represented in red and blue, respectively).

Figure 3.7a shows a HRTEM micrograph of D-ZnO taken from the nanoparticle squared in orange. Detail of the orange squared region and its corresponding power spectrum which reveals that this nanoparticle has a crystal phase that could be in agreement with the ZnO hexagonal phase (space group =P63mc) with $a=b=3.2900 \text{ \AA}$ and $c=5.3000 \text{ \AA}$. From the crystalline domain in **Figure 3.7a**, the ZnO lattice fringe distances were measured to be 0.266 nm, 0.284 nm, 0.163 nm and 0.275 nm, at 59.01° , 90.62° and 121.94° , which could be interpreted as the hexagonal ZnO phase, visualized along its [0001] zone axis.

Table 3.2. Comparison between the experimental and the theoretical bulk plane spacing distances and angles between planes.

Spot	Experimental (nm)	ZnO (P63mc) [0001]
1	0.266	0.285 (1-100)
2	0.284 (59.01° vs Spot 1)	0.285 (60.00°) (10-10)
3	0.163 (90.62° vs Spot 1)	0.165 (90.00°) (11-20)
4	0.275 (121.94° vs Spot 1)	0.285 (120.00°) (01-10)

Figure 3.7c shows a HRTEM micrograph of C-ZnO taken from the nanoparticle squared in orange. Detail of the orange squared region and its corresponding power spectrum which reveals that this nanoparticle has a crystal phase that could be in agreement with the ZnO hexagonal phase (space group =P63mc) with $a=b=3.2900 \text{ \AA}$ and $c=5.3000 \text{ \AA}$. From the crystalline domain in **Figure 3.7c**, the ZnO lattice fringe distances were measured to be 0.283 nm, 0.282 nm and 0.284 nm, at 63.03° and 122.66°, which could be interpreted as the hexagonal ZnO phase, visualized along its [0001] zone axis.

Table 3.3. Comparison between the experimental and the theoretical bulk plane spacing distances and angles between planes.

Spot	Experimental (nm)	ZnO (P63mc) [0001]
1	0.283	0.285 (01-10)
2	0.282 (63.03° vs Spot 1)	0.285 (60.00°) (10-10)
3	0.284 (122.66° vs Spot 1)	0.285 (90.00°) (1-100)

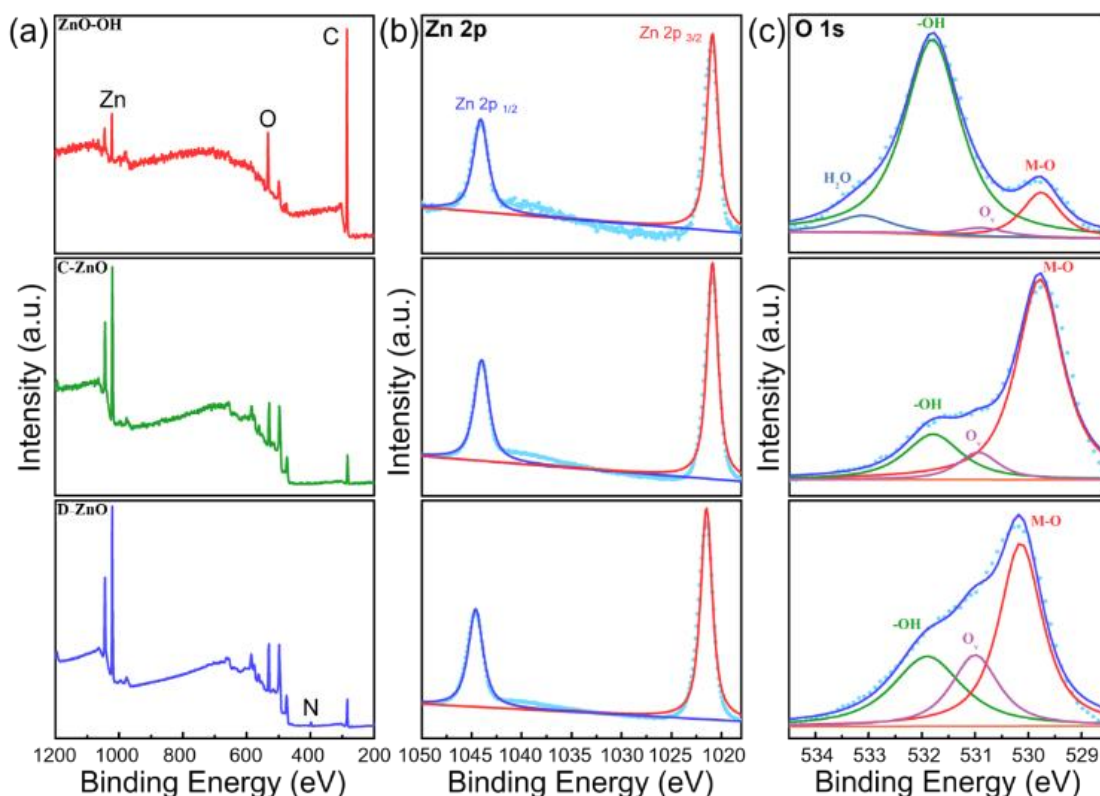


Figure 3.8. (a) XPS survey spectra, (b) high resolution XPS spectra of Zn 2p and (c) O 1s for ZnO-OH (top), C-ZnO (middle) and D-ZnO (bottom).

X-ray photoelectron spectroscopy (XPS) was used to characterize the chemical valence state and surface compositions of the different catalysts. **Figure 3.8a** shows the presence of C, O, and Zn elements in all samples. The Zn 2p XPS core level spectra for all samples can be deconvoluted into two peaks, corresponding to Zn 2p_{3/2} and Zn 2p_{1/2} centered at around 1021 and 1044 eV, respectively, which indicates the presence of Zn²⁺ in all samples (**Figure 3.8b**).^{21,33} The high-resolution XPS spectra obtained on the O 1s show three peaks in all three samples, corresponding to the typical metal-oxygen bond (Zn-O, 529.8 eV),^{20,21} oxygen vacancy (O_v, 531.0 eV),⁴³ and -OH (531.7 eV),^{44,45} respectively (**Figure 3.8c**).^{20,21,45,46} It is worth noting that there is a significant signal enhancement of the corresponding -OH peak obtained on the ZnO-OH sample in comparison to the C-ZnO and D-ZnO, which is ascribed to the higher density of surficial -OH groups. Besides, the integral-area ratios of the peak of surficial -OH groups to the peak of oxygen vacancy were calculated to be 51.3, 2.1, and 1.3 for ZnO-OH, C-ZnO and D-ZnO. The concentration of surficial -OH groups is much higher than that of

oxygen vacancies on the surface of ZnO-OH sample. All above observations demonstrated that the prepared ZnO-OH kept the basic skeleton of ZnO with the highest integral-area ratio of the peak of $-OH$ groups to the peak of oxygen vacancies.

3.3.3 Electrochemical Performance

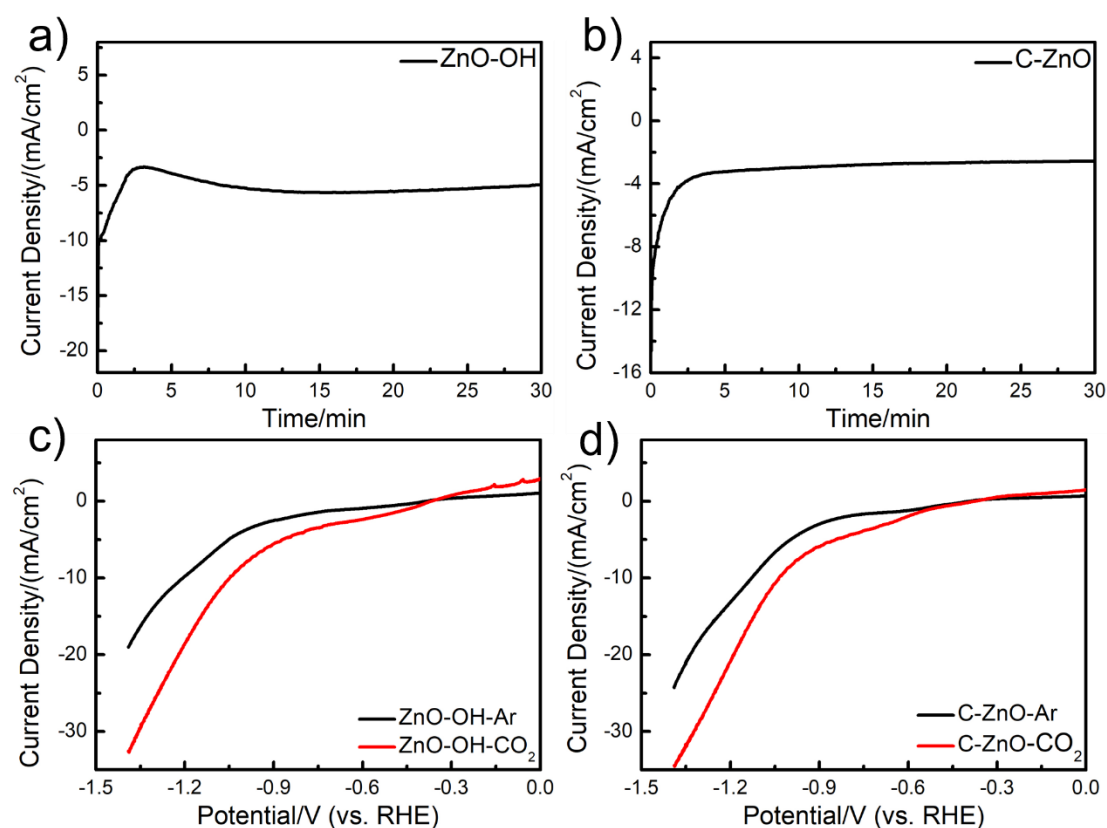


Figure 3.9. Electrode current recorded during reduction of (a) ZnO-OH, (b) C-ZnO samples at -0.70 V vs. RHE in 0.5 M NaHCO_3 purged with Ar gas. Linear sweep voltammetry (LSV) comparison for (c) ZnO-OH and (d) C-ZnO.

Next, electrochemical CO_2 RR performances of the different samples were evaluated in 0.5 M NaHCO_3 . All the prepared electrodes were firstly pre-treated at a constant potential of -0.70 V vs. RHE for 30 min until a stable current was reached (**Figures 3.9a-b**). Linear sweep voltammetry (LSV) curves for ZnO-OH were firstly performed in both Ar- and CO_2 -saturated 0.5 M NaHCO_3 electrolytes to roughly evaluate the eCO_2 RR performance. (**Figures 3.9c-d**). A large increase of the current density observed on ZnO-OH sample after replacement of Ar atmosphere by CO_2 suggested that CO_2 was

electrochemically reduced by the ZnO-OH sample.^{47,48} Meanwhile, no obvious redox peaks were observed in the CO₂-saturated aqueous solution, which displayed that ZnO-OH tended to react with CO₂ molecules instead of suffering from a self-reduction.²⁷

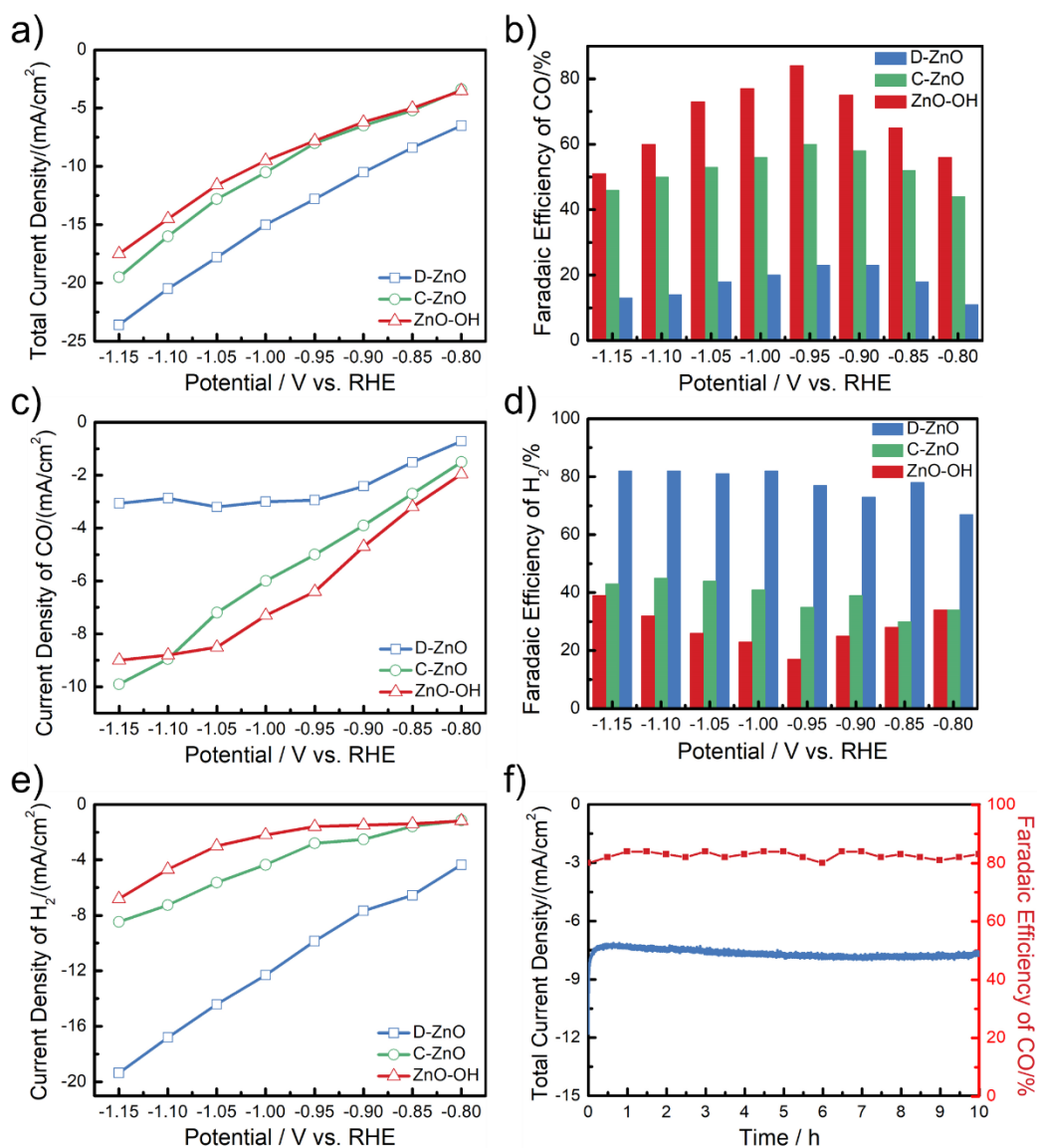


Figure 3.10. Electrocatalytic performance tests for ZnO-OH, D-ZnO and C-ZnO. (a) Total current density. (b) FE of CO at various potentials. (c) Current density of CO at various potentials (d) FE of H₂ at various potentials. (e) Current density of H₂ at various potentials on ZnO-OH, D-ZnO and C-ZnO. (f) Stability test for the ZnO-OH catalyst at -0.95 V vs. RHE.

Figure 3.10a summarizes the measured total current density for ZnO-OH, D-ZnO and C-ZnO samples. Although ZnO-OH and C-ZnO showed similar total reduction current

densities, ZnO-OH showed the highest selectivity towards CO in a potential range from -0.80 to -1.15 V vs. RHE, reaching the maximum FE (CO) (85 %) at -0.95 V vs. RHE (**Figure 3.10b**). To the best of our knowledge, such high selectivity for CO at a low applied potential is the best record in ZnO-based catalysts reported so far (**Table 3.4**). The largest potential-dependent CO partial current densities observed on ZnO-OH further demonstrated the excellent activity and selectivity towards CO (**Figure 3.10c**). As the potential shifted to more negative values, a decreasing trend of FE (CO) for ZnO-OH and C-ZnO was observed, which mainly stems from the dominance of the H₂ evolution over the eCO₂ RR (**Figure 3.10d**). This assumption was further confirmed by the potential-dependent H₂ current densities for the different catalysts (**Figure 3.10e**). To further investigate the stability of the ZnO-OH during the eCO₂ RR, a 10-h stability measurement was conducted. An eCO₂ RR current density of around -8.2 mA cm⁻² and a FE(CO) over 80 % were maintained during the 10 h test (**Figure 3.10f**).

Table 3.4. Faradaic Efficiency (CO) of the reported ZnO-based electrocatalysts for CO₂ electroreduction

Catalyst	Product	FE(CO)	Potential	Reference
ZnO nanosheet@Zn	CO	85 %	-2.0 V vs. Ag/AgCl	⁴⁹
ZnO with vacancy	CO	83 %	-1.10 V vs. RHE	⁵⁰
ZnO	Syngas	32 %	-1.0 V vs. RHE	⁵¹
ZnO with vacancy	CO	58 %	-0.79 V vs. RHE	⁵²
ZnO	CO	54 %	-1.40 V vs. RHE	⁵³
Ce-doped ZnO	CO	88 %	-1.0 V vs. RHE	⁵⁴
ZnO-OH	CO	85%	-0.95 V vs. RHE	This work

After the stability test, TEM analyses were performed to reveal the morphology and phase changes on the ZnO-OH sample, as shown in **Figure 3.11**. EELS compositional maps demonstrated that most of the ZnO-OH areas showed a uniform distribution of Zn and O. HRTEM analyses showed the presence of some metallic Zn nanoparticles with hexagonal phase (space group=P63/mmc). The presence of reduced Zn nanostructure can explain the slight efficiency loss after the stability test, evidencing the competition in the metal oxides between self-reduction and CO₂ reduction.^{27,55}

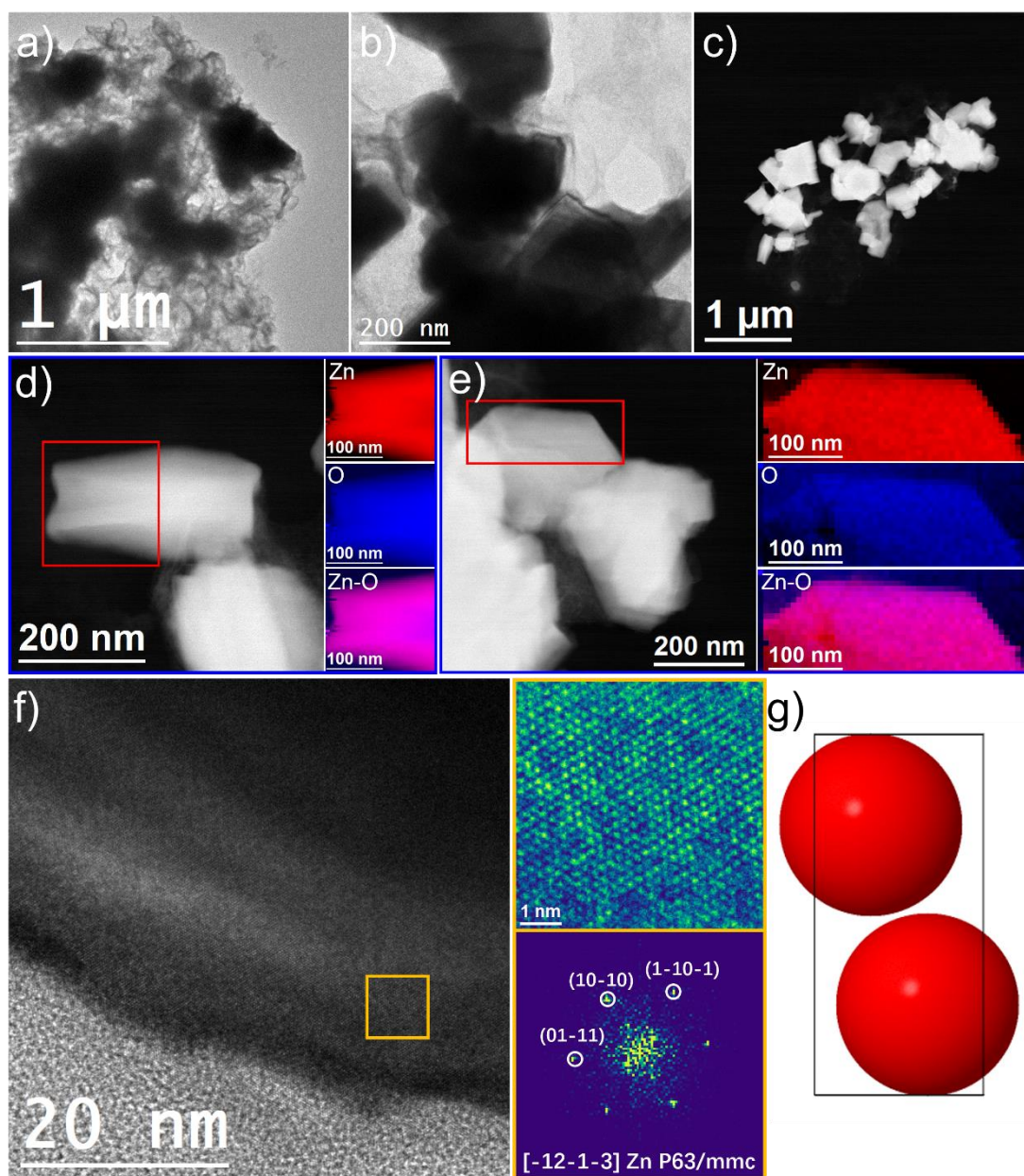


Figure 3.11. Morphological characterization of ZnO-OH sample after stability test. (a and b) BF TEM images, (c) HAADF STEM image. (d and e) HAADF STEM image and representative EELS chemical composition maps obtained from the red squared area of the STEM micrograph. Individual Zn $L_{2,3}$ -edges at 1020 eV (red), O K-edges at 532 eV (blue) and composite of Zn-O. (f) is HRTEM image and corresponding to FFT spectrum.

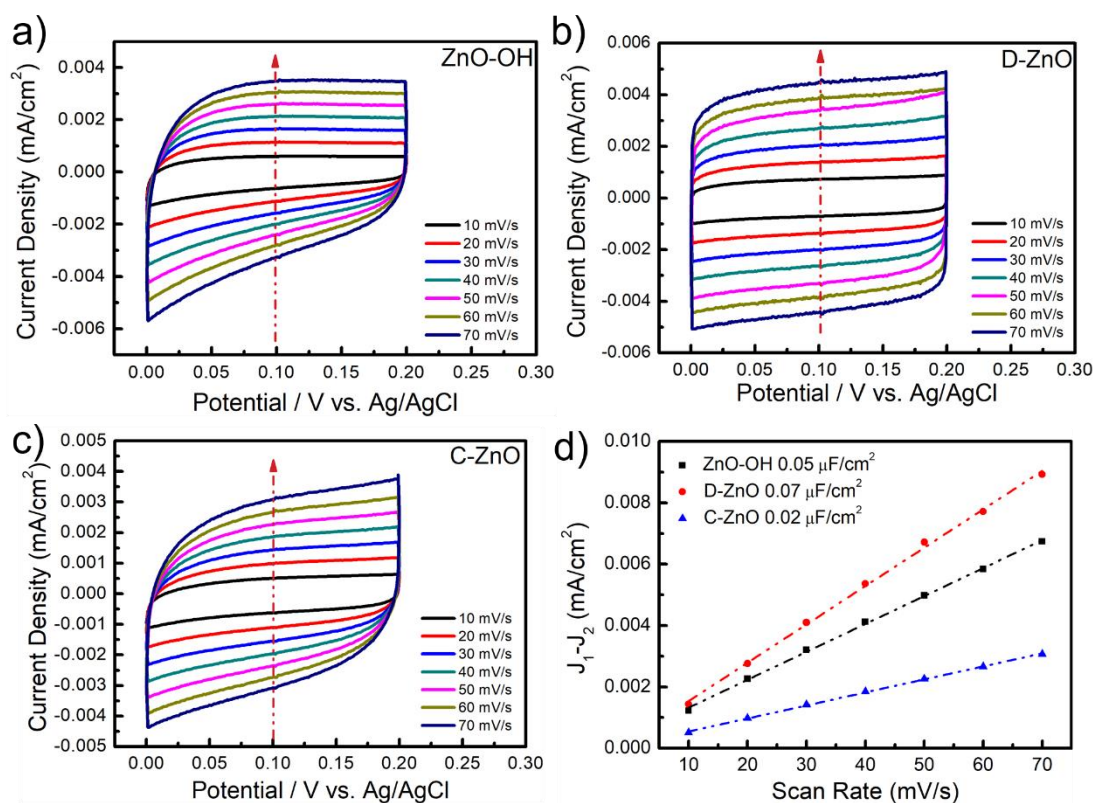


Figure 3.12. Cyclic voltammograms curves for (a) ZnO-OH, (b) D-ZnO, (c) C-ZnO and (d) Plots of the current density vs. scan rate for ZnO-OH, D-ZnO and C-ZnO electrodes.

In order to reveal the intrinsic catalytic performance on different samples, the electrochemical active surface area (ECSA) on different samples was measured. It is well known that an increase of ECSA often leads to the enhancement of the catalytic activity.³⁴ In order to further explain the catalytic efficiency on different samples, the ECSA is calculated by electrochemical double-layer capacitance (C_{dl}) of the active materials. As shown in **Figure 3.12**, the C_{dl} of three samples is obtained by CV (**Figure 3.12a-c**). By plotting the $\Delta J = J_a - J_c$ at 0.10 V vs. Ag/AgCl against the scan rate, the slope which is twice of C_{dl} could be obtained. As shown in **Figure 3.12d**, the C_{dl} of ZnO-OH, D-ZnO and C-ZnO samples is 0.05 $\mu\text{F cm}^{-2}$, 0.07 $\mu\text{F cm}^{-2}$ and 0.02 $\mu\text{F cm}^{-2}$, respectively, confirming that the higher intrinsic catalytic activity of the ZnO-OH is mainly due to the higher surficial -OH coverage on ZnO-OH sample, the higher activity towards CO₂ RR on ZnO-OH is also correlated to the inner nature of the catalysts.

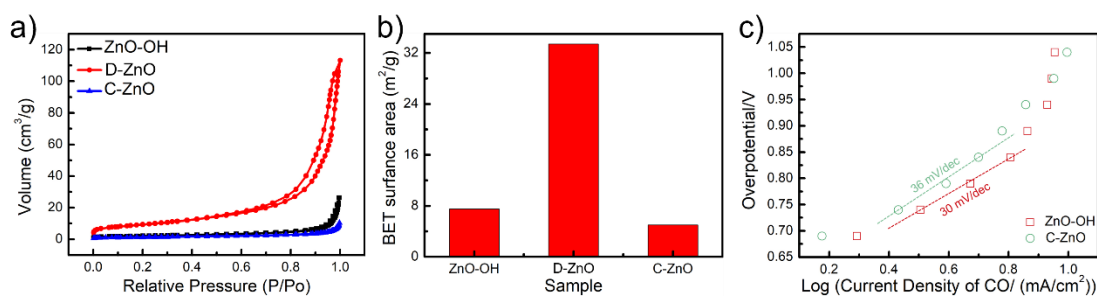


Figure 3.13. (a) N₂ adsorption and desorption isotherm and (b) BET surface areas for ZnO-OH, D-ZnO and C-ZnO. (c) Tafel Slope of ZnO-OH and C-ZnO.

Then, we further investigated the nitrogen adsorption-desorption isotherms and BET surface area on different samples (**Figures 3.13a-b**). It is well known that those electrocatalysts with high specific surface area should endow the efficient exposure of electrocatalytic active sites, fast electrolyte penetration/diffusion, and free diffusion of intermediates.^{57,58} In our case, the specific surface area of the ZnO-OH was much lower than that of D-ZnO, which further suggests that the intrinsic catalytic activity of ZnO-OH sample arise from the presence of surficial -OH group instead of the specific surface area. In addition, to investigate the reaction kinetics for CO₂ RR, Tafel slopes derived from the static state current densities for CO were calculated. The C-ZnO sample exhibits a Tafel slope of 36 mV dec⁻¹, close to 39 mV dec⁻¹, indicating that the rate-determining step (RDS) of CO₂ RR on C-ZnO powder corresponds to the initial proton-coupled electron transfer (PCET) (**Figure 3.13c**).⁵⁹ The much lower Tafel slopes (30 mV dec⁻¹) for the ZnO-OH catalyst indicated its remarkably improved kinetics towards CO conversion.⁶⁰⁻⁶²

In addition, we prepared a series of ZnO-OH-x derived from different ZIF-8-x intermediates. As shown in **Figure 3.14**, different intermediates were derived from ZIF-8 with different Zn(NO₃)₂ treatment, with no effect on the crystallinity of the final ZnO-OH after pyrolysis. Compared to other samples, the ZnO-OH-0.1 sample kept tiny size nanostructures, with diameters ~ 150 nm, similar to those of ZIF-8. Meanwhile, for ZnO-OH-0.6 sample, the significantly nanorods presented, as shown in **Figure 3.14f**, but it still kept a good crystallinity with ZnO. The catalytic effects of ZnO-OH-x samples were also studied. Compared to our optimized sample ZnO-OH (x=0.5), the other

samples showed lower FE(CO). Such a decreased selectivity is attributed to the introduced concentration of $\text{Zn}(\text{NO}_3)_2$.

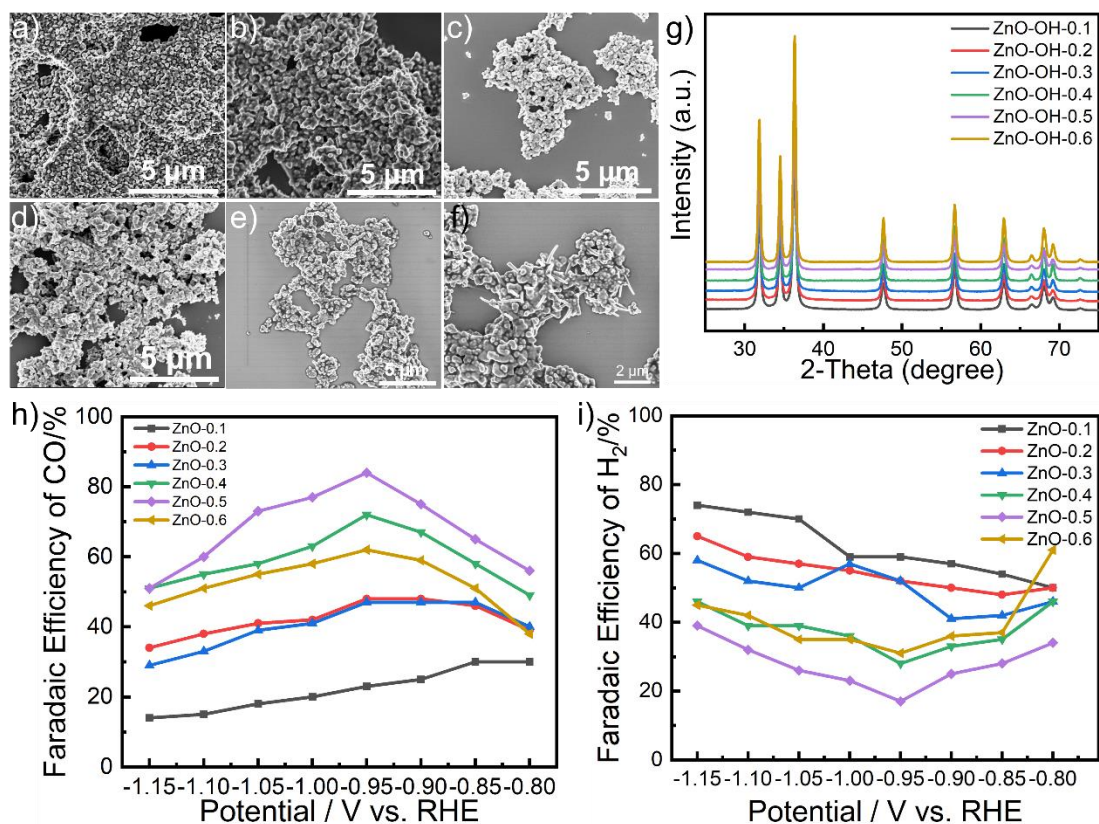


Figure 3.14. SEM images of (a-f) ZnO-OH-x ($x=0.1$ (a), 0.2 (b), 0.3 (c), 0.4 (d), 0.5 (e) and 0.6 (f)). (g) XRD patterns of ZnO-OH-x ($x=0.1$, 0.2 , 0.3 , 0.4 , and 0.6). FE of (h) CO and (i) H₂ at various potentials on different samples.

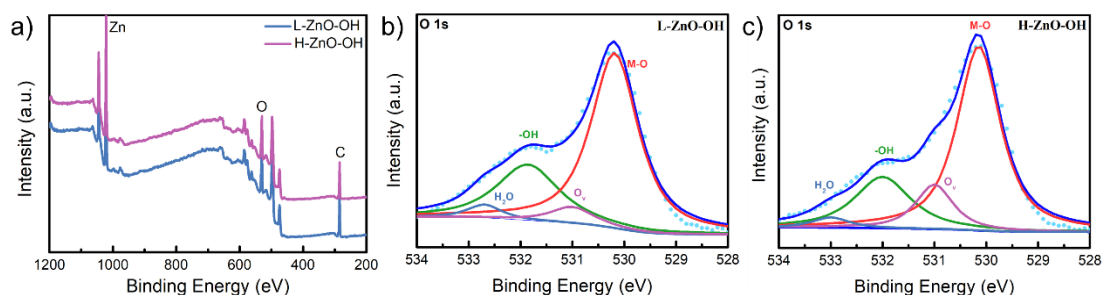


Figure 3.15. (a) XPS survey spectra, high resolution XPS spectra of O 1s for (b) L-ZnO-OH-0.4 and (c) H-ZnO-OH-0.6.

In order to reveal this phenomenon, we performed the XPS on the ZnO-OH ($x=0.4$ and $x=0.6$) samples, as shown in **Figure 3.15**. There is different ratio between O_v and surficial -OH observed in both samples, thus, their selectivity of corresponding ZnO-

OH to CO changed negatively. Therefore, we concluded that the enhanced CO₂ RR activity on optimized ZnO-OH we prepared is mainly influenced by the rationally surficial -OH modification derived from the ZIF-8 with Zn(NO₃)₂ treatment.

3.3.4 DFT Calculation

The CO₂ RR process for the ZnO and ZnO-OH models were studied by DFT calculations to shed light on the origin of the improved CO₂ RR. The free energy profiles at a potential of 0 V vs. RHE for the three elementary steps and the two important intermediates (COOH* and CO*) in the CO₂ RR process are shown in **Figure 3.16a**. The ΔG for the formation of COOH* over commercial ZnO and the ZnO-OH catalyst are -0.52 eV and -0.63 eV, respectively. The stronger stabilization of surface COOH* on the ZnO-OH could increase the selectivity for the desired product CO. Besides, the following dissociation of COOH* assisted by the proton-electron transfer to produce CO* and H₂O is an endothermic and the rate-determining step (RDS). To our excitement, ΔG increases by 1.72 eV and 1.5 eV on ZnO and ZnO-OH catalyst models, respectively, which means that the process of the CO* generation on ZnO-OH slab is thermodynamically more favorable than that on ZnO slab. As for the final step of CO desorption, the ΔG over the reference ZnO and the ZnO-OH catalyst are -0.59 eV and -0.26 eV, respectively. Such relatively weak binding of CO* and above stronger stabilization of COOH* steer the electron and proton transfer to the formation of CO product. Similar trends are also observed on the free energy profiles at -0.95 V (vs. RHE) (**Figure 3.16b**). The differential charge density for CO₂, CO, and COOH* on the ZnO-OH and ZnO slabs were also calculated in **Figures 3.16c-h**. The charge accumulation and deficit between them and the corresponding surface were presented with yellow and cyan iso-surfaces. Through contrastive analysis, the charge density difference of CO on the ZnO-OH slab was more prominent than that on ZnO slab. To summarize, the ZnO-OH slab stabilizes the key intermediates via electronic interaction, which in synergy leads to an enhanced CO selectivity.

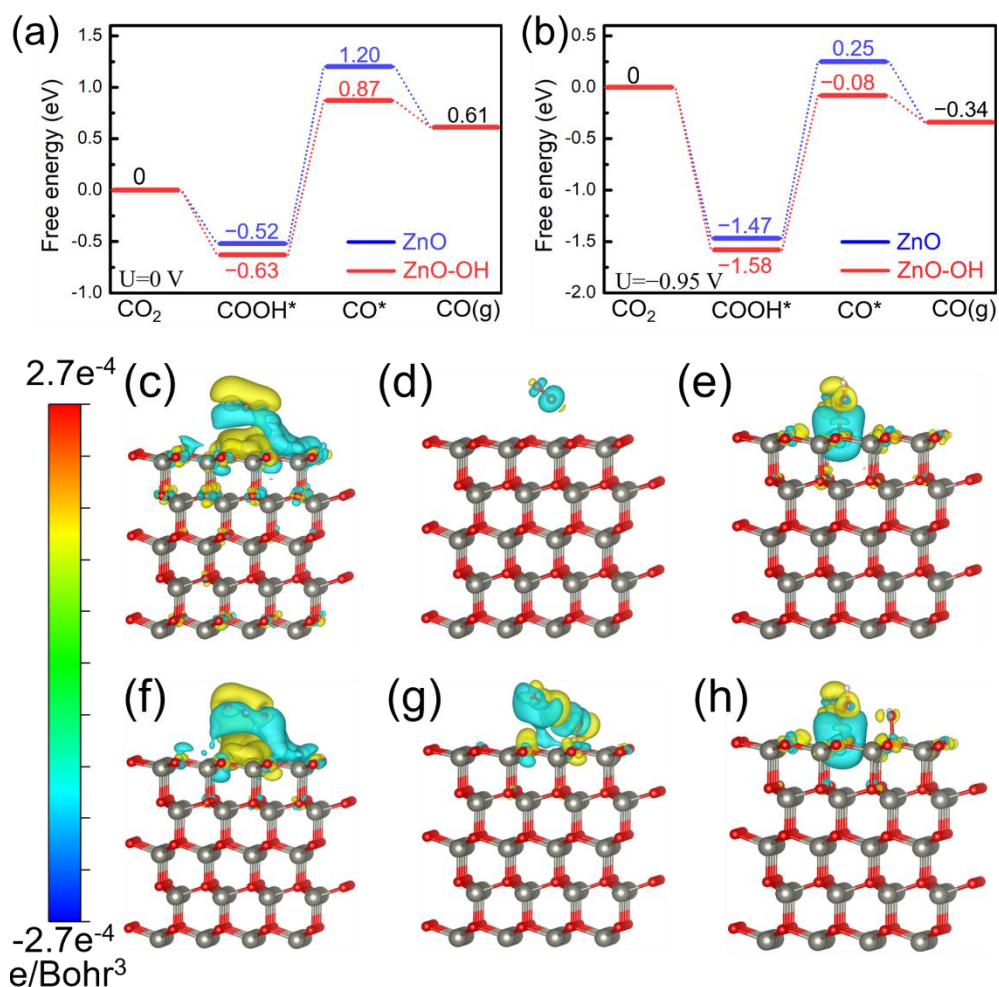


Figure 3.16. DFT Studies of CO_2 RR. Free energy profiles for the (a) CO_2 RR to CO at 0 V and (b) -0.95 V (vs. RHE) on the simulated models. Charge density difference for CO_2 , CO, and COOH^* adsorbed on a (c-e) ZnO slab and a (f-h) ZnO-OH slab. The grey, red, brown and pink spheres represent Zn, O, C and H atoms, respectively.

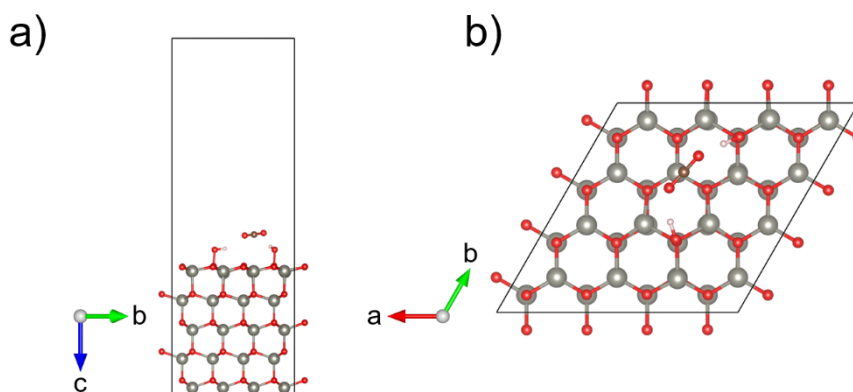


Figure 3.17. The (a) top and (b) side view of models for ZnO-OH slab with two -OH.

More importantly, the Gibbs free energy for CO_2 activation process on ZnO with two

surficial -OH decreased by *ca.* 0.17 eV with respect to the ZnO with only one surficial -OH, which revealed that more surficial -OH coverage enhanced the adsorption of CO₂ (**Figure 3.17**). These calculated results were in good agreement with the experimental observations that ZnO-OH sample exhibited better selectivity for CO₂ RR in comparison to the C-ZnO catalyst.

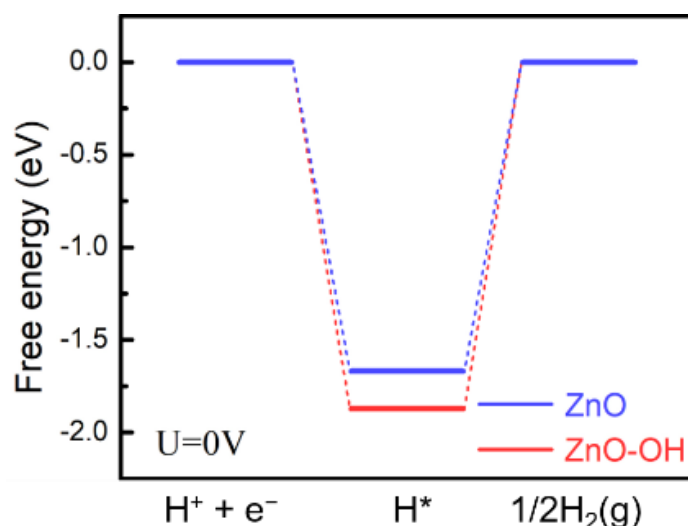


Figure 3.18. Free energy profiles for the HER to CO at 0 V on simulated models.

Additionally, HER as a competing side reaction was also studied (**Figure 3.18**). The stronger stability of H* on the surface of our OH modified catalysts seems to effectively suppress the HER. It can be concluded that the HER is less active on ZnO-OH than that on the reference ZnO sample (-1.87 eV and -1.67 eV, respectively), suggesting that HER occurs more easily on ZnO without the surficial -OH coverage. Taken all this into account, the surface hydroxyls can not only facilitate the formation of COOH* and CO* via electronic interaction, but also limit the undesired HER.

3.4 Summary

In summary, ZnO covered by surficial -OH groups was synthesized through a novel MOF-assisted method, which delicately optimize the interfacial microenvironment to promote the interfacial adsorption and activation of CO₂. The synthesized -OH-rich ZnO presents a FE_{CO} maximum of 85 % at -0.95 V vs. RHE, which is the best record

among the state-of-the-art ZnO catalysts. DFT calculations confirmed that the surface -OH firstly boost the adsorption of CO₂ at the interface and then promote the generation of COOH* and CO* intermediates. Our findings revealed that tuning the interfacial microenvironment via the introduction of dioxide-philic functional groups is a promising way to achieve the global optimization via promotion of interfacial adsorption and activation of CO₂, which paves a new way to rationally design future highly active electrocatalysts for eCO₂ RR.

References

1. Jin, S., Hao, Z., Zhang, K., Yan, Z. & Chen, J. Advances and Challenges for the Electrochemical Reduction of CO₂ to CO: From Fundamentals to Industrialization. *Angew. Chem. Int. Ed.* **60**, 20627–20648 (2021).
2. Zhong, M. *et al.* Accelerated discovery of CO₂ electrocatalysts using active machine learning. *Nature* **581**, 178-183 (2020).
3. Voiry, D., Shin, H. S., Loh, K. P. & Chhowalla, M. Low-dimensional catalysts for hydrogen evolution and CO₂ reduction. *Nat. Rev. Chem.* **2**, 1-17 (2018).
4. Jiang, X. *et al.* Carbon dioxide electroreduction over imidazolate ligands coordinated with Zn (II) center in ZIFs. *Nano Energy* **52**, 345-350 (2018).
5. Zhang, B. *et al.* Recent progress on hybrid electrocatalysts for efficient electrochemical CO₂ reduction. *Nano Energy* **80**, 105504 (2021).
6. Rawool, S. A. *et al.* Direct CO₂ capture and conversion to fuels on magnesium nanoparticles under ambient conditions simply using water. *Chem. Sci.* **12**, 5774-5786 (2021).
7. Navarro, R. M., Pena, M. & Fierro, J. Hydrogen production reactions from carbon feedstocks: fossil fuels and biomass. *Chem. Rev.* **107**, 3952-3991 (2007).
8. Liu, K., Wang, J., Shi, M., Yan, J. & Jiang, Q. Simultaneous achieving of high faradaic efficiency and CO partial current density for CO₂ reduction via robust, noble-metal-free Zn nanosheets with favorable adsorption energy. *Adv. Energy Mater.* **9**, 1900276 (2019).
9. Guo, Q. *et al.* Efficient and selective CO₂ reduction integrated with organic synthesis by solar energy. *Chem* **5**, 2605-2616 (2019).
10. Du, J. *et al.* Polyoxometalate-based electron transfer modulation for efficient electrocatalytic carbon dioxide reduction. *Chem. Sci.* **11**, 3007-3015 (2020).
11. Rosen, B. A. *et al.* Ionic liquid-mediated selective conversion of CO₂ to CO at low overpotentials. *Science* **334**, 643-644 (2011).
12. Zhu, D. D., Liu, J. L. & Qiao, S. Z. Recent advances in inorganic heterogeneous electrocatalysts for reduction of carbon dioxide. *Adv. Mater.* **28**, 3423-3452 (2016).
13. Zhang, W. *et al.* Progress and perspective of electrocatalytic CO₂ reduction for renewable carbonaceous fuels and chemicals. *Adv. Sci.* **5**, 1700275 (2018).
14. Huang, Q., Li, Q., Liu, J., Wang, R. & Lan, Y.-Q. Disclosing CO₂ activation mechanism by hydroxyl-induced crystalline structure transformation in electrocatalytic process. *Matter* **1**, 1656-1668 (2019).
15. Xu, S. & Carter, E. A. Theoretical insights into heterogeneous (photo) electrochemical CO₂ reduction. *Chem. Rev.* **119**, 6631-6669 (2018).
16. Zhao, K. & Quan, X. Carbon-Based Materials for Electrochemical Reduction of CO₂ to C₂+ Oxygenates: Recent Progress and Remaining Challenges. *ACS Catal.* **11**, 2076-2097 (2021).
17. Tan, D. *et al.* SnO₂/ZnO Composite Hollow Nanofiber Electrocatalyst for Efficient CO₂ Reduction to Formate. *ACS Sustain. Chem. Eng.* **8**, 10639-10645 (2020).
18. Nguyen, D. L. T. *et al.* Selective CO₂ reduction on zinc electrocatalyst: the effect of zinc oxidation state induced by pretreatment environment. *ACS Sustain. Chem. Eng.* **5**, 11377-11386 (2017).
19. Xiang, Q. *et al.* Heterostructure of ZnO Nanosheets/Zn with a Highly Enhanced Edge

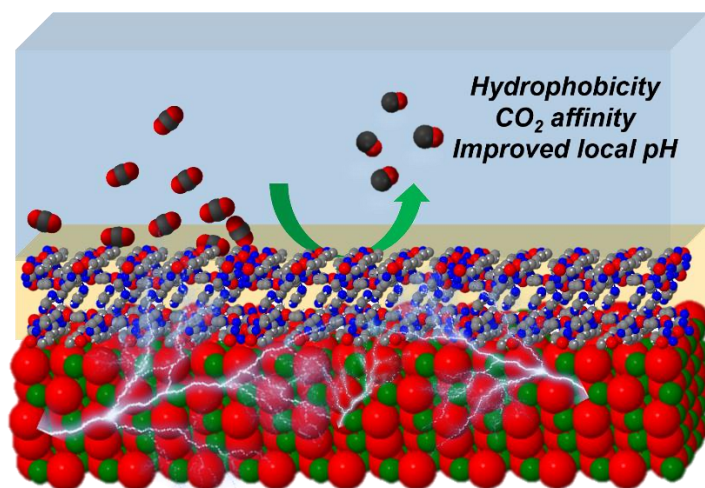
- Surface for Efficient CO₂ Electrochemical Reduction to CO. *ACS Appl. Mater. Interfaces* **13**, 10837-10844 (2021).
20. Geng, Z. *et al.* Oxygen vacancies in ZnO nanosheets enhance CO₂ electrochemical reduction to CO. *Angew. Chem. Int. Ed.* **130**, 6162-6167 (2018).
 21. Daiyan, R. *et al.* Uncovering Atomic-Scale Stability and Reactivity in Engineered Zinc Oxide Electrocatalysts for Controllable Syngas Production. *Adv. Energy Mater.* **10**, 2001381 (2020).
 22. Franco, F., Rettenmaier, C., Jeon, H. S. & Cuenya, B. R. Transition metal-based catalysts for the electrochemical CO₂ reduction: from atoms and molecules to nanostructured materials. *Chem. Soc. Rev.* **49**, 6884-6946 (2020).
 23. Liu, Y. *et al.* A magnetically separable photocatalyst based on nest-like γ -Fe₂O₃/ZnO double-shelled hollow structures with enhanced photocatalytic activity. *Nanoscale* **4**, 183-187 (2012).
 24. Resasco, J. *et al.* Promoter effects of alkali metal cations on the electrochemical reduction of carbon dioxide. *J. Am. Chem. Soc.* **139**, 11277-11287 (2017).
 25. Resasco, J., Lum, Y., Clark, E., Zeledon, J. Z. & Bell, A. T. Effects of anion identity and concentration on electrochemical reduction of CO₂. *ChemElectroChem* **5**, 1064-1072 (2018).
 26. Liu, P. & Zheng, N. Coordination chemistry of atomically dispersed catalysts. *Natl. Sci. Rev.* **5**, 636-638 (2018).
 27. Deng, W. *et al.* Crucial role of surface hydroxyls on the activity and stability in electrochemical CO₂ reduction. *J. Am. Chem. Soc.* **141**, 2911-2915 (2019).
 28. Yang, P. *et al.* The functionality of surface hydroxy groups on the selectivity and activity of carbon dioxide reduction over cuprous oxide in aqueous solutions. *Angew. Chem. Int. Ed.* **130**, 7850-7854 (2018).
 29. Peng, Y. *et al.* Molecular-level insight into how hydroxyl groups boost catalytic activity in CO₂ hydrogenation into methanol. *Chem* **4**, 613-625 (2018).
 30. Cui, C. *et al.* Promotional effect of surface hydroxyls on electrochemical reduction of CO₂ over SnOx/Sn electrode. *Journal of catalysis* **343**, 257-265 (2016).
 31. Yao, D. *et al.* The Controllable Reconstruction of Bi-MOFs for Electrochemical CO₂ Reduction through Electrolyte and Potential Mediation. *Angew. Chem. Int. Ed.* **60**, 18178-18184 (2021).
 32. Dou, S. *et al.* Boosting Electrochemical CO₂ Reduction on Metal–Organic Frameworks via Ligand Doping. *Angew. Chem. Int. Ed.* **58**, 4041-4045 (2019).
 33. Dou, S. *et al.* Boosting electrochemical CO₂ reduction on metal–organic frameworks via ligand doping. *Angew. Chem. Int. Ed.* **131**, 4081-4085 (2019).
 34. Zhang, T., Du, J., Xi, P. & Xu, C. Hybrids of Cobalt/Iron Phosphides Derived from Bimetal–Organic Frameworks as Highly Efficient Electrocatalysts for Oxygen Evolution Reaction. *ACS Appl. Mater. Interfaces* **9**, 362-370 (2017).
 35. Zheng, T. *et al.* Large-scale and highly selective CO₂ electrocatalytic reduction on nickel single-atom catalyst. *Joule* **3**, 265-278 (2019).
 36. Saliba, D., Ammar, M., Rammal, M., Al-Ghoul, M. & Hmadeh, M. Crystal growth of ZIF-8, ZIF-67, and their mixed-metal derivatives. *J. Am. Chem. Soc.* **140**, 1812-1823 (2018).
 37. Schwenzer, B., Pop, L. Z., Neilson, J. R., Sbardellati, T. B. & Morse, D. E. Nanostructured ZnS

- and CdS films synthesized using layered double hydroxide films as precursor and template. *Inorg. Chem.* **48**, 1542-1550 (2009).
38. Shinagawa, T. *et al.* Oriented transformation from layered zinc hydroxides to nanoporous ZnO: A comparative study of different anion types. *Inorg. Chem.* **57**, 13137-13149 (2018).
 39. Utama, M. I. B. *et al.* Incommensurate van der Waals epitaxy of nanowire arrays: a case study with ZnO on muscovite mica substrates. *Nano letters* **12**, 2146-2152 (2012).
 40. De La Mata, M. *et al.* Polarity assignment in ZnTe, GaAs, ZnO, and GaN-AlN nanowires from direct dumbbell analysis. *Nano letters* **12**, 2579-2586 (2012).
 41. De La Mata, M. *et al.* The role of polarity in nonplanar semiconductor nanostructures. *Nano letters* **19**, 3396-3408 (2019).
 42. Li, J. *et al.* Tuning the Electronic Bandgap of Graphdiyne by H-Substitution to Promote Interfacial Charge Carrier Separation for Enhanced Photocatalytic Hydrogen Production. *Adv. Funct. Mater.* **31**, 2100994 (2021).
 43. Lei, F. *et al.* Oxygen vacancies confined in ultrathin indium oxide porous sheets for promoted visible-light water splitting. *J. Am. Chem. Soc.* **136**, 6826-6829 (2014).
 44. Bang, S. *et al.* Photocurrent detection of chemically tuned hierarchical ZnO nanostructures grown on seed layers formed by atomic layer deposition. *Nanoscale Res. Lett.* **7**, 1-11 (2012).
 45. Kim, Y. H. *et al.* Organic electrolytes doped ZnO layer as the electron transport layer for bulk heterojunction polymer solar cells. *Solar RRL* **2**, 1800086 (2018).
 46. Jiang, L. *et al.* Low-temperature and solution-processable zinc oxide transistors for transparent electronics. *ACS omega* **2**, 8990-8996 (2017).
 47. Liu, S. *et al.* Elucidating the Electrocatalytic CO₂ Reduction Reaction over a Model Single-Atom Nickel Catalyst. *Angew. Chem. Int. Ed.* **59**, 798-803 (2020).
 48. Zhang, T. *et al.* Quasi-double-star nickel and iron active sites for high-efficiency carbon dioxide electroreduction. *Energy Environ. Sci.* **14**, 4847-4857 (2021).
 49. Xiang, Q. *et al.* Heterostructure of ZnO Nanosheets/Zn with a Highly Enhanced Edge Surface for Efficient CO₂ Electrochemical Reduction to CO. *ACS Appl. Mater. Interfaces* **13** (2021).
 50. Geng, Z. *et al.* Oxygen Vacancies in ZnO Nanosheets Enhance CO₂ Electrochemical Reduction to CO. *Angew. Chem. Int. Ed.* **57**, 6054-6059 (2018).
 51. Daiyan, R. *et al.* Uncovering Atomic-Scale Stability and Reactivity in Engineered Zinc Oxide Electrocatalysts for Controllable Syngas Production. *Adv. Energy Mater.* **10**, 2001381 (2020).
 52. Meng, N., Huang, Y., Liu, Y., Yu, Y. & Zhang, B. Electrosynthesis of urea from nitrite and CO₂ over oxygen vacancy-rich ZnO porous nanosheets. *Cell Reports Physical Science* **2**, 100378 (2021).
 53. Xue, L. *et al.* Surface modification and reconstruction of ZnO hollow microspheres for selective electroreduction of CO₂ to CO. *J. Alloys Compd.* **882**, 160703 (2021).
 54. Ren, X. *et al.* Oxygen vacancy enhancing CO₂ electrochemical reduction to CO on Ce-doped ZnO catalysts. *Surfaces and Interfaces* **23**, 100923 (2021).
 55. Luo, W. *et al.* Electrochemical reconstruction of ZnO for selective reduction of CO₂ to CO. *Appl. Catal. B Environ.* **273**, 119060 (2020).
 56. Kung, C.-W. *et al.* Copper Nanoparticles Installed in Metal–Organic Framework Thin Films

- are Electrocatalytically Competent for CO₂ Reduction. *ACS Energy Lett.* **2**, 2394-2401 (2017).
57. Ni, W. *et al.* Fluorine doped cage-like carbon electrocatalyst: an insight into the structure-enhanced CO selectivity for CO₂ reduction at high overpotential. *ACS nano* **14**, 2014-2023 (2020).
58. Liu, Y. *et al.* Facile synthesis of polypyrrole coated copper nanowires: a new concept to engineered core-shell structures. *Chem. Comm.* **48**, 2621-2623 (2012).
59. Dunwell, M., Luc, W., Yan, Y., Jiao, F. & Xu, B. Understanding surface-mediated electrochemical reactions: CO₂ reduction and beyond. *ACS Catal.* **8**, 8121-8129 (2018).
60. Zhao, C. *et al.* Solid-diffusion synthesis of single-atom catalysts directly from bulk metal for efficient CO₂ reduction. *Joule* **3**, 584-594 (2019).
61. Li, C. W. & Kanan, M. W. CO₂ reduction at low overpotential on Cu electrodes resulting from the reduction of thick Cu₂O films. *J. Am. Chem. Soc.* **134**, 7231-7234 (2012).
62. Gu, J., Hsu, C.-S., Bai, L., Chen, H. M. & Hu, X. Atomically dispersed Fe³⁺ sites catalyze efficient CO₂ electroreduction to CO. *Science* **364**, 1091-1094 (2019).

Chapter 4

Surface functionalization of ZnO nanorods with a MOF shell for Boosting CO Production in Electrocatalytic CO₂ Reduction



ZnO nanorods have been used as a metal source for the in-situ growth of a ZIF-8 shell layer. The optimized ZIF-8 shell interface with the ZnO NRs showed a remarkable CO₂ RR activity in 0.5 M NaHCO₃ solution, accompanied by an excellent selectivity with Faradaic efficiency of CO (85 %) at -1.05 V vs. RHE, which is superior to that of pristine ZnO NRs. This layer inherited the CO₂ affinity and hydrophobicity of ZIF-8, which promotes a high concentration of CO₂ molecules around the active sites. The nanoporous structure increased the local pH around the active sites, during the CO₂ RR, which furtherly suppressed the HER competing reaction.

4.1 Introduction

The use of the electrochemical CO₂ reduction reaction (eCO₂ RR) to produce various value-added chemicals and commodities is a promising method to tackle the anthropogenic CO₂ in the atmosphere, thus, achieving the sustainable redox cycle for energy storage and conversion.¹⁻³ Due to the sluggish reaction kinetics of CO₂ reduction and the presence of the competing hydrogen evolution reaction (HER) under aqueous conditions, substantial efforts have been invested towards the design of new electrocatalysts with improved catalytic activities.^{4,5} In addition to the improvement of catalytic materials, the local environment of the catalysts closely related to the transportation and local concentration of reaction species and intermediates also plays an important role for the enhancement of the eCO₂ RR performance.⁶⁻⁹ Therefore, design, fabrication, functionalization and/or construction of the interfacial microenvironment in the available electrodes is a wise strategy to combine materials with environmental effects, which could effectively achieve an improved activity and selectivity in comparison to the pristine catalysts.

The CO₂ reduction kinetics is largely limited by the local concentration of CO₂ at the electrode/electrolyte interface.^{10,11} Unfortunately, the low solubility of CO₂ in neutral pH aqueous electrolytes at ambient temperature deteriorates the CO₂ reduction process at the outset.¹² Sargent's group used field-induced reagent concentration (FIRC) to enhance the local concentration of CO₂ on the active surface, which realize the high selectivity of CO.^{13,14} Besides, the enhancement of the surface microenvironment hydrophobicity could reduce the activity of water dissociation to indirectly increase the selectivity towards CO₂.^{7,15} In addition, the local environment near the electrode surface has dynamic variation during the reaction process, which could be disturbed by the reaction itself.^{16,17} This change affects the kinetics and even reaction pathways. OH⁻ ions generated and accumulated at the surface of the cathode increase the pH at the electrode/electrolyte interface during the reactions. Züttel's group reported that the highly porous structure of a Zn-based electrocatalyst could

strengthen the local pH effect to enhance the CO selectivity by suppressing HER.¹⁸ There is growing evidence that accessibility of the catalyst to high concentrations of CO₂ and high local pH are closely linked to the overall activity and productivity of CO₂ RR. It is a reasonable method to construct an ideal interface microenvironment by adding a porous shell with CO₂ affinity to functionalize the catalyst surface and produce CO₂-rich regions with pH increasing gradient near the active sites.¹⁹

Recently, metal-organic frameworks (MOFs) have attracted a great attention because of their large specific surface area, permanent porosity, and variable pore environment.²⁰ Therefore, they are promising candidate materials to be used as a shell to modify the surface microenvironment of the inorganic metals or metal oxides with catalytic capacity in the energy field.^{21–23} In addition to the nature of the MOFs themselves, the synthetic strategies have enormous effects on the catalytic performance of the shell interface.²⁴ The capping agent-assisted methodology, not only prevents the aggregation of the inorganic nanostructures (e.g. metal or metal oxide nanoparticles, nanorods,...), but also raises the affinity between the surface of the catalyst and the MOF synthetic precursors. The later methodology has been used to obtain a wide range of functionalized compounds.²⁵ However, these introduced organic substances, which play a significant role in controlling the alignment of the interfaces, are sometimes very hard to be removed by a simple wash or distillation postprocess. Even worse, adsorption of surfactant may deteriorate the electrocatalytic activity of build electrode by disrupting the interface environment. In this way, inorganic template-assisted synthesis is more attractive in order to build an ideal interface environment.^{26,27} The metal oxide on the surface serves as the metal source for the direct growth of MOF shell. Zeolitic imidazolate frameworks (ZIFs), a subfamily of MOFs that have a crystal topological structure similar to zeolites, have been widely reported and studied, with more than 150 structures.²⁸ Among them, ZIF-8, characterized by its high chemical and thermal stability, large pore volume and surface area, and easy to prepare, has been widely studied.^{29,30} Most of zinc salts and even zinc oxide could be used as metal source for the synthesis of ZIF-8. Coincidentally, zinc

oxide (ZnO) has been widely investigated for generating CO with moderate selectivity.³¹ Thus, constructing a MOF layer on the surface of ZnO to improve eCO₂ RR is a reasonable catalytic system paradigm to validate our mentioned hypothesis.

In this work, we demonstrate how, by functionalizing the surface of ZnO nanorods by growing a ZIF-8 porous shell, we can improve the electrochemical reduction of CO₂ to CO. The optimized ZnO NR/ZIF-8 core-shell structure shows a remarkable CO₂ RR activity in 0.5 M NaHCO₃ solution, accompanied by an excellent selectivity with Faradaic efficiency of CO (85 %) at -1.05 V vs. RHE, which is superior to pristine ZnO nanorods and pristine ZIF-8 nanostructures. Moreover, the selectivity could be retained over 70 % in a range of working potentials from -0.90 to -1.15 V vs. RHE. This enhanced CO₂ reduction performance is attributed to the microenvironment created by the microporous MOF shell. This microenvironment has affinity towards CO₂, together with a strengthened local pH effect, as well as an appropriate hydrophobic ability.

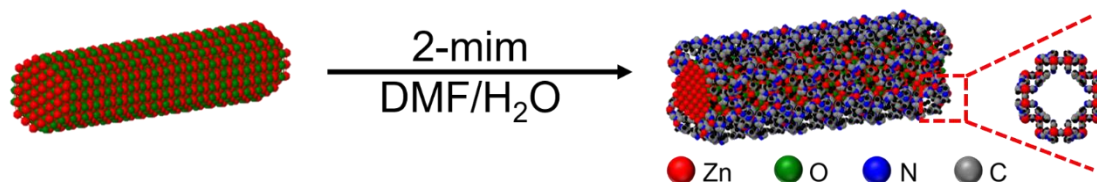


Figure 4.1 Schematic illustration of the synthesis of ZnO NR@ZIF-8 core-shell nanostructure.

The inorganic template-assisted synthesis procedure of ZnO NR@ZIF-8 samples is schematically displayed in **Figure 4.1**. Firstly, ZnO nanorods are prepared and then used as self-sacrificed templates for the subsequent ZIF-8 in-situ growth without adding any additional surfactant. During this in-situ growth process, by precisely controlling the ratio of the different solvent, various ZIF-8 shell thicknesses could be obtained. The detailed synthesis information is shown in **Section 4.2**.

4.2 Experimental Section

4.2.1 Materials and Methods

Materials: If not specified, all chemical reagents were purchased from Sigma-Aldrich. Zinc acetate hydrate ($\text{ZnAc}_2 \cdot 2\text{H}_2\text{O}$), zinc nitrate hexahydrate ($\text{Zn}(\text{NO}_3)_2 \cdot 6\text{H}_2\text{O}$), 2-methylimidazole (2-mim), sodium hydroxide (NaOH), N,N-dimethylformamide (DMF), ethanol, sodium hydroxide (NaOH) and sodium bicarbonate (NaHCO_3) were all of analytical grade and used as received without further purification. Meanwhile, all solutions were prepared with Milli-Q water ($\text{DI-H}_2\text{O}$, Ricca Chemical, ASTM Type I). The Nafion (N-117 membrane, 0.18 mm thick) was purchased from Alfa Aesar and kept in 0.5 M NaOH solution. The carbon paper was also purchased from Alfa Aesar.

Characterization: The X-ray diffraction patterns (XRD) were obtained through a Bruker D4 X-ray powder diffractometer using $\text{Cu K}\alpha$ radiation (1.54184 \AA). Field emission scanning electron microscopy (FESEM) images were collected on a FEI Magellan 400 L scanning electron microscope. The transmission electron microscopy (TEM) and high angle annular dark field scanning TEM (HAADF-STEM) images were obtained in a Tecnai F20 field emission gun microscope with a 0.19 nm point-to-point resolution at 200 kV equipped with an embedded Quantum Gatan Image Filter for EELS analyses. Images have been analyzed by means of Gatan Digital Micrograph software. X-ray photoelectron spectroscopy (XPS) was performed on a Phoibos 150 analyser (SPECS GmbH, Berlin, Germany) in ultra-high vacuum conditions (base pressure 4×10^{-10} mbar) with a monochromatic aluminum $\text{K}\alpha$ X-ray source (1486.74 eV). Binding energies (BE) were determined using the C 1s peak at 284.5 eV as a charge reference. Brunauer-Emmett-Teller (BET) surface areas were measured using nitrogen adsorption at 77 K. For BET measurement, samples were outgassed at 473 K during 12 h. Fourier transformed infrared (FTIR) spectroscopy data were recorded on an Alpha Bruker spectrometer.

4.2.2 Synthesis Methods

4.2.2.1 Preparation of ZIF-8

The fabrication process of ZIF-8 is similar to the reported in literature.³² A methanol aqueous solution containing 2-methylimidazole ($C_4H_6N_2$, 50 mL, 0.123 g) was added into the methanol aqueous solution of $Zn(NO_3)_2 \cdot 6H_2O$ (50 mL, 1.115 g) under magnetic stirring at room temperature to form a homogeneous solution. After reaction for 24 h without stirring, the sample was then taken out, washed by methanol several times, and vacuum dried overnight.

4.2.2.2 Preparation of ZnO Nanorods (ZnO NRs)

The ZnO NRs were prepared based on the previous literature with a minor modification.²⁷ Typically, 1.32 g $ZnAc_2 \cdot 2H_2O$ and 4.8 g NaOH were dissolved in 18 mL of distilled water. Then, 42 mL of glycerin was dropped in the above solution. After magnetic stirring for 15 min, the mixture was transferred to a Teflon-lined stainless-steel autoclave and was kept at 150 °C for 24 h. The products were collected by centrifugation and washed several times with deionized water and ethanol.

4.2.2.3 Preparation of ZnO NR@ZIF-8

The growth of ZIF-8 shell on the ZnO nanorods template proceeded via a simple chemical bath route. In a typical experiment, 2-methylimidazole (0.1650 g) and ZnO nanorods (0.0204 g) were in sequence added to a glassy bottle containing a mixed solvent of DMF/ H_2O (16 mL, 7:1 of v/v). After sonication for 5 min, the glassy bottle was transferred to an oven preheated to 70 °C. After the mixture reacted for 24 h, the white product was collected by centrifugation and washed by fresh DMF and ethanol for several times. Different ZnO NR@ZIF-8 were prepared by the similar method with different ratio of DMF/ H_2O (1:0, 2:1, 1:1, 1:2, 0:1)

4.2.3 Preparation of working electrodes

The detailed information is shown in **Chapter 2**. In this work, the catalyst loading mass is $\sim 3 \text{ mg/cm}^2$.

4.2.4 Electrochemical Measurement

The detailed information is shown in **Chapter 2**.

4.2.5 Calculation Method

The detailed information is shown in **Chapter 2**.

4.3 Results and Discussion

4.3.1 Sample Characterization

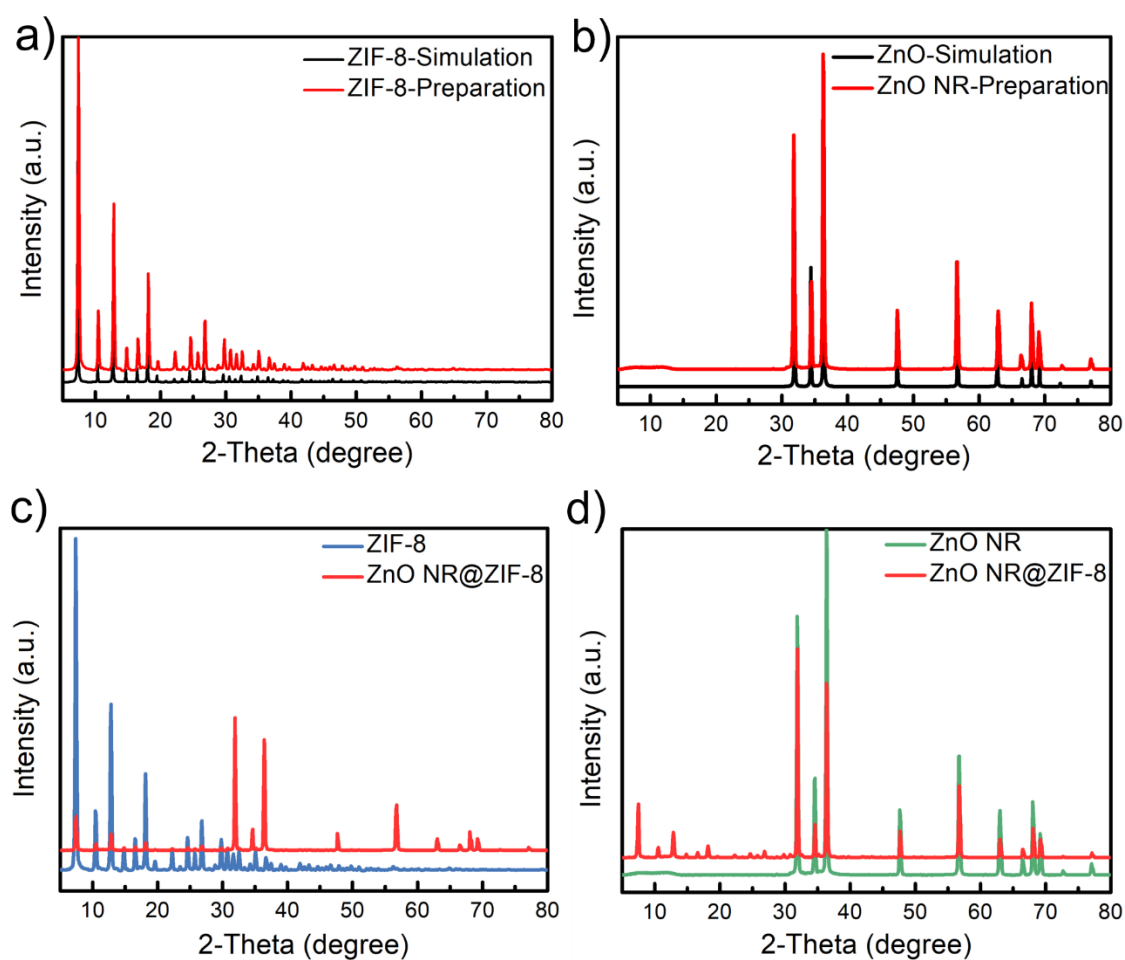


Figure 4.2. XRD patterns of (a) ZIF-8, (b) ZnO NR, (c) ZIF-8 and ZnO NR@ZIF-8 as well as (d) ZnO NR and ZnO NR@ZIF-8.

The crystallinity of the as-prepared samples is furtherly confirmed by powder X-ray

diffraction (XRD) measurements. As shown in **Figures 4.2a-b**, ZIF-8 and ZnO NR samples show the crystalline structures consistent with the simulated ones, proving the successful fabrication of ZIF-8 particles and ZnO NRs. Due to the difference of the feature peaks in spectrum, the XRD pattern for ZnO NR@ZIF-8 includes two kinds of distinct crystal structures clearly. Except for those diffraction peaks after 30° agree well with the XRD pattern of prepared ZnO NR, the new diffraction peaks before 20° are assigned to ZIF-8 (**Figure 4.2c-d**). This result confirms the existence of the ZIF-8 and ZnO NR structures in the synthesized samples.

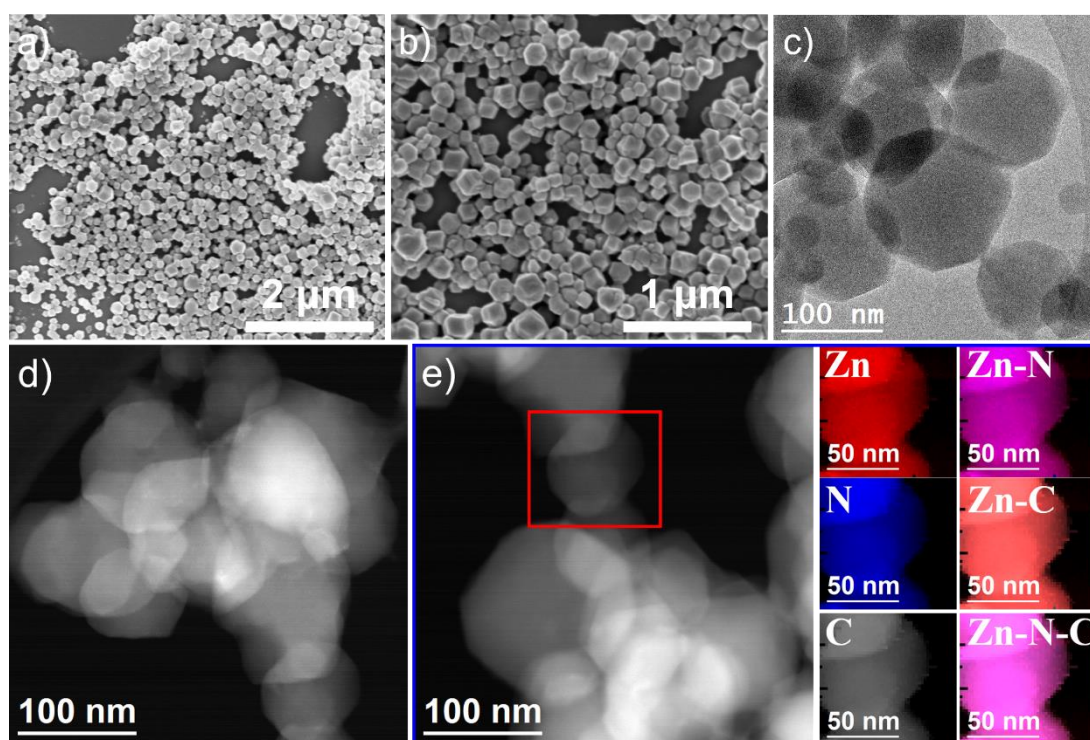


Figure 4.3. Morphology of ZIF-8. (a and b) SEM images, (c) BF TEM, (d) HAADF-STEM and (e) HAADF-STEM image of ZIF-8 and representative EELS chemical composition maps obtained from the red squared area of the STEM micrograph. Individual Zn $L_{2,3}$ -edges at 1020 eV (red), N K-edges at 401 eV (blue), and C K-edges at 285 eV (grey) as well as composites of Zn-N, Zn-C and Zn-N-C.

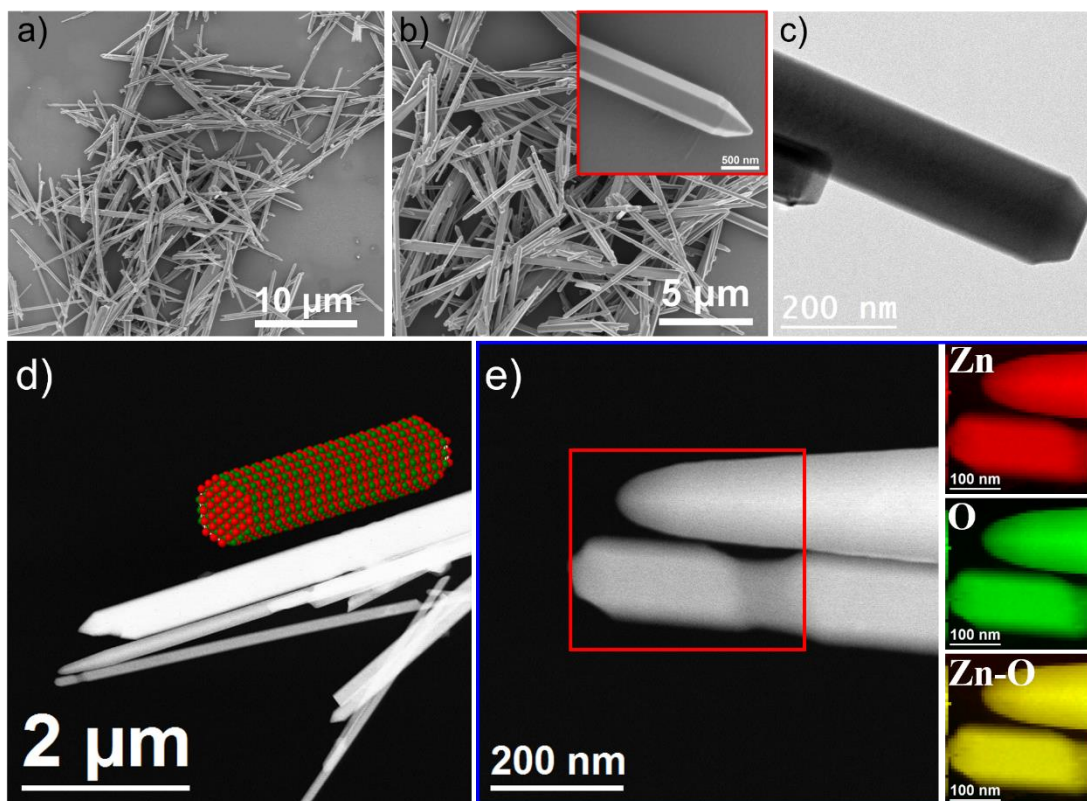


Figure 4.4. Morphology of ZnO NR. (a and b) SEM images, (c) BF TEM, (d) HAADF-STEM and (e) HAADF-STEM image of ZnO NR and representative EELS chemical composition maps obtained from the red squared area of the STEM micrograph. Individual Zn $L_{2,3}$ -edges at 1020 eV (red), O K-edges at 532 eV (green) as well as composites of Zn-O.

The morphologies of ZIF-8 and ZnO NR are investigated by field-emission scanning electron microscopy (FE-SEM) and transition electron microscopy (TEM). **Figure 4.3** reveals that ZIF-8 forms polyhedral crystals of about 200 nm in size. Meanwhile, as shown in **Figure 4.4**, the ZnO NR sample exhibits a rod-like shape nanostructures with a smooth surface, which are similar to the morphology observed in previous works for ZnO NRs.²⁷

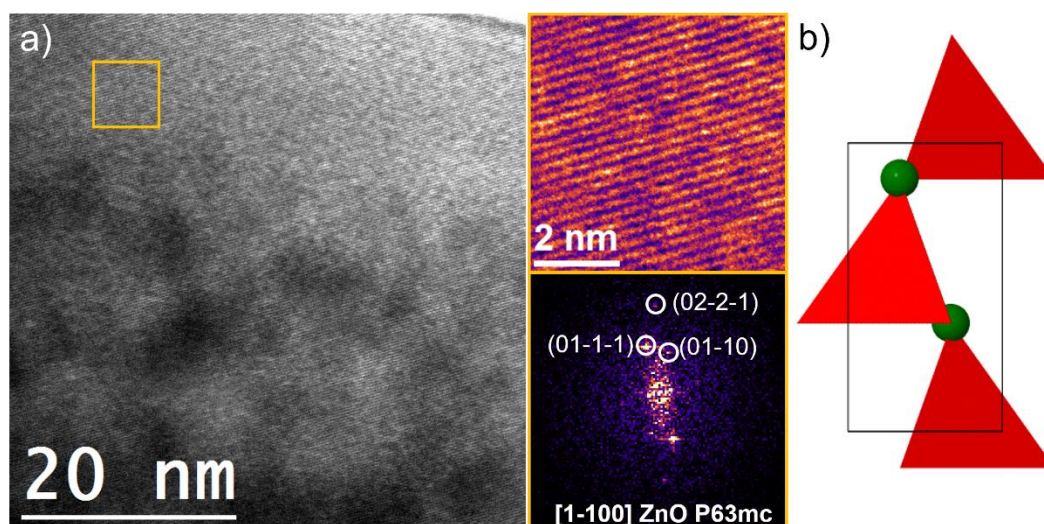


Figure 4.5 HRTEM micrograph of ZnO NR sample and detail of the orange squared region and its corresponding power spectrum as well as 1*1*1 unit crystal model of ZnO (Zn and O atoms are represented in red and green, respectively).

Figure 4.5 shows a HRTEM micrograph of a nanorod. Detail of the orange squared region and its corresponding power spectrum which reveals that this nanoparticle has a crystal phase that is in agreement with the ZnO hexagonal phase (space group =P63mc) with $a=b= 3.2900 \text{ \AA}$, and $c= 5.3000 \text{ \AA}$. From the crystalline domain in **Figure 4.5**, the ZnO lattice fringe distances were measured to be 0.247 nm, 0.134 nm and 0.275 nm, at 12.83° and 27.83° which could be interpreted as the hexagonal ZnO phase, visualized along its [1-100] zone axis.

Table 4.1 Comparison between the experimental and the theoretical bulk plane spacing distances and angles between planes.

Spot	Experimental (nm)	ZnO (P63mc) [1-100]
1	0.247	0.251 (01-1-1)
2	0.134 (12.83° vs Spot 1)	0.138 (13.22°) (02-2-1)
3	0.275 (27.83° vs Spot 1)	0.285 (28.26°) (01-10)

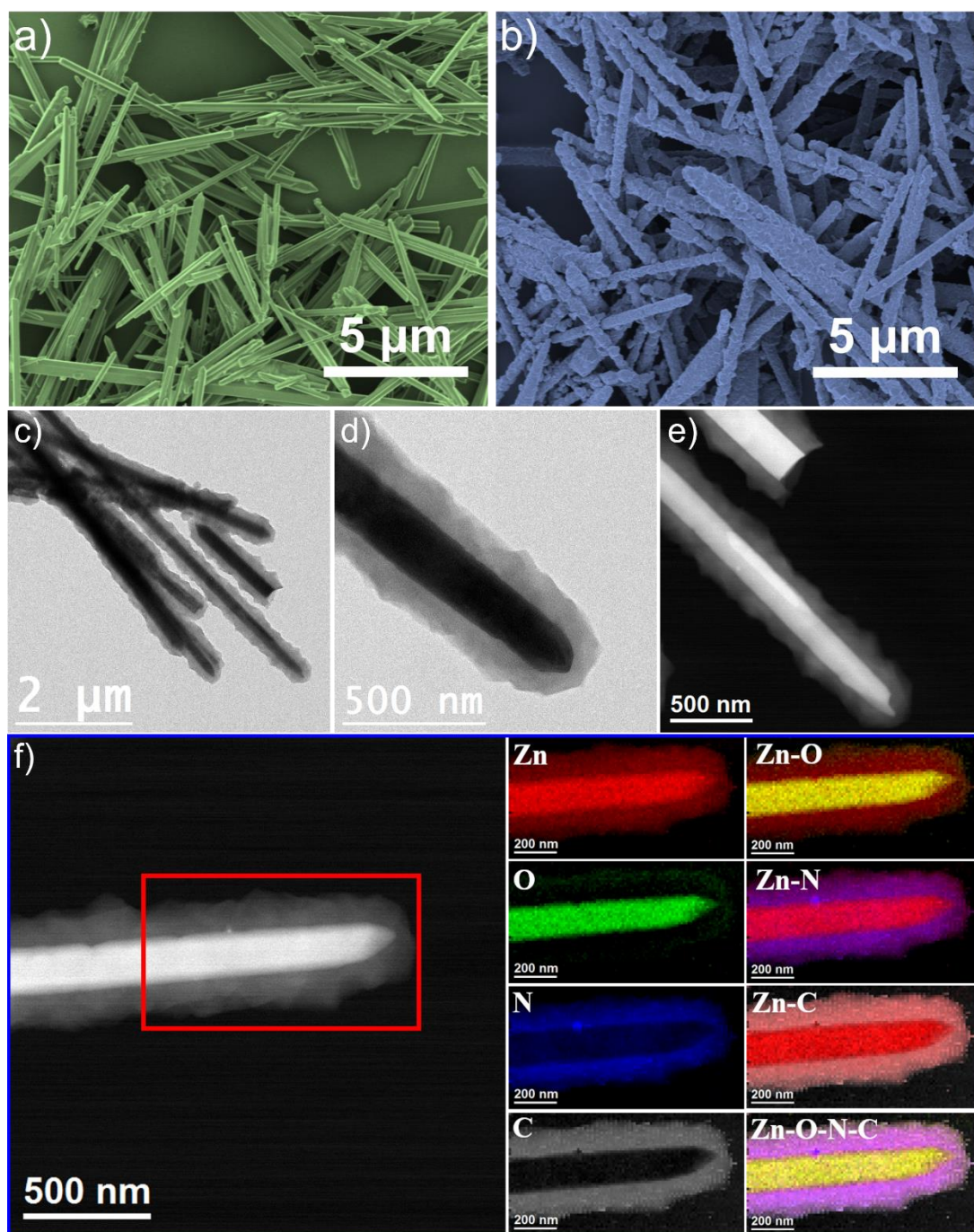


Figure 4.6. SEM image of (a) ZnO NR and (b) ZnO NR@ZIF-8. (c-d) BF TEM images, (e-f) HAADF-STEM images of ZnO NR@ZIF-8 and representative EELS chemical composition maps obtained from the red squared area of the STEM micrograph. Individual Zn $L_{2,3}$ -edges at 1020 eV (red), O K-edges at 532 eV (green), N K-edges at 401 eV (blue), and C K-edges at 285 eV (grey) as well as composites of Zn-O, Zn-N, Zn-C and Zn-O-N-C.

As shown in **Figures 4.6 a-b**, compared to bare ZnO NR, FE-SEM reveal the formation of a functional shell layer on the surface of the ZnO NRs. It is clearly observed that the ZnO NR@ZIF-8 sample inherits the rod-like structure of ZnO NR with a rough surface.

To further prove the distribution of ZIF-8 shell layer on the ZnO NRs, TEM was performed. Thanks to the difference of contrast in BF TEM and the high-angle annular dark-field scanning TEM (HAADF-STEM) image (**Figures 4.6c-d**), we could observe that the entire surface of ZnO NRs was fully and uniformly covered with a shell, demonstrating the success of the in-situ oriented growth of the ZIF-8 shell. Furthermore, elemental composition maps were obtained by means of electron energy loss spectroscopy (EELS) in STEM mode (**Figure 4.6f**), showing that N and C elements were mostly located at the outer layer of the nanorod, while Zn is found in the whole sample (core and shell), with relatively higher concentration at the core area. Note that N and C are only present in the shell, in good agreement with the ZIF-8 expected 2-methylimidazole ligand compositions (**Figures 4.3 and 4.4**).

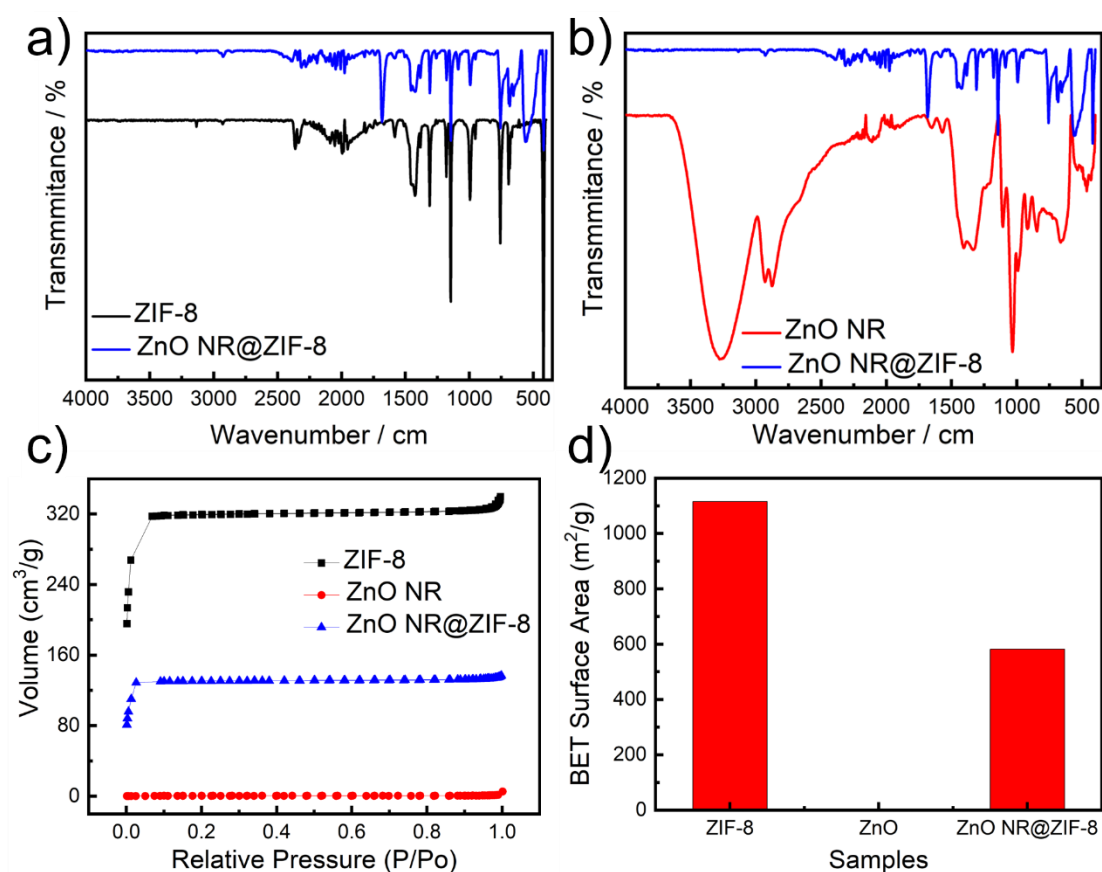


Figure 4.7. FTIR spectrum of (a) ZIF-8 and ZnO NR@ZIF-8, (b) ZnO NR and ZnO NR@ZIF-8. (c) N₂ adsorption and desorption isotherm and (d) BET surface areas of ZIF-8, ZnO NR and ZnO NR@ZIF-8.

Based on the Fourier transform infrared (FTIR) spectra, the typical vibrations of ZIF-8

crystals also appear in those of ZnO NR@ZIF-8. Meanwhile, the characteristic bands ascribed to Zn-O bond are also found in ZnO NR@ZIF-8 sample, which are similar to those of ZnO NR sample, further confirming the in-situ growth of the ZIF-8 shell on the ZnO NRs (**Figure 4.7a-b**). To further investigate the surface area influenced by the addition of the ZIF-8 shell on the as-prepared samples, N₂ adsorption-desorption measurements were performed and shown in **Figures 4.7c-d**. The ZnO NR@ZIF-8 sample shows a typical type I adsorption/desorption isotherm curve in **Figure 4.7c** and possesses a high specific surface area as shown in **Figure 4.7d**, which is similar to that of ZIF-8, indicating that ZnO NR@ZIF-8 sample has numerous micropores inherited from ZIF-8. Moreover, compared to the pristine ZnO NRs surface, the existence of high volume of micropores of ZIF-8 shell could improve the CO₂ affinity to enhance the CO₂ concentration around the active sites and nanoporous structure could form a microenvironment between the active sites and the electrolyte on the surface. The above results demonstrate that ZIF-8 shell successfully grow on the surface of ZnO NR by using the proposed self-sacrificed strategy. This integration way creates a unique interface between the active sites and surface electrolyte, which might potentially improve the catalytic performance of ZnO NR towards CO₂ RR as shown in the following.

4.3.2 Electrochemical Performance

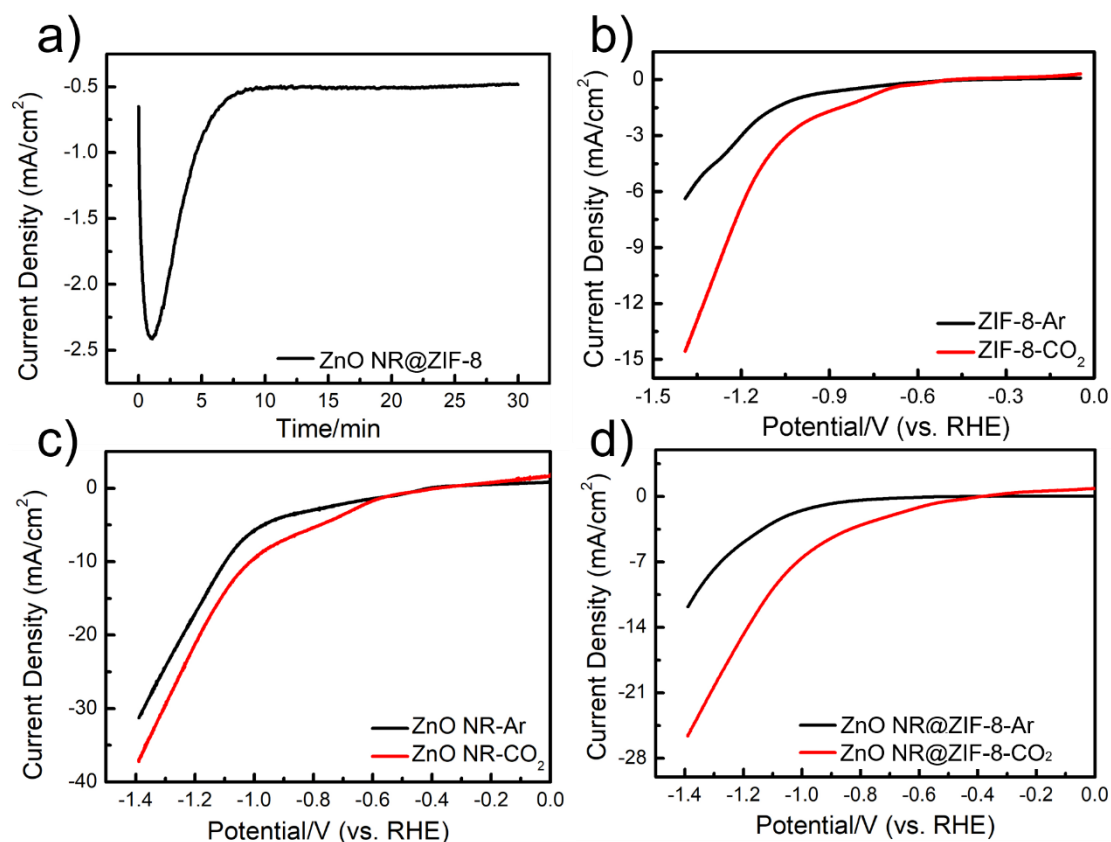


Figure 4.8. (a) Electrode current recorded during reduction of ZnO NR@ZIF-8 at -0.70 V vs. RHE in 0.5 M NaHCO_3 purged with Ar gas; (b, c and d) LSV curves of ZIF-8, ZnO NR and ZnO NR@ZIF-8 in Ar- and CO_2 -saturated 0.5 M NaHCO_3 solution.

The electrocatalytic activity of the different samples towards CO_2 RR are investigated in a typical three-electrode H-cell under CO_2 -saturated 0.5 M NaHCO_3 solution. The samples were previously coated on carbon paper ($1\text{ cm} \times 1\text{ cm}$) with a mass loading of $\sim 3.0\text{ mg cm}^{-2}$. Before the electrochemical measurements, all electrodes were pretreated to obtain the steady current at a constant potential of -0.70 V vs. RHE for 30 min, as shown in **Figure 4.8a**. Then, the electrocatalytic CO_2 RR performance of these samples was roughly evaluated by linear sweep voltammetry (LSV). As shown in **Figures 4.8b-d**, the ZnO NR@ZIF-8 sample presents a current reduction under Ar atmosphere, typically attributed to the HER. Upon saturating the solution with CO_2 , the current reduction increases. Similar peaks are observed on ZIF-8 and ZnO NR counterparts, indicating all samples have activity towards CO_2 electrochemical

reduction. The catalytic activities for CO₂ RR are further investigated by the chronoamperometry method. Meanwhile, the periodic quantification of the gas-phase products are detected by gas chromatography (GC). Online GC results show that CO and H₂ are the main gas products obtained for all the catalysts.

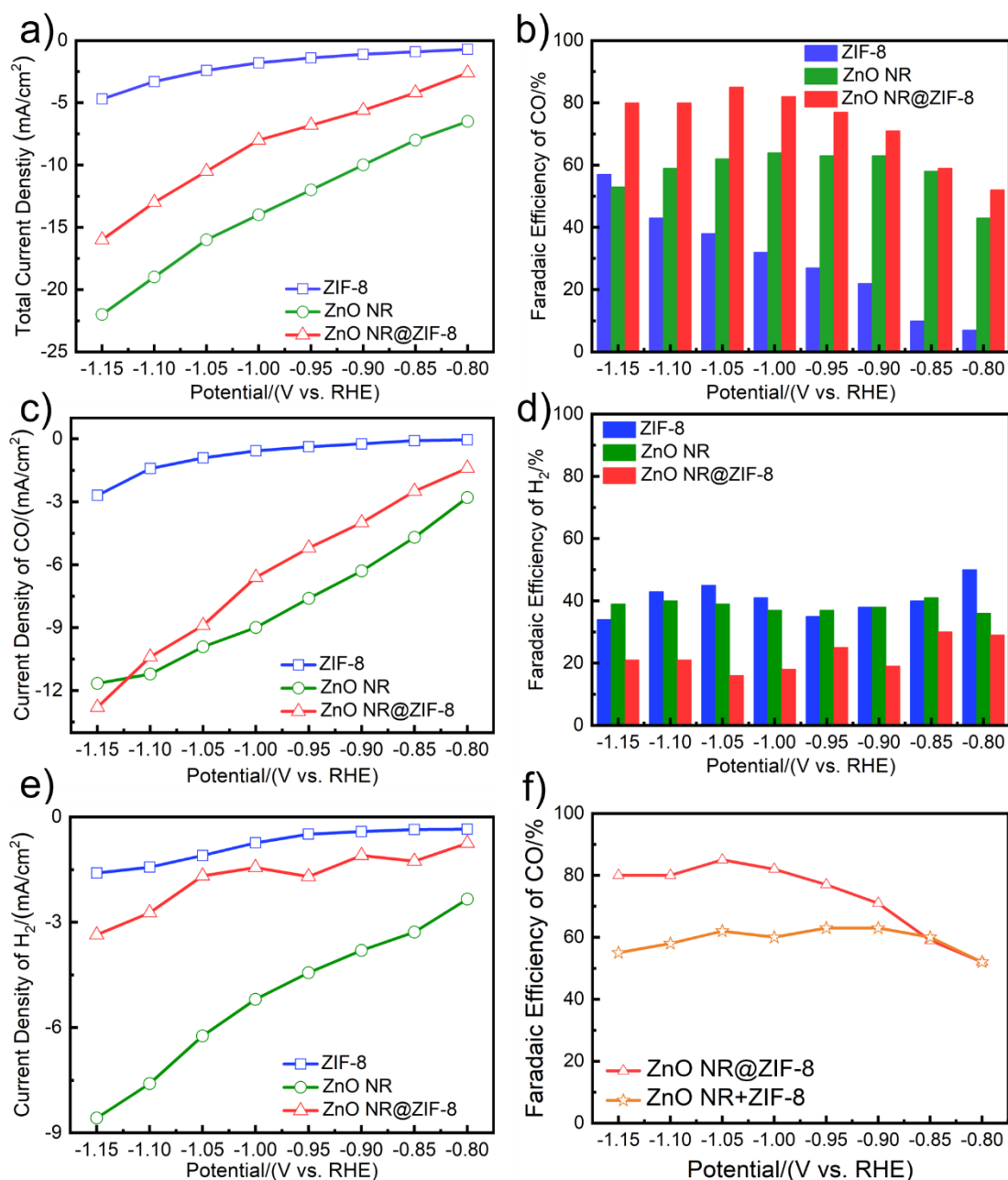


Figure 4.9. (a) Total current density, (b) FE of CO at various potentials, (c) current density for CO production, (d) FE of H₂ at various potentials, (e) current density for H₂ production on ZIF-8, ZnO NR and ZnO NR@ZIF-8. (f) FE of CO at various potentials on ZnO NR+ZIF-8 and ZnO NR@ZIF-8 electrodes.

The total current densities of the three samples are plotted against potential, as presented in **Figure 4.9a**. Compared to ZIF-8, the total current densities of ZnO NR@ZIF-8 and ZnO NR increase significantly at different applied potential, indicating the faster rate of reaction obtained on both samples because of the relatively high conductivity of ZnO NR. The cathodic compartment is continuously purged with CO₂ (20 ml min⁻¹). **Figure 4.9b** shows the ZnO NR@ZIF-8 exhibited obvious higher Faradaic efficiencies (FE) of CO than other samples at a cathode potential from -0.80 to -1.15 V vs. RHE. At -1.05 V vs. RHE, FE_{CO} of ZnO NR@ZIF-8 for CO production was up to 85 %, percentage that is above those obtained on ZIF-8 and ZnO NR samples. **Figure 4.9c** showed the potential-dependent CO partial current densities calculated based on the current densities and corresponding FE_{CO}. This latest result clearly revealed the high catalytic activity of ZnO NR@ZIF-8 catalyst for the CO₂ reduction toward CO, and further confirmed that the presence of the ZIF-8 shell enables to enhance the mass transport of a gaseous CO₂ feed towards the electrocatalyst surface. The high eCO₂ RR performance on ZnO NR@ZIF-8 is supported by the water contact angle measurement. As shown in **Figure 4.10**, ZnO NR@ZIF-8 with a water contact angle (CA) of 140° showed more hydrophobicity than pure ZnO (water CA of 100°). The reduction of water diffusion through the MOF layer could suppress the HER on the interface of ZnO NR@ZIF-8 (**Figure 4.9d**). The potential dependent H₂ current densities for the different catalysts are shown in **Figure 4.9e**. We further proved the improvement of the selectivity towards CO of the interface between ZnO and ZIF-8. The electrocatalytic activity of the physical mixture of ZnO and ZIF-8 was also investigated as a reference. Obviously, the functionalized NR surface of sample ZnO NR@ZIF-8 containing the ZIF-8 shell showed higher FE_{CO} and could suppress HER more effectively than the sample with a physical mixture of ZnO NRs and ZIF-8 nanostructures (ZnO NR+ZIF-8 sample) (**Figure 4.9f**).

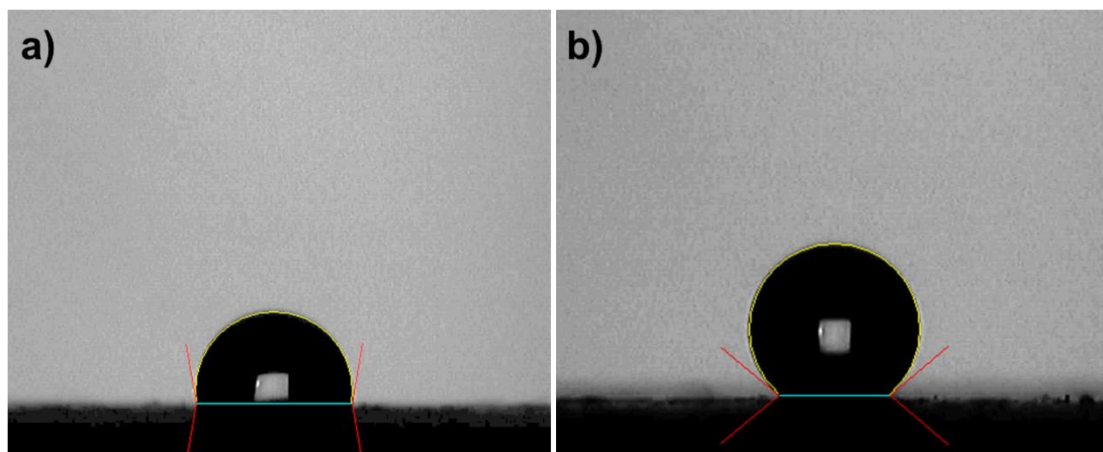


Figure 4.10. Water contact angles for (a) ZnO and (b) ZnO NR@ZIF-8 electrocatalysts deposited on the electrode surface.

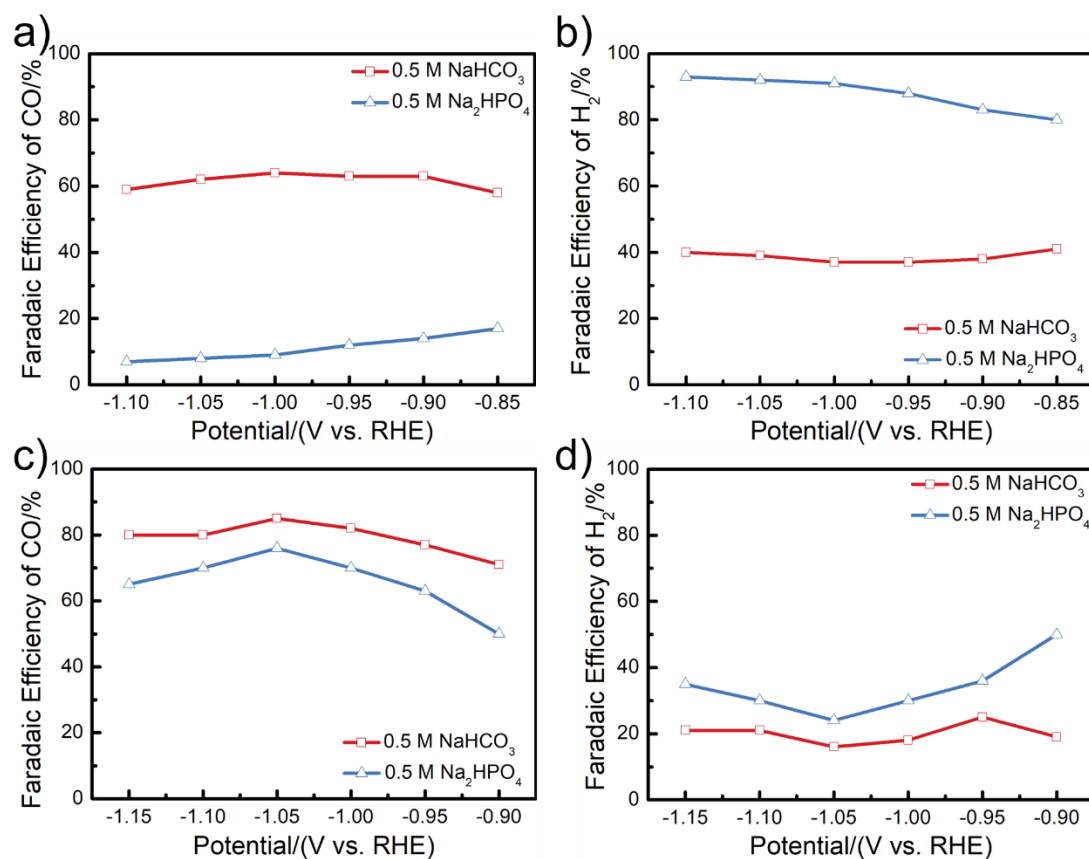


Figure 4.11. Faradic efficiency for CO and H₂ on (a and b) ZnO and (c and d) ZnO NR@ZIF-8 at various potentials in 0.5 M NaHCO₃ and 0.5 M Na₂HPO₄, respectively.

We propose that a local pH effect indirectly benefited the catalytic activity for CO₂ RR. The proton consumption in cathodic reactions (CO₂ RR and HER) would lead to the

local increase of the pH at the electrode/electrolyte interface. The rise of the local pH could suppress HER activity thus facilitating the CO₂ RR. On the contrary, a maintained low pH value at the interface would contribute and favor the H₂ evolution. To verify the local pH effect, the CO₂ RR was performed on ZnO and ZnO NR@ZIF-8 in 0.5 M Na₂HPO₄ and 0.5 M NaHCO₃, respectively. These two kinds of electrolytes have different buffer capacities (0.5 M Na₂HPO₄ > 0.5 M NaHCO₃). Compared to 0.5 M NaHCO₃, the FE for CO on the ZnO was significantly reduced (**Figure 4.11a**) and the FE for H₂ was enhanced (**Figure 4.11b**) in 0.5 M Na₂HPO₄. These results demonstrate that the local pH benefits the CO₂ RR. Interestingly, ZnO NR@ZIF-8 shows a similar FE for CO and H₂ in both electrolytes, respectively (**Figure 4.11 c-d**). The nanoporous shell structure of the functionalized surface, to a certain degree, could hinder the neutralization process for OH⁻ generated near the catalyst surface to keep higher local pH than in the electrolyte bulk solution, thus suppressing H₂ evolution with preferred CO₂ RR.

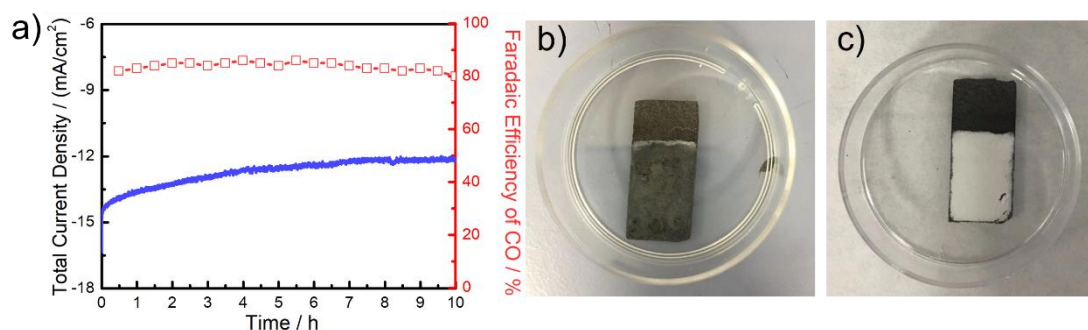


Figure 4.12. (a) Stability test of ZnO NR@ZIF-8 at -1.05 V vs. RHE. The color evolution of (b) ZnO NR and (c) ZnO NR@ZIF-8 after 10 h stability test.

Thanks to the CO₂ affinity of ZIF-8, the interface of ZnO NR@ZIF-8 could concentrate the CO₂ molecules on the electrode surface from the electrolyte bulk solution, increasing the local concentration of CO₂ around the active sites. The CO₂ RR process is a triple-phase model including gaseous CO₂, liquid water, and the solid catalyst. The water contact angle measurements proved that the MOF shell provides a relatively more hydrophobic microenvironment at the surface, which keeps higher density of

gaseous reactants in aqueous electrolytes during the electrochemical process. The higher CO₂ concentration at the interface, in turn, could also protect ZnO from reduction during the CO₂ RR. In order to evaluate the stability of the ZnO NR@ZIF-8 electrocatalyst, we performed a 10 h durability test at a constant -1.05 V vs. RHE cathode potential. The outlet gases were analyzed every 30 min by GC, while calculating the corresponding FE of CO. The current density of ZnO NR@ZIF-8 maintained a steady value of approximately -13 mA cm⁻² with no significant decay (**Figure 4.12a**) during the 10 h test, while the corresponding Faradaic efficiency of CO only decreased slightly to 80 % after the 10 h stability test. After stabilization, an obvious difference in the color of the electrode materials were appreciated by direct observation (**Figure 4.12b**). As observed from the optical images, the surface of the ZnO deactivated electrode was blackened after electrolysis. However, in the presence of the MOF shell, the color of the electrode remained unchanged, as it was expected from the higher concentration of CO₂ on the surface of ZnO NR@ZIF-8.

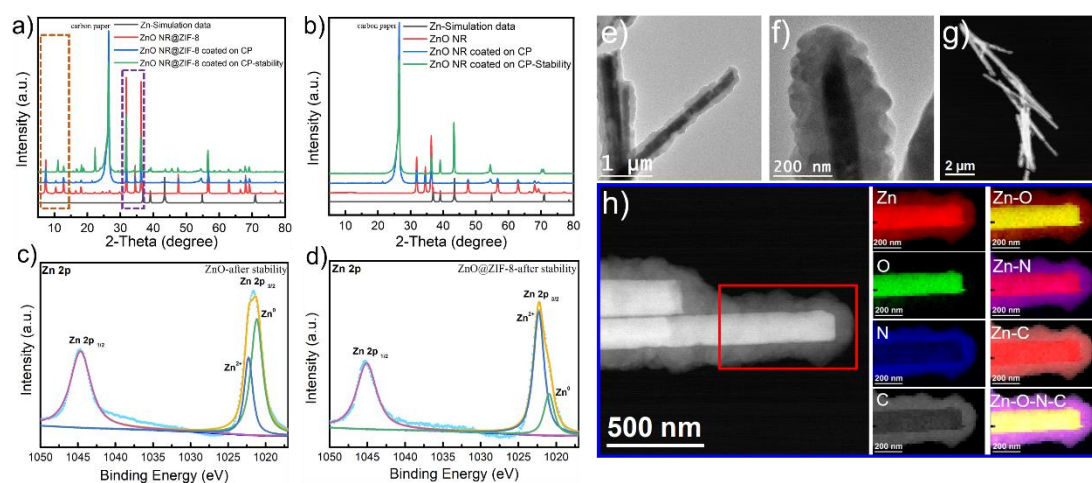


Figure 4.13. XRD patterns of (a) ZnO NR@ZIF-8 and (b) ZnO NR after stability test. High-resolution XPS Zn 2p spectrum of (c) ZnO NR@ZIF-8 and (d) ZnO NR after stability test. (e-f) BF TEM images, (g-h) HAADF-STEM images of ZnO NR@ZIF-8 after stability and representative EELS chemical composition maps obtained from the red squared area of the STEM micrograph. Individual Zn L_{2,3}-edges at 1020 eV (red), O K-edges at 532 eV (green), N K-edges at 401 eV (blue), and C K-edges at 285 eV (grey) as well as composites of Zn-N, Zn-C and Zn-N-C as well as composites of Zn-O, Zn-N, Zn-C and Zn-O-N-C.

XPS, XRD and TEM were used to obtain a more accurate analysis of the structure and

composition of the electrocatalyst after stabilization. XRD results of ZnO NR@ZIF-8-based electrode after the 10 h stability test only showed the characteristic peaks of ZnO and ZIF-8. However, in the XRD spectrum obtained on the ZnO-based electrode, new emerging peaks belonging to the characteristic peaks of metallic Zn could be observed (**Figure 4.13a-b**). Meanwhile, compared to the ZnO NR@ZIF-8, the pristine ZnO electrocatalyst presents a stronger peak of the zero-valence zinc, indicating a much stronger reduction of Zn^{2+} on the surface (**Figure 4.13c-d**). The morphology of ZnO NR@ZIF-8 did not change according to the results obtained by TEM and HAADF-STEM images. In addition, the EELS compositional maps showed that the interface between ZnO and ZIF-8 was still clearly observed.

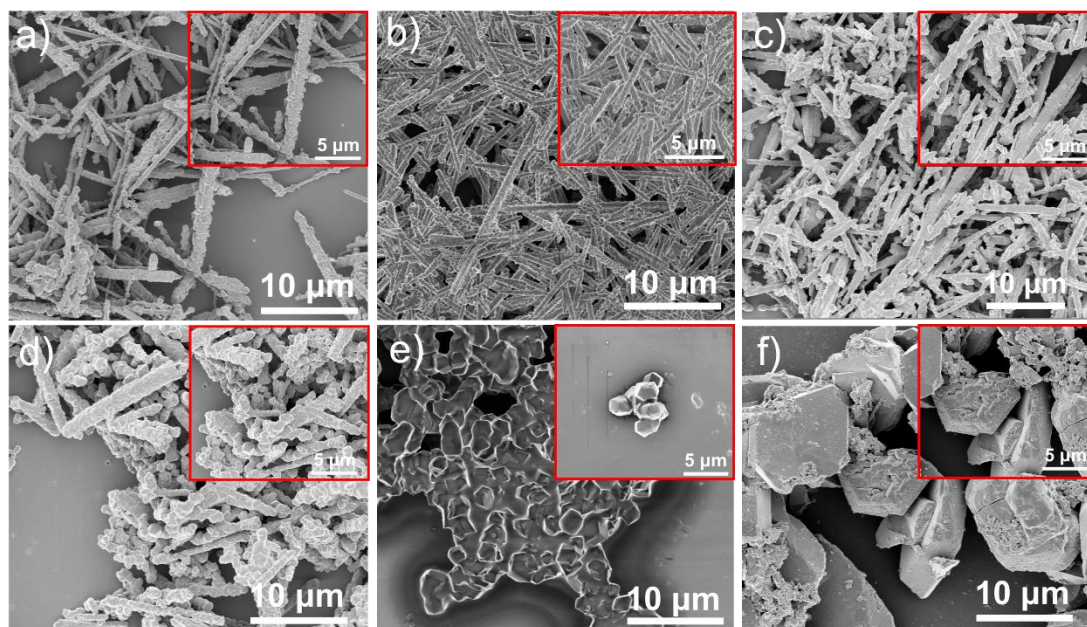


Figure 4.14. SEM images of (a-f) ZnO NR@ZIF-8-x ($x=1:0$ (a), $7:1$ (b), $2:1$ (c), $1:1$ (d), $1:2$ (e) and $0:1$ (f)).

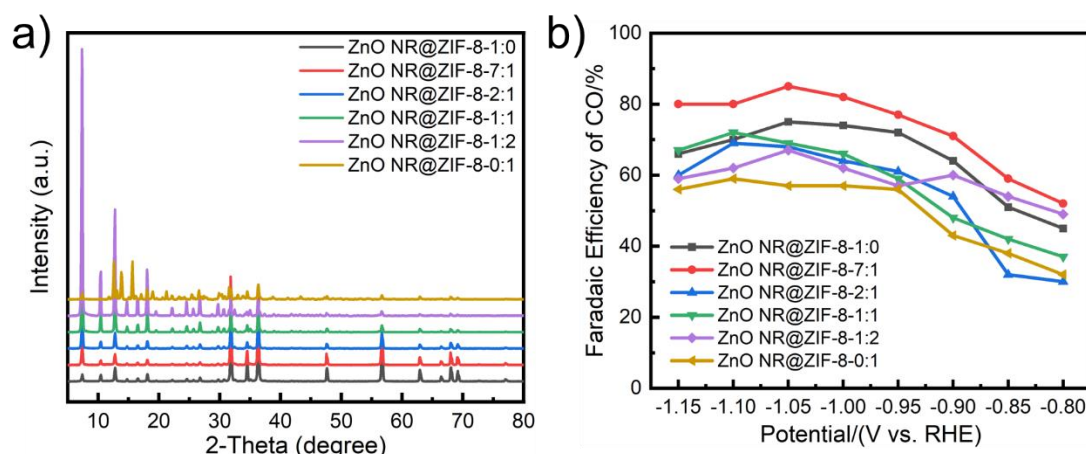


Figure 4.15. (a) XRD patterns of ZnO NR@ZIF-8-x. (b) FE of CO on ZnO NR@ZIF-8-x at different applied potentials.

In order to further improve the growth process of the ZIF-8 shell onto the ZnO NRs and better control the shell thickness, different solvent composition-dependent reactions were carried out (**Figures 4.14a-f**). When DMF was solely used as solvent (sample denoted as 1:0), only small proportion of ZnO NR were covered by the ZIF-8 shell. When H₂O was added into DMF with a certain ratio (i.e., DMF/H₂O = 7:1, 2:1, 1:1), ZIF-8 could grow on the surface of ZnO NRs showing a well-defined interface between ZnO and ZIF-8. XRD characterization confirmed the co-existence of ZnO and ZIF-8 structures in all this samples. When the H₂O content further increased (i.e., DMF/H₂O = 1:2 or 0:1), the ZnO nanorods were dissolved, and the samples only showed some freestanding ZIF-8 particles together with aggregates. The XRD pattern (**Figure 4.15a**) revealed that those spherical particles are not composed of ZIF-8. In addition, the CO selectivity (**Figure 4.15b**) obtained on different samples supported that the thickness of the ZIF-8 shell indeed influenced the eCO₂ RR performance, showing a maximum value for the ZnO NR@ZIF-8-7:1 sample.

4.4 Summary

In summary, the porous ZIF-8 shell grown on the surface of ZnO NRs could modify the microenvironment around the active sites and enhance the CO₂ RR. Thanks to this microenvironment at the interface between ZIF-8 and the ZnO surface, a faradaic

efficiency of CO (85 %) at -1.05 V vs. RHE could be obtained on the optimized electrocatalyst. The introduced ZIF-8 shell enabled a higher CO_2 concentration near the active interface and alleviated the water penetration to ZnO active sites. In addition, the highly porous structure strengthened an increase of the local pH at the interface between the ZIF-8 shell and the ZnO surface, which could furtherly enhance the catalytic selectivity and activity of CO_2 RR via suppressing the HER. This work provides valuable insights for the modification and enhancement of the microenvironment around the active sites for the CO_2 RR process, so as to improve the selectivity and activity of pristine catalysts.

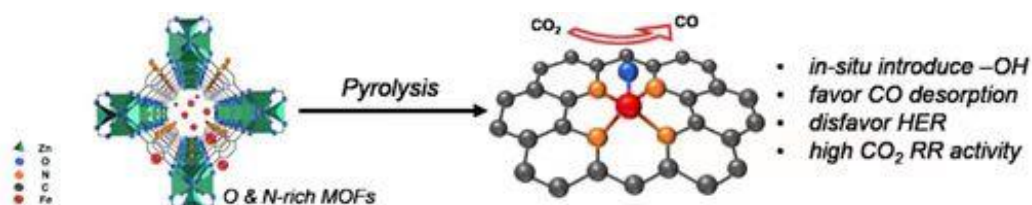
References

1. Li, L., Li, X., Sun, Y. & Xie, Y. Rational design of electrocatalytic carbon dioxide reduction for a zero-carbon network. *Chem. Soc. Rev.* **51**, 1234–1252 (2022).
2. Jin, S., Hao, Z., Zhang, K., Yan, Z. & Chen, J. Advances and Challenges for the Electrochemical Reduction of CO₂ to CO: From Fundamentals to Industrialization. *Angew. Chem. Int. Ed.* **60**, 20627–20648 (2021).
3. Qiao, J., Liu, Y., Hong, F. & Zhang, J. A review of catalysts for the electroreduction of carbon dioxide to produce low-carbon fuels. *Chem. Soc. Rev.* **43**, 631–675 (2013).
4. Zhang, T. *et al.* Quasi-double-star nickel and iron active sites for high-efficiency carbon dioxide electroreduction. *Energy Environ. Sci.* **14**, 4847–4857 (2021).
5. Zhang, T. *et al.* Site-Specific Axial Oxygen Coordinated FeN₄ Active Sites for Highly Selective Electroreduction of Carbon Dioxide. *Adv. Funct. Mater.* **32**, 2111446 (2022).
6. Shi, R. *et al.* Efficient wettability-controlled electroreduction of CO₂ to CO at Au/C interfaces. *Nat. Commun.* **11**, 3028 (2020).
7. Mu, S. *et al.* Molecular-Scale Insights into Electrochemical Reduction of CO₂ on Hydrophobically Modified Cu Surfaces. *ACS Appl. Mater. Interfaces* **13**, 47619–47628 (2021).
8. Li, J. *et al.* Efficient electrocatalytic CO₂ reduction on a three-phase interface. *Nat. Catal.* **1**, 592–600 (2018).
9. Chen, C., Li, Y. & Yang, P. Address the “alkalinity problem” in CO₂ electrolysis with catalyst design and translation. *Joule* **5**, 737–742 (2021).
10. Higgins, D., Hahn, C., Xiang, C., Jaramillo, T. F. & Weber, A. Z. Gas-Diffusion Electrodes for Carbon Dioxide Reduction: A New Paradigm. *ACS Energy Lett.* **4**, 317–324 (2019).
11. Kas, R. *et al.* Electrochemical CO₂ reduction on nanostructured metal electrodes: fact or defect? *Chem. Sci.* **11**, 1738–1749 (2020).
12. Weekes, D. M., Salvatore, D. A., Reyes, A., Huang, A. & Berlinguette, C. P. Electrolytic CO₂ Reduction in a Flow Cell. *Acc. Chem. Res.* **51**, 910–918 (2018).
13. Liu, M. *et al.* Enhanced electrocatalytic CO₂ reduction via field-induced reagent concentration. *Nature* **537**, 382–386 (2016).
14. Safaei, T. S. *et al.* High-Density Nanosharp Microstructures Enable Efficient CO₂ Electroreduction. *Nano Lett* **16**, 7224–7228 (2016).
15. Ge, W. *et al.* Dynamically Formed Surfactant Assembly at the Electrified Electrode–Electrolyte Interface Boosting CO₂ Electroreduction. *J. Am. Chem. Soc.* **144**, 6613–6622 (2022).
16. Yoon, Y., Hall, A. S. & Surendranath, Y. Tuning of Silver Catalyst Mesostructure Promotes Selective Carbon Dioxide Conversion into Fuels. *Angew. Chem. Int. Ed.* **55**, 15282–15286 (2016).
17. Hall, A. S., Yoon, Y., Wuttig, A. & Surendranath, Y. Mesostructure-Induced Selectivity in CO₂ Reduction Catalysis. *J. Am. Chem. Soc.* **137**, 14834–14837 (2015).
18. Nguyen, D. L. T. *et al.* Mass Transport Control by Surface Graphene Oxide for Selective CO Production from Electrochemical CO₂ Reduction. *ACS Catal.* **10**, 3222–3231 (2020).
19. Ma, M., Trześniewski, B. J., Xie, J. & Smith, W. A. Selective and Efficient Reduction of Carbon Dioxide to Carbon Monoxide on Oxide-Derived Nanostructured Silver Electrocatalysts. *Angew. Chem. Int. Ed.* **55**, 9748–9752 (2016).
20. Furukawa, H., Cordova, K. E., O’Keeffe, M. & Yaghi, O. M. The Chemistry and Applications of Metal-Organic Frameworks. *Science* **341**, 1230444 (2013).
21. Das, S. *et al.* Core–shell structured catalysts for thermocatalytic, photocatalytic, and electrocatalytic conversion of CO₂. *Chem. Soc. Rev.* **49**, 2937–3004 (2020).
22. Pipelzadeh, E., Rudolph, V., Hanson, G., Noble, C. & Wang, L. Photoreduction of CO₂ on ZIF-8/TiO₂ nanocomposites in a gaseous photoreactor under pressure swing. *Appl. Catal. B* **218**, 672–678 (2017).

23. Liu, Y. & Tang, Z. Multifunctional Nanoparticle@MOF Core–Shell Nanostructures. *Adv. Mater.* **25**, 5819–5825 (2013).
24. Dai, S., Tissot, A. & Serre, C. Recent Progresses in Metal–Organic Frameworks Based Core–shell Composites. *Adv. Energy Mater.* **12**, 2100061 (2022).
25. Lu, G. *et al.* Imparting functionality to a metal–organic framework material by controlled nanoparticle encapsulation. *Nat. Chem.* **4**, 310–316 (2012).
26. Young, C. *et al.* Controlled Chemical Vapor Deposition for Synthesis of Nanowire Arrays of Metal–Organic Frameworks and Their Thermal Conversion to Carbon/Metal Oxide Hybrid Materials. *Chem. Mater.* **30**, 3379–3386 (2018).
27. Zhan, W. *et al.* Semiconductor@Metal–Organic Framework Core–Shell Heterostructures: A Case of ZnO@ZIF-8 Nanorods with Selective Photoelectrochemical Response. *J. Am. Chem. Soc.* **135**, 1926–1933 (2013).
28. Kouser, S., Hezam, A., Khadri, M. J. N. & Khanum, S. A. A review on zeolite imidazole frameworks: synthesis, properties, and applications. *J. Porous Mater.* **29**, 663–681 (2022).
29. Park, K. S. *et al.* Exceptional chemical and thermal stability of zeolitic imidazolate frameworks. *PNAS* **103**, 10186–10191 (2006).
30. Luo, H., Li, B., Ma, J. & Cheng, P. Surface Modification of Nano-Cu₂O for Controlling CO₂ Electrochemical Reduction to Ethylene and Syngas. *Angew. Chem. Int. Ed.* **61**, e202116736 (2022).
31. Geng, Z. *et al.* Oxygen Vacancies in ZnO Nanosheets Enhance CO₂ Electrochemical Reduction to CO. *Angew. Chem. Int. Ed.* **57**, 6054–6059 (2018).
32. Dou, S. *et al.* Boosting Electrochemical CO₂ Reduction on Metal–Organic Frameworks via Ligand Doping. *Angew. Chem. Int. Ed.* **58**, 4041–4045 (2019).

Chapter 5

Site-Specific Axial Oxygen Coordinated FeN₄ Active Sites for Highly Selective Electroreduction of Carbon Dioxide



An atomically dispersed FeN₄ catalyst functionalized with an axial bonded O-containing coordination has been constructed via utilizing an oxygen and nitrogen-rich MOF (IRMOF-3) as the precursor. The obtained FeN₄-O active site exhibits an enhanced FE_{CO} (95 %) at -0.50 V vs. RHE, which is higher than that of the reported unmodified FeN₄ sites and even higher than many other state-of-the-art single atom catalysts (SACs). Transmission electron microscopy (TEM) and X-ray absorption spectroscopy (XAS) characterized the active sites local environment. Both experimental and theoretical results further proved that rationally engineering the coordination environment of FeN₄ via hydroxide subgroups can effectively boost the CO₂ RR activity through reducing the binding energies of CO desorption and disfavoring the hydrogen evolution reaction (HER).

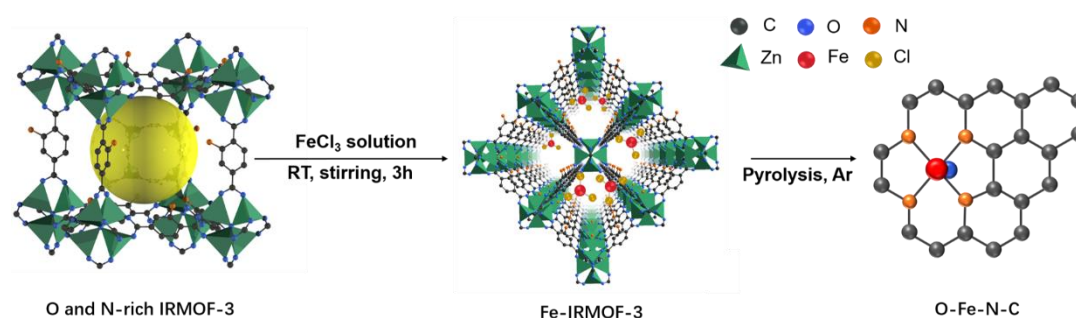
5.1 Introduction

The electrochemical CO₂ reduction reaction (CO₂ RR) into carbon-based fuels is an attractive strategy for utilizing CO₂ from large emission sources. In order to realize the anthropogenic carbon cycle, the electrocatalytic reduction of CO₂ to fuels can be powered by a renewable electricity source. After years of efforts to explore, CO serving as a product of CO₂ RR, which represents a crucial raw product in Fischer-Tropsch process for the production of value-added chemical feedstocks, is considered as a promising route for energy conversion and carbon recycling.¹⁻⁶ However, the inertness of the CO₂ molecule and the competitive hydrogen evolution reaction (HER) greatly limit the conversion efficiency towards a practical implementation.⁷⁻⁹

Atomically dispersed transition metals embedded in nitrogen-doped carbon matrices (M-N-C) have recently appeared at the forefront of CO₂ RR towards CO because of their feasible preparation, optimized atomic utilization and chemical stability.¹⁰⁻¹⁴ Based on previous studies, the four-coordinated M-N₄ moieties are considered as the main active centers in common M-N-C.^{15,16} However, the high structure/electron symmetry of the M-N₄ moiety, which results from the symmetrical planar structure, makes it chemically inert to a certain extent.¹⁷ Recently, the performance of M-N₄ moiety for CO₂ RR has been significantly improved through the introduction of an additional axial N ligand.¹⁸⁻²⁰ Such coordination can break the symmetrical electronic structure of M-N₄ and subsequently affect the binding energies for CO₂ RR intermediates (e.g., *COOH and *CO), which confirmed the key role of axial coordination.²¹ Inspired by this, it is anticipated that the catalytic activity of M-N₄ can be further boosted by introducing high-electronegativity atoms, such as O, in the axial direction. The high electronegativity of oxygen will not only break the electron symmetry, but also improve the strength of the electronic metal-support interaction (EMSI) in M-N₄ sites.²¹⁻²³ Unfortunately, the coordination configuration of oxygen atoms is difficult to be controlled accurately via traditional calcination methods. The type of oxygen will change and eventually disappear when the calcination temperature is above 500 °C,

which as a consequence hinders the successful coordination of O atoms with the metal site.²² Therefore, developing an effective method to realize the control on O atoms coordination, especially along the axial direction is highly desirable.

Metal-organic frameworks (MOFs), one embodiment of reticular chemistry, consisted on metal and organic ligands, are one type of ideal templates for the targeted creation of MN_4 sites.²⁴⁻²⁸ More importantly, the coordination of heteroatoms (e.g.: O, S, P, etc.) can be easily achieved after pyrolysis via the rational design of organic linkers with functional groups.²⁵ Herein, we propose a facile strategy, which uses an O- and N-rich isoreticular metal-organic framework-3 (IRMOF-3) for constructing an axial O coordination to the FeN_4 active sites. In comparison with FeN_4 structure, the as-prepared axial O coordinated FeN_4 (denoted as O-Fe-N-C) active sites showed an excellent CO_2 RR activity in 0.5 M $NaHCO_3$ solution, including a high Faradaic efficiency of CO (95 %) at -0.50 V vs. RHE, and a robust stability for 30 h. Such performance is superior to those of the previously reported Fe-N-C-based materials and comparable to the reported state-of-the-art single atom catalysts (SACs) even at a lower overpotential. Density functional theory (DFT) calculations revealed that the formed O-Fe-N-C not only facilitates CO desorption, but also limits the undesired HER. This work opens a new way of utilizing heteroatom-rich MOFs as an enabler to the rational design and development of high-efficient catalysts.



Schematic 5.1 Schematic illustration of the synthesis of O-Fe-N-C.

The synthesis steps for O-Fe-N-C were schematically displayed in **Figure 5.1**. In brief, the Fe-IRMOF-3 was firstly prepared by adding Iron salt into IRMOF-3. Afterwards, the

O-Fe-N-C was obtained through pyrolysis of the Fe-IRMOF-3 under argon atmosphere. A reference Fe-N-C sample without O coordination, was also synthesized through pyrolysis of Fe-ZIF-8 precursor prepared by adding FeCl₃ into N-rich ZIF-8. Meanwhile, a N-C catalyst was prepared by direct pyrolysis of IRMOF-3. The detailed synthesis information is shown in **Section 5.2**.

5.2 Experimental Section

5.2.1 Materials and Methods

Materials: If not specified, all chemical reagents were purchased from Sigma-Aldrich. Zinc nitrate hexahydrate (Zn(NO₃)₂·6H₂O), 2-aminoterphthalic acid, iron chloride hexahydrate (FeCl₃·6H₂O), 2-methylimidazole (2-mim), N,N-dimethylformamide (DMF), ethanol and sodium bicarbonate (NaHCO₃) were all of analytical grade and used as received without further purification. Meanwhile, all solutions were prepared with Milli-Q water (DI-H₂O, Ricca Chemical, ASTM Type I). The Nafion (N-117 membrane, 0.18 mm thick) was purchased from Alfa Aesar and kept in 0.5 M NaOH solution. The carbon paper was also purchased from Alfa Aesar.

Characterization: The X-ray diffraction patterns (XRD) were obtained through a Bruker D4 X-ray powder diffractometer using Cu K α radiation (1.54184 Å). Field emission scanning electron microscopy (FESEM) images were collected on a FEI Magellan 400 L scanning electron microscope. The transmission electron microscopy (TEM) and high angle annular dark field scanning TEM (HAADF-STEM) images were obtained in a Tecnai F20 field emission gun microscope with a 0.19 nm point-to-point resolution at 200 kV equipped with an embedded Quantum Gatan Image Filter for EELS analyses. Images have been analyzed by means of Gatan Digital Micrograph software. Parts of HAADF-STEM images and elemental mapping (EDX) were obtained in a spherical aberration-corrected (AC) transmission electron microscope FEI Themis Z and operated at 200 kV. X-ray photoelectron spectroscopy (XPS) was performed on a Phoibos 150 analyser (SPECS GmbH, Berlin, Germany) in ultra-high vacuum conditions

(base pressure 4×10^{-10} mbar) with a monochromatic aluminum K α X-ray source (1486.74 eV). Binding energies (BE) were determined using the C 1s peak at 284.5 eV as a charge reference. Raman spectra were obtained using Senterra.

5.2.2 Synthesis Methods

5.2.2.1 Preparation of IRMOF-3

The fabrication process of IRMOF-3 is according to previous report with minor modification.²⁹ Typically, 932 mg of $\text{Zn}(\text{NO}_3)_2 \cdot 6\text{H}_2\text{O}$ was dissolved in 100 mL DMF under magnetic stirring at room temperature to form a homogeneous solution. Then, 181 mg of 2-aminoterphthalic acid were added into the above mixture under ultrasonic until the formation of clear solution. The obtained homogeneous solution was transferred into the Teflon-lined stainless-steel autoclave and reacted at 100 °C for 24 h. After cooling to room temperature, the powder was collected by centrifugation, washed with ethanol and DMF several times to remove organic residual. The final products were then dried in vacuum at 65 °C for 4 h.

5.2.2.2 Preparation of ZIF-8

The fabrication of ZIF-8 is similar to the published report.³⁰ Typically, 1.115 g of $\text{Zn}(\text{NO}_3)_2 \cdot 6\text{H}_2\text{O}$ was dissolved in 50 mL methanol under magnetic stirring at room temperature to form a homogeneous solution. Then, 50 mL methanolic solution containing 1.232 g of 2-mim were added into the above mixture under ultrasonic until the formation of clear solution. The obtained homogeneous solution reacted at room temperature for 24 h without stirring. Then, the white powder was collected by centrifugation, washed with methanol several times to remove organic residual. The final products were then dried in vacuum at 60 °C overnight.

5.2.2.3 Preparation of Fe-IRMOF-3 and Fe-ZIF-8

In this procedure, the 100 mg of IRMOF-3 powder was dispersed in 10 mL DMF under

ultrasound for 10 min at room temperature. After forming a homogeneous solution, $\text{FeCl}_3 \cdot 6\text{H}_2\text{O}$ aqueous solution (10 mg/mL, 20 μL) was dropwise injected into the above solution under ultrasound for 5 min at room temperature. Next, the mixed solution was under magnetic stirring at room temperature for 3 h. After reacting, the powder was collected by centrifugation, washed with ethanol and DMF several times to remove organic residual and dried in vacuum at 65 $^{\circ}\text{C}$ for 6 h. Then, we obtained the Fe-IRMOF-3. Similarly, Fe-ZIF-8 was prepared by replacing IRMOF-3 with ZIF-8.

5.2.2.4 Preparation of Disperse Fe-N-C (denoted as O-Fe-N-C and Fe-N-C)

As-prepared Fe-IRMOF-3 (or Fe-ZIF-8, or IRMOF-3) powders were put at the porcelain boat. Subsequently, the samples were placed in a tube furnace and heated at 950 $^{\circ}\text{C}$ for 2 h with heating rate of 5 $^{\circ}\text{C}/\text{min}$ under an Ar atmosphere to yield disperse O-Fe-N-C (or Fe-N-C, or N-C).

5.2.2.5 Preparation of O-Fe-N-C-Acid

In order to remove the Fe nanoparticle in O-Fe-N-C, we treated the O-Fe-N-C sample using 1 M H_2SO_4 for 48 h. After acid process, the powder was collected by centrifugation, washed with DI- H_2O and dried in vacuum at 60 $^{\circ}\text{C}$ overnight. Then, we obtained the O-Fe-N-C-Acid.

5.2.3 Preparation of working electrodes

The detailed information is shown in **Chapter 2**. In this chapter, the catalyst loading mass used was equivalent to $\sim 1 \text{ mg}/\text{cm}^2$.

5.2.4 Electrochemical Measurement

The detailed information is shown in **Chapter 2**.

5.2.5 Calculation Method

The detailed information is shown in **Chapter 2**.

The mass activity (A/g) is calculated from the mass loading density (m) of catalyst (1.0 mg cm⁻²) and the measured partial current density j (mA/cm²) at -0.50 V vs. RHE.

$$\text{mass activity} = j_{\text{CO}}/m \quad (5.1)$$

5.2.6 XAFS Measurements:

The X-ray absorption fine structure spectra (Fe K-edge) were collected at 1W1B station in Beijing Synchrotron Radiation Facility (BSRF). The storage rings of BSRF were operated at 2.5 GeV with an average current of 250 mA. Using Si (111) double-crystal monochromator, the data collection was carried out in transmission/fluorescence mode using ionization chamber. All spectra were collected in ambient conditions.

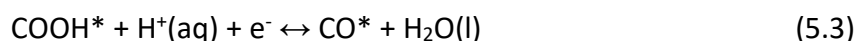
5.2.7 XAFS Analysis and Results:

The acquired EXAFS data was processed according to the standard procedures using the ATHENA module implemented in the IFEFFIT software packages. The k^3 -weighted EXAFS spectra were obtained by subtracting the post-edge background from the overall absorption and then normalizing with respect to the edge-jump step. Subsequently, k^3 -weighted $\chi(k)$ data of Fe K-edge were Fourier transformed to real (R) space using a hanning window ($dk=1.0 \text{ \AA}^{-1}$) to separate the EXAFS contributions from different coordination shells. To obtain the quantitative structural parameters around central atoms, least-squares curve parameter fitting was performed using the ARTEMIS module of IFEFFIT software packages.³¹⁻³³

5.2.8 DFT Calculations

The spin-polarized DFT calculations with projector augmented wave (PAW) method³⁴⁻³⁷ were performed using the Vienna Ab initio Simulation Package (VASP) code.³⁸ The Bayesian error estimation functional with van der Waals correlation (BEEF-vdW) was

employed to set the plane wave basis.³⁹ The convergence criteria was 0.05 eV/ Å in force and 1×10^{-4} eV in energy and the plane wave cutoff was 500 eV. The Monkhorst–Pack mesh k-point grids was $2 \times 2 \times 1$ for all models. All the vacuum thicknesses were higher than 15 Å. With the BEEF-vdW function, the energy of the gas phase molecules gave a systematic correction by +0.41 and +0.09 eV for gaseous CO₂ and H₂, respectively.^{40–42} For the electroreduction of CO₂ to CO, the following elementary steps were considered:



where (g), (aq) represent the gaseous phase and aqueous phase, respectively. The *, COOH* and CO* represent free site, adsorption state of COOH and CO, respectively. The reaction free energies of each steps were calculated by using the following formula:

$$G = E_{\text{DFT}} + E_{\text{ZPE}} + \int C_p dT - TS + E_{\text{sol}} \quad (5.5)$$

Where E_{DFT} is the DFT calculated energy, E_{ZPE} is the zero-point energy, C_p is the constant pressure heat capacity, T is temperture, S is the entropy and E_{sol} is solvation correction and for CO* was stabilized by 0.1 eV and COOH* by 0.25 eV.⁴³ The temperature of the reaction is 298.15 K. The free energy corrections for each species are shown in **Table 5.1**.⁴⁴

Table 5.1. Parameters used for the free energy corrections. T = 298.15 K.

Species	ZPE (eV)	$\int C_p dT$ (eV)	-TS (eV)
H ₂	0.28	0.09	-0.40
CO ₂	0.31	0.11	-0.66
CO	0.13	0.09	-0.61
H ₂ O	0.58	0.10	-0.67
H*	0.19	0.01	-0.01
CO*	0.22	0.08	-0.16
COOH*	0.62	0.10	-0.19

5.3 Results and Discussion

5.3.1 Sample Characterization

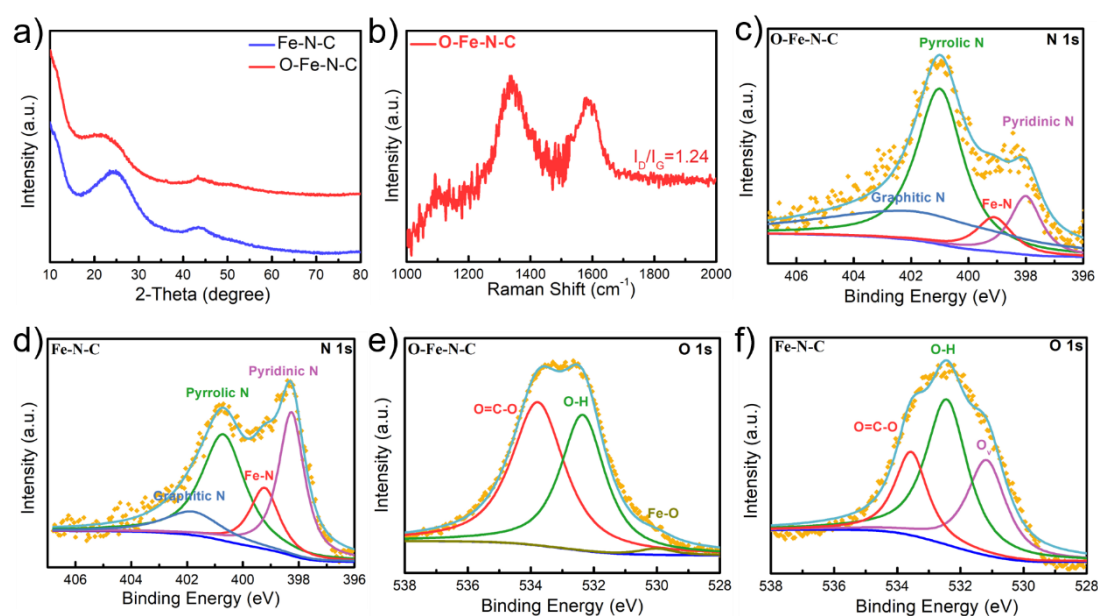


Figure 5.2. (a) XRD patterns of O-Fe-N-C and Fe-N-C samples. (b) Raman spectra of O-Fe-N-C. (c and d) High-resolution XPS N 1s spectrum, as well as (e and f) O 1s spectrum of O-Fe-N-C and Fe-N-C samples.

As shown in **Figure 5.2a**, two main peaks at around 25° and 43°, which belong to the (002) and (100) planes of graphitic carbon, were observed in O-Fe-N-C samples, indicating the successful conversion of MOFs into carbon-based materials without the

metal, metal oxide or metal carbide impurity structures.^{45,46} Similar results were also observed on the XRD patterns of Fe-N-C sample. The Raman spectra of O-Fe-N-C samples, featuring peaks at around 1365 cm^{-1} (D band) and 1590 cm^{-1} (G band), further confirmed the structure of graphitic carbon (**Figure 5.2b**).^{47,48} X-ray photoelectron spectroscopy (XPS) analysis was performed to investigate the chemical composition and elemental states of different samples. The high-resolution N 1s spectra obtained on both the O-Fe-N-C and Fe-N-C samples demonstrate the presence of pyridinic (398.6 eV), pyrrolic (401 eV), graphitic (402 eV), and Fe-N_x (399.4 eV) species (**Figures 5.2c-d**).^{23,46} In contrast to Fe-N-C (**Figures 5.2e**), an additional peak at 530 eV, corresponding to the Fe-O bond, was observed on sample O-Fe-N-C (**Figure 5.2f**), which indicated that the Fe-O chelation in O-Fe-N-C sample was retained after calcination.^{22,23,49}

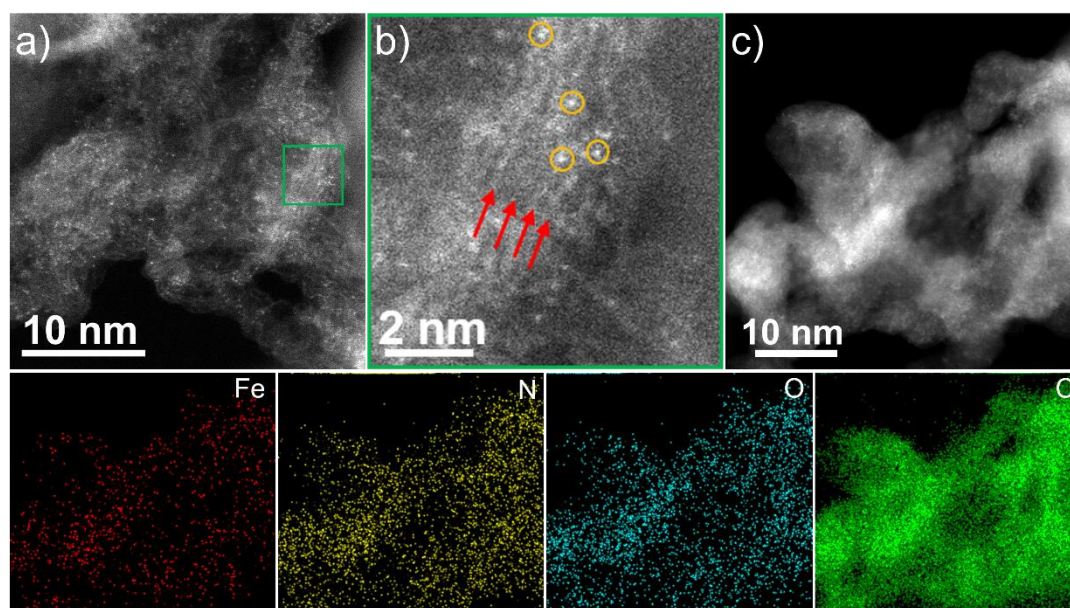


Figure 5.3 (a) HAADF-STEM image of O-Fe-N-C. The yellow circle is highlighting the presence of only one Fe cluster in the large area examined. The inset is an atomic resolution aberration-corrected HAADF STEM image obtained on a representative region of the O-Fe-N-C catalyst. (b) Magnified detail from (a) where the graphitic (001) planes can be observed (red arrows). Notice that dispersed Fe atoms (some of the highlighted with orange circles) are placed along the graphitic structures. (c) HAADF STEM image and (middle panel) representative EDS chemical composition maps in a selected region of the O-Fe-N-C sample.

The O-Fe-N-C sample was further characterized by aberration corrected (AC) high-

angle annular dark-field scanning transmission electron microscopy (HAADF STEM). Multiple areas of the O-Fe-N-C sample were examined and only few Fe nanoparticles could be observed (**Figure 5.3a**). Furthermore, AC HAADF STEM was employed for directly detecting the single Fe atoms distribution thanks to the different Z contrast among Fe, N, O and C elements. The representative HAADF STEM images showed isolated starry spots densely planted in the graphitic structure, which confirmed that Fe was atomically dispersed in the O-Fe-N-C sample (**Figure 5.3a inset-b**). Notice that the graphitic structure showed the typical (001) basal planes, which bend forming layered structures. In addition, the Fe atoms were mainly placed along these basal planes in a perfect single metal atom distribution (see in **Figure 5b** the red arrows pointing to the C-graphitic (001) planes, while the orange circles highlight the presence of single Fe atoms). EDS analyses revealed that Fe, N, O and C were homogeneously dispersed on the O-Fe-N-C sample (**Figure 5.3c** and middle panel in **Figure 5.3**). As a comparison, the morphology, elemental distribution and structural HAADF STEM characterization of Fe-N-C and N-C samples is shown in **Figure 5.4**.

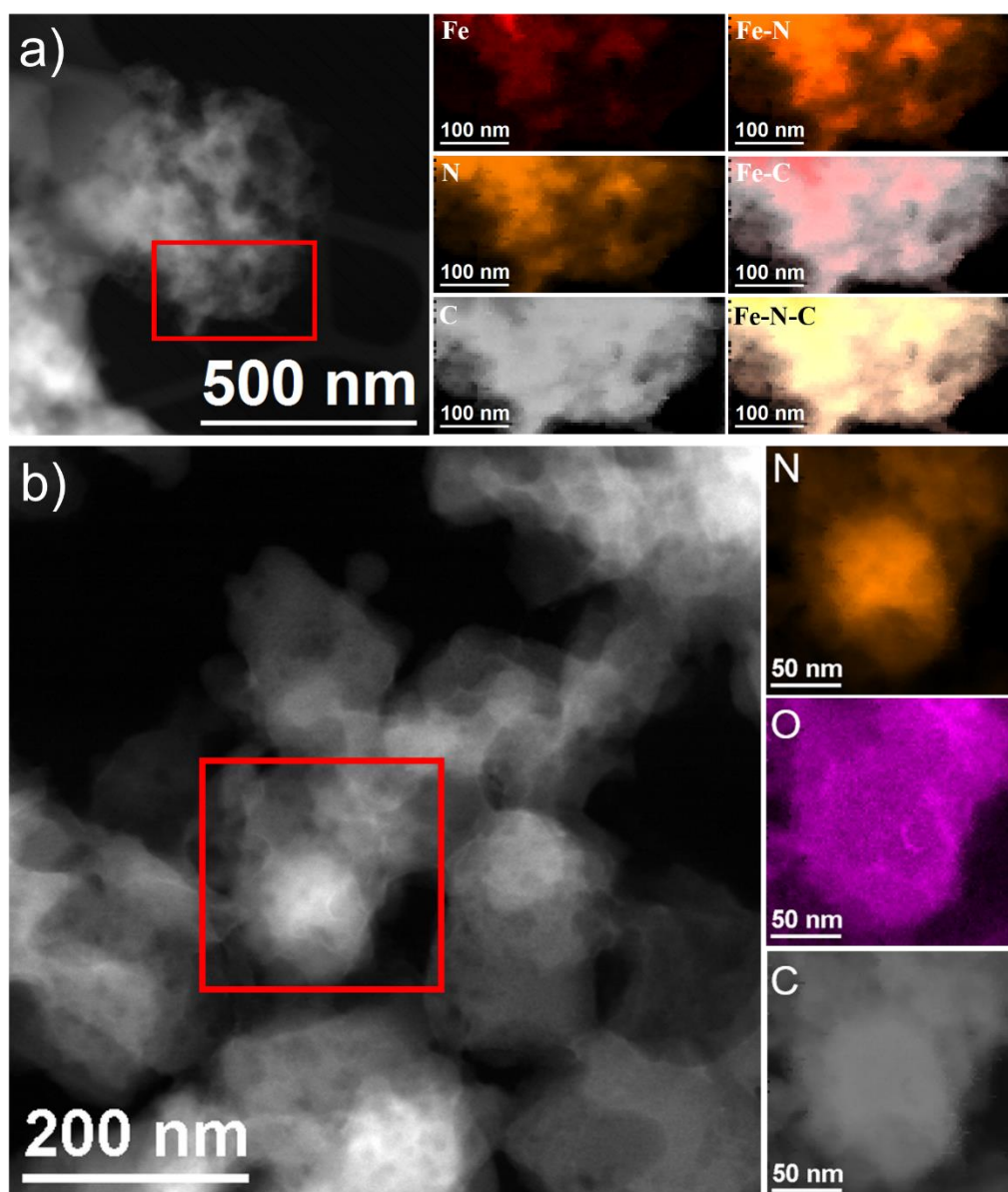


Figure 5.4. (a) HAADF-STEM image of Fe-N-C and representative EELS chemical composition maps obtained from the red squared area of the STEM micrograph. Individual Fe $L_{2,3}$ -edges at 708 eV (red), N K-edges at 401 eV (orange) and C K-edges at 285 eV (grey) as well as composites of Fe-N and Fe-C. (b) HAADF-STEM image of N-C and representative EELS chemical composition maps obtained from the red squared area of the STEM micrograph. Individual N K-edges at 401 eV (orange), O K-edges at 532 eV (blue) and C K-edges at 285 eV (grey).

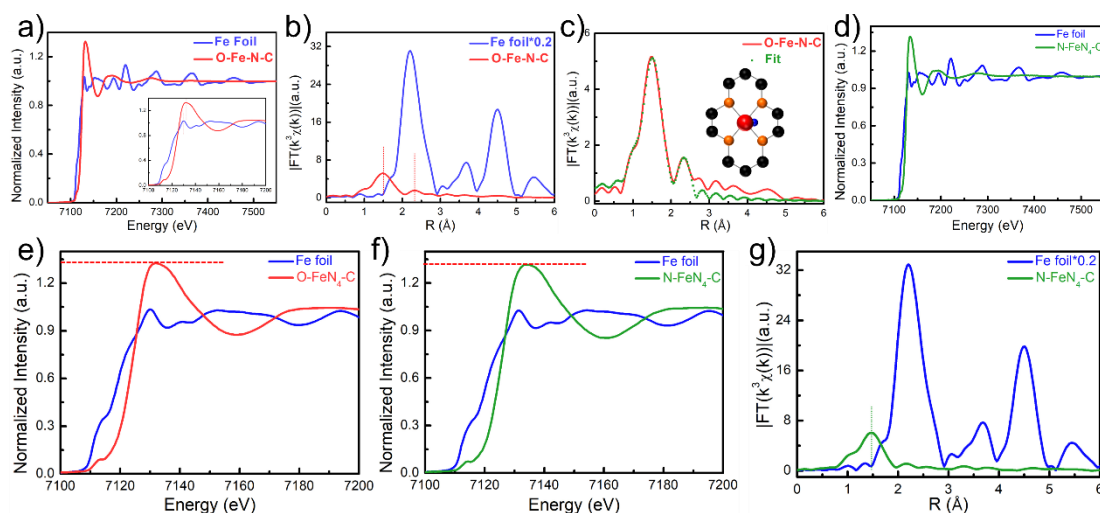


Figure 5.5. XANES spectra of (a) Fe K-edge XANES spectra, (b) Fourier transformation of the EXAFS spectra at R space. (c) Corresponding EXAFS fitting curves for the O-Fe-N-C sample (Fe, O, N, C atoms are represented in red, blue, orange and black, respectively). XANES spectra of (d) N-FeN₄-C at Fe K-edge. (e and f) The enlarged images of corresponding regions of (a and d). Fourier transformation of the EXAFS spectra at R space of the (g) N-FeN₄-C.

The detailed local chemical environment and electronic states of the Fe atoms in the catalysts was further disclosed via XAS analyses. Fe K-edge X-ray absorption near edge structure (XANES) spectra of O-Fe-N-C sample shifts towards higher binding energy compared to that of a standard Fe foil (**Figure 5.5a**), suggesting a positive charge state of Fe atoms in the O-Fe-N-C catalyst.^{50,51} Furthermore, the intrinsic structure of the reactive sites was corroborated by the Fourier transformed (FT) k^3 -weighted $\chi(k)$ -function of the Fe K-edge EXAFS in R space (**Figure 5.5b**). The dominant peak centered at around 1.5 Å for O-Fe-N-C sample was attributed to the light backscattering induced by light atoms (N, O or C) situated in the first coordination shell of the absorbing metal. The slight presence of a peak at ~2.27 Å, corresponding to the Fe-Fe bond, confirmed a co-existence of the atomically isolated Fe dispersion with a modicum presence of Fe nanoparticles, in accordance with the HAADF STEM results.^{14,47} The Fe K-edge EXAFS spectra were then fitted with the model structures depicted in the insets of **Figure 5.5c**. The structural parameters obtained from the fittings are shown in **Table 5.2**, including the coordination number (CN) and different bond distances. The optimized fitting results for O-Fe-N-C sample showed a CN-value of 5.1 and a mean bond length of 2.02

Å. Therefore, there are 5 coordination atoms around the Fe atoms in O-Fe-N-C sample, which differs from the previous reported M-N₄ sites derived from ZIF-8.^{8,52-56} Experimentally and theoretically, metal-nitrogen bonds are more likely than metal-carbon or metal-oxygen ones to form in-plane FeN₄ sites in the first coordination sphere.^{17,57} The higher average CN-value of 5 for Fe-N₄ catalysts strongly suggests that one axial O atom is coordinated in the axial direction of the FeN₄ moieties, resulting in coordinatively saturated iron cations, in line with the high oxophilicity of Fe.^{49,57,58} In this way, all the results obtained on the O-Fe-N-C sample revealed the presence of four in-plane nitrogen atoms and one oxygen atom as an axial coordination. In addition, we carried out more comparison synchrotron data to determine the structure of axial O coordinated FeN₄, including the -N-FeN₄-C, -O-FeN₄-C (O-Fe-N-C in our work). **Figure 5.5d** showed the Fe K-edge X-ray absorption near-edge structure (XANES) profiles for -N-FeN₄-C and Fe foil. -N-FeN₄-C exhibited similar energy absorption edge profiles in the energy range between 7120 and 7140 eV, indicating that the Fe atoms carried positive charges and could have been stabilized by N atoms in both samples.^{47,59} In the pre-edge region (**Figure 5.5e-f**), a weak peak at approximately 7113 eV was found in both samples, which was assigned to the 1s → 3d transition along with simultaneous charge transfer of ligand-to-metal, indicating that the dominant coordinated geometry around Fe was close to a square structure in the first coordination sphere.^{47,60,61} Interestingly, -O-FeN₄-C showed a higher intensity than -N-FeN₄-C, implying that the presence of O increased the oxidation state of Fe in -O-FeN₄-C, which could be explained by the electronegative difference between an axial O or N coordinated with Fe.^{22,62} Further local structural information was obtained from Fourier transformations-extended X-ray absorption fine structure (FT-EXAFS) on Fe-N-C catalyst, as shown in **Figure 5.5g**. Both -O-FeN₄-C and -N-FeN₄-C showed their main peak at ~1.5 Å, confirming that most of the Fe was present as atomically dispersed sites in both samples. However, compared to the position of the peak of Fe-N/O (1.5 Å) in -O-FeN₄-C, the peak of Fe-N in -N-FeN₄-C decreased to 1.48 Å, suggesting that the bond length of the coordination atoms around Fe had changed due to the presence of

a different axial coordination atom (O or N).^{22,49,57,58}

Table 5.2. EXAFS fitting parameters at the Fe K-edge for various samples

Sample	Shell	N ^a	R (Å) ^b	σ^2 (Å ² ·10 ⁻³) ^c	ΔE_0 (eV) ^d	R factor (%)
O-Fe-N-C	Fe-N(O)	5.1	2.02	9.8	0.2	0.8
	Fe-Fe	0.4	2.54	4.9	0.6	

^a N: coordination numbers; ^b R: bond distance; ^c σ^2 : Debye-Waller factors; ^d ΔE_0 : the inner potential correction. R factor: goodness of fit. S02 were set as 0.85/0.90 for Fe-N/Fe-Fe, which were obtained from the experimental EXAFS fit of reference FePc/Fefoil by fixing CN as the known crystallographic value and was fixed to all the samples.

5.3.2 Electrochemical Performance

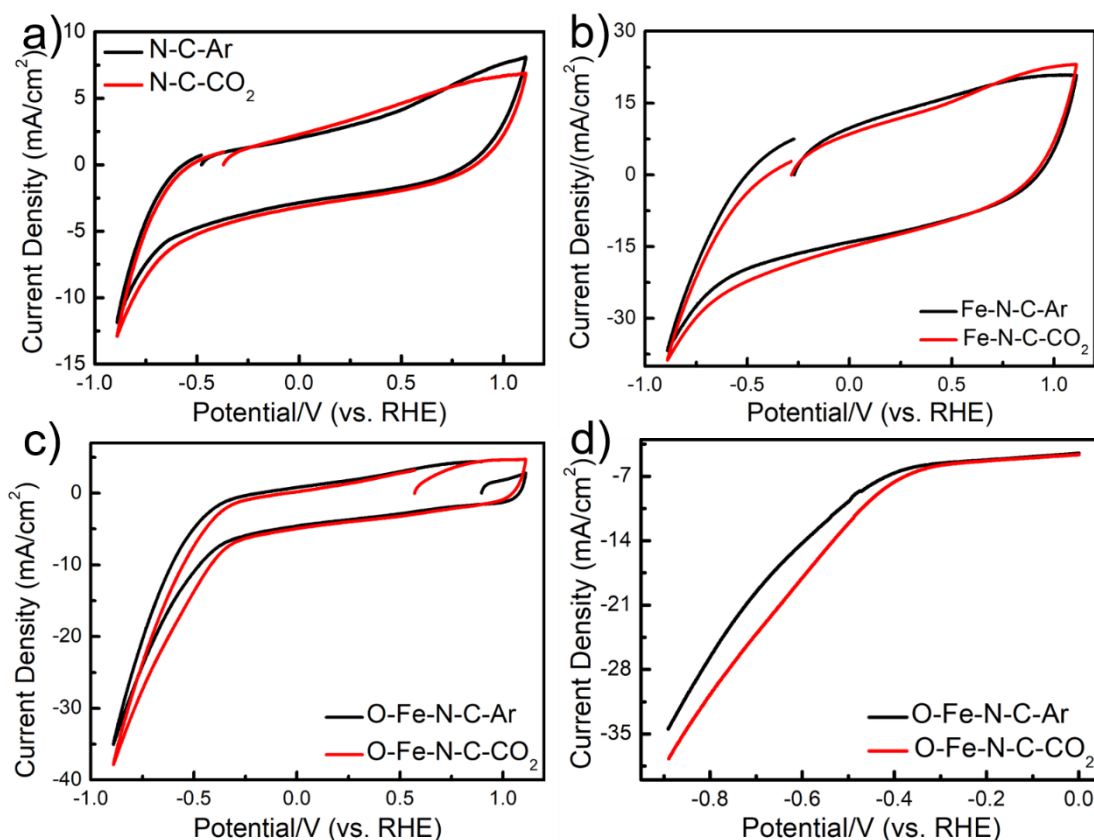


Figure 5.6. Cyclic voltammograms curves vs. RHE of (a) N-C, (b) Fe-N-C and (c) O-Fe-N-C obtained in Ar or CO₂-saturated 0.5 M NaHCO₃ solution. (d) is the LSV comparison for O-Fe-N-C in Ar-and CO₂-saturated 0.5 M NaHCO₃ solution.

The catalytic performance of the different samples was systematically studied in 0.5 M NaHCO₃. Firstly, the cyclic voltammetry (CV) curves were carried out to roughly

evaluate the electrocatalytic CO₂ RR performance. As shown in **Figure 5.6**, upon saturating the solution with CO₂, the increased reduction current on all samples suggested an efficient catalytic performance towards CO₂ RR.

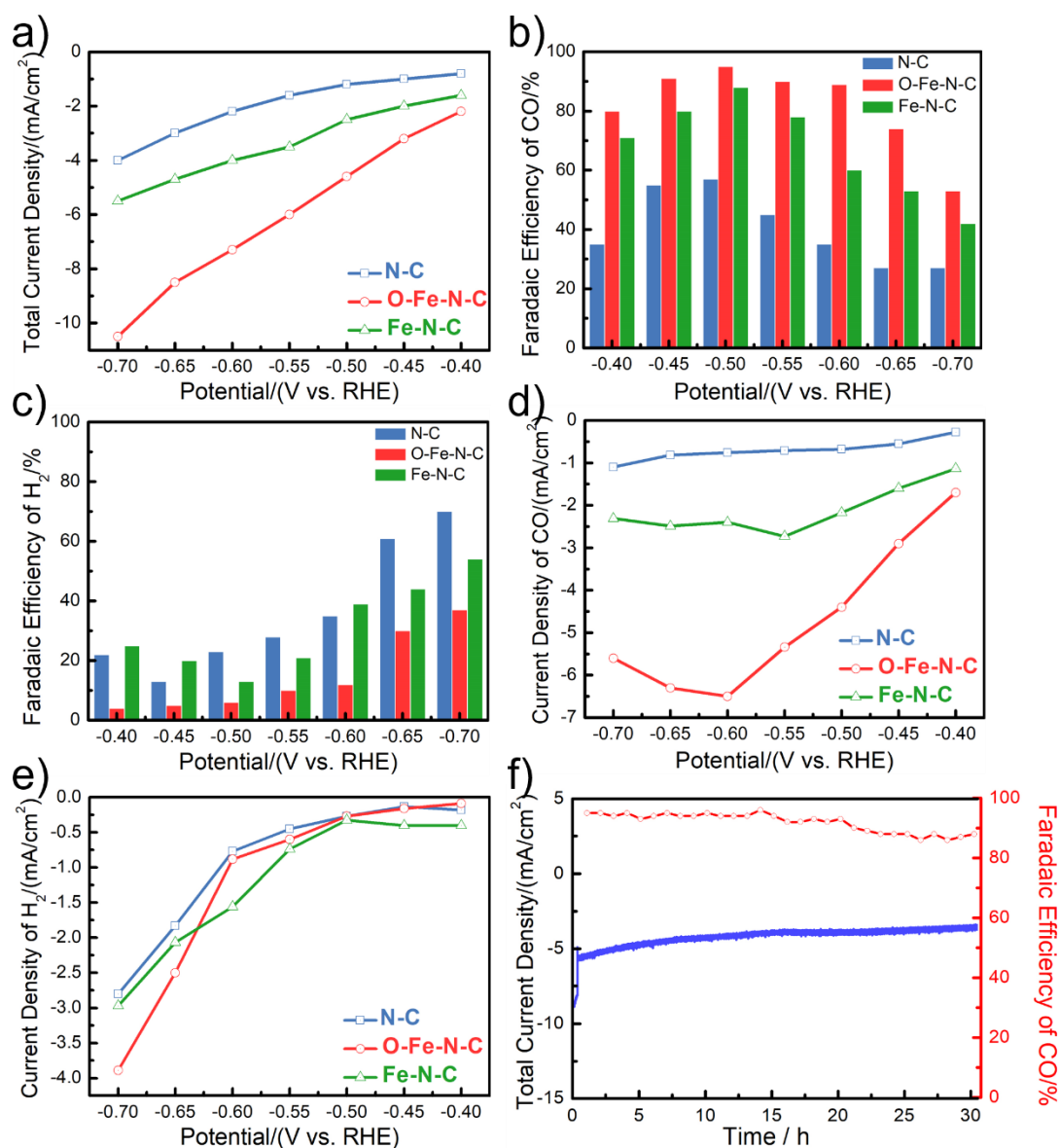


Figure 5.7. (a) Total current density, (b) FE of CO at various potentials, (c) current density for CO production, (d) FE of H₂ at various potentials, (e) current density for H₂ production on N-C, O-Fe-N-C and Fe-N-C. (f) Stability test of O-Fe-N-C at -0.50 V vs. RHE.

Compared to N-C without Fe atoms, the total current densities of O-Fe-N-C and Fe-N-C increased significantly at a wide range of applied potentials, indicating the crucial role of the Fe metal center in CO₂ RR (**Figure 5.7a**).⁶³ As expected, the best FE towards

CO in a potential range from -0.40 to -0.70 V vs. RHE was obtained for O-Fe-N-C, reaching the maximum FE (CO) of 95 % at -0.50 V vs. RHE (**Figure 5.7b**), which is superior to those of previously reported Fe-N-C-based catalysts and comparable to the state-of-the-art SACs, but even at lower overpotential (**Table 5.3**). The decreasing trend of FE (CO) for all samples as the potential shifted to more negative values mainly stems from the dominance of the H_2 evolution over the CO_2 RR (**Figure 5.7c**). The sums of FE for CO and H_2 are approximately 100 % for all samples, which indicates that no other products were produced. The potential-dependent CO/ H_2 partial current densities were also calculated based on the total current densities and the corresponding FE (CO) and FE (H_2) (**Figure 5.7d-e**). A long-term stability test for the O-Fe-N-C electrocatalyst was performed for 30 h at a constant -0.50 V vs. RHE cathode potential. The outlet gases were analyzed every 1 h by GC for calculating the corresponding FE of CO. The current density of O-Fe-N-C maintained a steady value of approximately -4.5 mA cm^{-2} with no significant decay (**Figure 5.7f**) during the 30-h test. The corresponding FE of CO decreased slightly to 88 % after 30 h stability test and no liquid product was detected by ^1H nuclear magnetic resonance (^1H -NMR) spectroscopy (**Figure 5.8**).

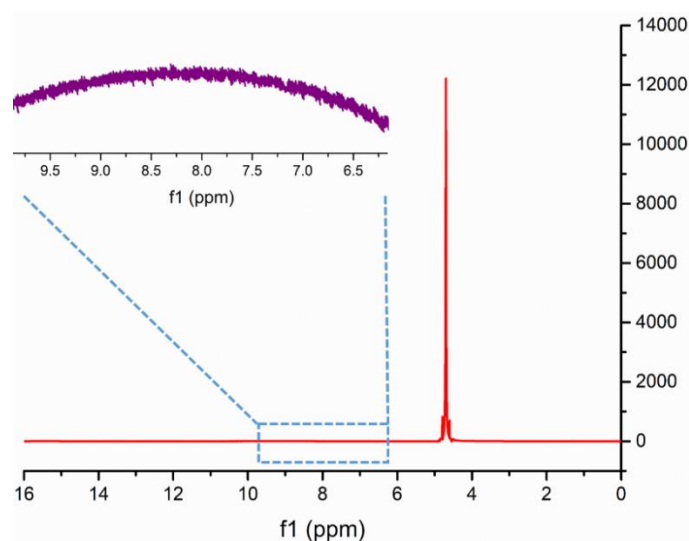


Figure 5.8. The representative ^1H -NMR spectra of the electrolyte after electrolysis of -0.50 V for O-Fe-N-C in CO_2 -saturated 0.5 M NaHCO_3 electrolyte for 30 h.

Table 5.3. Faradaic Efficiency (CO) of the reported single atom electrocatalysts for CO₂ electroreduction.

Catalyst	Product	FE(CO)	Potential	Reference
Fe ³⁺ @NG	CO	85 %	−0.68 V vs. RHE	64
Fe-N-C	CO	81 %	−0.57 V vs. RHE	14
Fe-N-C	CO	80 %	−0.50 V vs. RHE	65
Fe-N-PC	CO	90 %	−0.49 V vs. RHE	66
Fe ³⁺ -N-C	CO	90 %	−0.47 V vs. RHE	67
NPPCN	CO	95.9 %	−0.70 V vs. RHE	68
Fe-N-C	CO	95 %	−0.64 V vs. RHE	69
Fe/NCS	CO	87 %	−0.45 V vs. RHE	70
Fe-N-C	CO	93 %	−0.58 V vs. RHE	15
Fe-N-C	CO	86.9 %	−0.47 V vs. RHE	71
Bi SAC/NC	CO	97 %	−0.50 V vs. RHE	72
Ni-N-C	CO	71.9 %	−0.90 V vs. RHE	8
Ni-N-C	CO	98 %	−0.80 V vs. RHE	73
Ni-N-C	CO	98 %	−1.03 V vs. RHE	74
Co-N-C	CO	94 %	−0.775 V vs. RHE	75
Co-N ₅ /HNPCs	CO	99.4 %	−0.80 V vs. RHE	19
Co-N-C	CO	91 %	−0.60 V vs. RHE	76
Ni-N-C	CO	96 %	−0.70 V vs. RHE	77
Ni-N-C	CO	95 %	−0.90 V vs. RHE	78
Ag SAC/MnO ₂	CO	95.7 %	−0.85 V vs. RHE	79
Ni-N-C	CO	96 %	−0.80 V vs. RHE	80
Ni-N-C	CO	95.6 %	−0.65 V vs. RHE	81
Pd-N ₄	CO	55 %	−0.50 V vs. RHE	82
Ni-N ₄ /C-NH ₂	CO	95 %	−0.70 V vs. RHE	83
FeN ₅ -C	CO	~97 %	−0.46 V vs. RHE	18
Ni-N-C	CO	97 %	−0.80 V vs. RHE	84
Ni-N-C	CO	~97 %	−0.66 V vs. RHE	85
Ni-N-C	CO	96 %	−0.86 V vs. RHE	86
Cu-N-C	CO	96 %	−0.70 V vs. RHE	87
Ni-N-C	CO	~100 %	−0.75 V vs. RHE	88
O-Fe-N-C	CO	95 %	−0.50 V vs. RHE	This work

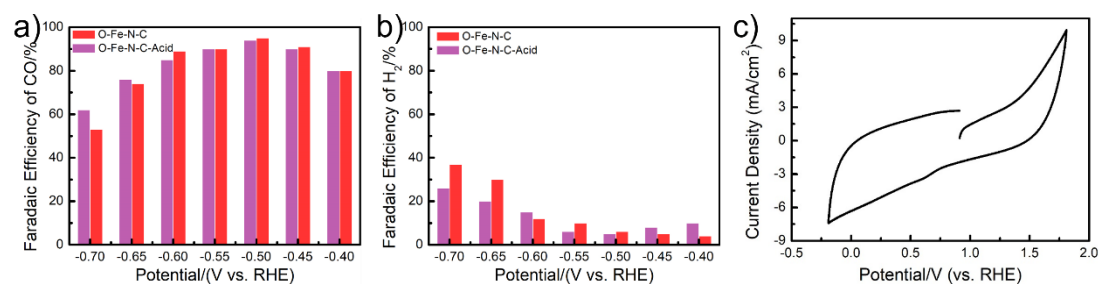


Figure 5.9 (a) FE of CO at various potentials and (b) FE of H₂ at various potentials on O-Fe-N-C and O-Fe-N-C-Acid. (c) CV curves of O-Fe-N-C in 0.5 M Ar-saturated NaHCO₃ electrolyte.

The intrinsic activity of the catalysts was further disclosed by the mass activities of N-C, Fe-N-C and O-Fe-N-C at -0.50 V vs. RHE. Compared to N-C (0.68 A g^{-1}) and Fe-N-C (2.2 A g^{-1}), a much higher mass activity of 4.4 A g^{-1} was obtained for O-Fe-N-C, revealing that the axial O coordination plays a key role toward CO₂ RR. In order to prove that the excellent CO₂ RR performance of the O-Fe-N-C catalyst was attributed to the highly dispersed single active sites rather than Fe nanoparticles or agglomerates, the O-Fe-N-C catalyst was treated with acid to remove the Fe nanoparticles. Inductively coupled plasma atomic emission spectroscopy was performed to evaluate the content of Fe in the O-Fe-N-C catalyst with and without the acid treatment (**Table 5.4**). Compared to the total Fe content in the O-Fe-N-C catalyst without acid treatment (0.73 %), the content of Fe single atoms embedded in the O-Fe-N-C sample after acid treatment, decreased to 0.41 % (wt %), suggesting that the Fe nanoparticles were successfully removed. In contrast to the sharp decrease of the amount of Fe, a neglectful depression of the catalytic activity for O-Fe-N-C after the acid treatment process was observed, as shown in **Figure 5.9a-b**, revealing the dominant impact of the exposed Fe single atoms on the high activity and selectivity. In addition, no Fe reduction/oxidation redox peaks for Fe appeared in the CV curve for the O-Fe-N-C sample (**Figure 5.9c**). In combination with the HAADF STEM, electron energy loss spectroscopy (EELS) elemental mapping, and high-resolution TEM (HRTEM) results, it could be corroborated that the Fe clusters were rigorously encapsulated by a few layers of carbon, which would encumber the interaction between the Fe nanoparticles and the electrolyte, resulting in an inactive performance of these Fe nanoparticles

(Figure 5.10).

Table 5.4. Fe loading ratios of different samples.

Samples	Feeding mass (Fe)	Acid treatment	Final product ratio (Fe)
O-Fe-N-C	20 μ L	No	0.73 %
O-Fe-N-C	20 μ L	Yes	0.41 %

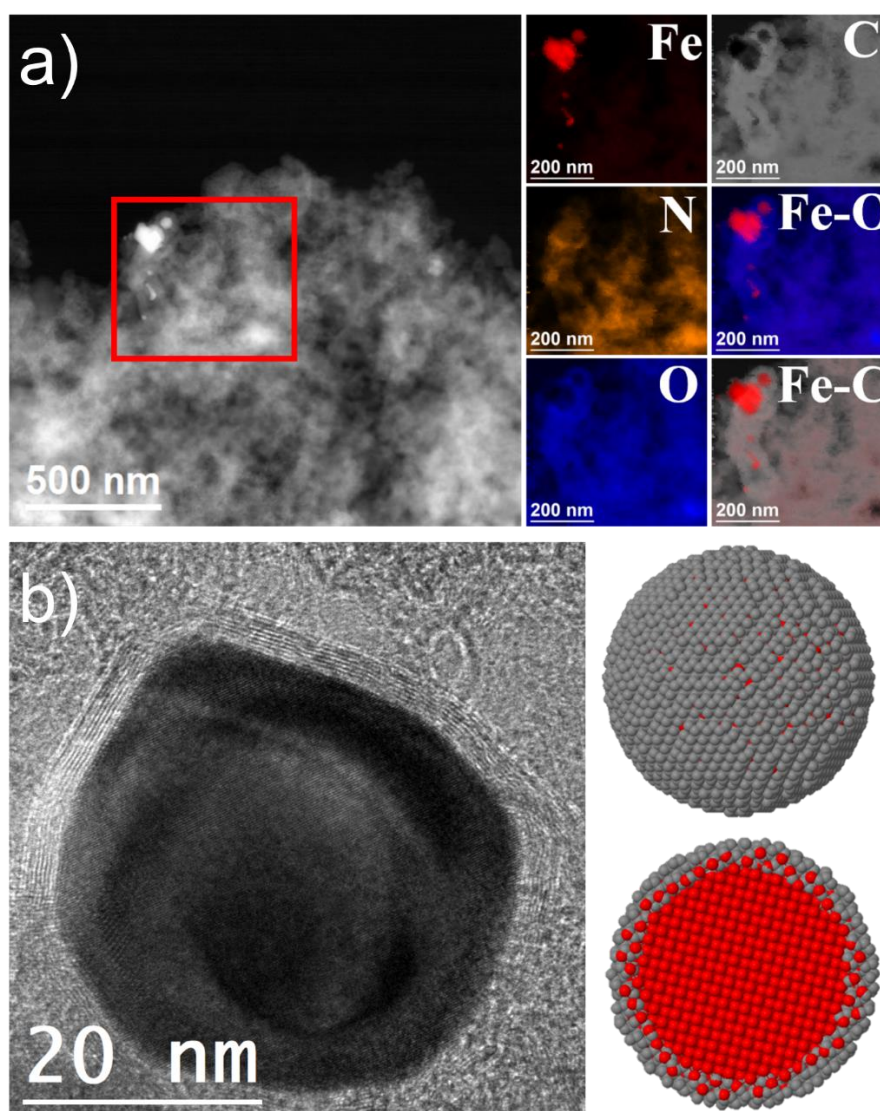


Figure 5.10. (A) HAADF-STEM image of O-Fe-N-C and representative EELS chemical composition maps obtained from the red squared area of the STEM micrograph. Individual Fe $L_{2,3}$ -edges at 708 eV (red), N K-edges at 401 eV (orange), O K-edges at 532 eV (blue) and C K-edges at 285 eV (grey) as well as composites of Fe-O and Fe-C. (B) HRTEM micrographs of O-Fe-N-C sample as well as atomic supercell model illustration of the Fe nanoparticle with carbon shell (Fe and C are represented in red and grey, respectively).

5.3.3 DFT Calculation

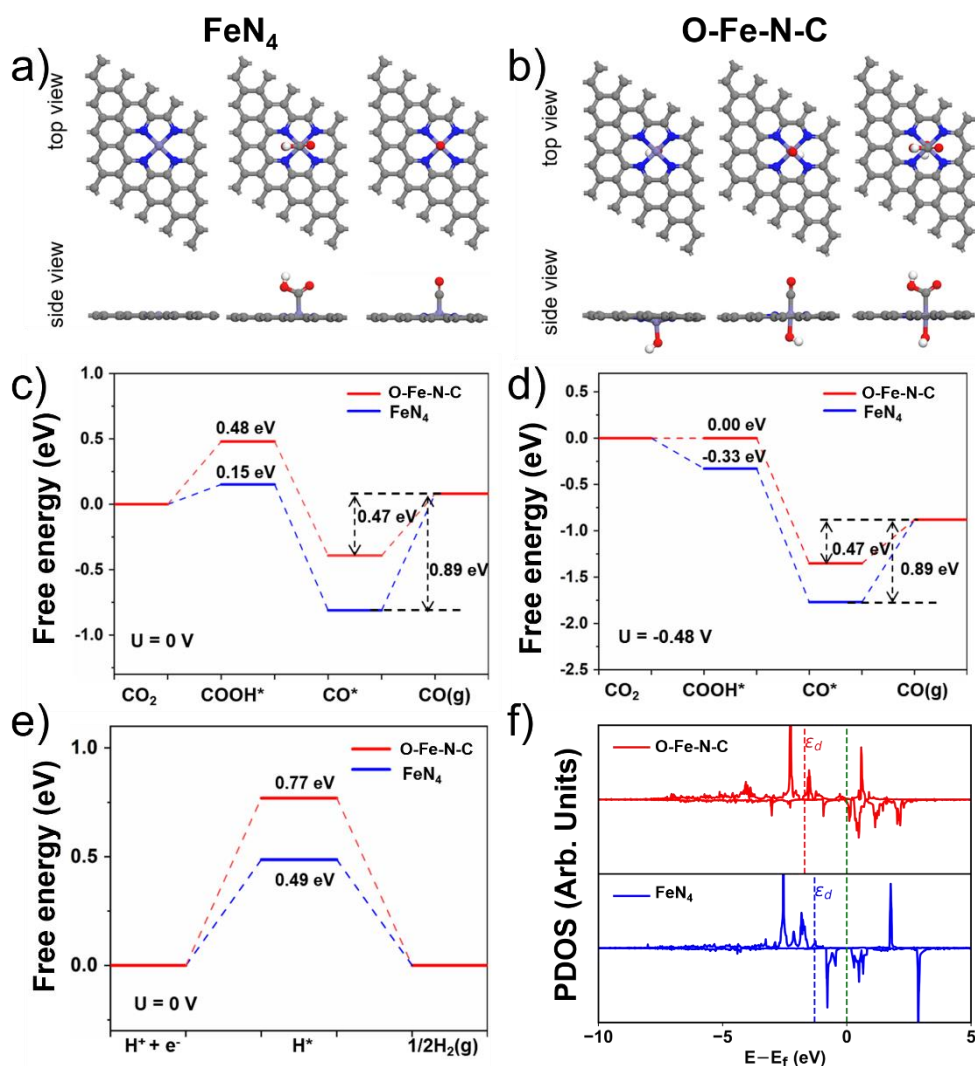


Figure 5.11. (a and b) Top view and side view optimized adsorption configuration on simulated FeN₄ and O-Fe-N-C (Fe, O, N and C atoms are represented in purple, red, blue and grey, respectively). (c) Free energy profiles for the CO₂ RR to CO at 0 V (vs. RHE) and (d) Free energy profiles for the CO₂ RR to CO at -0.48 V (vs. RHE) (e) Free energy profiles for the HER at 0 V (vs. RHE) on simulated FeN₄ and O-Fe-N-C. (f) Projected d-density of states (PDOS) of Fe over O-Fe-N-C and FeN₄ surfaces.

To further understand the intrinsic activity of the axial O group for CO₂ RR, DFT calculations were performed to calculate the free energies of possible intermediates in the reaction pathways from CO₂ to CO by using the computational hydrogen electrode model and parameters reported in the literature.⁸⁹⁻⁹² As the counterpart, we created a simulation model with an Fe atom coordinated with 4 N atoms (tetra-nitrogen) by replacing six C atoms in a graphene surface to represent the reported

normal FeN₄ catalysts.⁹³ For the O-Fe-N-C catalyst, an axial -OH ligand was added to coordinate with the Fe single atom in the simulated FeN₄ catalyst model. The optimized structures and the optimal adsorption configurations of reaction intermediates are shown in **Figure 5.11a** and **Figure 5.11b**. There are three elementary steps and two important intermediates (COOH* and CO*) involved in the CO₂ RR process. Their corresponding free energy profiles at a potential of 0 V vs. RHE are shown in **Figure 5.11c**. The ΔG for the formation of COOH* over O-Fe-N-C and normal FeN₄ were calculated to be 0.48 eV and 0.15 eV, respectively. The ΔG for the dissociation of COOH* assisted by proton-electron transfer to produce CO* and H₂O is downhill on both catalyst models. As for the final step of CO desorption, the ΔG over O-Fe-N-C is 0.47 V, which is significantly lower than that over normal FeN₄ (0.89 eV). Under these circumstances, it is obvious that the potential determining step (PDS) is COOH* formation ($\Delta G = 0.48$ eV) on O-Fe-N-C, while the CO desorption step is more difficult on normal FeN₄ ($\Delta G = 0.89$ eV). As the potential became more negative (-0.48 V vs. RHE), the ΔG for the formation of COOH* decreased, whilst the ΔG for the non-electrochemical step of CO desorption remained unchanged on both models (**Figure 5.11d**). Consequently, CO desorption became the most difficult step on both catalysts' surfaces at -0.48 V vs. RHE. The smaller ΔG of the O-Fe-N-C catalyst (0.47 eV) than the normal FeN₄ (0.89 e) indicated a superior catalytic activity for CO conversion from a thermodynamic perspective. In addition, HER as a side reaction was also considered, and its corresponding free energy profiles were shown in **Figure 5.11e**. It can be concluded that the HER is less active on O-Fe-N-C than that on normal FeN₄. All these results are in good agreement with the experiments. The projected density of states (PDOS) of O-Fe-N-C and normal FeN₄ surfaces were calculated to investigate the origin of the difference between adsorption of the reaction intermediates over these two catalysts, and the results are shown in **Figure 5.11f**. Compared to normal FeN₄, the d-band center of Fe-3d orbits shifted to a more negative value with introduction of an axial O group, which leads to weaker CO adsorption over the O-Fe-N-C, and thus improve the selectivity towards CO.⁹⁴

5.4 Summary

In summary, the axial O coordinated FeN₄ active site was precisely constructed by using a self-sacrificing O and N-rich IRMOF-3. The obtained FeN₄-O sites were experimentally proved to be much more active than the FeN₄ active sites, showing an excellent FE (CO) of 95 % at a low applied potential of -0.50 V vs. RHE. Such performance outperforms previously reported Fe-N-C-based catalysts and most of the reported single atom catalysts at lower overpotential. Meanwhile, DFT simulations revealed that the axial O coordination could not only weaken the binding energy of CO but also inhibit the competitive hydrogen evolution. This work opens a new way for engineering the coordination of FeN₄ sites via heteroatom-rich MOFs precursors.

References

1. Guo, Q. *et al.* Efficient and Selective CO₂ Reduction Integrated with Organic Synthesis by Solar Energy. *Chem* **5**, 2605-2616 (2019).
2. Yang, H. B. *et al.* Atomically Dispersed Ni(I) as the Active Site for Electrochemical CO₂ Reduction. *Nat. Energy* **3**, 140-147 (2018).
3. Nielsen, D. U., Hu, X.-M., Daasbjerg, K. & Skrydstrup, T. Chemically and electrochemically catalysed conversion of CO₂ to CO with follow-up utilization to value-added chemicals. *Nat. Catal.* **1**, 244-254 (2018).
4. You, B. & Sun, Y. Innovative Strategies for Electrocatalytic Water Splitting. *Accounts of Chem. Res.* **51**, 1571-1580 (2018).
5. Cheng, Q. *et al.* Encapsulation of Iron Nitride by Fe–N–C Shell Enabling Highly Efficient Electroreduction of CO₂ to CO. *ACS Energy Lett.* **3**, 1205-1211 (2018).
6. Huang, J. & Buonsanti, R. Colloidal Nanocrystals as Heterogeneous Catalysts for Electrochemical CO₂ Conversion. *Chem. Mater.* **31**, 13-25 (2019).
7. Pei, J. *et al.* N-Bridged Co–N–Ni: new bimetallic sites for promoting electrochemical CO₂ reduction. *Energy Environ. Sci.* **14**, 3019-3028 (2021).
8. Zhao, C. *et al.* Ionic Exchange of Metal–Organic Frameworks to Access Single Nickel Sites for Efficient Electroreduction of CO₂. *J. Am. Chem. Soc.* **139**, 8078-8081 (2017).
9. Zhang, T. *et al.* Quasi-double-star nickel and iron active sites for high-efficiency carbon dioxide electroreduction. *Energy Environ. Sci.* **14**, 4847-4857 (2021).
10. Varela, A. S. *et al.* Electrochemical Reduction of CO₂ on Metal-Nitrogen-Doped Carbon Catalysts. *ACS Catal.* **9**, 7270-7284 (2019).
11. Li, M. *et al.* Heterogeneous Single-Atom Catalysts for Electrochemical CO₂ Reduction Reaction. *Adv. Mater.* **32**, 2001848 (2020).
12. Zhang, G. *et al.* A general route via formamide condensation to prepare atomically dispersed metal–nitrogen–carbon electrocatalysts for energy technologies. *Energy Environ. Sci.* **12**, 1317-1325 (2019).
13. Nguyen, T. N., Salehi, M., Le, Q. V., Seifitokaldani, A. & Dinh, C. T. Fundamentals of Electrochemical CO₂ Reduction on Single-Metal-Atom Catalysts. *ACS Catal.* **10**, 10068-10095 (2020).
14. Hu, X.-M. *et al.* Selective CO₂ Reduction to CO in Water using Earth-Abundant Metal and Nitrogen-Doped Carbon Electrocatalysts. *ACS Catal.* **8**, 6255-6264 (2018).
15. Pan, F. *et al.* Unveiling Active Sites of CO₂ Reduction on Nitrogen-Coordinated and Atomically Dispersed Iron and Cobalt Catalysts. *ACS Catal.* **8**, 3116-3122 (2018).
16. Yang, X., Cheng, J., Xuan, X., Liu, N. & Liu, J. Boosting Defective Carbon by Anchoring Well-Defined Atomically Dispersed Ni–N₄ Sites for Electrocatalytic CO₂ Reduction. *ACS Sustain. Chem. Eng.* **8**, 10536-10543 (2020).
17. Wu, Y. *et al.* Boosting CO₂ Electroreduction over a Cadmium Single-Atom Catalyst by Tuning of the Axial Coordination Structure. *Angew. Chem. Int. Ed.* **60**, 20803-20810 (2021).
18. Zhang, H. *et al.* A Graphene-Supported Single-Atom FeN₅ Catalytic Site for Efficient Electrochemical CO₂ Reduction. *Angew. Chem. Int. Ed.* **58**, 14871-14876 (2019).
19. Pan, Y. *et al.* Design of Single-Atom Co–N₅ Catalytic Site: A Robust Electrocatalyst for CO₂ Reduction with Nearly 100% CO Selectivity and Remarkable Stability. *J. Am. Chem. Soc.* **140**, 4218-4221 (2018).

20. Chen, H. *et al.* Tuning the coordination number of Fe single atoms for the efficient reduction of CO₂. *Green Chem.* **22**, 7529-7536 (2020).
21. Qu, Q., Ji, S., Chen, Y., Wang, D. & Li, Y. The atomic-level regulation of single-atom site catalysts for the electrochemical CO₂ reduction reaction. *Chem. Sci.* **12**, 4201-4215 (2021).
22. Chen, Z. *et al.* Fe₁N₄-O₁ site with axial Fe-O coordination for highly selective CO₂ reduction over a wide potential range. *Energy Environ. Sci.* **14**, 3430-3437 (2021).
23. Wang, X. *et al.* Hierarchically micro- and meso-porous Fe-N₄O-doped carbon as robust electrocatalyst for CO₂ reduction. *Appl. Catal. B* **266**, 118630 (2020).
24. Ji, S. *et al.* Chemical Synthesis of Single Atomic Site Catalysts. *Chem. Rev.* **120**, 11900-11955 (2020).
25. Wei, Y.-S., Zhang, M., Zou, R. & Xu, Q. Metal-Organic Framework-Based Catalysts with Single Metal Sites. *Chem. Rev.* **120**, 12089-12174 (2020).
26. Hou, C.-C., Wang, H.-F., Li, C. & Xu, Q. From Metal-Organic Frameworks to Single/Dual-atom and Cluster Metal Catalysts for Energy Applications. *Energy Environ. Sci.* **13**, 1658-1693 (2020).
27. Jiao, L. & Jiang, H.-L. Metal-Organic-Framework-Based Single-Atom Catalysts for Energy Applications. *Chem* **5**, 786-804 (2019).
28. Zou, L., Wei, Y.-S., Hou, C.-C., Li, C. & Xu, Q. Single-Atom Catalysts Derived from Metal-Organic Frameworks for Electrochemical Applications. *Small* **17**, 2004809 (2021).
29. Lyle, S. J., Flaig, R. W., Cordova, K. E. & Yaghi, O. M. Facilitating Laboratory Research Experience Using Reticular Chemistry. *J Chem. Educ.* **95**, 1512-1519 (2018).
30. Dou, S. *et al.* Boosting Electrochemical CO₂ Reduction on Metal-Organic Frameworks via Ligand Doping. *Angew. Chem. Int. Ed.* **58**, 4041-4045 (2019).
31. Ravel, B. & Newville, M. ATHENA, ARTEMIS, HEPHAESTUS: data analysis for X-ray absorption spectroscopy using IFEFFIT. *J Synchrotron Radiat.* **12**, 537-541 (2005).
32. Baumgartel, H. EXAFS, SEXAFS, XANES: X-Ray Absorption - Principles, Applications, Techniques of EXAFS, SEXAFS and XANES. Von D. Koningsberger und R. Prins. John Wiley & Sons Ltd., Chichester 1988. 673 S., Abb., Tab., Formeln. ISBN 0-471-87547-3. *Nachrichten aus Chemie, Technik und Laboratorium* **36**, 650-650 (1988).
33. Rehr, J. J. & Albers, R. C. Theoretical approaches to x-ray absorption fine structure. *Rev. Mod. Phys.* **72**, 621-654 (2000).
34. Blöchl, P. E. Projector augmented-wave method. *Phys. Rev. B* **50**, 17953-17979 (1994).
35. Kresse, G. & Furthmüller, J. Efficient Iterative Schemes for ab Initio Total-Energy Calculations Using a Plane-Wave Basis Set. *Phys. Rev. B* **54**, 11169-11186 (1996).
36. Kresse, G. & Furthmüller, J. Efficiency of ab-initio total energy calculations for metals and semiconductors using a plane-wave basis set. *Comput. Mater. Sci.* **6**, 15-50 (1996).
37. Kresse, G. & Joubert, D. From Ultrasoft Pseudopotentials to the Projector Augmented-Wave Method. *Phys. Rev. B* **59**, 1758-1775 (1999).
38. Hafner, J. Ab-Initio Simulations of Materials Using VASP: Density-Functional Theory and Beyond. *J. Comput. Chem.* **29**, 2044 (2008).
39. Wellendorff, J. *et al.* Density Functionals for Surface Science: Exchange-Correlation Model Development with Bayesian Error Estimation. *Phys. Rev. B* **85**, 235149 (2012).
40. Studt, F. *et al.* The Mechanism of CO and CO₂ Hydrogenation to Methanol over Cu-Based Catalysts. *ChemCatChem* **7**, 1105-1111 (2015).
41. Studt, F., Abild-Pedersen, F., Varley, J. B. & Nørskov, J. K. CO and CO₂ Hydrogenation to Methanol Calculated Using the BEEF-vdW Functional. *Catal. Lett.* **143**, 71-73 (2013).

42. Christensen, R., Hansen, H. A. & Vegge, T. Identifying Systematic DFT Errors in Catalytic Reactions. *Catal. Sci. Technol.* **5**, 4946-4949 (2015).
43. Peterson, A. A., Abild-Pedersen, F., Studt, F., Rossmeisl, J. & Nørskov, J. K. How Copper Catalyzes the Electroreduction of Carbon Dioxide into Hydrocarbon Fuels. *Energy Environ. Sci.* **3**, 1311-1315 (2010).
44. Chan, K., Tsai, C., Hansen, H. A. & Nørskov, J. K. Molybdenum Sulfides and Selenides as Possible Electrocatalysts for CO₂ Reduction. *ChemCatChem* **6**, 1899-1905 (2014).
45. Ye, L. *et al.* Highly Efficient Porous Carbon Electrocatalyst with Controllable N-Species Content for Selective CO₂ Reduction. *Angew. Chem. Int. Ed.* **59**, 3244-3251 (2020).
46. Ren, W. *et al.* Isolated Diatomic Ni-Fe Metal–Nitrogen Sites for Synergistic Electroreduction of CO₂. *Angew. Chem. Int. Ed.* **58**, 6972-6976 (2019).
47. Ao, X. *et al.* Markedly Enhanced Oxygen Reduction Activity of Single-Atom Fe Catalysts via Integration with Fe Nanoclusters. *ACS Nano* **13**, 11853-11862 (2019).
48. Zhao, C. *et al.* Solid-Diffusion Synthesis of Single-Atom Catalysts Directly from Bulk Metal for Efficient CO₂ Reduction. *Joule* **3**, 584-594 (2019).
49. Gong, L. *et al.* Bridge Bonded Oxygen Ligands between Approximated FeN₄ Sites Confer Catalysts with High ORR Performance. *Angew. Chem. Int. Ed.* **59**, 13923-13928 (2020).
50. Lou, Y., Liu, J., Liu, M. & Wang, F. Hexagonal Fe₂N Coupled with N-Doped Carbon: Crystal-Plane-Dependent Electrocatalytic Activity for Oxygen Reduction. *ACS Catal.* **10**, 2443-2451 (2020).
51. Wang, J. *et al.* N-Coordinated Dual-Metal Single-Site Catalyst for Low-Temperature CO Oxidation. *ACS Catal.* **10**, 2754-2761 (2020).
52. Wang, Q. *et al.* Evolution of Zn(II) single atom catalyst sites during the pyrolysis-induced transformation of ZIF-8 to N-doped carbons. *Sci. Bull.* **65**, 1743-1751 (2020).
53. Yin, P. *et al.* Single Cobalt Atoms with Precise N-Coordination as Superior Oxygen Reduction Reaction Catalysts. *Angew. Chem. Int. Ed.* **55**, 10800-10805 (2016).
54. Wang, X. X. *et al.* Nitrogen-Coordinated Single Cobalt Atom Catalysts for Oxygen Reduction in Proton Exchange Membrane Fuel Cells. *Adv. Mater.* **30**, 1706758 (2018).
55. Li, J. *et al.* Atomically dispersed manganese catalysts for oxygen reduction in proton-exchange membrane fuel cells. *Nat. Catal.* **1**, 935-945 (2018).
56. Jiao, L. *et al.* From Metal–Organic Frameworks to Single-Atom Fe Implanted N-doped Porous Carbons: Efficient Oxygen Reduction in Both Alkaline and Acidic Media. *Angew. Chem. Int. Ed.* **57**, 8525-8529 (2018).
57. Li, J. *et al.* Volcano Trend in Electrocatalytic CO₂ Reduction Activity over Atomically Dispersed Metal Sites on Nitrogen-Doped Carbon. *ACS Catal.* **9**, 10426-10439 (2019).
58. Chen, Y. *et al.* Isolated Single Iron Atoms Anchored on N-Doped Porous Carbon as an Efficient Electrocatalyst for the Oxygen Reduction Reaction. *Angew. Chem. Int. Ed.* **56**, 6937-6941 (2017).
59. Cheng, X. *et al.* Nano-geometric deformation and synergistic Co nanoparticles—Co-N₄ composite sites for proton exchange membrane fuel cells. *Energy Environ. Sci.* **14**, 5958-5967 (2021).
60. Cartier, C. *et al.* X-Ray absorption spectroscopy of iron-(II) and -(III) basket-handle porphyrins. *J. Chem. Soc., Dalton Trans.*, 609-618 (1992).
61. Westre, T. E. *et al.* A Multiplet Analysis of Fe K-Edge 1s → 3d Pre-Edge Features of Iron Complexes. *J. Am. Chem. Soc.* **119**, 6297-6314 (1997).
62. Sun, X. *et al.* Phosphorus Induced Electron Localization of Single Iron Sites for Boosted CO₂ Electroreduction Reaction. *Angew. Chem. Int. Ed.* **60**, 23614-23618 (2021).

63. Bushuyev, O. S. *et al.* What Should We Make with CO₂ and How Can We Make It? *Joule* **2**, 825-832 (2018).
64. Bi, W. *et al.* Surface Immobilization of Transition Metal Ions on Nitrogen-Doped Graphene Realizing High-Efficient and Selective CO₂ Reduction. *Adv. Mater.* **30**, 1706617 (2018).
65. Huan, T. N. *et al.* Electrochemical Reduction of CO₂ Catalyzed by Fe-N-C Materials: A Structure–Selectivity Study. *ACS Catalysis* **7**, 1520-1525 (2017).
66. Chen, Y. *et al.* Fe and N Co-Doped Porous Carbon Nanospheres with High Density of Active Sites for Efficient CO₂ Electroreduction. *J. Phys. Chem. C* **123**, 16651-16659, doi:10.1021/acs.jpcc.9b02195 (2019).
67. Gu, J., Hsu, C.-S., Bai, L., Chen, H. M. & Hu, X. Atomically dispersed Fe³⁺ sites catalyze efficient CO₂ electroreduction to CO. *Science* **364**, 1091-1094 (2019).
68. Tuo, J. *et al.* Layered Confinement Reaction: Atomic-level Dispersed Iron–Nitrogen Co-Doped Ultrathin Carbon Nanosheets for CO₂ Electroreduction. *ChemSusChem* **12**, 2644-2650 (2019).
69. Wu, S. *et al.* Highly exposed atomic Fe–N active sites within carbon nanorods towards electrocatalytic reduction of CO₂ to CO. *Electrochim. Acta* **340**, 135930 (2020).
70. Zhu, Y. *et al.* Single-Atom Iron-Nitrogen Catalytic Site with Graphitic Nitrogen for Efficient Electroreduction of CO₂. *ChemistrySelect* **5**, 1282-1287 (2020).
71. Chen, X. *et al.* Metal–organic framework-derived mesoporous carbon nanoframes embedded with atomically dispersed Fe–N_x active sites for efficient bifunctional oxygen and carbon dioxide electroreduction. *Appl. Catal. B* **267**, 118720 (2020).
72. Zhang, E. *et al.* Bismuth Single Atoms Resulting from Transformation of Metal–Organic Frameworks and Their Use as Electrocatalysts for CO₂ Reduction. *J. Am. Chem. Soc.* **141**, 16569-16573 (2019).
73. Gong, Y.-N. *et al.* Regulating the Coordination Environment of MOF-Templated Single-Atom Nickel Electrocatalysts for Boosting CO₂ Reduction. *Angew. Chem. Int. Ed.* **59**, 2705-2709 (2020).
74. Yan, C. *et al.* Coordinatively unsaturated nickel–nitrogen sites towards selective and high-rate CO₂ electroreduction. *Energy Environ. Sci.* **11**, 1204-1210 (2018).
75. Wang, X. *et al.* Regulation of Coordination Number over Single Co Sites: Triggering the Efficient Electroreduction of CO₂. *Angew. Chem. Int. Ed.* **57**, 1944-1948 (2018).
76. Yang, H. *et al.* Highly efficient utilization of single atoms via constructing 3D and free-standing electrodes for CO₂ reduction with ultrahigh current density. *Nano Energy* **70**, 104454 (2020).
77. Yang, H. *et al.* Carbon dioxide electroreduction on single-atom nickel decorated carbon membranes with industry compatible current densities. *Nat. Commun.* **11**, 593 (2020).
78. Xiong, W. *et al.* Hollow Mesoporous Carbon Sphere Loaded Ni–N₄ Single-Atom: Support Structure Study for CO₂ Electrocatalytic Reduction Catalyst. *Small* **16**, 2003943 (2020).
79. Zhang, N. *et al.* Silver Single-Atom Catalyst for Efficient Electrochemical CO₂ Reduction Synthesized from Thermal Transformation and Surface Reconstruction. *Angew. Chem. Int. Ed.* **60**, 6170-6176 (2021).
80. Rong, X., Wang, H.-J., Lu, X.-L., Si, R. & Lu, T.-B. Controlled Synthesis of a Vacancy-Defect Single-Atom Catalyst for Boosting CO₂ Electroreduction. *Angew. Chem. Int. Ed.* **59**, 1961-1965 (2020).
81. Zhang, Y., Jiao, L., Yang, W., Xie, C. & Jiang, H.-L. Rational Fabrication of Low-Coordinate Single-Atom Ni Electrocatalysts by MOFs for Highly Selective CO₂ Reduction. *Angew. Chem. Int. Ed.* **60**, 7607-7611 (2021).
82. He, Q. *et al.* Accelerating CO₂ Electroreduction to CO Over Pd Single-Atom Catalyst. *Adv. Funct. Mater.* **30**, 2000407 (2020).

83. Chen, Z. *et al.* Amination strategy to boost the CO₂ electroreduction current density of M–N/C single-atom catalysts to the industrial application level. *Energy Environ. Sci.* **14**, 2349-2356 (2021).
84. Jiang, K. *et al.* Isolated Ni single atoms in graphene nanosheets for high-performance CO₂ reduction. *Energy Environ. Sci.* **11**, 893-903 (2018).
85. Wang, X. *et al.* Universal domino reaction strategy for mass production of single-atom metal-nitrogen catalysts for boosting CO₂ electroreduction. *Nano Energy* **82**, 105689 (2021).
86. Lu, Y. *et al.* Isolated Ni single atoms in nitrogen doped ultrathin porous carbon templated from porous g-C₃N₄ for high-performance CO₂ reduction. *Nano Energy* **77**, 105158 (2020).
87. Yang, F. *et al.* Scalable strategy to fabricate single Cu atoms coordinated carbons for efficient electroreduction of CO₂ to CO. *Carbon* **168**, 528-535 (2020).
88. Zheng, T. *et al.* Large-Scale and Highly Selective CO₂ Electrocatalytic Reduction on Nickel Single-Atom Catalyst. *Joule* **3**, 265-278 (2019).
89. Nørskov, J. K. *et al.* Origin of the Overpotential for Oxygen Reduction at a Fuel-Cell Cathode. *J. Phys. Chem. B* **108**, 17886-17892 (2004).
90. Liu, H., Liu, J. & Yang, B. Modeling the effect of surface CO coverage on the electrocatalytic reduction of CO₂ to CO on Pd surfaces. *Phys. Chem. Chem. Phys.* **21**, 9876-9882 (2019).
91. Liu, H., Liu, J. & Yang, B. Computational insights into the strain effect on the electrocatalytic reduction of CO₂ to CO on Pd surfaces. *Phys. Chem. Chem. Phys.* **22**, 9600-9606 (2020).
92. Li, J. *et al.* Tuning the Electronic Bandgap of Graphdiyne by H-Substitution to Promote Interfacial Charge Carrier Separation for Enhanced Photocatalytic Hydrogen Production. *Adv. Funct. Mater.* **31**, 2100994 (2021).
93. Li, J., Liu, J. & Yang, B. Insights into the adsorption/desorption of CO₂ and CO on single-atom Fe-nitrogen-graphene catalyst under electrochemical environment. *J. Energy Chem.* **53**, 20-25 (2021).
94. Liu, X. *et al.* Fe₂N nanoparticles boosting FeN_x moieties for highly efficient oxygen reduction reaction in Fe-N-C porous catalyst. *Nano Research* **12**, 1651-1657 (2019).

Chapter 6

General Conclusions and Outlook

In this dissertation, we devoted our efforts in order to regulate the catalytic performance on prepared catalysts via tailoring the apparent physical structures or chemical properties and intrinsic electronic structures. Based on the reaction mechanism of CO_2 to CO conversion, the different reaction steps, namely CO_2 adsorption, intermediate formation and desorption, have been taken into account in order to improve the design process of catalysts. As a result, the selectivity and activity of the fabricated catalysts could be improved by the optimization of one or more of these steps.

The structural characterization of as-prepared samples was achieved by the utilization of XRD, XPS, XAS, Raman spectroscopy; SEM, EDS and specially (S)TEM advanced techniques. In addition, combining different characterization and electrochemical methods, DFT theoretical calculations as an important method provided a prediction or support to testify our design and proposal reasonably.

Firstly, we synthesized ZnO-based catalysts with functional surficial $-\text{OH}$ groups which could promote the CO_2 adsorption at the beginning of the CO_2 -to- CO conversion. Then we constructed porous structures on the surface of ZnO nanorods to strengthen the local environment during the reaction process. The obtained microenvironment owned many properties such as hydrophobicity, high local pH as well as the ability to retain a high local concentration of CO_2 . All these properties could suppress the HER to enhance the efficiency of CO_2 RR. At the last step of the CO_2 -to- CO conversion, the desorption of the final intermediate CO^* could directly affect the selectivity for CO product. In order to improve this latest step, axial bonded O coordination to the typical FeN_4 single atom catalyst was achieved via utilizing an oxygen and nitrogen-rich MOF as precursor. In this way, a precise control of the electron structure of Fe sites was shown to weak the binding energy of CO to realize the effective desorption of CO^* .

6.1 General Conclusions

Low concentration of CO_2 around the active sites limits the following generation of

intermediates during the CO₂-to-CO conversion. Surface dioxide-philic functional groups could increase the affinity between CO₂ molecules and active sites at the stage from free state to adsorption state of CO₂. In **Chapter 3**, we have described a strategy to synthesize ZnO covered by dioxide-philic functional groups via a simple ZIF-8-assisted method. The synthesized –OH-rich ZnO presents a FE_{CO} maximum of 85 % at –0.95 V vs. RHE, which is the best record among the state-of-the-art ZnO-based catalysts. DFT calculations confirmed that –OH not only lower the barriers for adsorption of CO₂ at the interface at the initial stage but also promote the transformation and generation of COOH* and CO* intermediates.

During the CO₂ RR process, the local environment near the active sites presents a dynamic variation. This variation could disturb kinetics and the reaction pathway but also promote certain reactions. In addition to add functional groups on the surface of the active sites, it is more attractive to construct more complex structure to introduce more favourable condition to multi-proton and multi-electron CO₂ RR pathways in terms of improving the selectivity and productivity. In **chapter 4**, we utilized ZnO nanorods as metal source for the in-situ growth of ZIF-8 layer directly to construct interface structure. The optimized interface between ZnO NRs and ZIF-8 showed a remarkable CO₂ RR activity in 0.5 M NaHCO₃ solution, accompanied by an excellent selectivity with Faradaic efficiency of CO (85 %) at –1.05 V vs. RHE, which is superior to that of pristine ZnO NRs. This layer inherited the CO₂ affinity and hydrophobicity of ZIF-8 which realize the high concentrations of CO₂ molecules around the active sites. We evaluated the pristine ZnO NRs and ZnO@ZIF-8 in different electrolyte to verify the local pH effect induced by the porous structure on the surface of ZnO. The results confirmed that the nanoporous structure increased the local pH of active sites which could influence the reaction selectivity.

In CO₂ RR, binding energy between the intermediate CO* and active sites determines the type of final product. In other words, facilitating CO* desorption from active sites could improve the selectivity towards CO product. With this in mind, in **Chapter 5** we

changed the coordination state of FeN₄ active sites to effectively enhance the catalytic performance of the obtained catalysts via promoting the desorption of CO*. Precisely, active sites of Fe-N-C catalysts with an axial oxygen subgroup were prepared by using an oxygen and nitrogen-rich MOF, instead of simple N-containing precursors. The Zn-based IRMOF-3, assembled from Zn²⁺ nodes and 2-aminoterephthalic acid ligands, caters for the fabrication requirements, not only allowing the stabilization of foreign Fe ions as a self-sacrificial platform, but also providing nitrogen/oxygen-rich sources from organic ligands. TEM and XAS furtherly characterize the neighbouring environment of Fe active sites. Benefiting from the difference of local environment, catalysts show a remarkable CO₂ RR activity in 0.5 M NaHCO₃ solution, accompanied by an excellent selectivity with Faradaic efficiency of CO (95 %) at -0.50 V vs. RHE, as well as a robust stability, which are superior to those of the previously reported Fe-N-C-based materials. Moreover, the selectivity could be retained over 80 % in a range of working potentials from -0.40 to -0.60 V vs. RHE. The theoretical results further proved that axial O coordinated FeN₄ via oxygen-containing subgroups could effectively boost the CO₂ RR activity through reducing the binding energies of CO desorption and disfavoring the hydrogen evolution reaction (HER).

CO₂ RR is a reaction including gas, liquid and solid three phases involving a multi-proton and multi-electron process. We must balance all factors when optimizing the catalysts. From **chapter 3** to **Chapter 5**, we focused on different steps or intermediates of CO₂-to-CO conversion to optimize this conversion. The experimental and calculation results prove that our optimization strategies are reasonable.

6.2 Outlook

Over the past decade, enormous efforts have been made towards the design of electrocatalysts with improved CO₂ RR efficiencies. As a multi-path reaction, the reaction intermediates are complex during CO₂ RR. Through the real-time detection of the active sites and reaction intermediates, the dynamic process of the CO₂ RR will be

able to be clearly revealed, which will be helpful to precisely understand the catalytic mechanisms and design efficient CO₂ catalytic systems. In-situ/operando studies combined with other characterization methods will play key roles in revealing dynamic evolution of the catalysts and detecting intermediate states of the reaction processes. The deeper our understanding on the relationship of structures and catalytic performance, the more efficient and rational we can be in designing and synthesizing catalysts. In addition to the catalyst itself, the CO₂RR is extremely sensitive to the changes in local pH, electrolytes and cations. Integration and regulation of these factors could improve the catalytic performance in the practical application of neutralizing CO₂ emissions on a global scale. Therefore, new devices with long-term operation (>20000 hours) at substantial current density (> 200 mA cm⁻²) need to be explored. Until now, most of catalytic materials are studied and characterized in classical H-cell configurations, where current densities are limited. If we only use these results to optimize the catalytic properties rather than under more realistic operating conditions such as high current density, optimization direction may deviate. Therefore, the subtle flow cell reactors should be exploited as an important factor to evaluate the catalytic performance for new catalysts. Theoretical calculations and simulation can give deeper insights into both the stepwise elementary reaction mechanism and the catalytic performance. Recently, the constant improvement of computing power such as machine learning and deep learning, allows intelligent prediction of new catalysts. High-throughput methods furtherly realize efficient screening of potential catalysts.

Catalyst engineering and catalyst development strategies for e CO₂ RR are based on tailoring apparent physical structure and tailoring intrinsic electronic structures. In fact, in most cases these two kinds of strategies are not mutually exclusive and can be used to collaboratively solve problems and to maximize performance. With increased structural complexity, some new phenomena, such as the restructuring effect, tandem effect and multiscale effect, provide more possibilities to accelerate CO₂ activation and transformation.

No research field can solve this challenge alone. Interdisciplinary fields including chemistry, materials science, life sciences and systems analysis, should be mutually reinforcing and complementary. We are looking forward to realizing the goal of carbon neutrality in the foreseeable future.

List of Publications:

1. **Xu Han**, Ting Zhang, Martí Biset-Peiró, Xuan Zhang, Pengyi Tang, Weiqiang Tang,* Jian Li,* Joan Ramon Morante and **Jordi Arbiol***, Engineering the Interfacial Microenvironment to Realize the Global Optimization of Electrochemical CO₂ Reduction, *ACS Applied Materials & Interfaces*, **Under review**
2. **Xu Han**, Ting Zhang, Martí Biset-Peiró, Xuan Zhang, Joan Ramon Morante and **Jordi Arbiol***, Interface Engineering of MOFs-Based Heterostructures for Electrochemical CO₂ Reduction Reaction at A Wide Potential, **To be submitted**
3. **Xu Han**, et al. and **Jordi Arbiol***, Coordination Engineering of Zirconium Single Atom Catalyst for Electrochemical CO₂ Reduction Reaction, **In preparation**
4. **Xu Han**[†], Gerard Boix[†], Mateusz Balcerzak, Oscar Hernando Moriones, Mary Cano-Sarabia, Pilar Cortés, Neus Bastús, Victor Puentes, Montserrat Llagostera, Inhar Imaz* and Daniel MasPOCH*, Antibacterial films based on MOF composites that release iodine passively or upon triggering by near-infrared light, *Advanced Functional Materials*, 2022, 2112902.
5. Ting Zhang^{†*}, **Xu Han**[†], Hong Liu[†], Martí Biset-Peiró, Jian Li,* Xuan Zhang, Pengyi Tang, Bo Yang, Lirong Zheng,* Joan Ramon Morante, and **Jordi Arbiol***, Site-Specific Axial Oxygen Coordinated FeN₄ Active Sites for Highly Selective Electroreduction of Carbon Dioxide, *Advanced Functional Materials*, 2022, DOI: 10.1002/adfm.202111446.
6. Junshan Li, Xiang Wang, Congcong Xing, Luming Li, Shijia Mu, **Xu Han**, Ren He, Zhifu Liang, Paulina Martinez, Yunan Yi, Qianbao Wu, Huiyan Pan, **Jordi Arbiol**, Chunhua Cui, Yu Zhang, Andreu Cabot, Electrochemical reforming of ethanol with acetate Co-Production on nickel cobalt selenide nanoparticles, *Chemical Engineering Journal*, 2022, 440, 135817.
7. Ruifeng Du, Baoying Li, **Xu Han**, Ke Xiao, Xiang Wang, Chaoqi Zhang, **Jordi Arbiol**, Andreu Cabot, 2D/2D Heterojunction of TiO₂ Nanoparticles and Ultrathin G-C₃N₄ Nanosheets for Efficient Photocatalytic Hydrogen Evolution, *Nanomaterials*, 2022, 12, 1557.
8. Xiang Wang, Linlin Yang, Congcong Xing, **Xu Han**, Ruifeng Du, Ren He, Pablo Guardia, **Jordi Arbiol**, Andreu Cabot, MOF-Derived Ultrathin Cobalt Molybdenum Phosphide Nanosheets for Efficient Electrochemical Overall Water Splitting, *Nanomaterials*, 2022, 12, 1098.
9. Ruifeng Du, Ke Xiao, Baoying Li, **Xu Han**, Chaoqi Zhang, Xiang Wang, Yong Zuo, Pablo Guardia, Junshan Li, Jianbin Chen, **Jordi Arbiol**, Andreu Cabot, Controlled oxygen doping in highly dispersed Ni-loaded g-C₃N₄ nanotubes for efficient photocatalytic H₂O₂ production, *Chemical Engineering Journal*, 2022, DOI: 10.1016/j.cej.2022.135999
10. Mengyao Li, Dawei Yang, Jordi Jacas Biendicho, **Xu Han**, Chaoqi Zhang, Kun Liu, Jiefeng Diao, Junshan Li, Jing Wang, Marc Heggen, Rafal E Dunin - Borkowski, Jiaao Wang, Graeme Henkelman, Joan Ramon Morante, **Jordi Arbiol**, Shu-Lei Chou, Andreu Cabot, Enhanced Polysulfide Conversion with Highly Conductive and Electrocatalytic Iodine-Doped Bismuth Selenide Nanosheets in Lithium-Sulfur Batteries, *Advanced Functional Materials*, 2022, DOI: 10.1002/adfm.202200529.

11. Gerard Boix, **Xu Han**, Inhar Imaz, Daniel Maspoch*, Millimeter-Shaped Metal–Organic Framework/Inorganic Nanoparticle Composite as a New Adsorbent for Home Water-Purification Filters, *ACS Applied Materials & Interfaces*, 2021, 13, 17835-17843.
12. Ting Zhang, **Xu Han**, Hong Liu, Martí Biset-Peiró, Xuan Zhang, Pengyi Tang,* Bo Yang, Lirong Zheng,* Joan Ramon Morante, **Jordi Arbiol***, Quasi-Double-Star Nickel and Iron Active Sites for High-Efficient Carbon Dioxide Electroreduction, *Energy & Environmental Science*, 2021, 14, 4847-4857.
13. Xiang Wang, Congcong Xing, Zhifu Liang, Pablo Guardia, **Xu Han**, Yong Zuo, Jordi Llorca, **Jordi Arbiol**, Junshan Li, Andreu Cabot, Activating the lattice oxygen oxidation mechanism in amorphous molybdenum cobalt oxide nanosheets for water oxidation, *Journal of Materials Chemistry A*, 2022, 10, 3659-3666.
14. Wei Zhang+, Ning Han+, Jiangshui Luo*, **Xu Han**, Shihui Feng, Wei Guo, Sijie Xie, Zhenyu Zhou, Palaniappan Subramanian, Kai Wan, **Jordi Arbiol**, Chi Zhang, Shaomin Liu, Maowen Xu, Xuan Zhang*, Jan Fransaer*, Critical Role of Phosphorus in Hollow Structures Cobalt-Based Phosphides as Bifunctional Catalysts for Water Splitting, *Small*, 2021, DOI: 10.1002/smll.202103561.
15. Mengyao Li, Yu Liu*, Yu Zhang, **Xu Han**, Ke Xiao, Mehran Nabahat, **Jordi Arbiol**, Jordi Llorca, Maria Ibáñez, Andreu Cabot*, PbS-Pb-Cu_xS Composites for Thermoelectric Application, *ACS Applied Materials & Interfaces*, 2021, 13, 51373-51382.
16. Yu Zhang, Congcong Xing, Yu Liu, Mengyao Li, Ke Xiao, Pablo Guardia, Seungho Lee, **Xu Han**, Ahmad Ostovari Moghaddam, Joan Josep Roa, **Jordi Arbiol**, Maria Ibáñez, Kai Pan, Mirko Prato, Ying Xie, Andreu Cabot*, Influence of copper telluride nanodomains on the transport properties of n-type bismuth telluride, *Chemical Engineering Journal*, 2021, 418, 129374.
17. Mengyao Li, Yu Liu, Yu Zhang, **Xu Han**, Ting Zhang, Yong Zuo, Chenyang Xie, Ke Xiao, **Jordi Arbiol**, Jordi Llorca, Maria Ibáñez, Junfeng Liu,* Andreu Cabot,* Effect of the Annealing Atmosphere on Crystal Phase and Thermoelectric Properties of Copper Sulfide, *ACS Nano*, 2021, 15, 4967-4978.
18. Congcong Xing, Yongpeng Liu, Yu Zhang, Xiang Wang, Pablo Guardia, Liang Yao, **Xu Han**, Ting Zhang, **Jordi Arbiol**, Lluís Soler, Yufen Chen, Kevin Sivula, Néstor Guijarro, Andreu Cabot,* Jordi Llorca,* A Direct Z-Scheme for the Photocatalytic Hydrogen Production from a Water/Ethanol Mixture on CoTiO₃/TiO₂ Heterostructures, *ACS Applied Materials & Interfaces*, 2021, 13, 1, 449.
19. Jian Li, Amine Slassi, **Xu Han**, David Cornil, Minh-Huong Ha-Thi, Thomas Pino, Damien P Debecker, Christophe Colbeau-Justin, **Jordi Arbiol**, Jérôme Cornil, Mohamed Nawfal Ghazzal*, Tuning the Electronic Bandgap of Graphdiyne by H-Substitution to Promote Interfacial Charge Carrier Separation for Enhanced Photocatalytic Hydrogen Production, *Advanced Functional Materials*, 2021, DOI: 10.1002/adfm.202100994.
20. Junshan Li, Ruilin Wei, Xiang Wang, Yong Zuo, **Xu Han**, **Jordi Arbiol**, Jordi Llorca, Yaoyue Yang, Andreu Cabot*, Chunhua Cui*, Selective Methanol-to-Formate Electrocatalytic Conversion on Branched Nickel Carbide, *Angewandte Chemie International Edition*, 2020, 132, 21012-21016.
21. Dawei Yang, Chaoqi Zhang*, Jordi Jacas Biendicho, **Xu Han**, Zhifu Liang, Ruifeng Du, Mengyao Li, Junshan Li, **Jordi Arbiol**, Jordi Llorca, Yingtang Zhou, Joan Ramon Morante,

- Andreu Cabot*, ZnSe/N-doped carbon nanoreactor with multiple adsorption sites for stable lithium–sulfur batteries, *ACS Nano*, 2020, 14, 15492-15504.
22. Yong Zuo, Xijun Xu, Chaoqi Zhang, Junshan Li, Ruifeng Du, Xiang Wang, **Xu Han**, **Jordi Arbiol**, Jordi Llorca, Jun Liu, Andreu Cabot*, *Electrochimica Acta*, 2020, 349, 136369.
 23. Junshan Li, Xu Xijun, Xiaoting Yu, **Xu Han**, Ting Zhang, Yong Zuo, Chaoqi Zhang, Dawei Yang, Xiang Wang, Zhishan Luo, **Jordi Arbiol**, Jordi Llorca, Jun Liu, Andreu Cabot, Monodisperse CoSn and NiSn Nanoparticles Supported on Commercial Carbon as Anode for Lithium-and Potassium-ion Batteries, *ACS Applied Materials & Interfaces*, 2020, 12, 4, 4414.
 24. Yu Zhang, Yu Liu*, Mariano Calcabrini, Congcong Xing, **Xu Han**, **Jordi Arbiol**, Doris Cadavid, Maria Ibáñez, Andreu Cabot*, Bismuth telluride–copper telluride nanocomposites from heterostructured building blocks, *Journal of Materials Chemistry C*, 2020, 8, 14092-14099.
 25. Yong Zuo, Yongpeng Liu, Junshan Li, Ruifeng Du, **Xu Han**, Ting Zhang, **Jordi Arbiol**, Nuria J. Divins, Jordi Llorca, Nestor Guijarro, Kevin Sivula, and Andreu Cabot, In Situ Electrochemical Oxidation of Cu₂S into CuO Nanowires as a Durable and Efficient Electrocatalyst for Oxygen Evolution Reaction, *Chemistry of Materials*, 2019, 331, 7732.

High-efficient eCO₂ RR is still on the way

